

# **A Novel Approach for Practical Modelling of Steel Corrosion in Concrete**

by

**Mohammad Pour-Ghaz**

This thesis is submitted to the Faculty of Graduate Studies and Research in  
partial fulfilment of requirements for the degree of

**Master of Applied Science**

Department of Civil and Environmental Engineering

Carleton University

Ottawa, Ontario, Canada

The Master of Applied Science in Civil Engineering is a joint program with the  
University of Ottawa, administered by Ottawa-Carleton Institute for Civil Engineering

© 2007, Mohammad Pour-Ghaz



Library and  
Archives Canada

Bibliothèque et  
Archives Canada

Published Heritage  
Branch

Direction du  
Patrimoine de l'édition

395 Wellington Street  
Ottawa ON K1A 0N4  
Canada

395, rue Wellington  
Ottawa ON K1A 0N4  
Canada

*Your file* *Votre référence*

*ISBN: 978-0-494-33785-1*

*Our file* *Notre référence*

*ISBN: 978-0-494-33785-1*

#### NOTICE:

The author has granted a non-exclusive license allowing Library and Archives Canada to reproduce, publish, archive, preserve, conserve, communicate to the public by telecommunication or on the Internet, loan, distribute and sell theses worldwide, for commercial or non-commercial purposes, in microform, paper, electronic and/or any other formats.

The author retains copyright ownership and moral rights in this thesis. Neither the thesis nor substantial extracts from it may be printed or otherwise reproduced without the author's permission.

#### AVIS:

L'auteur a accordé une licence non exclusive permettant à la Bibliothèque et Archives Canada de reproduire, publier, archiver, sauvegarder, conserver, transmettre au public par télécommunication ou par l'Internet, prêter, distribuer et vendre des thèses partout dans le monde, à des fins commerciales ou autres, sur support microforme, papier, électronique et/ou autres formats.

L'auteur conserve la propriété du droit d'auteur et des droits moraux qui protègent cette thèse. Ni la thèse ni des extraits substantiels de celle-ci ne doivent être imprimés ou autrement reproduits sans son autorisation.

---

In compliance with the Canadian Privacy Act some supporting forms may have been removed from this thesis.

Conformément à la loi canadienne sur la protection de la vie privée, quelques formulaires secondaires ont été enlevés de cette thèse.

While these forms may be included in the document page count, their removal does not represent any loss of content from the thesis.

Bien que ces formulaires aient inclus dans la pagination, il n'y aura aucun contenu manquant.

  
**Canada**

## **Abstract**

A novel and practical model for predicting the corrosion rate of the steel reinforcement in concrete is developed. This model is based on Stern-Geary equations and includes the effects of concrete properties and the environmental conditions on corrosion. The influence of temperature, cover depth, concrete resistivity and the limiting current density is incorporated in the model. In addition, the half-cell potential measurement technique is modelled numerically, and guidelines for quantitative and qualitative interpretation of the half-cell results are provided. The half-cell potential measurements are related to the kinetics of the corrosion process, and a separate model for predicting the corrosion of steel in concrete through half-cell data is developed. A comprehensive verification study demonstrated the strength and the applicability of the developed models in different scenarios.

# Table of Contents

Title Page .....	i
Abstract.....	ii
Table of Contents.....	iii
Acknowledgements.....	viii
List of Figures.....	ix
List of Tables .....	xvi
Notations.....	xviii
1. Introduction.....	1
1.1. General.....	1
1.2. Problem definition and objectives .....	3
1.3. Brief background on the corrosion of steel in concrete .....	5
1.3.1. Corrosion of steel in concrete .....	5
1.3.2. Kinetics of corrosion.....	6
1.3.3. Polarization equations.....	10
1.3.3.1. Butler-Volmer kinetics equations .....	10
1.3.3.2. Stern-Geary polarization equations.....	11
1.4. Organization of the thesis .....	13
2. Literature Review.....	14
2.1. General.....	14
2.2. Empirical models .....	15
2.2.1. Alonso et al. (1988).....	15
2.2.2. DuraCrete (2000) .....	18

2.2.3. Liu and Weyers (1998) .....	19
2.2.4. Ahmad and Bhattachajee (2000).....	21
2.2.5. Morinaga (1990) .....	23
2.2.6. Morinaga (1996) .....	26
2.3. Mathematical models .....	28
2.3.1. Bazant (1979).....	28
2.3.2. Balabanic et al. (1995).....	31
2.3.3. Raupach and Gulikers (1999) .....	32
2.3.4. Gulikers (2005).....	34
2.3.5. Kranc and Sagues (1992).....	35
2.3.6. Takewaka et al. (2003).....	37
2.3.7. Song et al. (2005).....	40
2.3.8. Huet et al. (2006) .....	42
2.3.9. Maruya et al. (2003).....	44
2.3.10. Isgor (2001).....	47
2.4. Summary .....	48
3. Research Method.....	50
3.1. General.....	50
3.2. Virtual polarization resistance experiments.....	51
3.3. Polarization resistance technique.....	53
3.4. The governing equation and boundary conditions.....	58
3.5. Domain discretization .....	61
3.6. Non-linear solution algorithm.....	63

3.7. Program development .....	68
4. Theoretical Considerations.....	74
4.1. General.....	74
4.2. Micro- and macro-cell corrosion .....	74
4.3. Anode-to-cathode area (A/C) ratio .....	77
4.3.1. A/C ratio.....	78
4.3.2. Effect of concrete resistance on A/C .....	80
4.3.3. Effect of oxygen availability on A/C.....	82
4.3.4. The optimum A/C ratio.....	84
4.4. Kinetic parameters of steel corrosion in concrete.....	90
4.4.1. The effect of concrete cover thickness.....	90
4.4.2. The effect of temperature.....	92
4.4.2.1. Tafel slope.....	92
4.4.2.2. Exchange current density .....	94
4.4.2.3. Equilibrium potentials.....	95
4.4.3. Concrete resistivity .....	96
4.4.4. Limiting current density.....	97
5. Virtual Experiments .....	100
5.1. General.....	100
5.2. Study approach.....	101
5.3. Results.....	102
5.4. Discussion.....	107
5.5. Summary .....	118

6. Model Development.....	119
6.1. General.....	119
6.2. Non-linear regression analysis.....	120
6.3. Experimental verification.....	128
6.3.1. Lopez et al. 1993.....	128
6.3.2. Lopez and Gonzalez 1993.....	133
6.3.3. Ramezaniapour et al. 2007.....	136
6.4. Case Study: Coupled effect of concrete properties and environmental factors on the corrosion rate.....	142
6.5. Case Study: Comparison with existing models .....	146
6.6. Corrosion rate monitoring.....	155
7. Quantitative Interpretation of Half-Cell Potential Tests .....	158
7.1. General.....	158
7.2. Half-cell potential mapping .....	159
7.3. Potential mapping through numerical modelling.....	162
7.4. The effect of concrete resistivity.....	163
7.5. The effect of cover thickness .....	167
7.6. The effect of oxygen availability .....	170
7.7. The effect of A/C .....	172
7.8. Half-cell testing and corrosion rate.....	174
7.9. Case study .....	180
8. Conclusions .....	186
8.1. General.....	186

8.2. Conclusions of the study.....	188
8.3. Recommendations for future work .....	190
References.....	192
Appendix A: Auxiliary models used in the thesis .....	201
A.1. Concrete resistivity as a function of w/c ratio and degree of saturation (GjØrv et al. 1977).....	201
A.2. Amount of dissolved oxygen in water (Eaton and Mary 2005).....	204
A.3. Activation energy of resistivity (Chrisp et al. 2001).....	205
A.4. Activation energy of oxygen diffusion (Page and Lambert 1987).....	205
A.5. Conversion of concrete resistivity to concrete resistance (Luping 2002)...	206
A.6. Conversion of concrete resistivity to concrete resistance used by Lopez and Gonzalez (1993).....	206
A.7. Hydration of cement paste and oxygen diffusion coefficient calculation (Papadakis et al. 1991).....	206
A.8. Moisture diffusion and degree of saturation (Xi et al. 1994):.....	212
Appendix B: Results .....	214
B.1. Maximum corrosion current density .....	214
B.2 DVD contents.....	220

## **Acknowledgements**

I would like to sincerely thank my adviser Professor O. Burkan Isgor for his support throughout this research. Dr. Isgor is not only a great adviser, but also is a person with great heart. Working with him was a great experience which I shall never forget.

I would like to thank Mr. Pouria Ghods for his numerous contributions to this research. Mr. Ghods was a great colleague and more importantly a real friend.

I like to thank my father, for his financial and emotional support during this research without which this work would not have been accomplished.

I would like to thank my mother for her emotional support and encouragement through every step of this work. She has been my great motivator through every step in life.

Finally, I would like to thank my brothers, my brother-in-law and my beloved sister for their patience during this research.

The author would like to thank NSERC for the financial support provided for this research.

## List of Figures

Figure 1.1: Schematic illustration of polarization curves for anode and cathode.....	8
Figure 1.2: Schematic illustration of cathodic polarization curve including concentration polarization .....	9
Figure 1.3: Plot of polarization equation using Stern-Geary polarization equations (Ge 2006) .....	12
Figure 2.1: Coefficient of corrosion rate in Eq. (2.15) (Morinaga 1996).....	27
Figure 2.2: Illustration of an equivalent circuit .....	33
Figure 2.3: Illustration of internal and external concrete layers and diffusion path for each section of rebar (Takewaka et al. 2003) (Taken from the original paper).....	39
Figure 2.4: Illustration of adjustment considered for diffusion coefficient of diffusion path (Takewaka et al. 2003) (Taken from the original paper) .....	39
Figure 2.5: The algorithm for estimating the corrosion rate by Maruya et al. (2003) (Taken from the original paper).....	46
Figure 3.1: Illustration of the linear section of the polarization curves.....	54
Figure 3.2: Randles circuit.....	56
Figure 3.3: Polarization resistance test setup.....	57
Figure 3.4: Domain for uniformly depassivated steel in a concrete member .....	60
Figure 3.5: Illustration of the analysis domain and its boundaries .....	60
Figure 3.6: Sensitivity analysis for the type and number of elements .....	63
Figure 3.8: Number of iterations for a case with large $i_L$ ( $0.2 \text{ A/m}^2$ ) with modified and unmodified seed values: (a) 40 mm cover thickness ( $\xi=0.025$ ); (b) 100 mm cover thickness ( $\xi=0.025$ ) .....	66

Figure 3.9: Number of iterations for a case with intermediate $i_L$ ( $=0.02 \text{ A/m}^2$ ) with modified and unmodified seed values: (a) 40 mm cover thickness ( $\xi=0.025$ ); (b) 100 mm cover thickness ( $\xi=0.025$ ) .....	67
Figure 3.10: Number of iterations for a case with small $i_L$ ( $0.002 \text{ A/m}^2$ ) with modified seed values: (a) 40 mm cover thickness ( $\xi=0.001$ ); (b) 100 mm cover thickness ( $\xi=0.001$ ) .....	68
Figure 3.11: Flowchart of the MATLAB algorithm/program .....	72
Figure 3.12: Current density distribution at the interface of steel and concrete .....	73
Figure 4.1: Schematic illustration of anodic and cathodic polarization curves .....	77
Figure 4.2: Variation of A/C with corrosion potential in absence of concentration polarization and IR drop .....	80
Figure 4.3: Variation of A/C with concrete resistance .....	82
Figure 4.4: Effect of oxygen availability on the A/C.....	84
Figure 4.5: One dimensional corrosion problem .....	89
Figure 5.1: Distribution of the potential in the bulk of the concrete.....	104
Figure 5.2: Potential distribution at the surface of concrete .....	105
Figure 5.3: Potential distribution at the steel/concrete interface.....	105
Figure 5.4: Current density distribution at the steel/concrete interface .....	106
Figure 5.5: Variation of corrosion current with A/C .....	106
Figure 5.6: Variation of corrosion rate with temperature for different values of cover thickness: (a) $i_L = 0.2 \text{ A/m}^2$ and $\rho = 5000 \text{ } \Omega\cdot\text{m}$ , (b) $i_L = 0.008 \text{ A/m}^2$ and $\rho = 7500 \text{ } \Omega\cdot\text{m}$ , (c) $i_L = 0.005 \text{ A/m}^2$ and $\rho = 10000 \text{ } \Omega\cdot\text{m}$ .....	109

Figure 5.7: Variation of corrosion rate with temperature for different values of  $i_L$  (60 mm cover thickness): (a)  $\rho = 650 \Omega.m$ , (b)  $\rho = 1250 \Omega.m$ , (c)  $\rho = 5000 \Omega.m$ ..... 110

Figure 5.8: Variation of corrosion rate with temperature for different values of concrete resistivity (60 mm cover thickness): (a)  $i_L=0.2 A/m^2$ , (b)  $i_L=0.05 A/m^2$ , (c)  $i_L=0.005 A/m^2$  ..... 111

Figure 5.9: Variation of corrosion rate with cover thickness for different values of limiting current density at constant temperature (303°K) : (a)  $\rho = 5000 \Omega.m$ , (b)  $\rho = 2500 \Omega.m$ , (c)  $\rho = 650 \Omega.m$  ..... 113

Figure 5.10: Variation of corrosion current with cover thickness for different values of resistivity at constant temperature (303°K): (a)  $i_L=0.2 A/m^2$ , (b)  $i_L=0.05 A/m^2$ , (c)  $i_L=0.005 A/m^2$  ..... 114

Figure 5.11: Variation of corrosion rate with  $i_L$  for different cover thicknesses ( $\rho = 50 \Omega.m$ ): (a)  $T = 323^\circ K$ , (b)  $T = 303^\circ K$ , (c)  $T = 283^\circ K$  ..... 115

Figure 5.12: Variation of corrosion rate with  $i_L$  for different temperatures ( $\rho = 50 \Omega.m$ ): (a)  $d = 140 mm$ , (b)  $d = 60 mm$ , (c)  $d = 40 mm$ ..... 116

Figure 5.13: Schematic illustration of effect of temperature on the corrosion rate for large and small values of  $i_L$ ..... 117

Figure 6.1: Correlation between corrosion rate and limiting current density using modified root fit function. (a)  $T= 283^\circ K$ ,  $d=20 mm$  and  $\rho=50 \Omega.m$ , (b)  $T= 283^\circ K$ ,  $d=20 mm$  and  $\rho=350 \Omega.m$ ..... 123

Figure 6.2: Comparison of the actual results (the finite element method) with the regression analysis ..... 128

Figure 6.3: Comparison of the results of Lopez et al. (1993) with the average and maximum corrosion current densities obtained using the developed model: (a) Relative humidity = 50%, (b) Relative Humidity = 90%, (c) Saturated conditions ..... 133

Figure 6.4 : Comparison of the predicted average and maximum corrosion current density with the experimental data from Lopez and Gonzalez (1993)..... 136

Figure 6.5 : Comparison of the results of experiments by Ramezaniapour et al. (2007) with predicted average and maximum corrosion rates for concrete specimens with 35 mm cover depth: (a, b) After one year of exposure, (c, d) After four years of exposure ..... 140

Figure 6.6: Comparison of the results of experiments by Ramezaniapour et al. (2007) with predicted average and maximum corrosion rates for concrete specimens with 50 mm cover depth: (a, b) After one year of exposure, (c, d) After four years of exposure ..... 141

Figure 6.7: Comparison of the results of experiments by Ramezaniapour et al. (2007) with predicted average and maximum corrosion rates for concrete specimens with 70 mm cover depth: (a, b) After one year of exposure, (c, d) After four years of exposure ..... 142

Figure 6.8: Variation of corrosion rate with relative humidity for different w/c ratios. (a)  $T = 273^{\circ}\text{K}$ ,  $T = 298^{\circ}\text{K}$ ,  $T = 303^{\circ}\text{K}$ ,  $T = 323^{\circ}\text{K}$ ..... 145

Figure 6.9: Variation of corrosion rate with cover thickness for different cover thickness: (a) w/c ratio = 0.4, (b) w/c ratio = 0.5, (c) w/c ratio = 0.6..... 146

Figure 6.10: Exposure condition for the hypothetical case (“E.P” stands for “Exposure Period”)	148
Figure 6.11: Concrete resistivity corresponding to each exposure period	149
Figure 6.12: Amount of dissolved oxygen in water as a function of temperature	149
Figure 6.13: Variation of oxygen diffusion coefficient with relative humidity	150
Figure 6.14: Comparison of the corrosion rate obtained by different models	152
Figure 6.15: User interface of the developed computer program	156
Figure 6.16: Excel data input window	156
Figure 6.17: Temperature profile window	157
Figure 6.18: Relative humidity profile window	157
Figure 7.2: Potential distribution at the surface of steel and concrete: (a) $\rho = 50 \Omega.m$ , (b) $\rho = 5000 \Omega.m$ , (c) $\rho = 10000 \Omega.m$	165
Figure 7.3 Dependence of internal IR drop to resistivity	166
Figure 7.4: Potential distribution at the surface of concrete for different values of concrete resistivity	166
Figure 7.5: Distribution of potential and corrosion current density at the steel/concrete interface (A/C=1)	168
Figure 7.6: Potential distribution at the surface and steel/concrete interface: (a) $d = 20$ mm, (b) $d = 60$ mm, (c) $d = 100$ mm, (d) $d = 140$ mm	169
Figure 7.7: Dependence of IR-drop to cover thickness	170
Figure 7.8: Potential distribution at the surface and steel/concrete interface: (a) low oxygen, (b) Medium oxygen, (c) High oxygen	171
Figure 7.9: Distribution of potential at the steel/concrete interface	173

Figure 7.10: Potential distribution at the surface and interface of steel and concrete: (a) A/C = 0.1, (b) A/C = 0.25, (c) A/C = 0.5, (d) A/C = 1.0 .....	174
Figure 7.11: Variation of corrosion rate with average potential at the surface of concrete .....	179
Figure 7.12: Possible A/C ratios for different ranges of average potential .....	179
Figure 7.13: Illustration of the sample used by Luping (2002) (Taken from the original paper) .....	181
Figure 7.14: Results of the first comparative test (after 4 weeks) .....	183
Figure 7.15: Results of the second comparative test (after 13 weeks).....	185
Figure B.1: Variation of maximum corrosion rate with temperature for different values of cover thickness: (a) $i_L = 0.2 \text{ A/m}^2$ and $\rho = 5000 \text{ }\Omega\cdot\text{m}$ , (b) $i_L = 0.008 \text{ A/m}^2$ and $\rho = 7500 \text{ }\Omega\cdot\text{m}$ , (c) $i_L = 0.005 \text{ A/m}^2$ and $\rho = 10000 \text{ }\Omega\cdot\text{m}$ .....	214
Figure B.2: Variation of maximum corrosion rate with temperature for different values of $i_L$ (60 mm cover thickness): (a) $\rho = 650 \text{ }\Omega\cdot\text{m}$ , (b) $\rho = 1250 \text{ }\Omega\cdot\text{m}$ , (c) $\rho = 5000 \text{ }\Omega\cdot\text{m}$ .....	215
Figure B.3: Variation of maximum corrosion rate with temperature for different values of concrete resistivity (60 mm cover thickness): (a) $i_L=0.2 \text{ A/m}^2$ , (b) $i_L=0.05 \text{ A/m}^2$ , (c) $i_L=0.005 \text{ A/m}^2$ .....	216
Figure B.4: Variation of maximum corrosion rate with cover thickness for different values if limiting current density at constant temperature (303°K) : (a) $\rho = 5000 \text{ }\Omega\cdot\text{m}$ , (b) $\rho = 2500 \text{ }\Omega\cdot\text{m}$ , (c) $\rho = 650 \text{ }\Omega\cdot\text{m}$ .....	217

Figure B.5: Variation of maximum corrosion current with cover thickness for different values of resistivity at constant temperature (303°K): (a)  $i_L=0.2 \text{ A/m}^2$ , (b)  $i_L=0.05 \text{ A/m}^2$ , (c)  $i_L=0.005 \text{ A/m}^2$  ..... 218

Figure B.6: Variation of maximum corrosion rate with  $i_L$  for different cover thicknesses ( $\rho = 50 \text{ } \Omega\cdot\text{m}$ ). (a)  $T = 323^\circ\text{K}$ , (b)  $T = 303^\circ\text{K}$ , (c)  $T = 283^\circ\text{K}$ ..... 219

Figure B.7: Variation of maximum corrosion rate with  $i_L$  for different temperatures ( $\rho = 50 \text{ } \Omega\cdot\text{m}$ ). (a)  $d = 140 \text{ mm}$ , (b)  $d = 60 \text{ mm}$ , (c)  $d = 40 \text{ mm}$ ..... 220

## List of Tables

Table 1.1: Typical kinetic parameters of steel corrosion in concrete (Isgor 2001) .....	12
Table 2.1: The regression constants for Eq. (2.1) in carbonated mortars tested by (Alonso et al. 1988) .....	17
Table 2.2 : Experimental design implemented by Liu and Weyers (1998) .....	21
Table 2.3: Test parameters used by Ahmad and Bhattachajee (2000).....	23
Table 2.4: Design parameters in the tests conducted by Morinaga (1990).....	25
Table 2.5: Environmental parameters in the tests conducted by Morinaga (1990) .....	25
Table 5.1: Experimental variables and their values used in virtual experiments.....	102
Table 6.1: Constants of the model .....	127
Table 6.2: Input data for the model used to compare the model with experiments conducted by Lopez et al. (1993).....	130
Table 6.3: Input data for the model used to compare the results with experiments conducted by Lopez and Gonzalez (1993).....	135
Table 6.4: Mixture proportions of specimens tested by Ramezaniapour et al. (2007) .	137
Table 6.5: Input data of the model used for comparing the model with experimental study by Ramezaniapour et al. (2007) .....	139
Table 6.6: Concrete and structural design parameters .....	147
Table 6.7: Models used for estimating the corrosion rate and their input parameters....	151
Table A.1: Concrete resistivity as a function of w/c ratio at different degrees of saturation .....	202
Table A.2: Concrete resistivity as a function of degree of saturation for different values of w/c ratio .....	203

Table A.3 : Main components of Portland cement .....	209
Table A.4: Values of molar volume difference for different cement components .....	210
Table A.5: Molar weight and coefficient of reaction rates of major components of Portland cement .....	210
Table A.6: Chemical composition of clinker.....	210
Table A.7: The total porosity and the porosity of hardened cement paste with chemical composition provided by Papadakis et al. (1991) for Cement Type I.....	211
Table A.8: The total porosity and the porosity of hardened cement paste with chemical composition provided by Ramezaniapour et al. (2007) for Cement Type II.....	211
Table A.9: The total porosity and the porosity of hardened cement paste with chemical composition provided by Ramezaniapour et al. (2007) for Cement Type V.....	212
Table A.10: Cement type dependent parameters .....	213

# Notations

L	= Length	(e.g. mm)
M	= Mass	(e.g. kg)
E	= Energy	(e.g. J)
Q	= Potential	(e.g. volts)
R	= Resistance	(e.g. $\Omega$ )
t	= Time	(e.g. s)
T	= Temperature	(e.g. $^{\circ}\text{K}$ )
C	= Current	(e.g. A)
F	= Force	(e.g. N)
$\Delta\varepsilon_c$		= reduction in porosity due to carbonation
$\Delta\varepsilon_H(t)$		= reduction in porosity due to hydration
$\Delta\bar{V}_j$		= molar volume differences ( $\text{L}^3/\text{M}$ )
$\Delta U_\rho$		= activation energy of resistivity (E/M)
$\Delta U_D$		= activation energy of the oxygen diffusion (E/M)
$\Delta\phi$		= maximum potential difference at the surface of concrete (Q)
$\alpha$		= symmetry factor
$\beta_a$		= anodic Tafel slope (Q)
$\beta_c$		= cathodic Tafel slope (Q)
$\varepsilon$		= porosity of the concrete

$\varepsilon_o$	= porosity of fresh concrete
$\varepsilon_{air}$	= volume fraction of entrapped (or entrained) air
$\varepsilon_p$	= porosity of the cement paste
$\xi$	= relaxation factor
$\rho$	= concrete resistivity (R.L)
$\rho_a$	= density of aggregate (M/L <sup>3</sup> )
$\rho_c$	= density of cement (M/L <sup>3</sup> )
$\rho_w$	= density of water (M/L <sup>3</sup> )
$\phi$	= electric potential (Q)
$\phi_a$	= anodic potential (Q)
$\phi^\circ$	= seed value for potential (Q)
$\phi_a^\circ$	= anodic standard potential (Q)
$\phi_{ave}$	= average potential on the surface of concrete (Q)
$\phi_c$	= cathodic potential (Q)
$\phi_e$	= equilibrium potential (Q)
$\phi_c^\circ$	= cathodic standard potential (Q)
$\phi_{corr}$	= corrosion potential (Q)
$\phi_{Fe}^\circ$	= standard iron oxidation potential (Q)
$\phi_{O_2}^\circ$	= standard oxygen reduction potential (Q)
$\phi_{ma,a}$	= anodic macro-cell potential (Q)

$\phi_{ma,c}$	= cathodic macro-cell potential (Q)
$\phi_{mi,a}$	= anodic micro-cell potential (Q)
$\phi_{mi,c}$	= cathodic micro-cell potential (Q)
$\phi_p$	= polarization potential (Q)
$\phi_{pass}$	= potential of passive steel (Q)
$\phi_{pit}$	= pitting potential (Q)
$\phi_{st}$	= steel surface potential (Q)
$A$	= electrode surface area ( $L^2$ )
$A_a$	= anodic area ( $L^2$ )
$A_c$	= cathodic area ( $L^2$ )
$A_{corr}$	= corrosion rate coefficient
$A_p$	= polarized area of the steel ( $L^2$ )
$B$	= polarization constant (Q)
$C_{ad}$	= factor related to the heat of adsorption
$C_o^\circ$	= molar concentration in the bulk of the solution at the standard equilibrium condition ( $M/L^3$ )
$C_{coef}$	= cement type coefficient
$C_{Cl}$	= chloride content in the form of $CaCl_2$ or $NaCl$ ( $M/L^3$ )
$[Cl^-]$	= concentration of the free chloride ( $M/L^3$ )
$C_{cement}$	= cement content ( $M/L^3$ )
$C_f$	= water soluble (free) chlorides ( $M/L^3$ )

$C_f^*$	= free chloride content (% by weight of the cement) for complete destruction of passive film (M/L <sup>3</sup> )
$C_f'$	= free chloride content (% by weight of the cement) necessary for initiation of corrosion (M/L <sup>3</sup> )
$C_{O_2}$	= concentration of oxygen in the solution (concrete) (M/L <sup>3</sup> )
$C_{O_2}^s$	= concentration of oxygen at the surface of solution (concrete) (M/L <sup>3</sup> )
$C_{O_2}^{air}$	= concentration of oxygen in air (M/L <sup>3</sup> )
$C_{O_2,liquid}(x_2)$	= oxygen concentration in the pore solution per unit volume of concrete at $x_2$ (M/L <sup>3</sup> )
$C_{SO_2}$	= annual deposited SO <sub>2</sub> (M/L <sup>2</sup> )
$C_{salt}^{Air}$	= annual air-borne salts (M/L <sup>3</sup> )
$C_t$	= acid soluble chloride content (M/L <sup>3</sup> )
Chl	= chlorinity
C <sub>3</sub> S	= tricalcium silicate
C <sub>2</sub> S	= dicalcium silicate
C <sub>3</sub> A	= tricalcium aluminate
C <sub>4</sub> AF	= tetracalcium aluminoferrite
$D_{counter}$	= counter electrode diameter (L)
$D_{O_2}$	= concrete oxygen diffusion coefficient (L <sup>2</sup> /t)
$D_{O_2,liquid}$	= diffusion coefficient of species in pore solution (L <sup>2</sup> /t)
$F$	= Faraday's constant (Q/M)

$F_{Cl}$	= chloride content factor
$F_G$	= geometry factor (1/L)
$F_{Galv}$	= galvanic effect factor
$F_{Oxide}$	= factor related to the presence of oxide layer at the surface of steel
$F_{O_2}$	= oxygen availability factor
$I_{corr}$	= corrosion current (C)
$I_p$	= polarization current (C)
$L$	= Length of the polarized area of the rebar (L)
$L_{ac}$	= distance between the anode and cathode (L)
$L_{O_2}$	= length of oxygen diffusion path (L)
$N_{ct}$	= factor dependent of the cement
$P$	= pressure (F/L <sup>2</sup> )
$P_{wv}$	= water vapour pressure (F/L <sup>2</sup> )
$P_{corr}$	= corrosion penetration rate (L)
[OH <sup>-</sup> ]	= concentration of hydroxide ions (M)
$R$	= the universal gas constant ( E/M.T)
$R_{con}$	= concrete/mortar resistance (R)
$R_p$	= polarization resistance (R)
$R_{p,a}$	= anodic polarization resistance (R)
$R_{p,c}$	= cathodic polarization resistance (R)
$R_{st}$	= electrical resistance of steel (R)

$\tilde{R}$	= equivalent resistance (R)
$S_r$	= degree of water saturation
$T$	= temperature (T)
$T_c$	= temperature (T)
$V_a^{Fe^{2+}}$	= reaction rate of $Fe^{2+}$ in anodic control (M/L <sup>2</sup> .t)
$V_c^{Fe^{2+}}$	= reaction rate of $Fe^{2+}$ in cathodic control (M/L <sup>2</sup> .t)
$V_m$	= monolayer capacity
$V_{ct}$	= cement type factor
$W_t$	= total water content for unit value of material (M/L <sup>3</sup> )
$a/c$	= aggregate-cement ratio
$d$	= concrete cover thickness (L)
$d_{corr}$	= corrosion penetration (L)
$d_{rain}$	= the annual rainfall (L)
$d_{st}$	= diameter of reinforcing steel (L)
$f_e$	= exposure condition factor
$f_t$	= test method factor
$h$	= relative humidity
$i$	= current density into the electrolyte (C/L <sup>2</sup> )
$i^\circ$	= current density seed value (C/L <sup>2</sup> )
$i_a$	= anodic current density (C/L <sup>2</sup> )
$i_c$	= cathodic current density (C/L <sup>2</sup> )
$i_L$	= limiting current density (C/L <sup>2</sup> )

$i_{mi,a}$	= anodic micro-cell current density (C/L <sup>2</sup> )
$i_{mi,c}$	= cathodic micro-cell current density (C/L <sup>2</sup> )
$i_{oa}$	= anodic exchange current densities (C/L <sup>2</sup> )
$i_{oc}$	= cathodic exchange current densities (C/L <sup>2</sup> )
$i_{corr,ave}$	= average corrosion current density (C/L <sup>2</sup> )
$i_{corr,max}$	= maximum corrosion current density (C/L <sup>2</sup> )
$i_{pass}$	= passive current of steel (C/L <sup>2</sup> )
$i_{corr}$	= corrosion rate (C/L <sup>2</sup> )
$k_{O_2}$	= kinetic constant of oxygen reduction (L/t)
$k_c^\circ$	= rate constant at standard equilibrium condition (L/t)
$m_{corr}$	= amount of corrosion products (M/L <sup>2</sup> )
$n$	= normal to the equipotential lines
$n_{age}$	= age constant
$n_{ad}$	= number of adsorbed layers in saturated state
$n_e$	= valance number
$r$	= anode-to-cathode area ratio
$s_a$	= specific surface of the oxide layer per unit volume (1/L)
$t$	= time (t)
$t_0$	= initial time (t)
$t^*$	= time to consume all the gypsum in the cement (t)
$u_f$	= mass concentration of Fe(OH) <sub>2</sub> per unit volume of concrete (M/L <sup>3</sup> )

$u_w^A$	= amount of capillary water adjacent to anodic surface (M/L <sup>3</sup> )
$u_w^C$	= amount of capillary water adjacent to cathodic surface (M/L <sup>3</sup> )
$u_o^C$	= oxygen concentration adjacent to cathodic surface (M/L <sup>3</sup> )
w/c	= water-cement ratio
$z_c$	= number of electrons involved in cathodic reaction

# **1. Introduction**

---

## **1.1. General**

The deterioration of reinforced concrete structures due to chloride- or carbonation-induced steel corrosion is a major concern for infrastructure owners and operators. The corrosion of steel in concrete can manifest itself in the form of pitting or uniform corrosion, depending on the depassivation process. Pitting corrosion may be observed in cases where chloride ions accumulate locally around steel reinforcement in quantities larger than a threshold value. In the case of the carbonation of concrete cover, corrosion generally takes place uniformly along the reinforcement. The quantification of active corrosion rate of steel in concrete structures through nondestructive and rapid methods is a crucial task for scheduling maintenance/repair operations and for achieving accurate service life predictions. Significant progress has been made on the

nondestructive measurement of steel corrosion in concrete since early 1970s, and organizations such as RILEM have already made recommendations for best practices for quantifying corrosion rates (RILEM TC 154-EMC).

One of the most widely-used methods of measuring corrosion rate in concrete structures is by means of measuring the polarization resistance of the corroding system and using the Stern-Geary equation (Bohni 2005) to calculate the corrosion current density of active steel. Galvanostatic pulse technique, for instance, is a transient method that enables rapid measurement of polarization resistance, a requirement that is crucial for obtaining accurate mapping of the corrosion state in concrete. It should be noted that the calculations that are based on measured polarization resistance data provides instantaneous corrosion rates that are influenced greatly by environmental changes in temperature and humidity; therefore comparisons with actual corrosion rates, which can be determined through weight loss measurements, can only be carried out after integrating polarization resistance data over time. From a different perspective, in order to accurately predict the corrosion rates in concrete, one needs to monitor the polarization resistance frequently for a period of time so that temporal variations can be captured. Therefore, although the polarization resistance methods are quite practical for instantaneous monitoring of structures, they become significantly expensive and impractical if the monitoring is to be done continuously over long periods. Accurate modelling of steel corrosion in concrete structures is therefore a very important tool that can help solve the issue described above.

## 1.2. Problem definition and objectives

The present thesis addresses two problems associated with the corrosion monitoring of reinforced concrete structures. The first problem is regarding the modelling of steel corrosion in concrete, which is briefly described below and elaborated in the literature review of this thesis (in Chapter 2). The second one is related to the issues associated with one of the most widely used, practical, and standardized non-destructive methods for monitoring steel corrosion in concrete structures: half-cell potential method (ASTM C876-91, RILEM TC 154-EMC).

Although it is difficult, if not impossible, to completely replace the nondestructive testing methods with numerical models, accurate simulations combined with relatively infrequent, and hence inexpensive, polarization resistance measurements can be the answer to health monitoring of reinforced concrete infrastructure. Although this idea sounds quite promising, numerical modelling of active steel corrosion in concrete has its own challenges that can be summarized under the following categories: (1) difficulties in the estimation of parameters to carry out the simulations; (2) numerical difficulties in the solution of governing equation due to nonlinear boundary conditions (for the models that are based on the solution of Laplace's equation for electric potentials); and (3) challenges in modelling complicated geometries (e.g. reinforcement details) and non-homogeneous material properties. Despite these challenges, a number of corrosion models have already been developed (Isgor 2001, Kranc and Sagues 1994); particularly the ones that are based on the solution of Laplace's equation for electric potentials have been verified to be quite effective in simulating well-controlled experimental setups. On the other hand, these numerical models remain to be computationally expensive, and for practical applications,

are complex to be adopted by the general engineering community. Empirical models of steel corrosion in concrete, although very practical, are limited to the specific experimental design and test conditions. These models usually do not consider all mechanisms of corrosion and hence are not applicable to all scenarios. Therefore, there is significant need for a comprehensive mathematical model which considers all mechanism of steel corrosion in concrete, is based on the fundamentals of the corrosion theory, and takes the concrete properties and environmental factors into account. Such a model should also be practical to be used by engineering community and should not require in depth knowledge of corrosion science.

Another problem in the monitoring of corrosion in concrete structures originates from the problems associated with half-cell potential technique, a method that is very widely used by practicing civil engineers to predict the probability of corrosion. Despite its widespread application, half-cell potential mapping is usually associated with a number of practical difficulties. Although some of these practical difficulties can be minimized with the aid of experienced staff and accurate instrumentation, the interpretation of the half-cell potential mapping results remains to be a major challenge for engineers. In addition, the half-cell method does not provide any information about the type of corrosion (i.e. uniform or pitting). Having information about the type of corrosion in some cases is more important than knowing the probability of corrosion and no quantitative relationship has been introduced in the literature among the results of half-cell potential mapping, the factors affecting the corrosion kinetics, and the corrosion rate of steel in concrete. Hence, there is a need for developing such a relationship, which

quantitatively relates the potential readings on the surface of concrete to the corrosion rate of reinforcement and allow engineers to gain more information from half-cell tests.

The main objective of this thesis is to address these two issues using a theoretical/numerical approach. It is intended that a closed-form relationship will be developed for each problem. The model that will be developed to predict the rate of steel corrosion in concrete will be verified using available experimental data. A computer program that is based on the proposed model will be developed for monitoring corrosion in reinforced concrete structures. To address the second issue, a model will be developed to relate the half-cell potential measurements to the kinetics of steel corrosion in concrete. The developed model is intended to provide additional information for the better interpretation of the results of half-cell potential mapping.

### **1.3. Brief background on the corrosion of steel in concrete**

#### **1.3.1. Corrosion of steel in concrete**

Steel in concrete is generally well protected against corrosion by a passive film that is quite stable in the high alkaline environment provided by concrete. Penetration of aggressive agents such as chloride ions through concrete cover and/or the carbonation of concrete cover, however, may result in the destruction of the passive film (depassivation) and the initiation of active corrosion. The first phase of this process (i.e. the penetration of aggressive agents through the concrete cover to the level of reinforcing steel) is called the initiation stage, and the second phase (i.e. after depassivation of steel) is referred as the propagation stage. The depassivation of steel marks the end of the initiation stage and the beginning of propagation stage.

Corrosion science is a complicated but a well-established field. It is impossible to present all the details of corrosion theory in the scope of a thesis. Here, on the other hand, basic definitions and principles of the kinetics of corrosion are provided so that the relevant theory, on which the current research is built, can be presented.

### 1.3.2. Kinetics of corrosion

Corrosion is a destructive electrochemical process consisting of two half-cell reactions: oxidation and reduction. In the case of corrosion of steel in the alkaline environment of concrete, oxidation and reduction reactions can be presented by Eqs. (1.1) and (1.2), respectively:



The oxidation reaction takes place at the anodes, and the reduction reaction takes place at the cathodes. The produced electrons at the anodes are consumed at the cathodes, and the process is completed by the migration of hydroxide ions from the cathodes to the anodes. The potential of the anode or the cathode when no transfer of electrons takes place is referred as open-circuit potential and is measured with respect to a reference electrode such as standard hydrogen electrode (S.H.E.) or saturated calomel electrode (S.C.E.). The open-circuit potentials for the anode and the cathode ( $\phi_a^{\circ}$  and  $\phi_c^{\circ}$  respectively) are illustrated in Figure 1.1. The transfer of electrons from the anode to the cathode reduces the potential difference between the two, and the change in potential from the open-circuit potential is called polarization. This is also illustrated schematically in Figure 1.1. In this figure, due to the passage of current,  $I_l$ , from the anode to the

cathode, anode polarizes to more positive potentials, and the cathode polarizes to more negative potentials. The amount of polarization is usually measured in volts. It should be noted in Figure 1.1 that the current is in logarithmic scale, and this type of diagram, in which the potential is plotted vs. logarithm of the current, is called polarization diagram. The curves corresponding to the anode and the cathode in a polarization diagram are called anodic and cathodic polarization curves, respectively. The slope of the polarization curves are defined as Tafel slopes and are usually measured in volts/dec. Note that the anodic and cathodic polarization curves do not intersect. This is due to resistance of the electrolyte between the anode and the cathode, which can never be zero for concrete. When this resistance is significantly large, the amount of current (and hence the amount of polarization) is dependent on the resistance of the electrolyte; in these circumstances the corrosion is said to be under resistance control.

The passing current from the anode to the cathode during active corrosion is called the corrosion current (represented with  $I$ ). If the corrosion current is divided by the anodic or the cathodic surface area, the anodic or the cathodic current densities (represented with  $i$ ) will be respectively obtained. If the anode-to-cathode area ( $A/C$ ) ratio is equal to unity, the anodic and cathodic current densities will be equal. The anodic current density is also known as corrosion current density. It should be noted that the polarization diagrams are sometimes prepared by considering the anodic or cathodic current densities instead of the corrosion current. The corresponding values of the current (or the current density) to open-circuit potentials of the anode and the cathode in Figure 1.1 are called anodic and cathodic exchange current (density,  $i_{oa}$  and  $i_{oc}$ ), respectively.

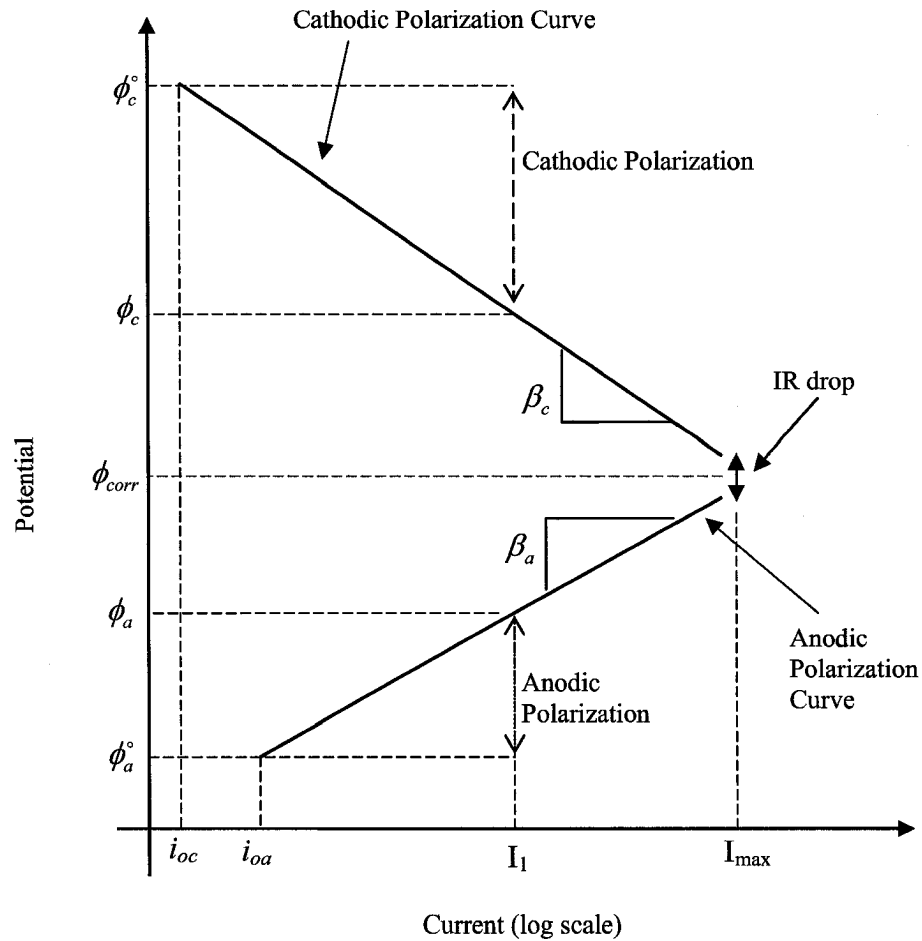


Figure 1.1: Schematic illustration of polarization curves for anode and cathode

Polarization is generally categorized as activation polarization and concentration polarization. Activation polarization is caused by slow electrode reactions (Uhlig and Revie 1985), and is characterized by a straight line in polarization diagrams. Concentration polarization is caused by the slow supply of ions/molecules to the electrode (e.g. the lack of oxygen on the cathodic surfaces of steel in concrete). This type of polarization is characterized by the curving of the polarization curve, as illustrated in Figure 1.2. As far as steel corrosion in concrete is concerned, concentration polarization

only occurs at cathodic sites of steel; activation polarization occurs at both surfaces. Figure 1.2 schematically illustrates the concentration polarization. As the concentration polarization increases (e.g. due to the lack of oxygen), the straight line (activation polarization) starts to curve downwards (concentration polarization) at smaller currents. If the effect of concentration polarization is very high, the corrosion is said to be under concentration (or diffusion) control. Note that the concentration polarization curve becomes asymptotic at a current (density) called limiting current (density). The mathematical forms of the polarization behaviour have been proposed in the literature in terms of closed-form relationships. In the following section, two of these relationships are presented.

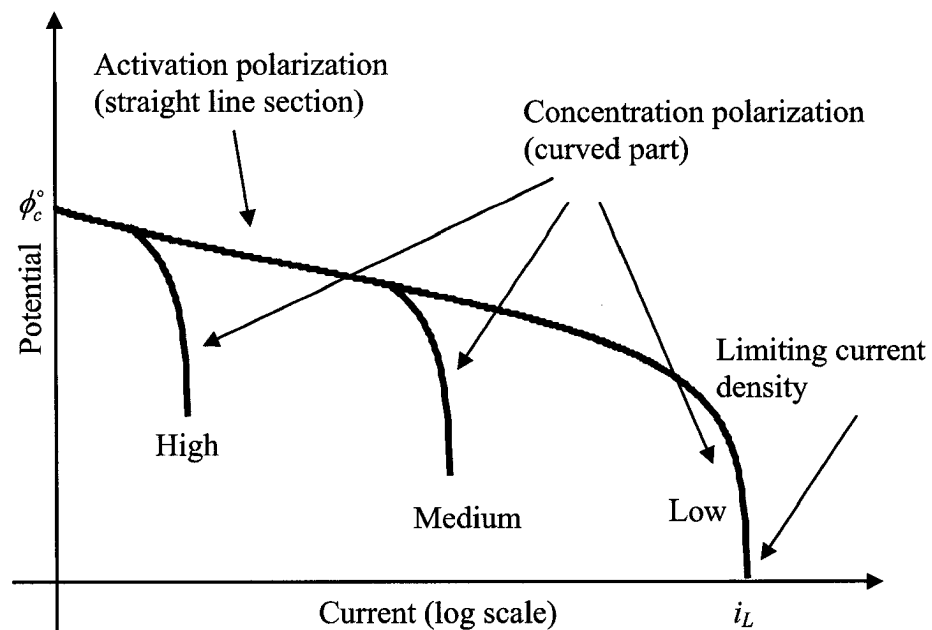


Figure 1.2: Schematic illustration of cathodic polarization curve including concentration polarization

### 1.3.3. Polarization equations

#### 1.3.3.1. Butler-Volmer kinetics equations

The original form of Butler-Volmer kinetics introduced in the corrosion literature (Brad and Faulkner 2001) does not take the concentration polarization into account. However, concentration polarization was later introduced into Butler-Volmer equations by modifying the cathodic current density (Kranc and Sagues 1997).

$$i_a = i_{o,a} \exp\left(\frac{\phi_a^\circ - \phi_{corr}}{\beta_a}\right) \quad (1.3)$$

$$i_c = \left[\frac{C_{O_2}}{C_{O_2}^s}\right] i_{o,c} \exp\left(\frac{\phi_{corr} - \phi_c^\circ}{\beta_c}\right) \quad (1.4)$$

where  $i_a$  and  $i_c$  ( $A/m^2$ ) are respectively the anodic and cathodic current densities,  $\beta_a$  and  $\beta_c$  (volts/dec) are respectively the anodic and cathodic Tafel slopes,  $i_{o,a}$  and  $i_{o,c}$  ( $A/m^2$ ) are respectively the anodic and cathodic exchange current densities,  $\phi_{corr}$  (volts) is the corrosion potential, as illustrated in Figure 1.1,  $C_{O_2}$  and  $C_{O_2}^s$  are respectively the concentration of oxygen in the solution (here the concrete pore solution) and concentration of oxygen at the surface of the solution.

It is noted here that, in the original form of the Butler-Volmer kinetics the term in brackets in Eq. (1.4) is equal to unity. Furthermore, this equation does not produce the curves illustrated in Figure 1.2 and only modifies the cathodic current density. This effect, however, does not comply with real experiments in many situations (Uhlig and Revie 1985).

### 1.3.3.2. Stern-Geary polarization equations

Stern and Geary (1957) introduced a new set of equations of anodic and cathodic polarization. The major improvement in this approach was in that the concentration polarization was considered as a separate term. Stern-Geary polarization equations for anode and cathode are as follows:

$$\phi_a = \phi_a^o + \beta_a \log \frac{i_a}{i_{oa}} \quad (1.5)$$

$$\phi_c = \phi_c^o + \beta_c \log \frac{i_c}{i_{oc}} - \frac{2.303RT}{z_c F} \log \frac{i_L}{i_L - i_c} \quad (1.6)$$

where  $\phi_a$  and  $\phi_c$  (volts) are anodic and cathodic potentials (see Figure 1.1),  $z_c$  is the number of electrons involved in cathodic reaction,  $R$  ( $\approx 8.314$  J/mole.K) is the universal gas constant,  $F$  ( $\approx 96500$  C/mole) is the Faraday's constant,  $T$  ( $^{\circ}\text{K}$ ) is temperature, and  $i_L$  ( $\text{A/m}^2$ ) is the limiting current density. The third term on the right hand side of Eq. (1.6) is for concentration polarization. Theoretically, this term can also be included in anodic polarization equation; however, since in the steel corrosion in concrete, the only form of concentration polarization is due to the lack of oxygen at the cathodic surfaces, it is only included in cathodic polarization equation. Plotting Eq. (1.6) for different values of cathodic current density will result in polarization curves, as illustrated schematically in Figure 1.2.

The kinetic parameters of corrosion (e.g. Tafel slopes, exchange current densities, etc.), as defined for Eqs. (1.5) and (1.6), of all metals need to be obtained experimentally. These parameters depend on many external factors (e.g. temperature); this dependence will be discussed in detail in Chapter 4. Table 1.1 presents typical values of the kinetic parameters of the steel corrosion in concrete at room temperature.

Table 1.1: Typical kinetic parameters of steel corrosion in concrete (Isgor 2001)

Kinetic Parameter	Value	Unit
Standard Iron Oxidation Potential ( $\phi_{Fe}^{\circ}$ )	-0.780	volts (S.C.E.)
Standard Oxygen Reduction Potential ( $\phi_{O_2}^{\circ}$ )	0.160	volts (S.C.E.)
Anodic Tafel Slope ( $\beta_a$ )	0.90	volts/dec
Cathodic Tafel Slope ( $\beta_c$ )	-0.180	volts/dec
Anodic Exchange Current Density ( $i_{oa}$ )	$300 \times 10^{-6}$	$A/m^2$
Cathodic Exchange Current Density ( $i_{oc}$ )	$10 \times 10^{-6}$	$A/m^2$

If the Stern-Geary polarization equations are plotted for the values presented in Table 1.1, Figure 1.3 will be obtained. It is noted that in this figure the current density is not in logarithmic scale.

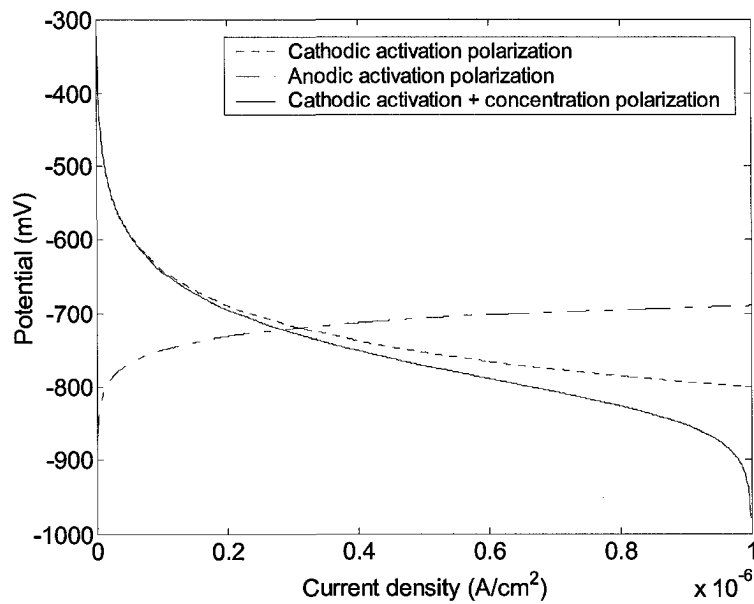


Figure 1.3: Plot of polarization equation using Stern-Geary polarization equations  
(Ge 2006)

## 1.4. Organization of the thesis

Chapter 1 of this thesis is an introduction to the problem of steel corrosion in concrete; this chapter briefly outlines the kinetics of corrosion and introduces the terminologies used throughout the thesis. Chapter 2 provides a literature review on the modelling of the corrosion of steel in concrete; previously developed prominent mathematical and empirical models are presented and their strengths and limitations are discussed. Chapter 3 provides the research method used in this thesis, introduces the concept of virtual experiments and evaluates the efficiency of the numerical process used in the study. Chapter 4 provides detailed theoretical considerations and formulations used in the modelling process; it introduces the concept of optimum A/C ratio, which is a fundamental concept used in this thesis. Chapter 5 presents the results of the numerical analyses and virtual experiments; the objective of this chapter is to demonstrate that the numerical procedure undertaken here agrees with experimental observations. In Chapter 6, the results of the virtual experiments are analysed and a closed-form solution representing the results of numerical analyses is obtained. This chapter provides a comprehensive verification of the model and demonstrates an application. Chapter 7 deals with the numerical modelling of half-cell potential measurement tests; in this chapter, a model relating the half-cell potential measurements to the kinetics of corrosion is developed and verified.

## **2. Literature Review**

---

### **2.1. General**

This chapter presents a review of previously developed models for predicting corrosion rate of steel reinforcement in concrete. These models can be classified under two categories: empirical and mathematical. Empirical models are based on observed correlation between corrosion rate of steel in concrete and different parameters affecting it. Mathematical models are based on either the mathematical representation of the controlling mechanisms of corrosion or the complex numerical modelling of polarization of steel. In this chapter, both experimental and mathematical models are presented. The assumptions which these models are based on are evaluated; their strengths and weaknesses are discussed. It should be noted that, the notations used in the original research reports and papers that are reviewed in

this chapter have been converted to a common set of variables for consistency. The actual notation of variables can be found in the respective original references. It is acknowledged that some of the variables have been defined multiple times; however, this is done intentionally since the units that are defined by different research studies show significant variance and the equations that these variables are used in are quite sensitive to the units. Furthermore, in introducing the model, the oldest model in each category is introduced first and the closest models in concept follow afterward.

## **2.2. Empirical models**

Empirical models are based on the observed relationship between the corrosion rate of steel and different parameters affecting it such as concrete properties and environmental conditions. Although these models are easy to use, since they are bound by the experimental conditions that they are derived from and do not consider the fundamental mechanisms of corrosion from a theoretical point of view, their applicability and reliability can be limited. In the following sections, prominent empirical models for the determination of steel corrosion rate in concrete are presented.

### **2.2.1. Alonso et al. (1988)**

Alonso et al. (1988) developed an experimental model by correlating the electrical resistance of mortar to the corrosion rate of steel. The experimental study consisted of casting mortar specimens with water/cement/sand ratio of 0.5/1/3 and curing them for 28 days in a chamber maintained at 100% relative humidity (RH) and  $20 \pm 2$  °C temperature. Six types of cement were used to prepare the mortar specimens:

Ordinary Portland Cement (OPC), Sulphate Resistance Portland Cement (SRPC), Slag Cement (SC), Pozzolanic Cement (Pozz C), Fly Ash Cement (FAC) and Ordinary Portland Cement with 30% Fly Ash (OPC + 30% FA). After curing, the specimens were carbonated at 50% and 70% RH where the carbonation process was controlled by monitoring the weight of the specimens. The corrosion rate of the steel was measured by means of the polarization resistance method at 50% and 100% RH, as well as in partial water immersion.

Equation (2.1) represents the model which shows that corrosion rate is proportional to the reciprocal of the concrete resistance:

$$i_{corr} = \log(i_{const}) + C_{coef} \log(R_{con}) \quad (2.1)$$

where  $i_{corr}$  ( $\mu\text{A}/\text{cm}^2$ ) is the corrosion rate,  $R_{con}$  ( $\Omega$ ) is the concrete/mortar resistance,  $i_{const}$  ( $\approx 10^4$ ) is a constant, and  $C_{coef}$  is a coefficient that is a function of the cement type, which is given for each mortar tested in this study in Table 2.1. Since the coefficient for all cement types is very close to negative unity, it was stated that the effect of cement type can be omitted from Eq. (2.1). Although using this model is convenient due to its simplicity, it suffers from drawbacks that can be summarized as follows:

(1) The corrosion rate is represented only as a function of mortar resistance, not resistivity. Although the resistance of concrete is related to its resistivity, since it is also a function of geometry, it can be highly influenced by the measurement technique (Luping 2002).

(2) Since the only considered controlling mechanism of corrosion is mortar resistance, the model fails to predict the corrosion rate under diffusion control mechanism (e.g. corrosion in concrete with high degree of water saturation).

(3) Since the mechanism of depassivation (i.e. its pattern on the steel surface) is different in carbonated and chloride-contaminated mortars, the model may not be used for chloride-induced corrosion.

(4) Due to extensive carbonation, the steel can be considered to be uniformly depassivated; therefore the results cannot be extrapolated to pitting corrosion.

(5) Polarization resistance method has been shown to have inherent errors that can be as large as 100% depending on the case tested (Andrade and Gonzalez 1978); therefore the model given in Eq. (2.1) is likely to include an inherent error.

The model developed by Alonso et al. (1988) was modified later by others to include the effect of additional parameters such as environmental factors and concrete properties; these models will be discussed in the following section.

Table 2.1: The regression constants for Eq. (2.1) in carbonated mortars tested by (Alonso et al. 1988)

Type of Mortar	$C_{coef}$	$R^2$ of the Regression Analysis
SC	-1.07	0.951
OPC	-0.72	0.907
OPC+30% FA	-1.08	0.912
Pozz C	-1.06	0.916
FAC	-1.06	0.920
SRPC	-1.11	0.973
All mortars	-0.97	0.89

### 2.2.2. DuraCrete (2000)

Since estimating the corrosion rate of steel reinforcement by measuring the electrical resistance of concrete is convenient, there has been growing interest for developing models that are based on the relationship between corrosion rate and concrete resistance. As described in the previous section, such a model was developed by Alonso et al. (1988). The model given by Eq. (2.1) was later modified to include environmental parameters in the European DuraCrete project (2000) such that the corrosion rate can be predicted using:

$$i_{corr} = \frac{10^4}{\rho(t)} F_{Cl} F_{Galv} F_{Oxide} F_{O_2} \quad (2.2)$$

where  $\rho$  ( $\Omega.m$ ) is the concrete resistivity,  $F_{Cl}$  is the chloride content factor,  $F_{Galv}$  is the galvanic effect factor,  $F_{Oxide}$  is a factor related to the presence of oxide layer at the surface of steel, and  $F_{O_2}$  is the oxygen availability factor. The concrete resistivity at time  $t$ ,  $\rho(t)$  ( $\Omega.m$ ), in Eq. (2.2) is given as:

$$\rho(t) = \rho(t_0) f_e f_t \left( \frac{t}{t_0} \right)^{n_{age}} \quad (2.3)$$

where  $\rho(t_0)$  ( $\Omega.m$ ) is concrete resistivity measured at time  $t_0$ ,  $f_e$  is the exposure condition factor,  $f_t$  is the test method factor, and  $n_{age}$  is age constant .

Equation (2.2) is an improved version of Eq. (2.1) in three ways: Firstly, the concrete resistivity is considered instead of concrete resistance. This makes the DuraCrete model independent of geometry and concrete resistance measurement method. Secondly, the effect of aging on the concrete resistivity is considered using

Eq. (2.3). Finally, the introduction of the environmental factors in Eq. (2.2) reduces the scatter observed in the predictions of Eq. (2.1).

Despite the improvements in the DuraCrete model, there is a lack of data to quantify the introduced factors and their interactions (Raupach 2006). Furthermore, this model is developed only for chloride-induced corrosion; therefore the corrosion rate of carbonation-induced corrosion may not be estimated accurately since chloride contamination reduces the concrete resistivity whereas carbonation increases it. In addition, DuraCrete model, similar to Alonso's model given in Eq. (2.1), only considers the resistance control mechanism and ignores all the other control mechanisms such as diffusion and activation. This causes the model to be limited to a certain relative humidity range. Furthermore, the effect of temperature, although it can be considered through concrete resistivity to some extent, is ignored. It should be noted that temperature directly affects the kinetic parameters of steel corrosion, as it will be demonstrated in the following chapters, and for accurate prediction of corrosion rates, the effect of temperature variations should be considered.

### **2.2.3. Liu and Weyers (1998)**

Liu and Weyers (1998) developed an empirical model by testing large specimens simulating concrete bridge decks. For developing this model, a total of 44 specimens were cast with different values of chloride content and cover thickness, which are summarized in Table 2.2. The w/c ratio of the specimens was between 0.41 and 0.45.

Corrosion rate and electrical resistance of the specimens were measured with 3-Electrode-Polarization (3LP) and Gecor devices. Temperature was monitored with

a T-type thermocouple embedded at rebar depth. At the final stage of the experiment, metal mass loss measurements were performed in accordance with ASTM G1-90 method C3.5. During a 5-year outdoor exposure of the specimens, a total of 2927 measurements were recorded by 3LP and Gecor devices. The model presented by Eq. (2.4) was constructed by a regression analysis on the data recorded by 3LP. No correlation between the considered parameters and corrosion rate was observed using Gecor device.

$$\ln 1.08i_{corr} = 7.89 + 0.7771 \ln 1.69C_i - \frac{3006}{T} - 0.000116R_{con} + 2.24t^{0.215} \quad (2.4)$$

where  $C_i$  (kg/m<sup>3</sup> of cement) is acid soluble chloride content as determined by ASTM C1152,  $T$  (°K) is temperature, and time,  $t$ , is given in years. A separate model considering the water soluble (free) chlorides,  $C_f$ , that were determined using ASTM C1218 was also proposed by these researchers:

$$\ln 1.08i_{corr} = 8.37 + 0.618 \ln 1.69C_f - \frac{3034}{T} - 0.000105R_{con} + 2.32t^{0.215} \quad (2.5)$$

Although three different cover thicknesses were considered in experimental design, it was observed that cover thickness imposes a nominal effect on the corrosion rate and hence was eliminated in the regression analysis. However, closer examination of the above equations shows the effect of cover thickness is incorporated implicitly into the model since concrete resistance is considered instead of concrete resistivity: concrete resistance is a function of cover thickness. The independent effect of cover thickness on the corrosion rate would have been observed if concrete resistivity had been considered instead of concrete resistance.

Chloride contamination also influences the concrete resistance significantly (Hunkeler 1994), but in these models the chloride content is considered as an independent variable. In other words, in these models chloride content has both explicit and implicit effects on the corrosion rate.

Liu and Weyers also compared the corrosion rates measured using 3LP and Gecor with the mass loss method. Results indicate that 3LP overestimates and Gecor underestimates the corrosion rate. Measurements of 3LP are generally 15 times larger than Gecor and 4 times larger than weight loss measurements. The overestimation of the 3LP was not considered in regression analysis.

As the other two models described before, oxygen availability, which is a major limiting factor of corrosion rate in concretes with high degree of saturation, is not considered in the Liu and Weyers model either. Therefore it fails to predict the corrosion rate under diffusion control mechanism when the concrete resistivity is not the main controlling factor.

Table 2.2 : Experimental design implemented by Liu and Weyers (1998)

Chloride series, kg/m <sup>3</sup> of cement	0.00	0.36	0.71	1.42	2.85	5.69	7.20
Cover depth, mm							
25	---	---	---	---	---	---	4
51	2	3	9	3	3	3	---
76	2	3	3	3	3	3	---

#### 2.2.4. Ahmad and Bhattachajee (2000)

A model correlating the effect of w/c ratio, cement content and chloride content to steel corrosion rate was developed experimentally by Ahmad and

Bhattachajee (2000). Table 2.3 presents the values of the parameters used in the experiments. Three values of each parameter (for a total of 27 specimens) were considered to capture quadratic, bilinear and linear variation of corrosion rate with each parameter. The result was the model given in the following equation:

$$i_{corr} = 37.726 + 6.120C_{Chloride} - 2.231A_{cement}^2 B_{w/c} + 2.722B^2 C_{Chloride}^2 \quad (2.6)$$

where  $i_{corr}$  is in  $\text{nA/cm}^2$ , and  $A_{cement}$ ,  $B_{w/c}$  and  $C_{Chloride}$  are given in the following equations:

$$A_{cement} = \frac{C_{cement} - 300}{50} \quad (2.7)$$

$$B_{w/c} = \frac{w/c - 0.65}{0.075} \quad (2.8)$$

$$C_{Chloride} = \frac{C_{Cl} - 2.5}{1.25} \quad (2.9)$$

where  $C_{cement}$  ( $\text{kg/m}^3$ ) is the cement content and  $C_{Cl}$  (represented in % by weight of cement) is the chloride content in the form of  $\text{CaCl}_2$ .

Although the parameters considered in developing this model affect the corrosion rate significantly, no environmental factors such as relative humidity or temperature are considered. As other models discussed previously, since it does not consider the relative humidity, the model fails to predict the corrosion behaviour under diffusion control mechanism. Furthermore, since it does not include the temperature effect, its range of applicability is quite narrow.

Table 2.3: Test parameters used by Ahmad and Bhattachajee (2000)

Test parameters	Values
$C_{Cl}$ , CaCl <sub>2</sub> (% by weight of cement)	1.25, 2.5, 3.75
$C_{cement}$ , Cement content (kg/m <sup>3</sup> )	250, 300, 350
w/c ratio	0.575, 0.65, 0.725

### 2.2.5. Morinaga (1990)

Two empirical models for predicting steel corrosion rate due to chloride ingress and carbonation were developed by Morinaga (1990). To develop the chloride-induced corrosion model, chloride contaminated specimens were exposed to outdoor environment for a 10-year period, and the corrosion rate of steel in each specimen was determined by mass loss method. Considered design parameters are presented in Table 2.4. Equation (2.10) represents the model developed by regression analysis using the obtained results:

$$i_{corr} = \left\{ -0.51 - 7.60C_{Cl} + 44.97(w/c)^2 + 67.95C_{Cl}(w/c)^2 \right\} \times (d_{st}/d^2) \quad (2.10)$$

where  $i_{corr}$  in this equation was represented in terms of  $10^{-4}$  g/cm<sup>2</sup>/year;  $C_{Cl}$  (% by weight of mixing water) is the chloride content in the form of NaCl;  $d_{st}$  (mm) is the diameter of reinforcing steel and  $d$  (mm) is the cover thickness. The  $R^2$  of the regression analysis for Eq. (2.10) was reported as 0.95. The corrosion rate model given in Eq. (2.10) does not include the effect of environmental parameters. In order to develop a more comprehensive model, the effect of environmental parameters on the chloride-induced corrosion rate was investigated by exposing grout coated rebars to different environmental conditions for 8 years. Table 2.5 presents the environmental data used in the tests. The same chloride contamination levels as

presented in Table 2.4 were chosen for the grout coating. Equation (2.11) is the developed model whose  $R^2$  was reported as 0.835:

$$\begin{aligned} i_{corr} = & 2.59 - 0.05T - 6.89(h - 0.45) - 22.87C_{O_2}^{air} - 0.99C_{Cl} \\ & + 0.14T(h - 0.45) + 0.51TC_{O_2}^{air} + 0.01TC_{Cl} + 60.81(h - 0.45)C_{O_2}^{air} \\ & + 3.36(h - 0.45)C_{Cl} + 7.32C_{O_2}^{air}C_{Cl} \end{aligned} \quad (2.11)$$

where  $i_{corr}$  is presented in ( $\times 10^{-4}$  g/cm<sup>2</sup>/year),  $T$  is in (°C),  $h$  (%) is the relative humidity,  $C_{O_2}^{air}$  (%) is the concentration of oxygen in air. It should be noted that this model does not include any mix design parameter, such as w/c ratio, in its formulation.

The effect of environmental parameters on the carbonation-induced corrosion rate was presented as:

$$\begin{aligned} i_{corr} = & 21.84 - 1.35h - 234.76C_{O_2}^{air} + \\ & 2.33Th + 4.42TC_{O_2}^{air} + 250.55hC_{O_2}^{air} \end{aligned} \quad (2.12)$$

where all variables are defined as in Eq. (2.11).

For developing this model, specimens were carbonated to the rebar depth and exposed to different environments consisting of two temperatures (20 and 40 °C), five values of relative humidity (0, 51, 62, 100%, and underwater), and three oxygen concentrations of air (0, 10, and 20%). It was observed that even in the absence of oxygen, the corrosion of rebar proceeded to produce iron carbonate. Therefore, in calculating the carbonation-induced corrosion rate, iron carbonate was considered as a corrosion product; however, in reality, the concentration of carbon dioxide may not be significant enough to produce iron carbonate at the surface of rebar. It is likely that the model presented here overestimates the corrosion rate of rebar in the case of

carbonated concrete; however, no verifications for any of the models were presented by Morinaga.

Table 2.4: Design parameters in the tests conducted by Morinaga (1990)

<b>Factor</b>	<b>Levels</b>
Concrete type	Ordinary, Light-weight
Water-cement ratio	0.40, 0.55 ,0.70
Chloride content (%) (NaCl by weight of mixing water)	0, 0.1, 0.5, 1.0, 1.5, 3.0
Direction of reinforcing steel	Horizontal, Vertical
Diameter of reinforcing steel (mm)	9, 25
Cover thickness (mm), for 9 mm steel for 25 mm steel	4, 6, 9, 12, 16, 22, 29, 37 5, 8, 13, 20, 27, 37

Table 2.5: Environmental parameters in the tests conducted by Morinaga (1990)

<b>Factors</b>	<b>Levels</b>
Temperature (°C)	20, 40
Relative humidity (%)	0, 51, 62, 100, and underwater
Oxygen concentration of air (%)	0, 10, 20

Morinaga's models can be considered to be quite comprehensive since they are built on long-term studies that cover a large number of test variables. Nevertheless, in the case of chloride-induced corrosion the design and environmental parameters were separated from each other, and no guideline was provided for merging them. In practice, these parameters cannot be considered separately. It should also be noted that for investigating the environmental effects on the chloride-induced corrosion, grout coated rebars were used instead of concrete or mortar specimens. Extrapolating the results from grout coated specimens to concrete and mortar is prone to error since many properties (e.g. porosity, water content,

diffusivity) of grout coatings are substantially different from those of the concrete and mortar.

### 2.2.6. Morinaga (1996)

Morinaga (1996) proposed a model for predicting the corrosion rate of steel in cracked concrete. The assumption behind this model was that when concrete cover cracks the corrosion rate of steel increases due to the abundant supply of oxygen and water. Hence, it was assumed that steel in cracked concrete would be exposed to the same conditions as freely corroding steel specimens and will corrode with the same rate. Based on this hypothesis two sets of tests were carried out to develop the model.

In the first experiment, 100x100x5 mm steel plates were exposed to 43 different environmental conditions. The weight losses of the steel specimens and the environmental parameters were recorded periodically. Equation (2.13) presents the relationship among corrosion depth, environmental parameters and the period of exposure:

$$d_{corr} = A_{corr} \sqrt{t} \quad (2.13)$$

$$A_{corr} = -11.5 + 9.30T_c - 0.0306d_{rain} + 2.52C_{salt}^{Air} + 0.135C_{SO_2} \quad (2.14)$$

where  $d_{corr}$  (mm) is the corrosion penetration;  $T_c$  ( $^{\circ}$ C) is the annual average temperature;  $d_{rain}$  (mm) is the annual rainfall;  $C_{salt}^{Air}$  (ppm) is the annual air-borne salts, and  $C_{SO_2}$  (mg/100cm<sup>2</sup>) is the annual deposited SO<sub>2</sub>.

In the second experiment, bare reinforcing bar specimens were exposed to six different environmental conditions (temperature and relative humidity), and the weight loss of specimens was measured over a 3-year period. Eq. (2.15) represents

the relationship between the weight loss, environmental parameters and exposure time.

$$m_{corr} = B_{corr}t \quad (2.15)$$

where  $m_{corr}$  ( $10^{-4}$  g/cm<sup>2</sup>) is the amount of corrosion products, and  $t$  (years) is the duration of exposure. The value of the corrosion rate coefficient,  $B_{corr}$ , can be found in Figure 2.1.

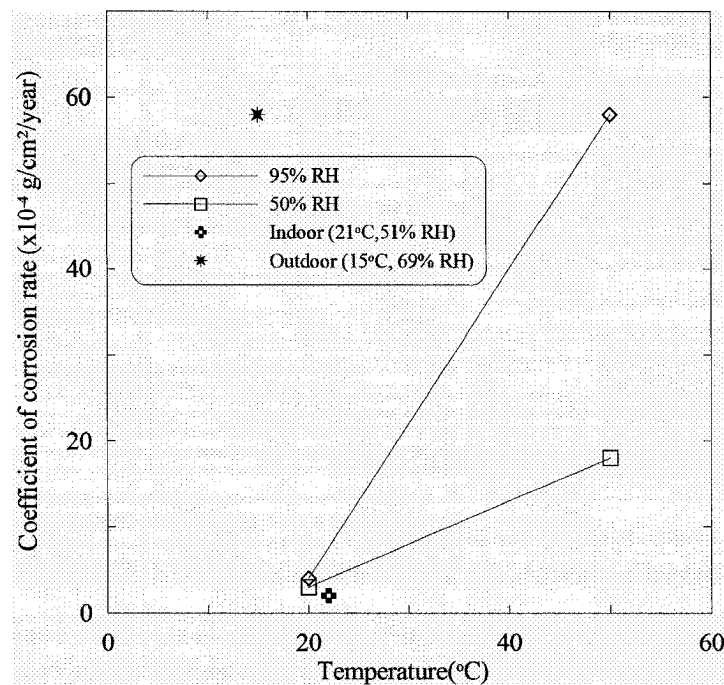


Figure 2.1: Coefficient of corrosion rate in Eq. (2.15) (Morinaga 1996)

Although there is an expected relationship between the presence of cover cracks and corrosion rate in reinforced concrete structures (Isgor and Razaqpur 2006), the hypothesis used in the design of this experimental study (i.e. assuming that the corrosion rate would be the same for steel in cracked concrete and freely corroding steel specimens) is subject to debate. Since the exposed areas and conditions of exposure and chemistry of the environment in the two cases are substantially

different, the formation of anodes and cathodes as well as the kinetics of corrosion can be expected to be different as well.

### **2.3. Mathematical models**

A number of mathematical models for estimating steel corrosion rate in concrete have been introduced in the literature. These models are based on either the mathematical representation of controlling mechanisms of corrosion or complex numerical modelling of polarization of steel. It should be noted that since it is possible and practical to numerically include multiple mechanisms that may affect corrosion, the latter approach has been gaining more interest. In the following sections, prominent mathematical models are presented.

#### **2.3.1. Bazant (1979)**

A mathematical model for estimating the corrosion rate of steel in submerged reinforced concrete structures was developed by Bazant (1979). In this model, the potentials of anodic and cathodic sites of steel were calculated using the Nernst equation. In using the Nernst equation, the concentration of species (i.e. iron ions, hydroxyl ions and oxygen) were calculated from the mix proportions, the pH of the pore solution and by considering the diffusion of species through concrete cover. Equations (2.16) and (2.17), respectively, present the potentials of anodic and cathodic sites of steel that are used as electric potential boundary conditions for field equations presented by Eq. (2.18) and Eq. (2.19). It is noted that substituting Eq. (2.19) in Eq. (2.18) will result in the Laplace's equation for electric potential.

$$\phi_a = \phi_{st} + 0.357 - 0.02961 \log \frac{u_f}{u_w^A} \quad (2.16)$$

$$\phi_c = \phi_{st} - 1.187 - \log \frac{u_o^C}{u_w^C} \quad (2.17)$$

$$\rho i = -\nabla \phi \quad (2.18)$$

$$\nabla i = 0 \quad (2.19)$$

In the above equations,  $\phi$  (mV) is the electric potential resulting from the electrochemical reaction, and subscripts a and c are representative of “anodic” and “cathodic” respectively.  $\phi_{st}$  is the steel surface potential, and its value is an unknown to be calculated for submerged structures and equals zero for structures exposed to air.  $u_f$  is the mass concentration of  $\text{Fe}(\text{OH})_2$  per unit volume of concrete,  $u_w^A$  is the amount of capillary water (gram per cubic meter of concrete) adjacent to the anodic surface,  $u_w^C$  is the amount of capillary water (gram per cubic meter of concrete) adjacent to cathodic surface, and  $u_o^C$  is the oxygen concentration (kilogram per cubic meter of concrete) adjacent to cathodic surface.

In addition to the electric field equation and potential boundary conditions presented above, Bazant introduced governing differential equations for the diffusion process and their boundary conditions and formulated the problem as a boundary value problem which can be solved by a numerical technique such as the finite element method. Although the model proposed by Bazant provides great insights to the problem of steel corrosion in concrete, it has a number of drawbacks. One of the main drawbacks is that it ignores the activation polarization, and only considers concentration polarization. Although ignoring the activation polarization might be a

reasonable assumption in highly-saturated concretes, since for saturated conditions the oxygen diffusion process is very slow, and the effect of concentration polarization is dominant, this assumption is not valid for concretes with low degree of saturation in which activation polarization is a significant term. Furthermore, since anodic sites are only affected by activation polarization, ignoring this type of polarization implies that anodic sites do not polarize and hence corrosion proceeds at the anodic equilibrium potential. Bazant, argues that the anodic sites do polarize due to oxygen supply (i.e. concentration polarization) since the term  $u_f$  is a function of oxygen availability; however, this argument is not valid since  $u_f$  is a function of the rate of transportation of  $\text{OH}^-$  in the bulk of the concrete which is taken care of through considering the resistivity of concrete.

According to Eq. (2.16) anodic potential is dependent on the diffusion of ferrous hydroxide away from the rebar, since  $u_f$  is the concentration of ferrous hydroxide and if this term is constant (i.e. ferrous hydroxide does not diffuse away from the anodic surface) the potential of the anodic sites will be constant. However, assuming that the diffusion of ferrous hydroxide away from the anodic surface will cause the polarization of anodic sites may not be a valid assumption in more advanced stages of corrosion when large amount of corrosion products are formed next to the rebar and the diffusion of ferrous hydroxide away from the surface may not cause a significant variation in the concentration of ferrous hydroxide next to the rebar.

Bazant's approach makes the model geometry dependent since the boundary conditions should be set according to the geometry of the problem and the location of

anodic and cathodic sites. Furthermore, the term  $u_f$  appearing in the anodic polarization is a function of corrosion rate which makes the problem non-linear. Due to geometry dependence and non-linearity of the problem, the model can be expensive computationally even in simple geometries.

Despite all the drawbacks, Bazant's approach was later used by Balabanic et al. (1995) for modelling the corrosion of rebar in a cylindrical concrete specimen, which is discussed in the following section.

### **2.3.2. Balabanic et al. (1995)**

By developing a non-linear algorithm for solving the coupled equations of electric potential and oxygen diffusion, applying the framework suggested by Bazant (1979), Balabanic et al. (1995) introduced a model for estimating the corrosion rate of steel in concrete cylinders. This 3-D domain was reduced to a 2-D domain considering axisymmetry, and the system of governing partial differential equations (i.e. Laplace's equation for electric potentials and diffusion equation for oxygen diffusion in concrete) were solved numerically by the finite element method. Electrical resistivity and oxygen diffusion coefficient of concrete were considered to be constant.

In constructing this model, the anodic boundary condition proposed by Bazant was modified such that it was considered to be fixed at the standard potential of steel (i.e. ferrous hydroxide concentration variation is ignored). The boundary condition on the cathodic surfaces was defined by Eq. (2.17) as suggested by Bazant (1979). The model was used to investigate the effect of w/c ratio, cover thickness and the degree of saturation on the corrosion rate of rebar.

Since the model developed by Balabanic et al. (1995) is based on the framework developed by Bazant (1979), it has the same limitations as discussed in the previous section. By considering a constant potential for anodic boundary conditions, the polarization behaviour of steel is modified significantly. As discussed before the polarization of steel surface is a function of corrosion rate, making the boundary conditions nonlinear; therefore the solution of Laplace's equation requires a nonlinear solution algorithm. The model proposed by Balabanic et al. (1995) hence oversimplifies the problem.

### 2.3.3. Raupach and Gulikers (1999)

Another way of modelling corrosion of steel in concrete is through equivalent circuits. In this approach, the macro-cell current flowing from anodic to cathodic sites is calculated using Ohm's law by dividing the potential difference between passive and active sites on the steel surface to the equivalent circuit resistance, which is the sum of concrete resistance, and anodic and cathodic polarization resistances. A schematic of a typical equivalent circuit is illustrated in Figure 2.2. Equation (2.20) represents Ohm's law used in equivalent circuit model.

$$I_{corr} = \frac{\phi_{O_2}^{\circ} - \phi_{Fe}^{\circ}}{R_{p,c} + R_{con} + R_{p,a} + R_{st}} \quad (2.20)$$

where  $\phi_{Fe}^{\circ}$  is the anodic equilibrium potential,  $\phi_{O_2}^{\circ}$  is the cathodic equilibrium potential,  $R_{p,c}$  is the cathodic polarization resistance,  $R_{p,a}$  is the anodic polarization resistance and  $R_{st}$  is the electrical resistance of steel. In Eq. (2.20) resistance of steel can be neglected due to high conductivity, and the polarization resistance of anode

and cathode can be calculated using Butler-Volmer kinetics (Brad and Faulkner 2001), which is discussed further in Chapter 1.

Raupach and Gulikers (1999) applied this model to two different hypothetical cases: (1) plan-parallel where anodic and cathodic sites are located on different rebars; this type of corrosion is usually encountered in bridge slabs that experience salt penetration from one side; (2) Coplanar where anodic and cathodic sites are located at distinguishable parts of the same rebar. In both cases the exact location and dimensions of the anodic and cathodic sites were assumed, and then the concrete matrixes as well as anodic and cathodic sites were modelled by using discrete elements. Although equivalent circuit model considers activation and resistance control mechanisms of corrosion, its application to real world situations is very limited since to apply this model, the exact distribution of the anodic and cathodic sites on the steel surface should be known in advance.

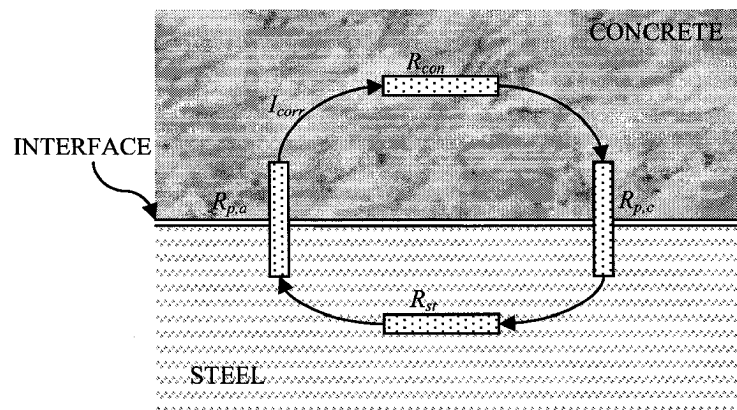


Figure 2.2: Illustration of an equivalent circuit

Although this model was initially developed for macro-cell corrosion, Gulikers (2005) combined this model with the results of the experimental model proposed by Alonso et al. (1988) and obtained a new model for uniform corrosion of steel in concrete. This model will be discussed in the following section.

#### 2.3.4. Gulikers (2005)

According to equivalent circuit model, the potential difference between the anodic and cathodic sites comprises of three contributions from anodic polarization, cathodic polarization and  $IR$  drop. Anodic and cathodic polarizations can be calculated using Butler-Volmer kinetics, and  $IR$  drop can be calculated using Ohm's law.

Using this approach for calculating the potential difference between anodic and cathodic sites, Gulikers (2005) developed a relationship between corrosion current density and concrete resistance. Concrete resistance then was converted to concrete resistivity by considering a geometry (i.e. shape) factor. This geometry factor was found by comparing the equations resulting from equivalent circuit model and the model proposed by Alonso et al. (1988); the value for the geometry factor suggested was  $578 \times 10^{-3}$ . Equation (2.21) provides the resulting model:

$$i_{corr} = \frac{F_G^{-0.8125} 98.696 \times 10^{-3}}{\rho^{0.8125}} \quad (2.21)$$

where  $i_{corr}$  is in ( $A/m^2$ ) and  $F_G$  ( $m^{-1}$ ) is the geometry factor.

This model improves Alonso et al.'s model in two ways: (1) since concrete resistance is replaced with concrete resistivity, the model is independent of the geometry of the problem; (2) since equivalent circuit model considers some of the

effects of kinetic parameters of controlling mechanisms of corrosion, it provides a more robust framework. However, it still shares the same disadvantages of Alonso et al.'s model as it also fails to predict the corrosion behaviour under diffusion control. Furthermore, Gulikers's model is constructed considering constant kinetic parameters of concrete which may vary substantially due to environmental effects such as temperature, relative humidity and concrete properties such as w/c and porosity.

### **2.3.5. Kranc and Sagues (1992)**

One of the most comprehensive models for predicting the corrosion rate in concrete was introduced by Kranc and Sagues (1992). This model is based on the coupled solution of Laplace's equation for electric potential and steady-state oxygen diffusion using the finite difference method. In solving the Laplace's equation for electric potential, boundary conditions of anodic and cathodic sites were set according to Butler-Volmer kinetics. While the dissolution of iron was considered to take place only on the anodic sites, oxygen reduction was considered to take place on both anodic and cathodic sites. Boundary conditions were set according to the considered geometry of the problem, possible paths of oxygen diffusion and exposure condition. In this model the concrete resistivity and the oxygen diffusion coefficient of concrete can be considered as functions of the degree of saturation (Kranc and Sagues 1994, Kranc and Sagues 1997) This model can be used effectively for investigating different aspects of the rebar corrosion such as determining the polarization diagrams of steel (Kranc and Sagues 1992), and investigating the effects of counter electrode polarization (Kranc and Sagues 1997).

However, due to the limitations of the finite difference method, the model can be used to model pre-defined geometries; therefore, boundary conditions can only be set specific to the considered geometry of the problem. Setting the boundary conditions requires prediction of the depassivated zones of the rebar. Since depassivation of steel in concrete is a complex process, depassivated zones of the rebar can not be predicted easily.

Since this model is based on the numerical solution of Laplace's equation with Butler-Volmer boundary conditions, fundamental understanding of the numerical procedures and electrochemistry of corrosion are essential for accurate interpretation of the results. Considering Butler-Volmer boundary conditions necessitates the non-linear solution of Laplace's equation, which can be computationally expensive and time consuming. The increase in time and computational expense of the solutions are more pronounced in the case complicated geometries.

There has been a growing interest in the numerical solutions of Laplace's equation subjected to polarized boundary conditions among researchers. Finite element and boundary value methods have been extensively used for this purpose (Redaelli et al. 2006, Warkus et al. 2006), and good agreement between these methods were obtained. This is due to the fact that simulation of potential distribution in the bulk of the concrete using these numerical methods has a sound physical meaning, and the only drawback of these methods is their dependence on the geometry of the problem. This drawback is addressed in this thesis by using the finite element method in different context which makes the results reasonably geometry independent. The details of the research method can be found in Chapter 3.

### 2.3.6. Takewaka et al. (2003)

The model developed by Takewaka et al. (2003) is, in fact, a computer simulation of reinforced concrete matrix. In this model, reinforced concrete matrix was simulated by the random distribution of pore space and aggregate particles according to mix proportions and gradation. Pores were classified as water-filled and air-filled, and the water content of concrete was defined as the ratio of the volume of the water-filled pores to total volume of the pores. Aggregates were also divided into wet and dry categories. Interfacial transition zone (ITZ) around the aggregates was considered water-filled and air-filled depending on whether they surround dry or wet aggregates. This is illustrated in Figure 2.3. Furthermore, the concrete matrix was considered consisting of internal and external layers where the internal layer contains 10% higher relative humidity.

The rebar was divided into 1-cm length sections, and straight diffusion paths to each section of the rebar were considered; this is illustrated in Figure 2.3. The length and the diffusion coefficient of the diffusion paths passing through pores or aggregates were adjusted considering the water content of each zone (e.g. pores, ITZ, aggregates), as illustrated in Figure 2.4. Aggregates were considered impermeable, and the presence of cracks on the surface of concrete was considered by modifying these diffusion paths and their diffusion coefficient.

The concentration of chloride ions, through diffusion, at the surface of each 1-cm section of the rebar was monitored continuously, and a section of rebar was considered anodic when the concentration of chloride ions reached a predefined threshold value. The corrosion rate of each section was considered to be under anodic

or cathodic control depending on the proceeding reaction, and the rate of the reaction was estimated using Eq. (2.22) and Eq. (2.23) for cathodic and anodic control, respectively:

$$V_c^{Fe^{2+}} = C_{O_2}^{air} \frac{A_c}{A_a} \frac{D_{O_2} \left( \frac{d}{L_{O_2,c}} \right)^2}{L_{O_2,c}} \quad (2.22)$$

$$V_a^{Fe^{2+}} = C_{O_2}^{air} \frac{D_{O_2} \left( \frac{d}{L_{O_2,a}} \right)^2}{L_{O_2,a}} \quad (2.23)$$

where  $V_c^{Fe^{2+}}$  ( $\text{mol.m}^{-2}.\text{s}^{-1}$ ) is the reaction rate of  $Fe^{2+}$  in cathodic control,  $V_a^{Fe^{2+}}$  ( $\text{mol.m}^{-2}.\text{s}^{-1}$ ) is the reaction rate of  $Fe^{2+}$  in anodic control,  $C_{O_2}^{air}$  ( $\text{mol/m}^3$ ) is the concentration of oxygen in air,  $A_c$  ( $\text{m}^2$ ) is the cathodic area,  $A_a$  ( $\text{m}^2$ ) is the anodic area,  $d$  (m) is the cover thickness,  $L_{O_2}$  (m) is the length of oxygen diffusion path assumed in the model,  $D_{O_2}$  ( $\text{m}^2/\text{s}$ ) is the concrete oxygen diffusion coefficient. The smaller of the two reaction rates was used as the corrosion rate of the system. Using the calculated corrosion rate, the amount of mass loss per unit time can also be calculated. Since the amount of water present in the concrete can be a limiting factor for cathodic reduction of oxygen, the corrosion loss is obtained from Eq. (2.22), and Eq. (2.23) was modified considering the concrete water content.

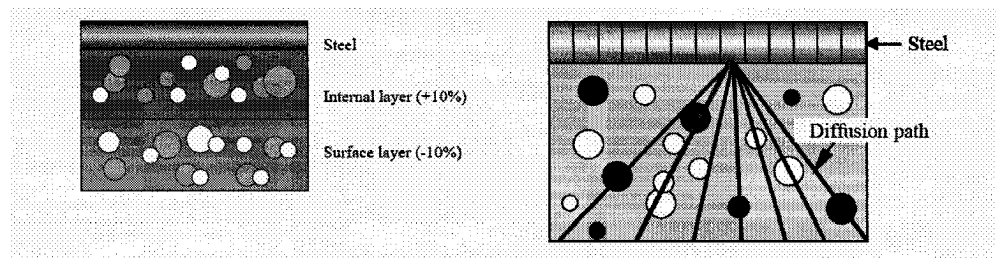


Figure 2.3: Illustration of internal and external concrete layers and diffusion path for each section of rebar (Takewaka et al. 2003) (Taken from the original paper)

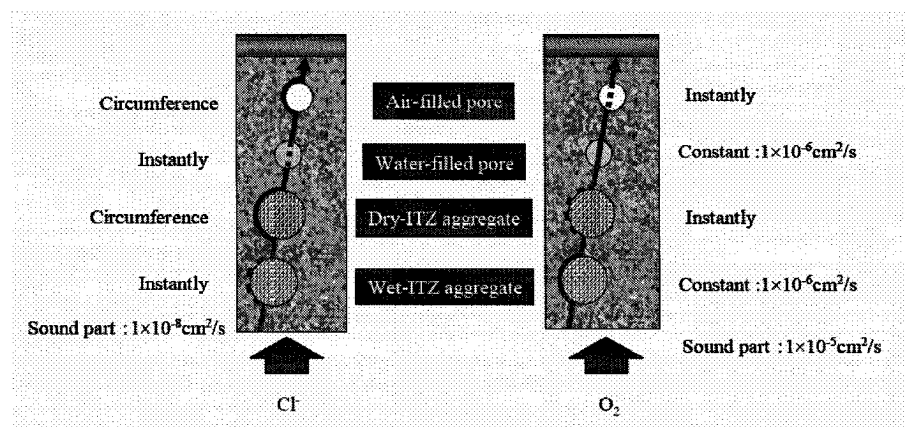


Figure 2.4: Illustration of adjustment considered for diffusion coefficient of diffusion path (Takewaka et al. 2003) (Taken from the original paper)

Although this model considers the effect of relative humidity, it ignores the effect of the one of the important environmental parameters: temperature. The effect of temperature, although it can be included in the model through the oxygen diffusion coefficient to some extent, is not considered in developing this model. Considering the effect of temperature through the oxygen diffusion coefficient in Eqs. (2.22) and

(2.23) do not take care of the changes that kinetic parameters of corrosion would experience.

While temperature is ignored, the distance from the sea shore is considered as a parameter in this model and the concentration of chloride at the surface of concrete is considered a function of the distance from sea shore. Consequently, carbonation as a cause of depassivation is ignored. In addition, this model is based on the macro-cell corrosion, and each steel section can be either anodic or cathodic at a given time. Although this assumption is usually valid for chloride-induced corrosion, in homogeneously chloride-contaminated or carbonated concretes more uniform corrosion is observed, and the macro-cell assumption may not be valid.

It should also be mentioned that regardless whether the corrosion is controlled anodically or cathodically, the reaction rates calculated by Eqs. (2.22) and (2.23) are based on oxygen diffusion, which makes the process governed by diffusion control. However, in addition to diffusion control, corrosion process can be under activation or resistance control as well (Ghods et al. 2007); under activation and resistance control Takewaka et al. model fails to predict the corrosion rate accurately.

#### **2.3.7. Song et al. (2005)**

Song et al. (2005) developed a model consisting of initiation and propagation stages. The initiation stage of the model considers the chloride ingress and carbonation of concrete, which were modelled using the finite element method. The propagation stage of corrosion, which will be represented here, was modelled considering uniform corrosion of the reinforcement.

If sufficient amount of oxygen is available, the corrosion current density, in propagation stage, was calculated depending on the state of the passive layer. If oxygen availability is limited, corrosion current density was considered to be equal to the limiting current density. According to this model if steel is in passive state the corrosion rate was calculated using:

$$\log i_{corr} = \log i_{oa} \quad (2.24)$$

where  $i_{corr}$  is in (A/m<sup>2</sup>), and  $i_{oa}$  (A/m<sup>2</sup>) is the iron exchange current density. If the passive film is not completely destroyed, the corrosion current density would be calculated using the following equations:

$$\log i_{corr} = \frac{0.998 - 0.06\text{pH} - 0.059 \log i_{oc} + \beta \log i_{oa}}{\beta + 0.059} \quad (2.25)$$

$$\beta = \frac{0.059 \times (C_f^* - C_f')}{C_f - C_f'} \quad (2.26)$$

where  $i_{oc}$  (A/m<sup>2</sup>) is the oxygen reduction exchange current density,  $C_f$  is the free chloride content (% by the weight of the cement),  $C_f^*$  is the free chloride content (% by the weight of the cement) for complete destruction of passive film,  $C_f'$  is the free chloride content (% by the weight of the cement) necessary for initiation of corrosion. If the passive film is completely destroyed the corrosion rate was calculated using Eq. (2.27).

$$\log i_{corr} = 8.458 - 0.508\text{pH} + 0.51 \log i_{oc} + 0.51 \log i_{oa} \quad (2.27)$$

The formulations used for estimating the corrosion rate in this model are very basic and, the electrochemical principles of these formulations are not discussed in detail in the published work by authors (Song et al. 2005). However, since corrosion

current density formulations are based on the state of passive film, uncertainties are to be expected due to complex mechanism of depassivation. Inadequate referencing and the lack of elaboration of the published work (Song et al. 2005) prevent further discussion of the model.

### **2.3.8. Huet et al. (2006)**

The fact that oxygen diffusion is a slow process in concrete with high degree of saturation and can be the controlling mechanism of steel corrosion forms the basis of the model developed by Huet et al. (2006). In developing this model it was assumed that (1) only the dissolved oxygen in the pore solution next to steel may be reduced, i.e. the kinetics of gaseous oxygen reduction is far lower than that of dissolved oxygen; (2) oxygen reduction obeys the first order kinetics law, i.e. the kinetics of oxygen reduction depends only on the concentration of dissolved oxygen; and (3) oxygen reduction takes place at the surface of the reinforcement and within the conductive oxide layer formed on the steel surface, and the rate of the oxygen consumption depends on the specific surface area of this porous oxide layer. Fick's second law of diffusion was corrected for this consumption and solved under steady-state conditions for oxygen concentration profile in the bulk of concrete. The oxygen concentration was then related to oxygen reduction current using Faraday's law. Eqs. (2.28) and (2.29) present the model developed by Huet et al.:

$$i_c = n_e F s_a \lambda k_{O_2} \varepsilon^2 S_r C_{O_2,liquid}(x_2) \quad (2.28)$$

$$\lambda = \sqrt{\frac{D_{O_2,liquid}}{s_a k_{O_2} \varepsilon^2 S_r}} \quad (2.29)$$

where  $i_c$  (A/m<sup>2</sup>) is the rate of cathodic reaction, and  $i_c$  is considered to be equal to the corrosion rate,  $n_e$  is the valance number,  $F$  ( $\approx 96500$  C/mole) is the Faraday's constant,  $s_a$  ( $\approx 3.7 \times 10^7$  m<sup>2</sup>/m<sup>3</sup>) is the specific surface of the oxide layer per unit volume,  $k_{O_2}$  ( $\approx 10^{-5}$  ms<sup>-1</sup>) is the kinetic constant of oxygen reduction,  $S_r$  is the degree of water saturation,  $\varepsilon$  is the porosity of the concrete considering the same porosity for oxide layer,  $C_{O_2,liquid}(x_2)$  (mol/m<sup>3</sup>) is oxygen concentration in the pore solution per unit volume of concrete and  $x_2$  represents the surface of the concrete,  $D_{O_2,liquid}$  (m<sup>2</sup>s<sup>-1</sup>) is the diffusion coefficient of species in pore solution.

By comparing the results of the model with experimental data in the literature Huet et al. found that their model overestimates the corrosion rate for all degrees of saturation, and kinetics of the cathodic reaction itself fails to predict the corrosion behaviour of steel in concrete. They suggested that other control mechanisms such as oxygen diffusion through the cover and anodic control should be taken into account. Although the major drawback of the model is acknowledged by the researchers, it should be noted that this model does not consider the resistance control mechanism of corrosion. Since concrete is a high-resistance media even, when the degree of saturation is high (Gjørsv et al. 1977), the resistivity of concrete can be a controlling parameter in steel corrosion (Alonso et al. 1988).

### 2.3.9. Maruya et al. (2003)

A comprehensive model for the service life prediction of reinforced concrete structures consisting of initiation and propagation stages was developed Maruya et al. (2003). The initiation stage of this model considers different transport mechanisms. In the propagation stage, the corrosion rate of reinforcement was estimated using an algorithm illustrated in Figure 2.5 in which the corrosion rate was calculated considering both micro- and macro-cell corrosion.

Based on this algorithm,  $[Cl^-]/[OH^-]$  (ratio of the concentration of the free chloride to concentration of hydroxide ions) was calculated at each node through the data obtained from the initiation stage; if this ratio was larger than 4.7 the node was considered depassivated and its potential was calculated using:

$$\phi_{pit} = -0.015 - 0.31 \log \frac{[Cl^-]}{[OH^-]} \quad (2.30)$$

where  $\phi_{pit}$  (volts) is the pitting potential. If  $[Cl^-]/[OH^-]$  was smaller than 4.7 for a given node, the node was considered passive and the corresponding potential was calculated using:

$$\phi_{pass} = \phi_{O_2}^\circ + \beta_c \log \frac{i_{pass}}{i_{oc}} \quad (2.31)$$

where  $\phi_{pass}$  (volts) is the potential of passive steel,  $\phi_{O_2}^\circ$  (volts) is the standard potential of oxygen reduction;  $i_{oc}$  (A/cm<sup>2</sup>) is the cathodic exchange current density,  $i_{pass}$  (A/cm<sup>2</sup>) is the passive current of steel,  $\beta_c$  (volts/decade) is the cathodic Tafel slope.

By comparing  $\phi_{pit}$ ,  $\phi_{pass}$  and  $\phi_{O_2}^\circ$ , and using the Nernst anodic equation, the micro-cell

potential and micro-cell current of each node was calculated; however, the basic steps of these calculations were not elaborated in the published work.

Based on the obtained values for micro-cell potential and micro-cell current, macro-cell corrosion was modelled by polarizing the electrodes (using Butler-Volmer kinetics) from the micro-cell corrosion potential and micro-cell current using:

$$\begin{aligned} \phi_{ma,c} - \phi_{ma,a} &= (\phi_{mi,c} + \beta_c \log(i_{corr} / i_{mi,c})) \\ -(\phi_{mi,a} + \beta_a \log(i_{corr} / i_{mi,a})) &= L_{ac} \rho i_{corr} \end{aligned} \quad (2.32)$$

where  $\phi_{ma,c}$  and  $\phi_{ma,a}$  (volts) are cathodic and anodic macro-cell potentials respectively,  $\phi_{mi,c}$  and  $\phi_{mi,a}$  (volts) are cathodic and anodic micro-cell potentials respectively,  $i_{corr}$  ( $A/cm^2$ ) is the corrosion rate,  $i_{mi,c}$  and  $i_{mi,a}$  ( $A/cm^2$ ) are the anodic and cathodic micro-cell currents respectively,  $L_{ac}$  (cm) is the distance between the anode and cathode,  $\rho$  ( $\Omega.m$ ) is the concrete resistivity;  $\beta_c$  and  $\beta_a$  (volts/decade) are cathodic and anodic Tafel slopes given as follows:

$$\beta_a = -0.012139 \ln(C_f) + 0.1916 \quad (2.33)$$

$$\beta_c = -0.037379 \ln(C_f) + 0.2597 \quad (2.34)$$

where  $C_f$  ( $lb/m^3$ ) is the free chloride concentration per unit volume of concrete. The locations of anodic and cathodic sites were specified due to exposure condition and Eq. (2.32) was solved for all the possible circuits, and the total macro-cell current was calculated by integrating macro-cell current of all electrodes. Resulting total macro-cell current then was compared with limiting current density, and the smaller was selected as the actual corrosion rate.

Although this model integrates micro- and macro-cell corrosion, and considers the exposure conditions for specifying the anodic and cathodic sites, it is based on

purely empirical equations which are mostly derived using simulated solutions instead of concrete media. Electrochemical behaviour of steel in concrete is substantially different from its electrochemical behaviour in simulated solutions such as saturated calcium hydroxide (Stanish et al. 2004) since the former is a porous media whereas the latter is a solution. Extrapolating the results obtained from simulated solutions to concrete should be treated with caution since they do not necessarily yield the actual behaviour.

The model is also dependent on the geometry of the problem; this suggests that each problem should be considered separately for different exposure conditions. Furthermore, this model follows an iterative algorithm which can be quite expensive computationally. It should also be noted that the effect of temperature on kinetic parameters of corrosion is not included in the model, nor the kinetic parameters defined in a way that the effect of temperature can be included later.

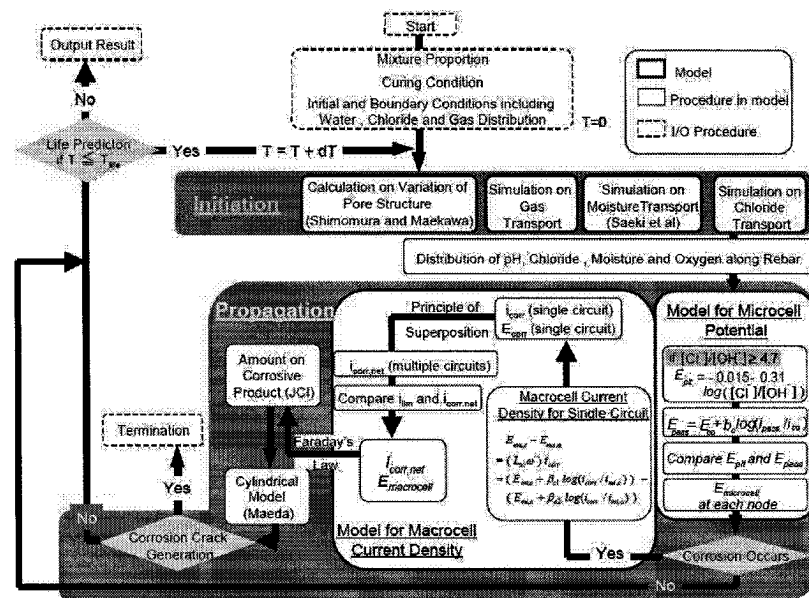


Figure 2.5: The algorithm for estimating the corrosion rate by Maruya et al. (2003)

(Taken from the original paper)

### 2.3.10. Isgor (2001)

While all numerical methods that consider initiation and propagation stages of corrosion discussed so far consider separate and sequential initiation and propagation stages, the model introduced by Isgor (2001) casts these two stages in the same time and space domain. This approach in modelling allows the change of initiation stage parameters such as temperature, relative humidity and the pH of pore solution during the propagation stage. Hence, not only the effect of propagation stage can be considered on the properties of concrete, but also the variation in exposure conditions can be considered during the propagation stage.

The other major improvement in this model (compared to the previously discussed numerical models) is that the effect of environmental parameters such as temperature, relative humidity and concrete properties such as resistivity and pH are considered on the corrosion rate of steel. Also, the effect of rust production on the properties of concrete such as pH is incorporated in this model, addressing most shortcomings associated with models discussed in previous sections.

This model is constructed using the finite element method for solving the Laplace's equation for electric potential subjected to Stern-Geary polarization equations for which a non-linear algorithm is implemented. The effects of temperature, relative humidity, pH and oxygen availability are implemented solving the respective quasi-harmonic equations of these parameters using a coupled solution algorithm. This approach enables consideration of appropriate time-dependent values of resistivity and oxygen throughout the domain and accurate simulation of the corrosion process.

In this model, both chloride ingress and carbonation of concrete cover are considered as causes of depassivation. However, since there is little agreement on the chloride threshold value which causes depassivation in the former case, two different approaches for specifying the anodic and cathodic sites are implemented in this model: (1) The chloride threshold value can be specified in the developed program of the model so that the depassivated sites can be recognized according to exposure conditions, the resulting chloride concentration and the pH of the pore solution; (2) the anodic and cathodic sites can be specified explicitly (or a uniform A/C can be specified). Implementing these options for specifying the anodic and cathodic sites makes the model more flexible. Further details of this model can be found in Isgor and Razaqpur (2006).

Although this model is comprehensive and is applicable to all scenarios of corrosion of steel in concrete, it is based on numerical methods and does not provide a closed-form solution which can be used easily by engineers and requires fundamental knowledge of numerical methods and electrochemistry of the corrosion process.

## **2.4. Summary**

During the last decade there have been numerous attempts for developing experimental and mathematical models for estimating the corrosion rate of steel in concrete. Experimental models, despite being very practical, are bound by the experimental setup and conditions that they were obtained from. Furthermore, they consider only a limited number of parameters and mechanisms that may influence the corrosion rate. Although a number of mathematical models can be quite practical;

they generally oversimplify the corrosion problem in concrete. Most of these practical mathematical models need to make assumptions of fixed geometry and fixed boundary conditions. In addition, in order to eliminate the numerical difficulties to obtain closed-form equations, they simplify the boundary conditions by ignoring one or more control mechanisms of corrosion; these simplifications limit the applicability of these models. The mathematical models that are based on the solution of the Laplace's equation have more flexibility in the geometry definition; however, defining complex geometries can only be done at the expense of computational efficiency. Especially, when multiple mechanisms of corrosion are considered through non-linear boundary conditions (e.g. Stern-Geary equations), these models can become quite impractical to use for the general civil engineering population. It should be noted that these complex models are quite useful in carrying out comprehensive academic research studies since they can be used to carry out virtual experiments, sensitivity analyses and parametric studies.

The literature review presented here, therefore, demonstrates that there is a need for developing a practical and comprehensive mathematical model which can accurately predict the corrosion rate of steel in concrete structures. Such a model should consider all control mechanisms of the corrosion (e.g. activation, diffusion and resistance controls) so that its applicability in real world scenarios are not limited. The development of such a model is the main objective of the present work.

### **3. Research Method**

---

#### **3.1. General**

As concluded from the literature review, there is a need for developing a practical and comprehensive mathematical model which can accurately predict the corrosion rate of steel in concrete structures. It has also been shown that numerical models that are based on the solution of Laplace's equation with appropriate boundary conditions can be quite useful in carrying out comprehensive academic research studies since they can be used to conduct virtual experiments, sensitivity analyses and parametric studies. In the present study, an innovative approach utilizing the finite element method to simulate actual corrosion rate measurements that are based on the polarization resistance technique will be used to carry out virtual experiments. The results of the virtual experiments will be statistically analyzed to

develop closed-form mathematical models representing the effects of the parameters tested.

In this chapter, the method used to carry out this study is explained. The concept of virtual polarization resistance experiments in reinforced concrete structures is introduced. The virtual experiments that will be carried out to develop a comprehensive model for the corrosion of steel in concrete are developed. The domain of the problem, the governing differential equation (i.e. Laplace's equation), and the boundary conditions for developing the virtual experiments are defined. The numerical procedure to solve the governing equation is discussed and its efficiency is evaluated. Finally, the algorithm of a computer program that was developed for carrying out the virtual experiments is presented.

### **3.2. Virtual polarization resistance experiments**

During the past decades almost every field of science and engineering observed significant advances partly as a result of enhanced utilization of virtual experiments. Civil Engineering has also experienced this trend, especially in the fields of soil mechanics and structural analysis. Although the term "virtual experiment" has been widely used, its definition may vary substantially from one branch of science to the other. Clearly, not every computer simulation can be labelled as a virtual experiment; therefore in this work, the following definition is proposed: *a virtual experiment is a computer simulation of time-consuming, expensive, and sometimes unpractical physical tests for deducing engineering conclusions.*

The main reason for growing interests in virtual experiments is that they serve as low-cost and efficient alternatives to complicated, and potentially very expensive,

physical experiments: A comprehensive experimental program that may take decades and cost multi-million dollars to carry out can be completed in a relatively short period of time for only the cost of the computing time. Furthermore, when a certain experiment requires precisely controlled conditions, well-designed virtual experiments can become the first choice over physical tests since the control of most conditions (e.g. environmental conditions, test setup, etc.) can be difficult in the latter.

Precise control of the environmental conditions is a major challenge in corrosion studies, especially in the investigation of steel corrosion in concrete structures. Since the complex matrix of concrete undergoes major alterations as a result of small variations in the surrounding environment, the control and monitoring of the varying circumstances can become hard, if not impossible. For example, temperature change within concrete not only affects the kinetics of steel corrosion directly, but also influences the chemistry of the cementitious system. Nowadays, accelerated corrosion testing is the most commonly used method for investigating the durability of concrete structures; however, due to the inherent difficulties of the subject and inaccuracies/uncertainties associated with the corrosion measurement techniques in a material like concrete that has high resistivity, the results of these studies are mostly subject to debate. Well-designed virtual experiments that are built on solid theoretical and numerical foundations can help to eliminate this problem. Carrying out an experiment numerically has the following additional advantages:

(1) In real experiments only measurable parameters can be considered as experimental variables, whereas, in virtual experiments parameters that are not

measurable directly (e.g. limiting current density) can be included as experimental variables;

(2) In real experiments dependent parameters such as temperature and concrete resistivity cannot be varied independently; however, in virtual experiments this is possible;

(3) In real experiments a number of parameters such as A/C ratio cannot be controlled precisely due to the uncertain nature of the depassivation process in concrete, whereas, in virtual experiments the value of these parameters can be specified.

Due to the aforementioned benefits, in this thesis virtual experiments have been chosen over physical experiments to investigate the corrosion of steel in concrete, with the ultimate goal of developing a practical and comprehensive model. The physical experiment that will be simulated will be the polarization resistance technique, which is one of the most widely used procedures for measuring corrosion in reinforced concrete structures. By doing so, a critical investigation of this measurement technique will also be made. In the following section, a brief description of the polarization resistance technique is provided. Further information on this technique can be found in (Clear 1989, John et al. 1992, Feliu et al. 1990, Rodriguez et al. 1995).

### **3.3. Polarization resistance technique**

As discussed in previous chapters, corrosion proceeds at corrosion potential,  $\phi_{corr}$ , at which anodic and cathodic polarization curves converge. Close to this potential, both anodic and cathodic polarization equations (assuming high oxygen

availability) are linear. Hence, if a small external current is applied to the system the potential of the corroding system will vary linearly. This is illustrated schematically in Figure 3.1.

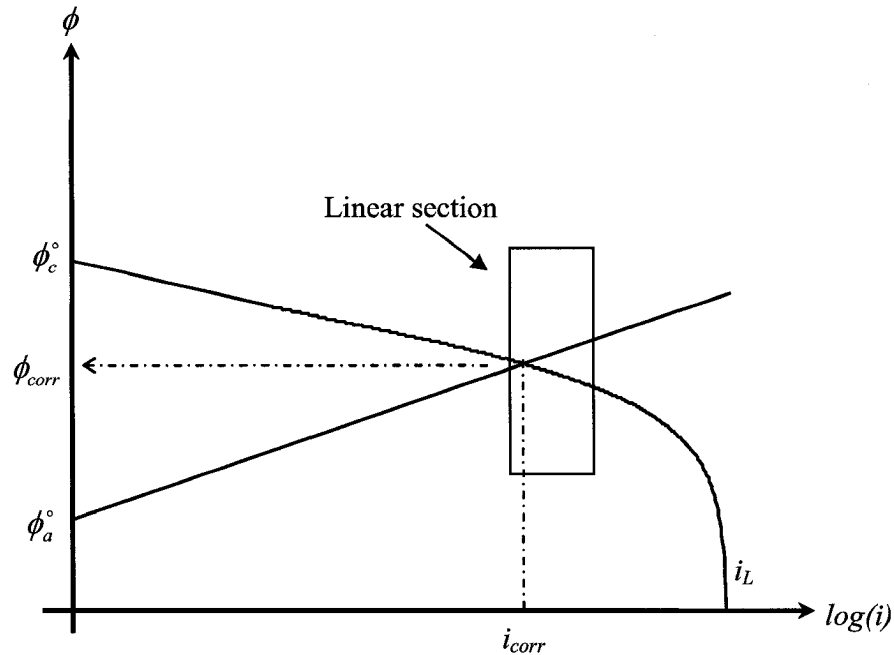


Figure 3.1: Illustration of the linear section of the polarization curves

Applying the Ohm's law to this linear region, the following will be obtained (Uhlig and Revie 1985):

$$R_p = \left. \frac{\Delta\phi_p}{\Delta I_p} \right|_{I_p \rightarrow 0, \phi_p \rightarrow \phi_{corr}} \quad (3.1)$$

where  $R_p$  ( $\Omega$ ) is the polarization resistance,  $\phi_p$  (volts) is the polarization potential and  $I_p$  (A) is the polarization current. In the above equation, when polarization current approaches to zero, polarization potential approaches to corrosion potential. In other words, when  $I_p$  is zero the system is not disturbed, and corrosion proceeds at  $\phi_{corr}$ .

The main objective of the polarization resistance technique is to measure the polarization resistance,  $R_p$ , so that it can be used in the following equation to obtain the corrosion rate (Andrade and Gonzalez 1978):

$$i_{corr} = \frac{B}{A_p R_p} \quad (3.2)$$

where  $i_{corr}$  (A/cm<sup>2</sup>) is the corrosion rate,  $A_p$  (cm<sup>2</sup>) is the polarized area of the steel, and  $B$  (26 mV/dec for actively corroding steel) is the polarization constant calculated using (Stern and Geary 1957):

$$B = \frac{\beta_a \beta_c}{2.303(\beta_a + \beta_c)} = 26 \text{ mV/dec} \quad (3.3)$$

There are two static methods for measuring the polarization resistance: (1) potentiostatic approach, in which a constant external potential is applied to the system and the corresponding response is recorded in the term of polarization current; (2) galvanostatic approach, in which a constant external current (polarization current) is applied to the system and the corresponding potential (polarization potential) is recorded.

The dynamic method for measuring the polarization resistance is also based on the same principles as discussed above, and the only difference is that the response of the system is measured under transient state: a pulse of current is applied to the system and the potential change on the system is recorded. By considering Randles circuit (see Figure 3.2) as the model of the system the obtained data for potential are fitted to the curve representing the Randles curve and the polarization resistance, equivalent capacitance and ohmic resistance of the system are obtained.

The test setup of both (static and dynamic) methods is the same and is shown in Figure 3.3. In the beginning, the instrument records the corrosion potential,  $\phi_{corr}$ , using the reference electrode and the potential difference between the two sensors. If the system is galvanostatic, a small current is applied to the rebar using the counter electrode, and the potential change of the system is recorded using the reference electrode to calculate the polarization resistance,  $R_p$ . Furthermore, a current is applied to the system using the external counter electrode (also referred to as the “guard ring”) until the potential difference between the sensors returns to the potential difference of the undisturbed system, which was recorded at the beginning of the measurement. This ensures confinement of the polarized length of the rebar, which is necessary for using Eq. (3.2).

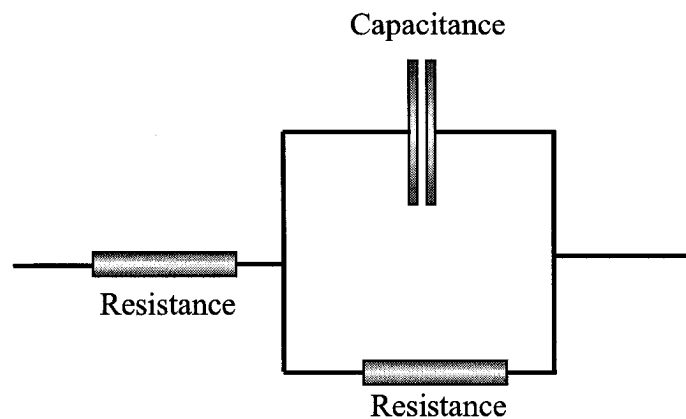


Figure 3.2: Randles circuit

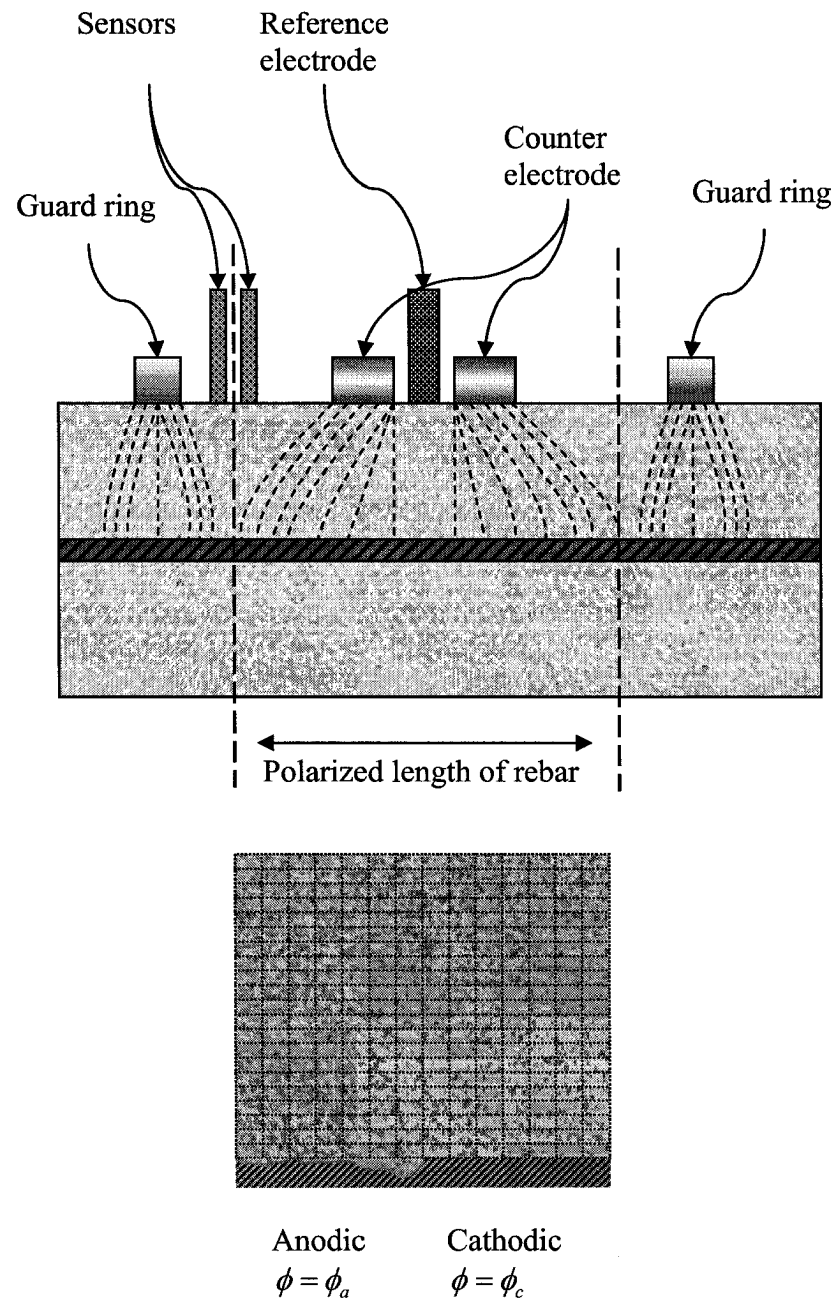


Figure 3.3: Polarization resistance test setup

### 3.4. The governing equation and boundary conditions

The equation governing the potential distribution in a corroding system can be derived from first principles. Assuming electrical charge conservation and isotropic conductivity, the potential distribution can be represented by the Laplace's equation (Munn and Devereux 1991):

$$\nabla^2 \phi = 0 \quad (3.4)$$

Equation (3.4) gives the potential distribution at any point of the domain of problem. Since the objective is to simulate the polarization resistance method the domain of the problem is chosen to be a part of the bulk of the concrete which includes the polarized length of the rebar as illustrated in Figure 3.3. It should be noted that the same domain also represents the corrosion of uniformly depassivated steel in a reinforced concrete member in which anodes and cathodes can be assumed to be uniformly distributed along the length of the reinforcement, as illustrated in Figure 3.4. Once the potential distribution along the steel is known, the current density at any point on the steel surface can be calculated by (Munn and Devereux 1991):

$$i = -\frac{1}{\rho} \frac{\partial \phi}{\partial n} \quad (3.5)$$

where  $i$  ( $A/m^2$ ) is the current density into the electrolyte computed at a specific point on the steel surface,  $\rho$  ( $\Omega.m$ ) is the concrete resistivity, and  $n$  is the normal to the equipotential lines. The rate of rust production at the anodic regions on the steel surface can be calculated by the Faraday's law. Therefore, once the current densities

on the steel surface are calculated, the determination of the rate and amount of corrosion becomes a straightforward task.

The boundary conditions of the domain, as illustrated in Figure 3.5, are defined at: (1) anodic interface where iron oxidation takes place ( $\Gamma_a$ ); (2) cathodic interface where oxygen reduction takes place ( $\Gamma_c$ ), and (3) concrete surface or the symmetry axes where no current flux exists ( $\Gamma_o$ ). Concrete surface boundary condition should be specified by no flux, and the first two types of boundary conditions, i.e. anodic and cathodic, can be identified by referring to the electrochemical nature of corrosion process, which will be elaborated as follows.

The corrosion of steel in concrete is a result of the redox (reduction and oxidation) reaction between iron dissolution in pore water and oxygen reduction on the steel surface as described by Eqs. (1.1) and (1.2), respectively (see Chapter 1). The produced current in this process causes the change in potential and hence polarization of both anodic and cathodic sites. The anodic and cathodic polarization can be expressed by Stern-Geary equations, i.e. Eqs. (1.5) and (1.6), respectively (Uhlig and Revie 1985). The second terms on the right-hand side of both equations represent the activation polarization. Although the anodic reaction can be assumed to be controlled only by activation polarization, the effect of concentration polarization on the cathodic reaction cannot be ignored since the oxygen concentration around the cathodic sites on the steel surface may be low due to slow oxygen diffusion, resulting in further polarization. The concentration polarization in the cathodic reaction is considered through the third term on the right hand side of Eq. (1.6).

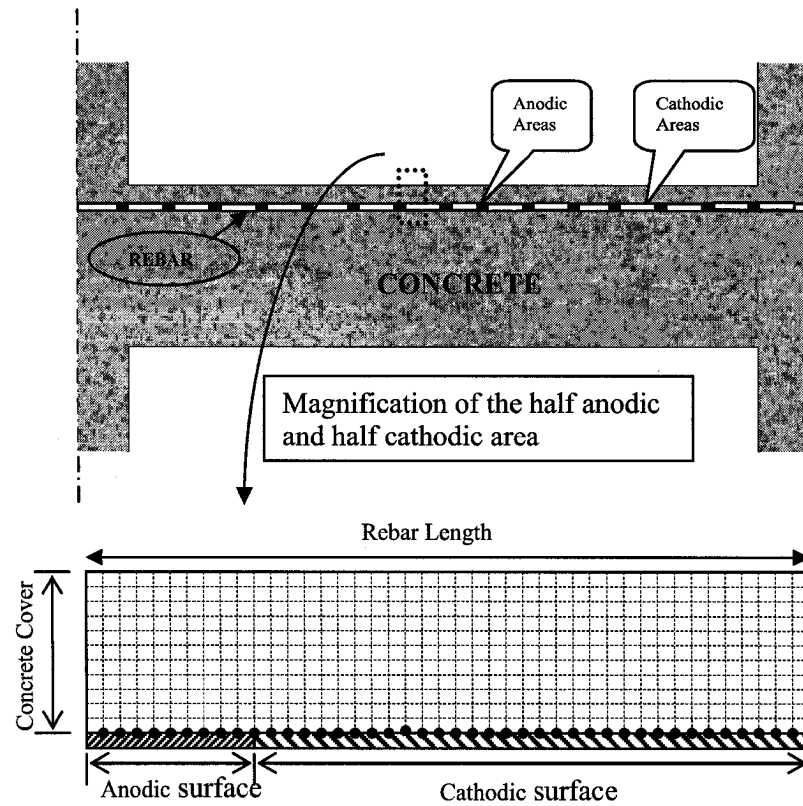


Figure 3.4: Domain for uniformly depassivated steel in a concrete member

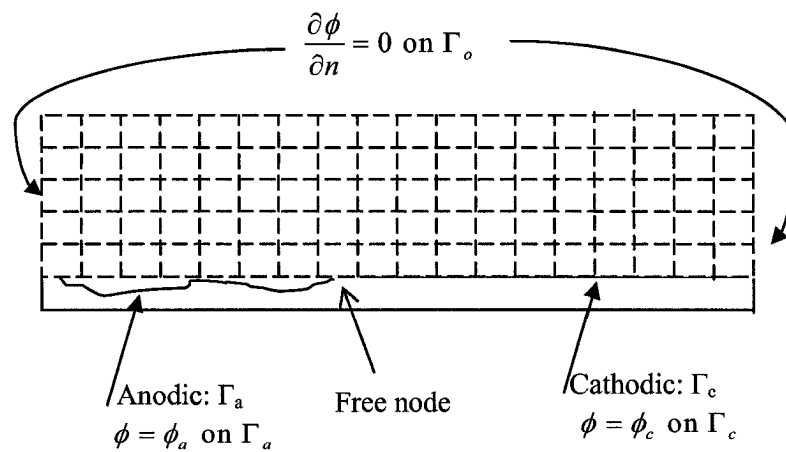


Figure 3.5: Illustration of the analysis domain and its boundaries

Prescribing the value of anodic and cathodic potentials according to Stern-Geary polarization equations, using Eqs. (1.5) and (1.6), results in Dirichlet boundary conditions at anodic and cathodic sites. No flux boundary conditions at all other boundaries can be defined through the Neumann condition on the concrete surfaces, as illustrated in Figure 3.5. Equations (1.5) and (1.6) suggest that the boundary conditions of anodic and cathodic sites are substantially different from each other. Since the anodic and cathodic surfaces are linked, assigning the shared node either boundary condition will result in convergence issues. To overcome this problem, the boundary condition at the transition point from anode to cathode (called “free node” hereafter) was not defined, and the values of potential and current at this node were determined from the solution of the Laplace’s equation. It is interesting to note that, in fact, the physics of corrosion also suggests that the points of contact between anode and cathode can not be defined as either since they may show both behaviours at different times during the corrosion process (Uhlig and Revie 1985); therefore this assumption can be justified theoretically.

### **3.5. Domain discretization**

The domain of the problem in this work is considered to be 300 mm in length (i.e. the polarized length of the rebar), which is large enough such that it does not impose any significant effect on the rate of steel corrosion that is expressed in terms of current density. The height of the domain is dependent on the cover thickness considered in the problem, which is one of the experimental variables considered in this study.

The shape and the number of elements used to discretize the domain is a significant factor that may affect the convergence and the accuracy of the solution. For discretizing the domain two types of elements (triangular and rectangular) were examined. Sensitivity analyses have shown that when triangular elements are used, results are highly dependent to the number of elements unless very fine meshes are used. On the other hand, using rectangular elements does not introduce any problems with uneven mesh quality since the domain is rectangular; the mesh quality will be uniform at every point in the domain. For this reason, it is possible to use a coarser mesh when rectangular elements are used. It was found that the optimum size of the rectangular elements for discretizing the domain is 5x5 mm. Smaller elements not only do not affect the results significantly, but also introduce convergence problems due to the sharp potential gradients between anodic and cathodic sites of the reinforcement.

Figure 3.6 illustrates the results of a sensitivity analysis for the shape and the number of elements. In this figure, the domain of the problem is discretized with two element types with different number of elements. As it can be seen in the figure, for a given A/C ratio, the results of three cases are in the same order of magnitude but show variations up to 4 times. The fluctuations at low A/C ratios can be observed when triangular elements are used. The results of the corrosion current in meshes with triangular elements are always smaller than those with rectangular elements. This is mainly due to (1) the higher round-off error associated with the calculation of flux at the steel/concrete interface for triangular elements; (2) better interpolation of the field

variable (i.e. electric potential) in rectangular elements. An extensive sensitivity analysis regarding to the size of rectangular elements can be found in (Ge 2006).

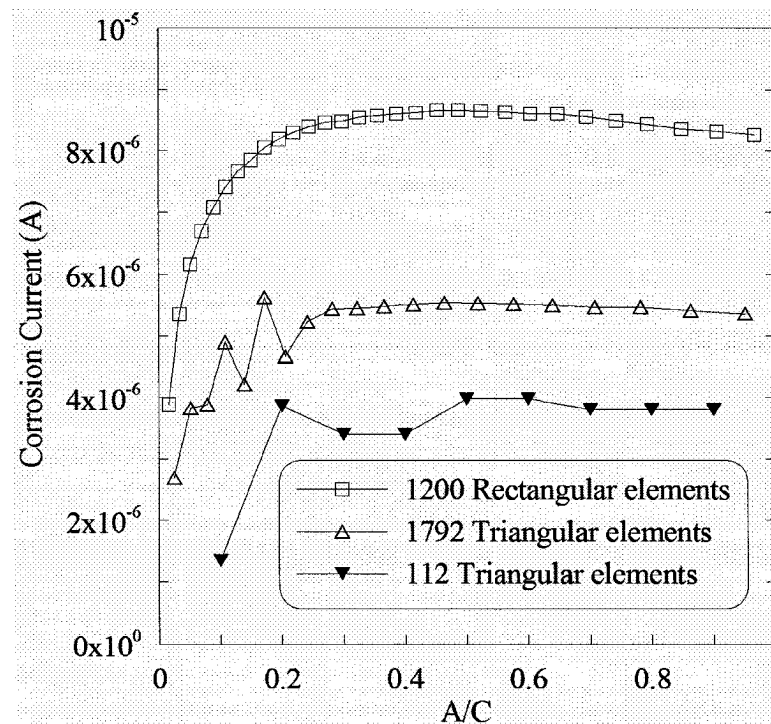


Figure 3.6: Sensitivity analysis for the type and number of elements

### 3.6. Non-linear solution algorithm

The solution of Eq. (3.4), subject to the boundary conditions defined by Eqs. (1.5) and (1.6), is highly non-linear due to the fact that the current densities,  $i_a$  and  $i_c$  that are used to calculate the anodic and cathodic boundary conditions (i.e. Eqs. (1.5) and (1.6), respectively) require the potential gradients as per Eq. (3.5), which can only be calculated from the results of the solution itself. Among a number of available non-linear solution algorithms for solving these types of equations, here, a modified version of the direct iteration method (MDIM), which is a generalized form of

Pichard iteration (Bhat and Chakraverty 2004), is implemented. The MDIM uses the same approach as Pichard iteration, albeit with a relaxation factor,  $\xi$ . In the MDIM, the boundary conditions on the steel surface, assuming Dirichlet-type definition, are determined as:

$$\phi^{k+1} = (1 - \xi)\phi^k + \xi f(i^k) \quad (3.6)$$

where  $\xi$  is between 0 and 1. The new boundary condition  $\phi^{k+1}$  is calculated as a weighted average of the boundary condition of the previous iteration and the boundary condition provided by the polarization equation,  $f(i^k)$ . The MDIM has an inherent measure of trust that the new iterate is moving towards a converged solution. It should be noted that when  $\xi = 1$ , the MDIM is the same as Pichard Iteration.

To start the iteration process (first iteration) seed values for potential and current density should be provided at each node on the steel surface. The examination of the results of many cases has proven that the distribution of seed values at the surface of steel has a significant impact on the number of iterations. Hence, to start the iteration process seed values for potential and corrosion current density ( $\phi^\circ$  and  $i^\circ$  respectively; see Eq. (3.6)) were distributed based on the results of a case with similar properties (resistivity, temperature, A/C, etc.) for which the convergence is less nonlinear. What determines the degree of nonlinearity is mostly the value of the limiting current density,  $i_L$ . As illustrated in Figure 3.7, for large values of  $i_L$ , the convergence of the problem is not generally difficult. As the value of  $i_L$  decreases, reaching to convergence requires more iterations and smaller relaxation factors. This is due to the fact that as the limiting current density decreases, the slope of the polarization curve at convergence point approaches to infinity, resulting in a large

shift in potential even with very small changes in current density, causing the answer to fluctuate around the limiting current density.

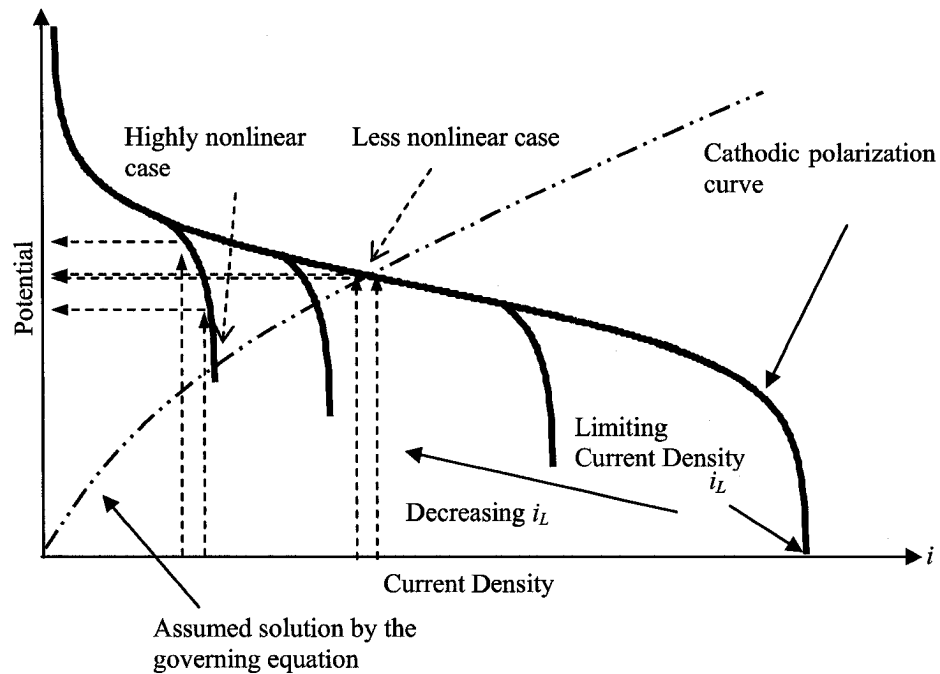


Figure 3.7: Schematic illustration of converged solution

The other provision considered to increase the rate of convergence of the cases with very low limiting current density is the further modification of the seed value distribution with respect to the previous case during the iterations. When the limiting current density is very low, corrosion tends to proceed close to the limiting current density at every point, leaving the previously discussed distribution of seed value (i.e. based on the results of a case with similar properties) ineffective. Thus, in these cases the seed value at every point is modified again and is shifted to values closer to the limiting current density. Without this approach convergence to a solution requires significantly large number of iterations, if possible at all.

Figure 3.8 compares the number of iterations to convergence (with modified and unmodified seed values) for a case with large limiting current density (e.g.  $i_L = 0.2 \text{ A/m}^2$ ). The number of iterations when unmodified seed values are used is almost 350 times larger than the case (cover thickness = 40 mm), for which the seed values are modified. As the concrete cover thickness increases, the number of iterations substantially decreases for both approaches; however, the number of iterations that is required to reach convergence when unmodified seed values are used is still larger. The number of iterations decreases with the increase of cover thickness since this results in smaller potential gradients (or current densities) in the bulk of concrete, resulting in lower degree of nonlinearity.

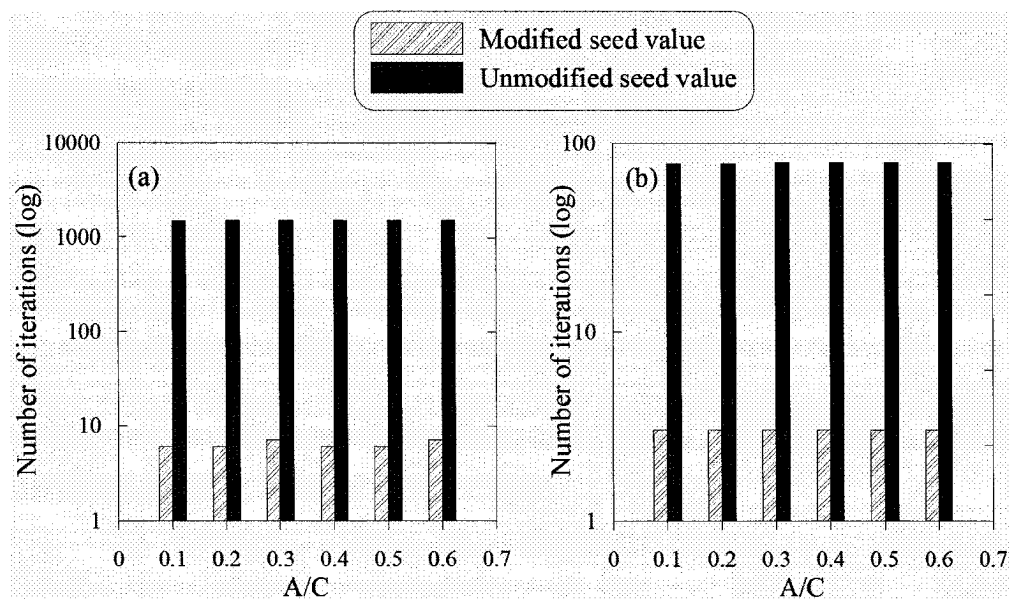


Figure 3.8: Number of iterations for a case with large  $i_L$  ( $0.2 \text{ A/m}^2$ ) with modified and unmodified seed values: (a) 40 mm cover thickness ( $\xi = 0.025$ ); (b) 100 mm cover thickness ( $\xi = 0.025$ )

Figure 3.9 compares the number of iterations for a case with a moderate limiting current density ( $i_L = 0.02 \text{ A/m}^2$ ). Substantially smaller number of iterations can also be observed for this case when modified seed values are used. It should be noted that the number of iterations for the cases with unmodified seed values is almost the same for different cover thicknesses; however, the number of iterations decreased with increasing cover thickness when modified seed values are used.

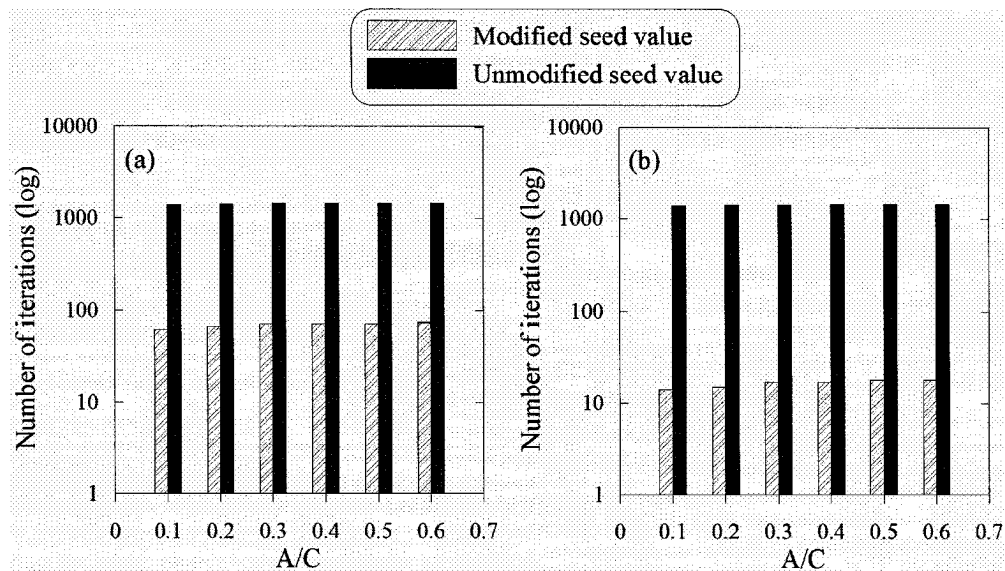


Figure 3.9: Number of iterations for a case with intermediate  $i_L (=0.02 \text{ A/m}^2)$  with modified and unmodified seed values: (a) 40 mm cover thickness ( $\xi=0.025$ ); (b) 100 mm cover thickness ( $\xi=0.025$ )

Figure 3.10 compares the number of iterations of the two approaches (i.e. modified and unmodified seed values) for a very small  $i_L (0.002 \text{ A/m}^2)$ . It can be observed that when unmodified seed values are used, the solution did not reach convergence. On the other hand, the cases with modified seed values reach convergence after approximately 400 iterations. It should be noted that Figure 3.9-(b)

and Figure 3.10-(b) illustrate the convergence in cases with 100 mm cover thickness. The fact that the number of iterations in the cases with low limiting current density is significantly larger illustrates the importance of this factor on the convergence process. Hence, MDIM with modified seed values has been implemented in the present work for solving the Laplace's equation. For this purpose, a customised computer program in MATLAB was developed. The algorithm of the program is discussed in the next section.

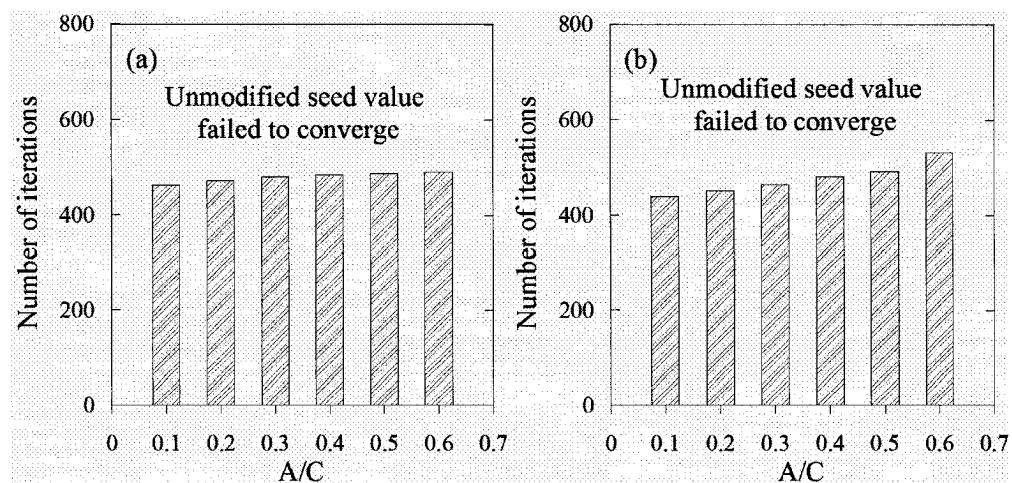


Figure 3.10: Number of iterations for a case with small  $i_L$  ( $0.002 \text{ A/m}^2$ ) with modified seed values: (a) 40 mm cover thickness ( $\xi=0.001$ ); (b) 100 mm cover thickness ( $\xi=0.001$ )

### 3.7. Program development

A comprehensive program has been developed in MATLAB for carrying out the virtual experiments described in this chapter. This program is developed around a finite element solver developed on the Fortran platform at Carleton University (Isgor

2001). Figure 3.11 represents the flowchart of the algorithm used in the MATLAB program.

In the first part of the program, input data to the program is provided by the user. Based on the provided data, the temperature dependent kinetic parameters of corrosion are calculated. Note that the formulation and theoretical background for these calculations are provided in Chapter 4. In addition, based on the provided  $i_L$  value, a value for relaxation factor,  $\xi$ , is chosen by the program such that smaller values of limiting current density require a smaller relaxation factor.

In a parallel process, the domain of the problem is destretized depending on the cover thickness provided by the user, and the seed values are distributed along the steel/concrete interface. Depending on the A/C ratio of the case considered, the boundary conditions are set and the finite element solver is run. At the end of the run, the convergence criterion is checked: The convergence criterion consist of comparing the potential of each node in two consecutive iterations. If the difference between the two consecutive iterations is less than the user defined criterion (0.001 volts is the default value), the iterations can be terminated. Meanwhile, after each iteration, the value of the corrosion current density at the steel/concrete interface is controlled to be in an acceptable range, which is determined considering the polarization behaviour of the steel. More specifically, the current density at each node should be larger than the corresponding exchange current density (depending on whether the node is anodic or cathodic) and smaller than the limiting current density for cathodic area. After convergence, the obtained data including the corrosion current density, the potential distribution (on the surfaces of steel and concrete and within the bulk of the concrete)

are recorded. The seed values for the entire domain are recorded and updated for the next cases to be run.

To obtain the corrosion rate of steel, the corrosion current of each case is calculated by numerically integrating the area under the curve representing the anodic current density distribution. Figure 3.12 illustrates the current density distribution curves of anodic and cathodic sections of steel for different A/C ratios; it is noted that positive corrosion current density corresponds to anodic oxidation of steel and negative current density corresponds to cathodic oxygen reduction. The A/C ratio which has the maximum area under the anodic section (i.e. corrosion current) is the optimum A/C ratio; the theoretical details of the optimum A/C will be discussed in Chapter 4. The corrosion current of the optimum A/C ratio is then divided by the anodic area of the steel and the average corrosion current density is obtained. The average corrosion current density obtained in this way corresponds to the corrosion current density measured in the field by polarization resistance technique.

Since the corrosion current is normalized over the anodic surface of the steel, the average corrosion current density is always smaller than the maximum corrosion current density which occurs at the transition point from anode to cathode; in Figure 3.12 the maximum corrosion current density occurs at  $A/C = 0.1$ . Using the average corrosion current density obtained above as representative of corrosion rate, one may significantly underestimate the corrosion rate. To overcome this problem, the maximum corrosion current density of all the A/C ratios is also recorded as the maximum corrosion current density. The maximum corrosion current density is

representative of the pitting corrosion current density, which is further explained in the following chapter.

It is important to note that if one were to conduct real experiments for all the cases that are analysed in this study, leaving the feasibility of conducting these tests aside, it is estimated that a period of 4 to 5 years needs to be devoted to the laboratory investigation. On the other hand, the runtime for 16,000 cases using virtual experiments was 144 hours (not consecutively) using a regular Pentium 4 PC with 1 GB RAM.

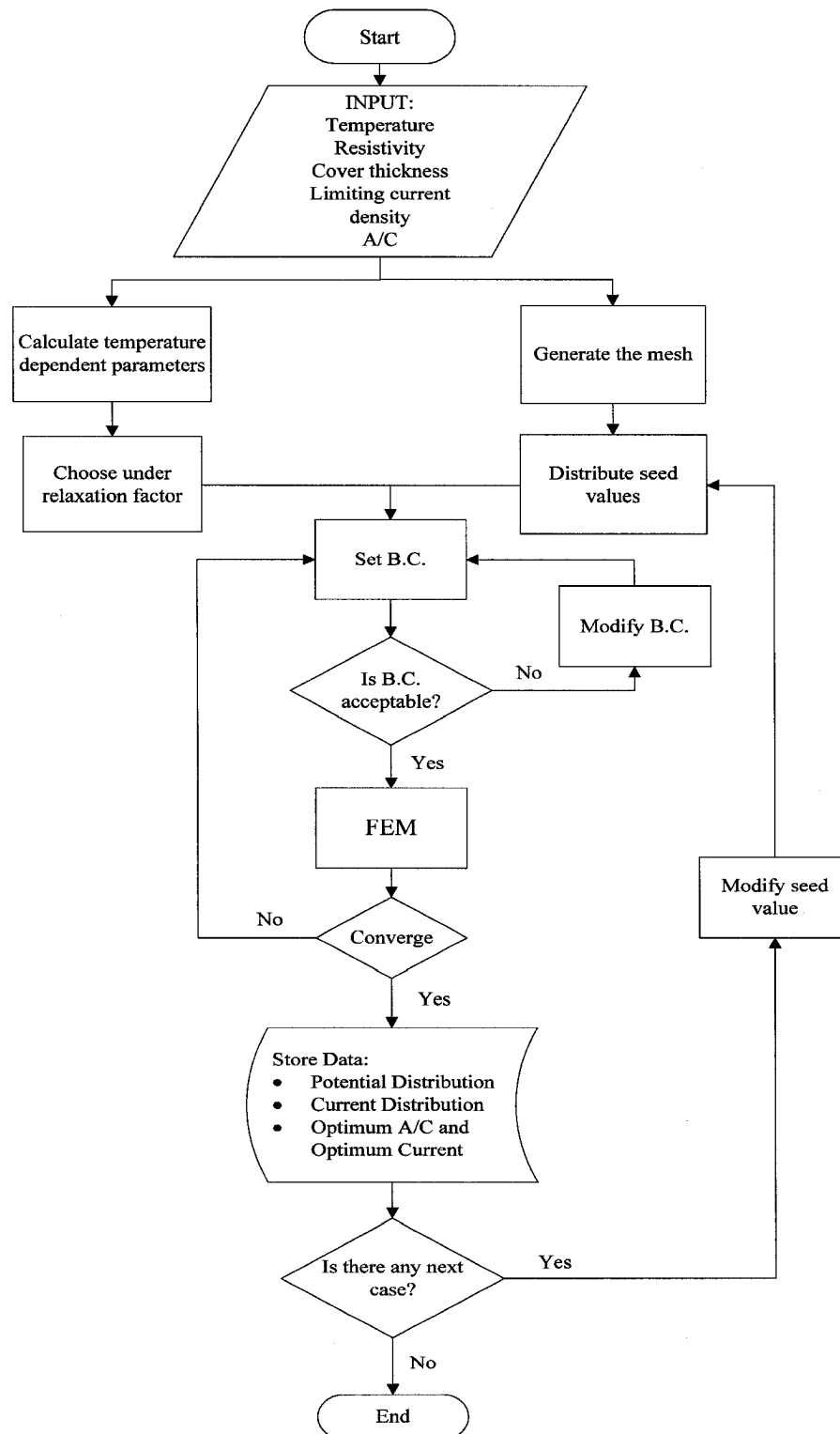


Figure 3.11: Flowchart of the MATLAB algorithm/program

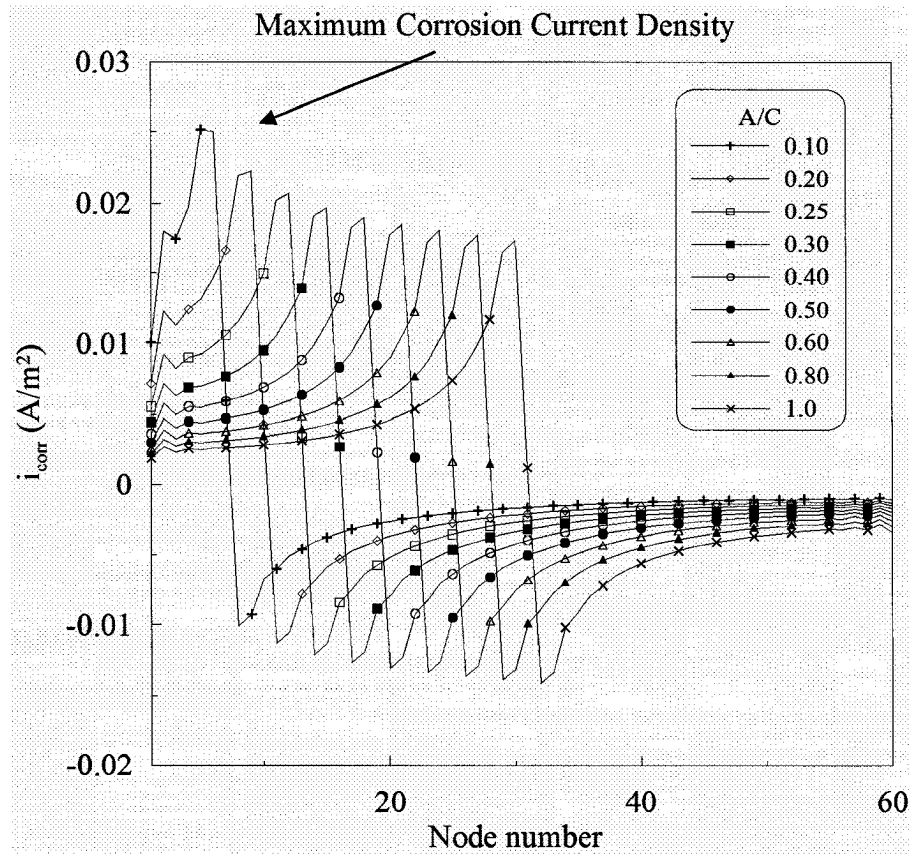


Figure 3.12: Current density distribution at the steel/concrete interface

## **4. Theoretical Considerations**

---

### **4.1. General**

The main objective of this chapter is to present the theoretical background used in this study for considering the effect of different parameters on the kinetics of steel corrosion in concrete. Furthermore, the definition of micro- and macro-cell corrosion is re-examined; a qualitative investigation on the A/C ratio is carried out, and the concept of optimum A/C ratio is presented.

### **4.2. Micro- and macro-cell corrosion**

The corrosion of steel in concrete, depending on the spatial separation of anodic and cathodic sites, is categorised as micro-cell or macro-cell corrosion. Based on the generally accepted definition, in micro-cell corrosion the anodic and cathodic

sites are microscopically separated and their location changes with time (Bohni 2005); whereas, in macro-cell corrosion the anodic and cathodic sites are macroscopic and have fixed locations (Bohni 2005). In macro-cell corrosion, if the relative area of the anodic sites to cathodic sites is small, it is called pitting corrosion (Bohni 2005). Despite this definition, people working in the area of corrosion of steel in concrete do not always agree on the type of corrosion in a given situation. Indeed, there is a lack of clear distinction between the micro-cell and macro-cell corrosion in the literature, and a criterion to differentiate between the two types of corrosion should be proposed.

Figure 4.1 illustrates the polarization curves of the anodic and cathodic sites for an A/C ratio of 1. If the electrical resistance of the solution is negligible (virtually zero), the corrosion will proceed at potential  $\phi_1$ , and both the anode and cathode will have potentials equal to this potential. In this case, the anode and cathode can convert to each other very easily since they do not need to overcome any thermodynamic barrier (e.g. large resistance). When the corroding system has this type of kinetics, the corrosion can be referred to as micro-cell corrosion. On the other hand, if the solution has a considerable electrical resistance, the potential difference between the anode and cathode will be significant. This is illustrated in Figure 4.1 where anode and cathode potentials are  $\phi_2$  and  $\phi_3$ , respectively. In the latter case, anode and cathode cannot convert to each other, since the thermodynamic barrier between them is significantly large. Accordingly, if there is a potential difference between the anode and cathode the corrosion can be categorized as macro-cell corrosion.

Indeed, the electrical resistance of the solution plays an important role in determining the type of corrosion, but it should be noted that the resistance is a

function of resistivity and the relative distance between the anode and cathode. Hence, if the solution has a very high resistivity (e.g. in the case of concrete) corrosion will more likely proceed in the form of macro-cell corrosion, unless the relative distance between the anodic and cathodic sites are very small.

A very important point should be kept in mind with regard to the corrosion of steel in concrete: Anodic oxidation of steel cannot occur on passive steel; hence passive steel can only show cathodic behaviour. On the other hand, oxygen reduction may occur on both passive and active steel. Therefore, the type of the corrosion, in the case of steel corrosion in concrete, also depends on the depassivation of steel. When steel is uniformly depassivated (e.g. due to uniform chloride contamination or carbonation), the anodic and cathodic reactions will occur on the same surface and very close to each other. In this case, the resistance of concrete can be ignored since the relative distance of the anode and cathode is very small. Therefore the potential of the surface can be considered to be the same at each point, resulting in micro-cell corrosion. On the other hand, when only a section of the steel is depassivated (e.g. due to chloride attack) the relative distance between the anode and cathode is not negligible (and hence resistance is not negligible). In this case, there exists a potential difference between the anode and the cathode; hence the corrosion can be regarded as macro-cell corrosion. In the latter case, if the oxygen reduction also occurs on the anodic surface, the corrosion process is a combination of micro-cell and macro-cell corrosion. The above discussion clearly shows that the potential difference between the anodic and cathodic sites is a better criterion for categorizing the type of corrosion process.

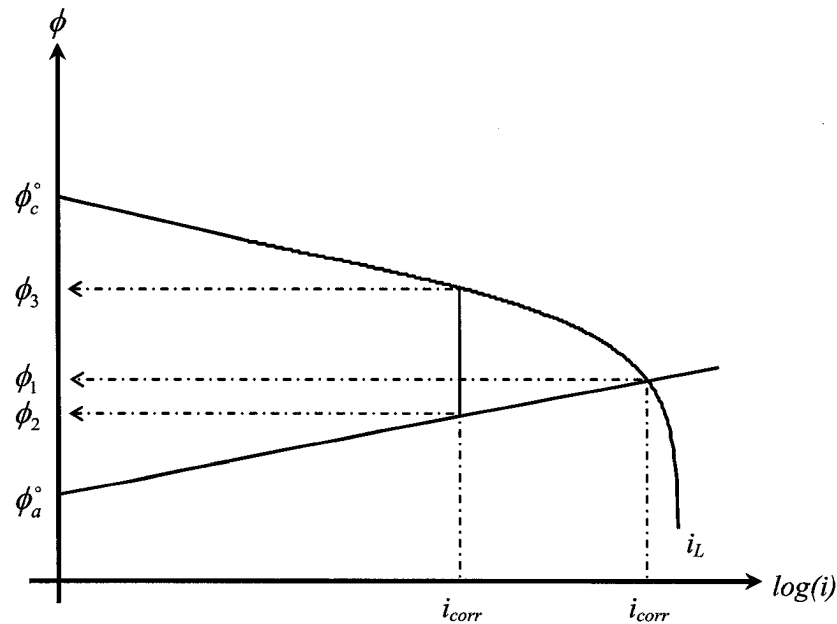


Figure 4.1: Schematic illustration of anodic and cathodic polarization curves

### 4.3. Anode-to-cathode area (A/C) ratio

The existence of the A/C ratio has been a subject to debates (Uhlig and Revie 1985) since some researchers believe that the anodic and cathodic reactions can occur on the same surface, and A/C ratio does not bear any physical meaning. Nevertheless, Stern introduced this parameter in his earlier work (Stern and Geary 1957), and by considering some simplifying assumptions argued that an optimum A/C exists for which the corrosion rate reaches to its maximum value. In this section qualitative and quantitative considerations will be provided on the A/C ratio, and the concept of optimum A/C for steel corrosion in concrete without simplifying assumptions used by Stern will be discussed.

#### 4.3.1. A/C ratio

According to Ohm's law the potential difference between an anode and a cathode can be expressed by:

$$\phi_c - \phi_a = I_{corr} R_{con} \quad (4.1)$$

where  $I_{corr}$  (A) is the corrosion current,  $R_{con}$  ( $\Omega$ ) is the concrete resistance between the anode and the cathode,  $\phi_a$  (volts) and  $\phi_c$  (volts) are potentials of the anode and the cathode, respectively, which can be represented by Stern-Geary polarization equations (Eqs. (1.5) and (1.6)). By neglecting the concentration polarization in Stern-Geary cathodic polarization equation (Eq. (1.6)), and assuming that the anode and the cathode are closely located (or the resistivity of the solution is very low) that the resistance of the solution can be ignored, Eq. (4.1) can be written as:

$$\phi_c - \phi_a = 0 \quad (4.2)$$

Therefore, the potential of the anode and the cathode will be equal to the corrosion potential:

$$\phi_{corr} = \phi_c = \phi_a \quad (4.3)$$

By substituting  $\phi_{corr}$  in the Stern-Geary anodic and cathodic polarization equations (Eqs. (1.5) and (1.6)), and reorganizing the terms, the following two equations for the anodic and the cathodic current densities can be obtained:

$$i_a = i_{o_a} \exp\left(\frac{2.303(\phi_{corr} - \phi_a)}{\beta_a}\right) \quad (4.4)$$

$$i_c = i_{o_c} \exp\left(\frac{2.303(\phi_c - \phi_{corr})}{\beta_c}\right) \quad (4.5)$$

Since the produced currents due to oxygen reduction and steel oxidation are equal, one can write:

$$I_{corr} = i_a A_a = i_c A_c \quad (4.6)$$

where  $A_a$  and  $A_c$  represent the anodic and cathodic areas respectively. By substituting Eq. (4.4) and (4.5) in the above equation and representing the A/C with  $r$ :

$$r = \frac{A_a}{A_c} = \frac{i_c}{i_a} = \frac{i_{o_c} \exp\left(\frac{2.303(\phi_c - \phi_{corr})}{\beta_c}\right)}{i_{o_a} \exp\left(\frac{2.303(\phi_{corr} - \phi_a)}{\beta_a}\right)} \quad (4.7)$$

All parameters on the right hand side of Eq. (4.7) are constant except for corrosion potential,  $\phi_{corr}$ . Figure 4.2 illustrates the A/C ratio as a function of  $\phi_{corr}$ . It can be concluded from this figure that if an A/C ratio (other than 1) does not exist,  $\phi_{corr} \approx -0.588$  volts, which is not always the case; different values of corrosion potential observed in experiments suggest the existence of A/C ratio other than 1.

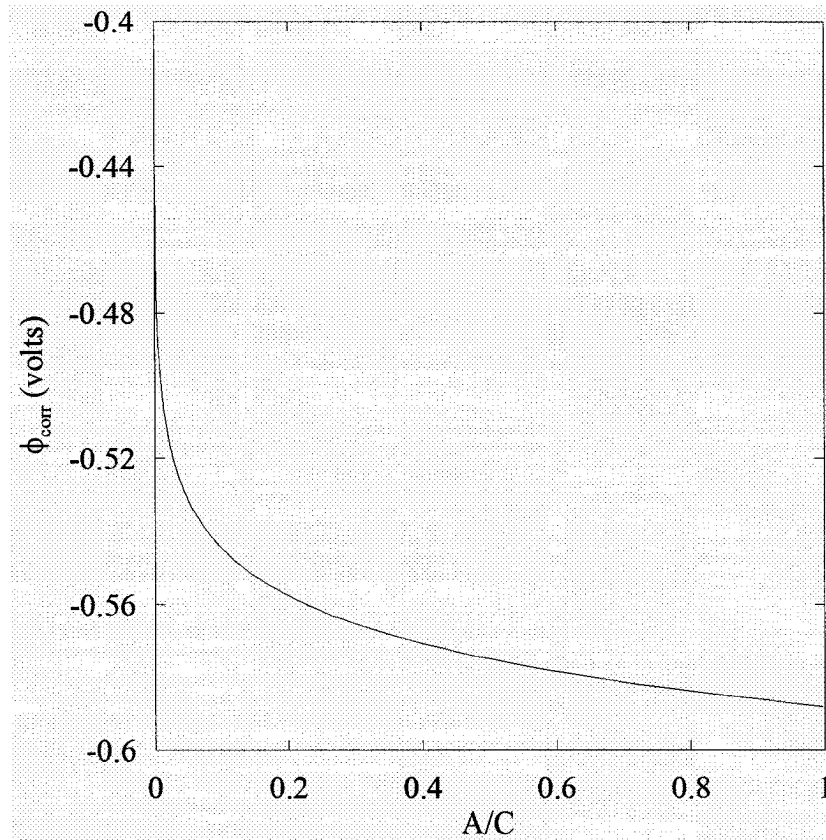


Figure 4.2: Variation of A/C with corrosion potential in absence of concentration polarization and IR drop

#### 4.3.2. Effect of concrete resistance on A/C

In the previous section the effect of concrete resistance in Eq. (4.1) was ignored, however, in this section the effect of concrete resistance will be included and only the effect of concentration polarization in cathodic polarization (Eq. (1.6)) will be neglected. Therefore, Eq. (4.1) can be rewritten as:

$$\phi_c - \phi_a = \phi_{O_2}^o + \beta_c \log \frac{i_c}{i_{oc}} - \phi_{Fe}^o - \beta_a \log \frac{i_a}{i_{oa}} = I_{corr} R_{con} \quad (4.8)$$

Substituting Eq. (4.6) into Eq. (4.8) and considering, A/C ratio,  $r = A_a/A_c$ , the following will be obtained:

$$\underbrace{\phi_{O_2}^o - \phi_{Fe}^o}_{Cn_1} - \underbrace{\beta_c \log i_{oc} + \beta_a \log i_{oa}}_{Cn_2} + \beta_c \log i_a r - \beta_a \log i_a = i_a A_a R_{con} \quad (4.9)$$

$$i_a A_a R_{con} = Cn_1 + Cn_2 + \beta_c \log i_a + \beta_c \log r - \beta_a \log i_a \quad (4.10)$$

By reorganizing Eq. (4.10) for A/C ratio and assuming  $A_a=1$ , the following will be resulted:

$$r = \exp\left(-\frac{2.303}{\beta_c}(Cn_1 + Cn_2 - i_a R_{con} + (\beta_a - \beta_c) \log i_a)\right) \quad (4.11)$$

Equation (4.11) suggests that the A/C ratio is a function of concrete resistance at every given anodic current density. Figure 4.3 illustrates the effect of concrete resistance on the A/C ratio. It can be observed from this figure that as the concrete resistance decreases all the curves converge to the same value, in other words, the effect of concrete resistance on the A/C can be ignored for concrete resistances less than 0.01  $\Omega$ . This is a very significant observation since the concrete resistance (for fixed values of anodic and cathodic areas) consists of contributions from concrete resistivity and the relative distance between the anode and cathode. Assuming the concrete resistivity is a constant value, decrease of concrete resistance can be interpreted as decrease of the relative distance between the anode and the cathode. This means that even in the case of micro-cell corrosion (where the distance between the anode and cathode is virtually zero) the A/C ratio exists.

It is noted that although the effect of concrete resistance on the A/C ratio decreases for high values of the former, at high resistance values, A/C ratio always

exists since high resistance (according to Ohm's law) causes a significant potential difference between the anode and cathode resulting in complete separation of anode and cathode, and since the rate of the reaction on the anodic and cathodic sites are not the same, A/C can not be always equal to unity.

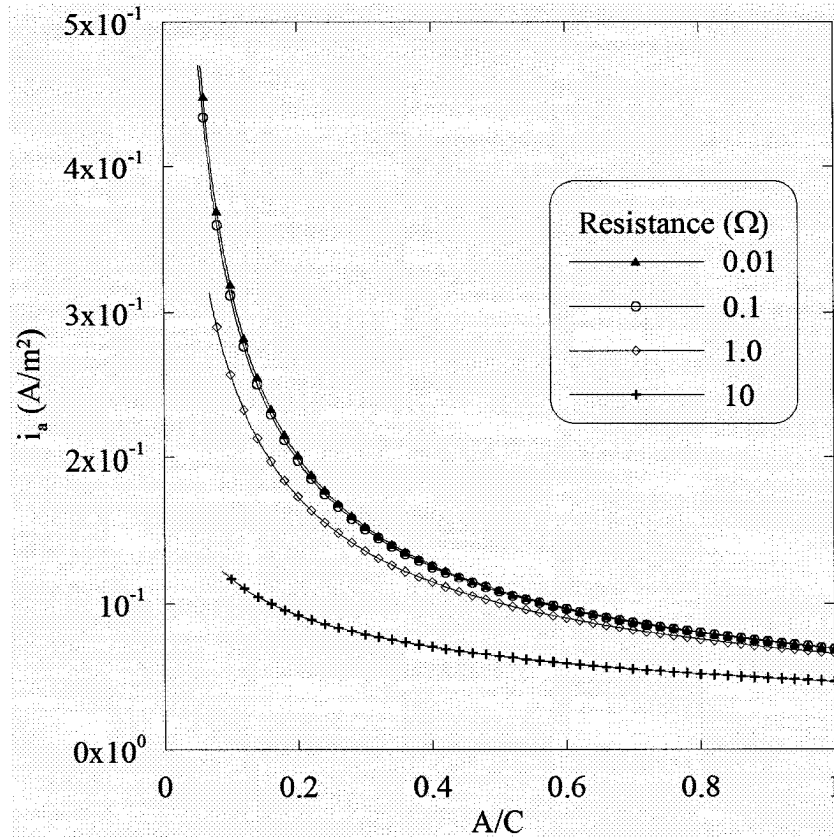


Figure 4.3: Variation of A/C with concrete resistance

#### 4.3.3. Effect of oxygen availability on A/C

Investigating the effect of oxygen availability on the A/C ratio is feasible through the non-linear solution of Eq. (4.9) by considering the concentration polarization as well. However, this approach will significantly compound the

complexity of the problem. To overcome this problem another approach is suggested herein.

The physical meaning of the concentration polarization in Eq. (1.6) suggests that the maximum value of the cathodic current density is equal to the limiting current density. Hence, the maximum value of the anodic current density can be obtained from Eq. (4.6) when cathodic current density is equal to limiting current density, that is:

$$i_{a,\max} = \frac{i_L}{r} \quad (4.12)$$

By plotting this equation for different values of limiting current density and superimposing the plots on Figure 4.3, the effect of limiting current density on the A/C ratio can be investigated.

Figure 4.4 illustrates the effect of limiting current density on the A/C ratio for two different values of limiting current density. It can be seen from this figure that when the value of limiting current density is relatively large, it does not impose any effect on the A/C ratio, however, as the limiting current density decreases its effect manifests itself. It can be concluded from this figure that the effect of limiting current density on A/C ratio depends on the values of limiting current density and the concrete resistance between anode and cathode.

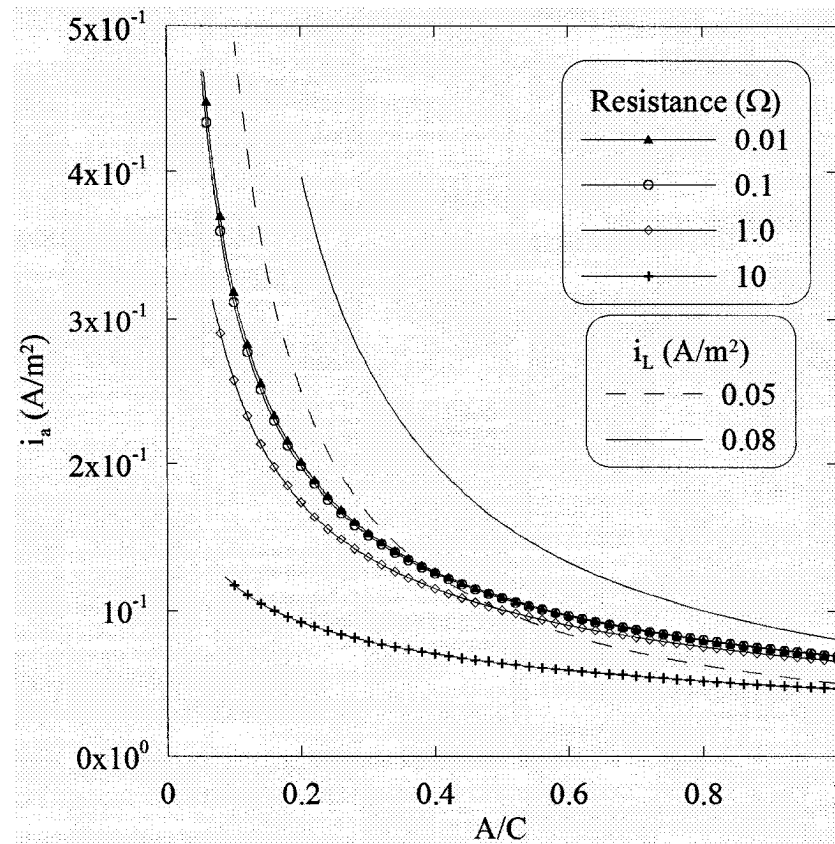


Figure 4.4: Effect of oxygen availability on the A/C

#### 4.3.4. The optimum A/C ratio

Stern studied the effect of A/C on the corrosion rate of a metal in a system where both anodic and cathodic polarization follows Tafel behaviour (i.e. governed by activation polarization only) and  $IR$  drop is negligible (Stern and Geary 1957). Based on this study, it was analytically demonstrated that maximum corrosion current,  $I_{corr}$ , occurs when

$$\frac{A_a}{A_c} = \frac{\beta_a}{\beta_c} \quad (4.13)$$

This means that for a metal with similar anodic and cathodic Tafel slopes (i.e.  $\beta_a \approx \beta_c$ ), the maximum corrosion rate occurs at an A/C ratio of unity. At any other A/C ratio, the corrosion rate would be smaller, reaching zero at a ratio equal to zero or infinity (Uhlig and Revie 1985). It is well established that the corrosion of steel in concrete is rather complicated, and using Stern's assumptions may oversimplify the problem (Isgor and Razaqpur 2006). In order to apply the same approach to the problem of steel corrosion in concrete and prevent the oversimplification the following approach is undertaken herein.

Figure 4.5 illustrates one anode and one cathode separated by a concrete layer. It should be noted that although this model can represent a number of scenarios for corrosion of steel in concrete structures, it is not a typical problem that is encountered in the real world. However, for the purpose of proving the concept before the detailed finite element investigation of a more realistic system, the arrangement in Figure 4.5 will be simulated using a closed-form solution. The maximum corrosion current,  $I_{corr}$ , of a one-dimensional problem shown in this figure can be obtained as follows.

As was discussed in Chapter 3, the electric potential distribution at any point in the bulk of the concrete can be found by solving the Laplace's equation (Eq. (3.4)), and the current density at any point on the steel surface can be calculated using Eq. (3.5). The boundary conditions of the Laplace's equation are defined by Eq. (1.5) and Eq. (1.6) respectively. Hence, the distribution of potentials in the one-dimensional domain presented in Figure 4.5 can be determined by solving the Laplace's equation.

$$\frac{\partial^2 \phi}{\partial^2 x} = 0 \Rightarrow \phi = ax + b \quad (4.14)$$

The solution constants,  $a$  and  $b$ , can be obtained from the anodic and cathodic boundary conditions defined by Eq. (1.5) and Eq. (1.6) respectively.

$$\phi = \phi_a @ x = 0 \quad (4.15)$$

$$\phi = \phi_c @ x = L \quad (4.16)$$

such that

$$\phi = \frac{\phi_c - \phi_a}{L} x + \phi_a \quad (4.17)$$

where  $L$  (m) is the distance between the anode and the cathode. The current density,  $i$ , at any point on the steel surface is calculated using Eq. (3.5). Thus:

$$\frac{\partial \phi}{\partial x} = \frac{\phi_c - \phi_a}{L} \quad (4.18)$$

$$\phi_c - \phi_a = i \rho L = \frac{I_{corr}}{A} \rho L \quad (4.19)$$

$$R_{con} = \rho \frac{L}{A} \quad (4.20)$$

$$\phi_c - \phi_a = I_{corr} R \quad (4.21)$$

where  $A$  (m<sup>2</sup>) is the electrode surface area. Substituting the polarization equations (Eqs. (1.5) and (1.6)) in Eq. (4.21), the following relationship can be obtained:

$$I_{corr} R_{con} = \left[ \phi_c^\circ + \beta_c \log \left( \frac{i_c}{i_{oc}} \right) - \frac{2.303RT}{z_c F} \log \left( \frac{i_L}{i_L - i_c} \right) \right] - \left[ \phi_a^\circ + \beta_a \log \left( \frac{i_a}{i_{oa}} \right) \right] \quad (4.22)$$

Using Eq. (4.6) to substitute for  $I_{corr}$  in the above equation:

$$(i_a A_a) R_{con} = \underbrace{\phi_c^\circ - \phi_a^\circ - \beta_c \log i_{oc} + \beta_c \log r + \beta_a \log i_{oa}}_{C_1} + \underbrace{(\beta_c - \beta_a) \log i_a}_{C_2} - \underbrace{\frac{2.303RT}{z_c F}}_{C_3} \log \left( \frac{i_L}{i_L - i_a r} \right) \quad (4.23)$$

or

$$(i_a A_a) R_{con} = C_1 + C_2 \log i_a + C_3 \log \left( \frac{i_L}{i_L - r i_a} \right) \quad (4.24)$$

Equation (4.24) is the closed-form solution of the Laplace's equation for anodic current density. Using a nonlinear solution algorithm and the parameters in Table 1.1 the corrosion current,  $I_{corr} = i_a A_a$ , for the one-dimensional problem defined in Figure 4.5 can easily be calculated. In Figure 4.6, the corrosion current,  $I_{corr}$ , vs.  $A/C$ , for various oxygen concentrations and concrete resistivities are plotted by solving Eq. (4.24) numerically. It is clear from this figure that there is an optimum value of  $A/C$  for which the corrosion current reaches its maximum value. Based on the basic thermodynamic principles, this maximum can be interpreted as corresponding to the state at which the total energy is minimized by achieving an optimum (or equilibrium)  $A/C$ , along the reinforcement. In this thesis, the  $A/C$  that leads to the maximum corrosion current will be defined as the "equilibrium state." It should be noted that there are claims against this argument as a number of researchers

state that anodes and cathodes on the steel surface can form at the same location at the microscopic level; hence it is impossible to define an A/C (Uhlig and Revie 1985). Although this claim has its merits, as was qualitatively investigated, a macro-level A/C ratio can always be defined, and this approach will be adopted here in this thesis.

Figure 4.6 provides additional information about the corrosion behaviour of steel in concrete. One of these is that an increase in oxygen concentration increases the corrosion current; however, the rate of the change of corrosion current diminishes as the oxygen concentration gets larger. This implies that there is an upper limit for corrosion current in high oxygen concentration conditions beyond which the oxygen concentration does not play a significant role. Furthermore, at high oxygen concentrations, the equilibrium states of both high and low concrete resistivities occur almost at the same value of A/C. However, there is a major difference in corresponding A/C at low oxygen concentrations. It can be stated that for high oxygen concentration the A/C corresponding to the equilibrium state is almost independent of the resistivity of concrete. Here the importance of concentration polarization and resistivity of concrete pore solution in the corrosion of steel in concrete structures is clearly observed. One should also note in Figure 4.6 that the line connecting the maximum values of the corrosion rate for different concentrations of the oxygen shows almost linear variation of the equilibrium states.

As a summary, the one-dimensional analysis is presented here proves the following concepts for further study of uniform corrosion of steel in concrete structures:

- There is an optimum A/C that gives the maximum corrosion current, which may be interpreted as corresponding to the equilibrium state of the thermodynamic system.
- The equilibrium state of corrosion follows a pattern that is affected by oxygen concentration and resistivity of concrete.
- The effect of oxygen concentration, and therefore concentration polarization, on the corrosion rate can be significant.
- The effect of concrete resistivity on the corrosion rate needs to be incorporated while studying the corrosion of steel in concrete.

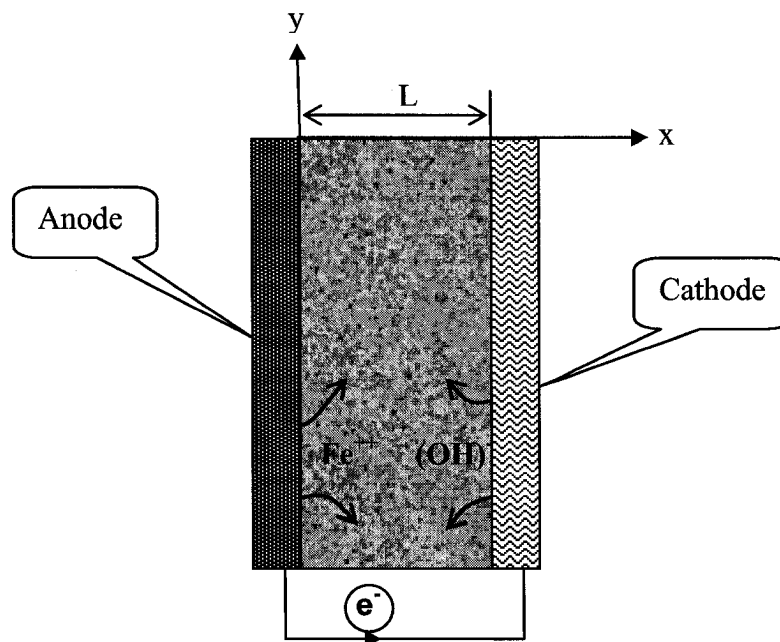


Figure 4.5: One dimensional corrosion problem

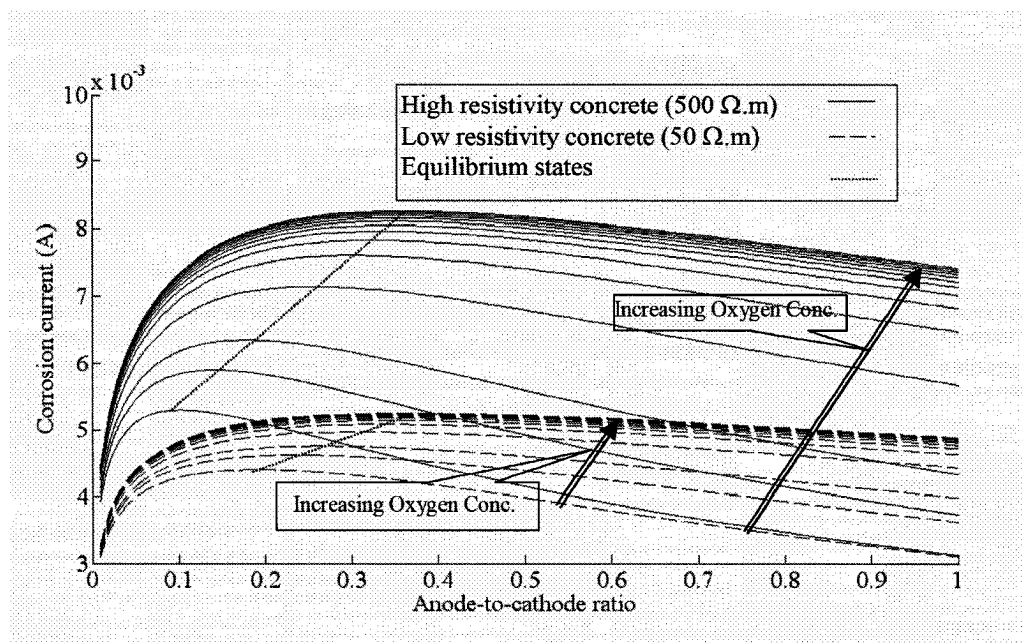


Figure 4.6: The effect of A/C ratio on corrosion current for 1D

#### 4.4. Kinetic parameters of steel corrosion in concrete

##### 4.4.1. The effect of concrete cover thickness

The effect of cover thickness on the corrosion of steel in concrete manifests itself through oxygen diffusion, i.e. through concentration polarization of the cathodes. The limiting current density is the main parameter that controls the relationship between the amount of oxygen available on the cathodic surfaces and the amount of polarization. The common approach to treat this process is to consider cover thickness as a diffusion layer (the Nernst diffusion layer), through which steady-state diffusion of oxygen takes place. With this approach, the limiting current density,  $i_L$ , can be calculated as a closed-form equation as a function of concrete cover thickness,  $d$ , in the following form (Bohni 2005):

$$i_L = n_e F \frac{D_{O_2} C_{O_2}^s}{d} \quad (4.25)$$

where  $i_L$  (A/m<sup>2</sup>) is the limiting current density,  $n_e$  (n=4) is the number of electrons,  $F$  ( $\approx 96500$  C/mole) is the Faraday's constant,  $D_{O_2}$  (m<sup>2</sup>/s) is the concrete oxygen diffusion coefficient,  $C_{O_2}^s$  (mole/m<sup>3</sup>) is the amount of dissolved oxygen in water, and  $d$  (m) is the cover thickness.

It should be cautioned that the oxygen diffusion coefficient of concrete can change in orders of magnitude with relative humidity (Papadakis et al. 1991), and when the limiting current density is calculated through Eq. (4.25), for low values of relative humidity, the limiting current density can be significantly large, even greater than 1.0 A/m<sup>2</sup> (Ghods et al. 2007). However, even when the relative humidity is very low, there exists a very thin layer of pore solution around the steel reinforcement, preventing the limiting current density to reach such unrealistically large values. If Eq. (4.25) is used such that  $d$  is equal to the thickness of the thin layer of pore solution (which can be reasonably assumed to be equal to the thickness of a stagnant layer of solution next to an electrode submerged in liquid electrolyte  $\approx 0.05$  cm with diffusion coefficient of  $9.3\sim 5.2 \times 10^{-5}$  cm<sup>2</sup>/s (Uhlig and Revie 1985)), rather than the concrete cover thickness, the limiting current density will be in the range of 0.1-0.25 A/m<sup>2</sup> (Ghods et al. 2007). It should be mentioned that more complex models can be used to treat the oxygen diffusion as a transient phenomenon consisting of two phases: (1) diffusion through concrete cover and, (2) diffusion through thin pore solution layer. However, this non-linear approach requires the accurate prediction of

the pore solution distribution in concrete, which is not a practical task (Isgor and Razaqpur 2004).

In this thesis, the steady-state approach (i.e. Eq. (4.25)) will be used for calculating the limiting current density since steel corrosion is more prominent when relative humidity of concrete is relatively large (Lopez and Gonzalez 1993), for which the concrete cover acts as the diffusion layer. In the current study, to incorporate the presence of the thin pore solution layer around the reinforcement, and to prevent the limiting current density reach unrealistically large values, an upper limit of  $0.6 \text{ A/m}^2$  is imposed.

#### 4.4.2. The effect of temperature

##### 4.4.2.1. Tafel slope

A wide range of values has been recommended for anodic and cathodic Tafel slopes of the passive and active steel in concrete (Andrade and Gonzalez 1978, Elsener 2002, Bertolini et al. 2004, Kranc and Sagues 1994). From theoretical point of view, as per Eqs. (4.26) and (4.27), temperature is one of the major factors that influence the Tafel slopes. Tafel slopes increase with increasing temperature via:

$$\beta_a = \frac{2.303RT}{\alpha zF} \quad (4.26)$$

$$\beta_c = \frac{2.303RT}{(1 - \alpha)zF} \quad (4.27)$$

where  $\beta_a$  and  $\beta_c$  (volt/dec) are the anodic and cathodic Tafel slopes respectively,  $R$  ( $\approx 8.314 \text{ J/(mole.K)}$ ) is the universal gas constant,  $T$  ( $^{\circ}\text{K}$ ) is temperature,  $z$  is the valance, and  $\alpha$  is the symmetry factor. If  $\alpha$  in Eqs. (4.26) and (4.27) is considered

constant (Hurlen 1960), by assuming a reference value for Tafel slopes at a reference temperature, Eq. (4.26) and Eq. (4.27) can be written as:

$$\beta_a = \beta_{a_0} \frac{T}{T_0} \quad (4.28)$$

$$\beta_c = \beta_{c_0} \frac{T}{T_0} \quad (4.29)$$

In Eqs. (4.28) and (4.29) the change in Tafel slopes for the range of temperature concerned in this study (i.e. 10°C to 50°C) is always smaller than 7 per cent. In contrast to this theoretical deduction, the experimental investigations suggest somewhat different variation of Tafel slopes with temperature: Elsener (2005) and Garces et al. (2005) suggest that the anodic and cathodic Tafel slopes slightly decrease with increasing temperature. Experimental investigations carried out by Kriksunov (1995) even show that Tafel slopes are independent of temperature, and fluctuations can be considered as experimental noise. Many attempts to explain the observed variation of Tafel slopes with temperature can be found in (Gileadi 1987) and in the monograph by Conway (1989). Due to these contradictions, in the present work, constant values for the anodic (90 mV/dec) and cathodic (-180 mV/dec) Tafel slopes are considered. It should be noted that these Tafel slopes yield a polarization constant,  $B$ , of 26 mV/dev according to Eq. (3.3) which is in agreement with the experimental observations for actively corroding steel in concrete (Andrade and Gonzalez 1978).

#### 4.4.2.2. *Exchange current density*

In general, the exchange current density of metals can be affected by the pH of the solution, temperature (Hurlen 1960) and characteristics of the substrate (Bockris et al. 1968). The pH of pore solution next to reinforcing steel after onset of corrosion can be assumed to be constant due to the formation of saturated hydrous ferrous oxide on the surface of steel (Uhlig and Revie 1985) and high buffer capacity of concrete pore solution. Hence, the exchange current density of rebar can be considered independent of pH. The effect of temperature on the anodic and cathodic exchange current densities, on the other hand, can not be ignored. Numerical investigations have proven that with variation of exchange current density, corrosion rate changes appreciably (Ge and Isgor 2007). The strong dependency of exchange current density on temperature in acidic solutions can be found in earlier works (Hurlen 1960). However, closer examination of the activation energies obtained by Hurlen (1960) suggests that the activation energy for acidic solutions does not apply for highly alkaline electrolytes such as concrete pore solution, and other approaches may be necessary for investigating the effect of temperature on the exchange current density. To the knowledge of author, there is a lack of experimental data for exchange current density of steel in high pH solutions at different temperatures. To overcome this problem a theoretical approach is undertaken.

From theoretical point of view, exchange current density can be expressed as (Tanaka and Tamamushi 1964):

$$i_o = z_e F C_o^\circ k_c^\circ e^{\frac{\alpha z_e F \phi_e}{RT}} \quad (4.30)$$

where  $i_o$  (A/cm<sup>2</sup>) is the exchange current density,  $C_o^\circ$  is the molar concentration in the bulk of the solution at the standard equilibrium condition,  $k_c^\circ$  (cm/s) is the rate constant at standard equilibrium condition, and  $\phi_e$  (volts) is the equilibrium potential. If two values for the exchange current density ( $i_{o,1}$  and  $i_{o,2}$ ) at two different temperatures ( $T_1$  and  $T_2$ ), respectively, are considered, using Eq. (4.30) the following Arrhenius-type relationship can be obtained:

$$\frac{i_{o,1}}{i_{o,2}} = e^{\frac{\alpha z_e F \phi_e}{R} \left( \frac{1}{T_1} - \frac{1}{T_2} \right)} \quad (4.31)$$

Using this equation along with an experimental value for exchange current density at a reference temperature, the effect of temperature on the equilibrium exchange current density can be analyzed. In the current investigation, the reference values for anodic and cathodic exchange current density at 21°C are considered  $i_{oa} = 3 \times 10^{-4}$  and  $i_{oc} = 1 \times 10^{-5}$  (A/m<sup>2</sup>) respectively.

#### 4.4.2.3. Equilibrium potentials

The variation of standard reduction potential of the anodic and cathodic half-cell reactions with temperature can be expressed with Eqs. (4.32) and (4.33) respectively (Bard et al. 1985):

$$\phi_{Fe,T}^{\circ} = \phi_{Fe,T_o}^{\circ} + 0.000052 \times (T - T_o) \quad (4.32)$$

$$\phi_{O_2,T}^{\circ} = \phi_{O_2,T_o}^{\circ} - 0.001680 \times (T - T_o) \quad (4.33)$$

where  $\phi_{Fe}^{\circ}$  (volts) is the standard potential of iron reduction,  $\phi_{O_2}^{\circ}$  (volts) is standard potential of oxygen reduction, and  $T_o$  ( $^{\circ}\text{K}$ ) is the reference temperature. Comparison of the two equations suggests that the variation of the reduction potential of the anodic half-cell reaction is much smaller than that of cathodic reaction. In fact, the variation of anodic reduction potential with the temperature range considered herein (283~323 $^{\circ}\text{K}$ ) is negligible; nevertheless, variation of both equilibrium potentials using Eq. (4.32) and Eq. (4.33) are considered in the present work.

#### 4.4.3. Concrete resistivity

The effect of resistivity is considered by a many researchers to be one of the important factors affecting the corrosion rate of reinforcing steel in concrete (Alonso et al. 1988, Gulikers 2005, Ghods et al. 2007). A number of parameters (e.g. relative humidity, temperature, the presence of external ions such as chlorides, w/c ratio, and cement type) can significantly change the resistivity of concrete (Gjørsv et al. 1977). Establishing a reasonable relationship between relative humidity and resistivity is not an easy task, on the other hand, such a relationship exists between water saturation and concrete resistivity (Gjørsv et al. 1977). Since the data obtained by Gjørsv et al. (1977) is purely empirical and no mathematical expression was reported by these researchers, such an expression is developed in this thesis, which is provided in the appendix A. By relating the relative humidity to water saturation using an adsorption

isotherm (Xi et al. 1994), a relationship between the relative humidity and concrete resistivity can be established.

The relationship between the concrete resistivity and temperature has been previously proposed in the form of Arrhenius type equation (Chrisp et al. 2001):

$$\rho = \rho_0 e^{\frac{\Delta U_\rho}{R} \left( \frac{1}{T} - \frac{1}{T_0} \right)} \quad (4.34)$$

where  $\Delta U_\rho$  (kJ/mole) the activation energy of resistivity. In this equation, the values of activation energy suggested by Chrisp et al. (2001) are a function of water saturation and decrease with increasing water saturation: 39 kJ/mol for 55% saturation and 27 kJ/mol for 100% saturation. The values of activation energy are reported as point data in (Chrisp et al. 2001), hence, by carrying out a regression analysis, a relationship (mathematical expression) between the activation energy and the degree of saturation can be found. Such an analysis is carried out in this study, the result of the analysis is provided in the appendix A. The values suggested by Chrisp et al. (2001) are also in agreement with the suggested values by Hope and Ip (1987). In addition to relative humidity and temperature, other factors, such as the presence of external ions such as chlorides, water-cement (w/c) ratio, cement type, can also affect concrete resistivity. In the present work, these effects will be considered implicitly as part of the reference resistivity,  $\rho_0$ .

#### 4.4.4. Limiting current density

The limiting density in the current study is calculated using Eq. (4.25) and is a function of concrete cover thickness,  $d$ , oxygen diffusion coefficient,  $D_{O_2}$  and amount of dissolved oxygen on surface of concrete,  $C_{O_2}^s$ . Among these factors, oxygen

diffusion coefficient can be represented as a function of relative humidity and porosity via:

$$D_{O_2} = 1.92 \times 10^{-6} \varepsilon_p^{1.8} (1-h)^{2.2} \quad (4.35)$$

where  $\varepsilon_p$  is the porosity of the cement paste and  $h$  is the relative humidity. Detailed calculation of  $\varepsilon_p$  based on concrete mix design properties can be found in (Papadakis et al. 1991) and also provided in appendix A. The temperature dependency of the oxygen diffusion coefficient can be expressed by Arrhenius type equation:

$$D_{O_2,T} = D_{O_2,T_0} e^{\frac{\Delta U_D}{R} \left( \frac{1}{T_0} - \frac{1}{T} \right)} \quad (4.36)$$

where  $\Delta U_D$  (kJ/mole) is the activation energy of the oxygen diffusion coefficient. The value of activation energy,  $\Delta U_D$ , in Eq. (4.36) is proposed by Page and Lambert (1987) as a function of w/c. It is interesting to note that activation energy increases by w/c initially (until w/c = 0.5) and decreases afterwards; the same behaviour is observed for activation energy of chloride diffusion (Page et al. 1981). Since no explicit relationship between the value of activation energy and oxygen diffusion coefficient is presented in (Page and Lambert 1987), such a relationship is obtained by conducting regression through the experimental suggested values (Page and Lambert 1987), details of which can be found in the appendix A.

Temperature also affects the amount of dissolved oxygen in water i.e. a rise in temperature will decrease the amount of dissolved oxygen (hence limiting current density),  $C_{O_2}^s$ , and this effect can be quantified through using Henry's law (Eaton and Mary 2005):

$$\begin{aligned} \text{Ln}C_{O_2}^s = & -139.344 + \left( \frac{1.575 \times 10^5}{T} \right) - \left( \frac{6.642 \times 10^7}{T^2} \right) \\ & + \left( \frac{1.244 \times 10^{10}}{T^3} \right) - \left( \frac{8.622 \times 10^{11}}{T^4} \right) \end{aligned} \quad (4.37)$$

where in the above equation  $C_{O_2}^s$  (mg/litre) is the amount of dissolved oxygen in water at standard condition pressure (i.e. 101.325 kPa). For the purpose of steel corrosion in concrete the above equation provides a good approximation even in non-standard conditions. A complete formulation can be found in the appendix A.

## **5. Virtual Experiments**

---

### **5.1. General**

This chapter presents the results of the numerical investigation of steel corrosion in concrete through simulated polarization resistance tests. The main objective of this chapter is to show that the developed numerical simulation is capable of capturing the experimentally observed behaviour of corrosion of steel in concrete (e.g. increase of corrosion rate with temperature). In this chapter only the independent effects of the considered parameters (i.e. temperature, cover thickness, limiting current density, and resistivity) on the corrosion rate of steel in concrete are discussed. The mutual dependence of parameters (e.g. dependence of limiting current density and concrete resistivity to temperature) will be discussed in Chapter 6.

## 5.2. Study approach

Using the research method described in Chapter 3, 16,000 polarization resistance tests were simulated by varying temperature, concrete cover thickness, concrete resistivity and limiting current density for a number of A/C ratios that varies between 0.1 to 1.0. The cover thickness is varied between 20 mm to 140 mm, a range that covers most civil engineering structures. Reinforced concrete structures are generally exposed to a narrow range of temperature variations (-40°C to +50°C). However, since for most cases corrosion is negligible at low temperatures, the temperature in this study is varied between 10°C and 50°C. Unlike temperature, concrete resistivity can vary in a wide range, as much as five orders of magnitude for different environmental conditions (e.g. temperature and the degree of saturation) (Gjørsv et al. 1977, Chrisp et al. 2001). In this thesis, the concrete resistivity is considered between 50 and 10000  $\Omega\cdot\text{m}$  to cover all extremes. The lower end of the spectrum corresponds to saturated poor-quality concrete and the higher end of the spectrum corresponds to dry good-quality concrete. To investigate the effect of limiting current density on the corrosion rate (i.e. the effect of concentration polarization on the cathodic reaction) a wide range for the limiting current density between 0.002  $\text{A}/\text{m}^2$  and 0.6  $\text{A}/\text{m}^2$  is analyzed. As discussed in Chapter 4, the upper limit is imposed in order to use Eq. (4.25). The lower value is chosen such that it is not smaller than the passivating current density of steel (Alonso et al. 1988). Table 5.1 represents the experimental variables of the experiment, their units, and all the considered values for each variable. It is noted that, the considered parameters are not independent of each other (e.g. temperature affects the resistivity and limiting current

density). However, they are considered independent in each virtual experiment so that the individual effects of each parameter can be studied in detail.

Table 5.1: Experimental variables and their values used in virtual experiments

Experimental Variable	Units	Values
Temperature ( $T$ )	$^{\circ}\text{K}$	283, 298, 303, 313, 323
Cover thickness ( $d$ )	mm	20, 40, 60, 100, 140
Limiting current density ( $i_L$ )	$\text{A}/\text{m}^2$	0.002, 0.005, 0.008, 0.02, 0.05, 0.08, 0.2, 0.6
Resistivity ( $\rho$ )	$\Omega\cdot\text{m}$	50, 350, 650, 1250, 2500, 5000, 7500, 10000
A/C	---	0.1, 0.18, 0.25, 0.33, 0.43, 0.54, 0.67, 0.76, 0.93, 1

### 5.3. Results

By simulating the polarization resistance for each case (e.g.  $T = 283$  K,  $d = 20$  mm,  $i_L = 0.002$  A/m<sup>2</sup>,  $\rho = 50$   $\Omega\cdot\text{m}$ , A/C=0.1) a set of data is obtained, which includes (1) potential distribution in the bulk of the concrete, (2) potential distribution on the surface of concrete, (3) potential distribution at the steel/concrete interface, (4) current distribution at the steel/concrete interface, (5) corrosion current and the number of iterations to convergence. For the sake of comparison, however, the data are presented in the groups of 10. All the experimental variables except A/C (i.e. temperature, cover thickness, limiting current density and resistivity) in each group are constant.

Figure 5.1 illustrates the potential distribution in the bulk of the concrete for four different values of A/C for a typical case. Although the potential distributions of only 4 cases are illustrated herein, the data for all other A/C are obtained from the virtual experiments. In addition to the potential distribution in the bulk of the

concrete, the distribution of the potential at the surface of the concrete and steel/concrete interface is also obtained for each case. Figure 5.2 and Figure 5.3 illustrate the potential distribution on the surface of concrete and at the steel/concrete interface for all A/C ratios.

One of the most useful outcomes of the virtual experiments is the current density distribution at the steel/concrete interface. Figure 5.4 illustrates this current density distribution for all A/C ratios. The positive section of each curve is representative of the anodic current density and the negative section represents the cathodic current density. For every A/C ratio, the anodic section of each curve reaches to the maximum current density at the point of transition from anodic to cathodic section. The largest, maximum current density (in Figure 5.4 the largest maximum current density corresponds to maximum current density of A/C = 0.1) is considered the maximum corrosion current density of all the cases. The maximum corrosion current density is representative of the pitting corrosion, if the form of corrosion is pitting.

The total corrosion current (or simply “corrosion current”) of each case is the area under the anodic section of each current density curve. Figure 5.5 illustrates the corrosion currents corresponding to each A/C. The maximum corrosion current corresponds to the equilibrium state, and its A/C is the optimum A/C, as previously discussed in Chapter 4. For example the maximum current density in Figure 5.5 corresponds to A/C = 0.54, hence, the optimum A/C is equal to 0.54. The maximum corrosion current is then normalised over the anodic section of the steel to obtain average corrosion current density.

The results, summarized above for typical cases, are obtained for all 16,000 virtual experiments are stored as MS-Excel files. Due to the large volume of the raw data, only the processed data are presented and discussed in the next sections; however, complete raw results of the virtual experiments are available on DVD, which is enclosed to this thesis.

As it was discussed above, two values for corrosion rate of steel in concrete were obtained: average corrosion current density and maximum corrosion current density. Since the trend of variation of both corrosion rates (average and maximum corrosion current density) with different parameters is the same and the only difference is the magnitudes, only the results of average corrosion current density is presented hereafter in this chapter. However, the graphs illustrating the variation of maximum corrosion current density is included in the appendix B.

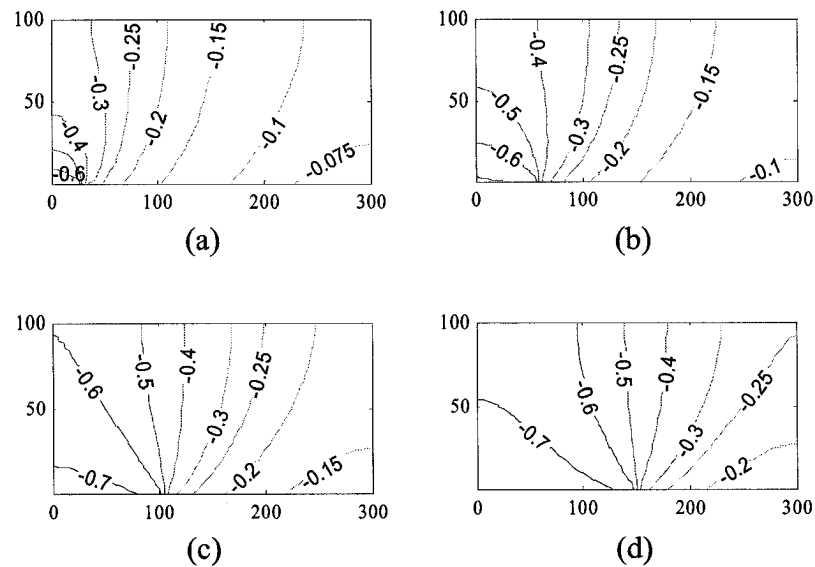


Figure 5.1: Distribution of the potential in the bulk of the concrete

(a)  $A/C = 0.1$ , (b)  $A/C = 0.25$ , (c)  $A/C = 0.54$ , (d)  $A/C = 1$

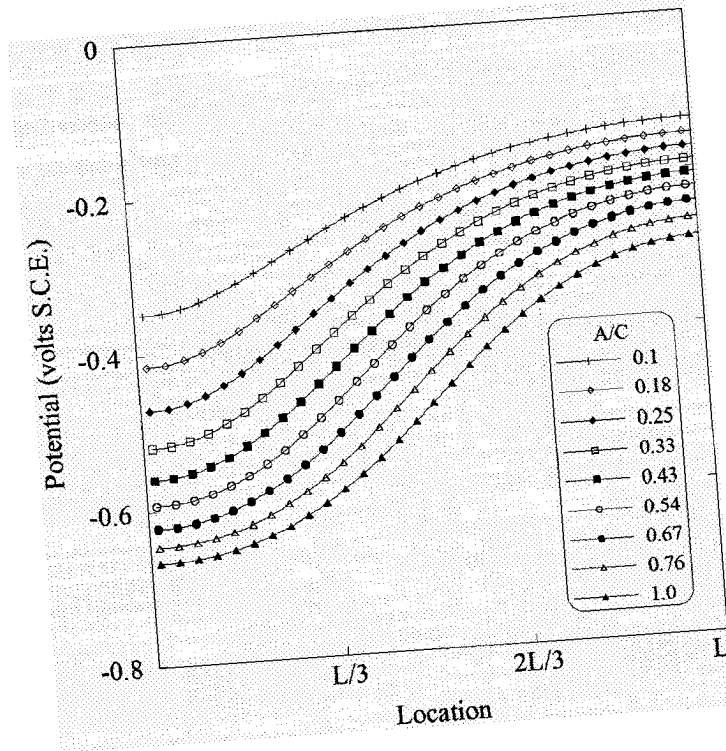


Figure 5.2: Potential distribution at the surface of concrete

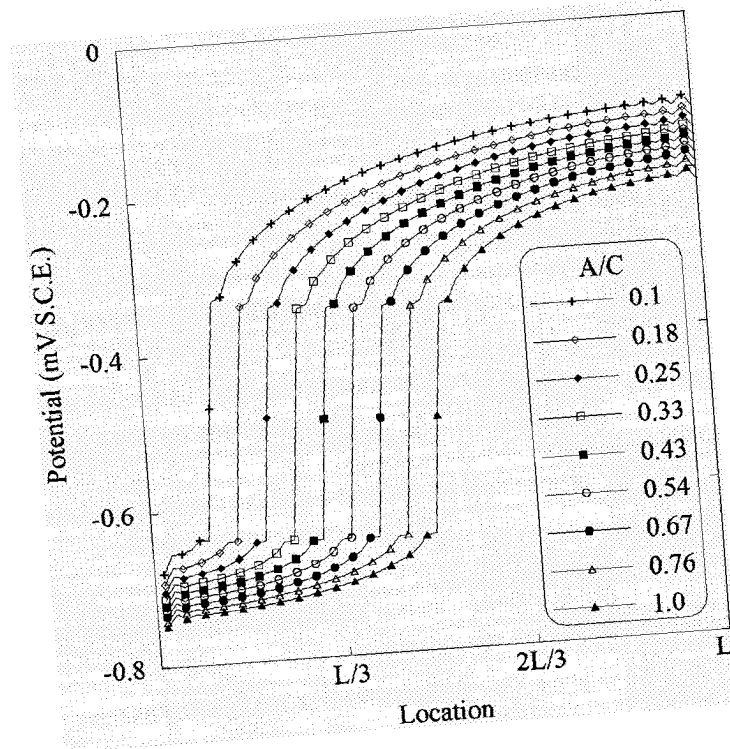


Figure 5.3: Potential distribution at the steel/concrete interface

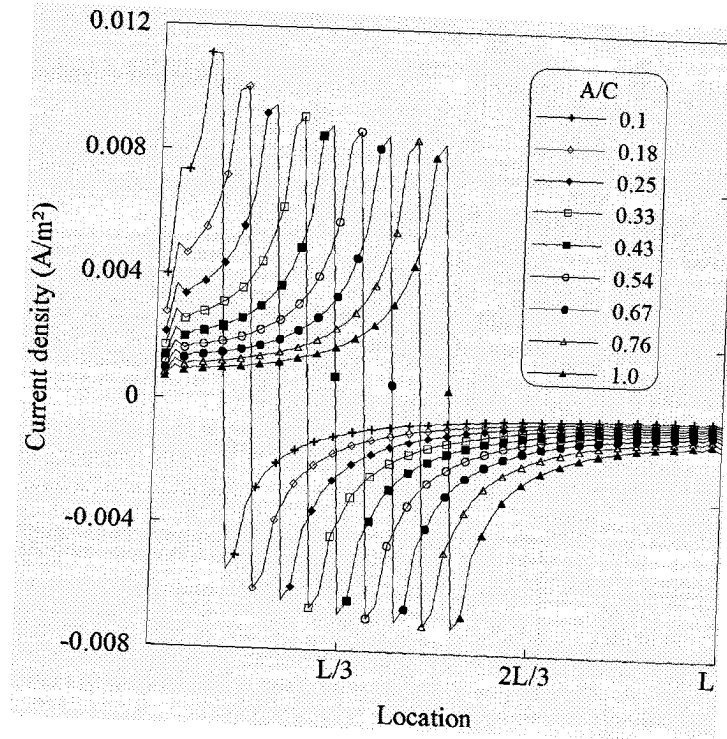


Figure 5.4: Current density distribution at the steel/concrete interface

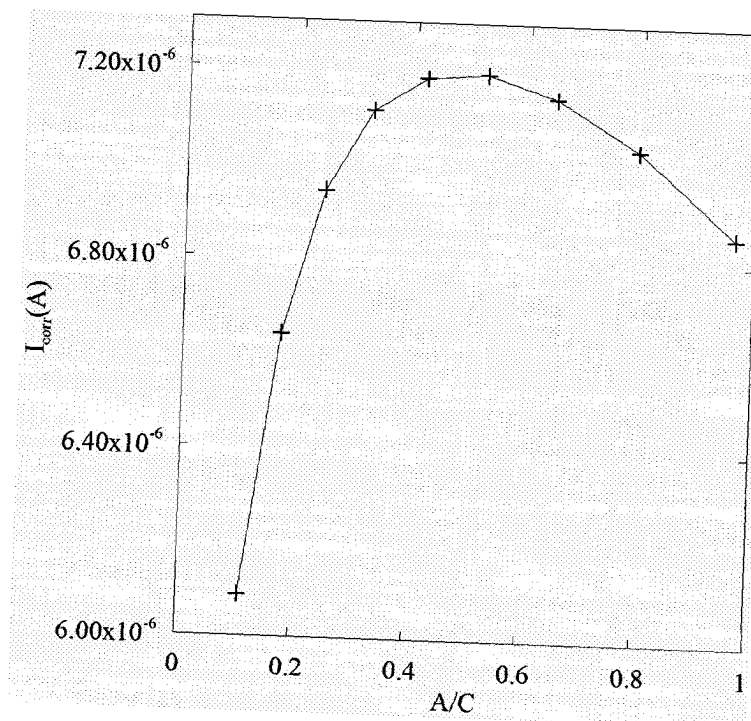


Figure 5.5: Variation of corrosion current with A/C

## 5.4. Discussion

The discussions on the effect of individual parameters on the corrosion rate presented in this section are on the same data obtained from the virtual experiments but present the results from different perspectives.

Figure 5.6 to Figure 5.8 illustrate the effect of temperature on the average corrosion rate of steel in concrete for different combinations of limiting current density, concrete resistivity and cover thickness. It should be noted that the cases presented in Figure 5.6 have been chosen to comply with actual scenarios, i.e. the limiting current density is expected to be low when the concrete resistivity is high since good-quality concrete generally has high resistivity and low oxygen diffusion coefficient. As shown in this figure, the corrosion rate increases almost linearly with temperature in all cases. In Figure 5.6-(a) ( $i_L = 0.2 \text{ A/m}^2$  and  $\rho = 5000 \text{ } \Omega\cdot\text{m}$ ) corrosion rate increases 16% for 140 mm cover thickness over the range of temperature from 283°K to 323°K; the increase for the same range is 11% for 20 mm cover thickness. It can be observed in Figure 5.6-(c) ( $i_L = 0.005 \text{ A/m}^2$  and  $\rho = 10000 \text{ } \Omega\cdot\text{m}$ ) that the increase of corrosion rate with temperature for 140 mm and 20 mm cover thickness are 17% and 10%, respectively. However, the plots in Figure 5.6 show the effect of temperature on corrosion rate while both limiting current density and concrete resistivity are changing. In order to see the individual effects of these two components on the relationship between the corrosion rate and temperature, Figure 5.7 and Figure 5.8 are plotted.

Figure 5.7 shows an almost linear increase of corrosion rate with temperature for different values of limiting current density in concrete with 60 mm cover

thickness. It can be observed that irrespective of the limiting current density, temperature increases the corrosion rate for all values of concrete resistivity. Also in Figure 5.7, it can be observed that for high values of concrete resistivity, the effect of limiting current density on the corrosion rate decreases. In Figure 5.7-(c), it is obvious that the limiting current density has almost no effect on the corrosion rate at different temperatures (i.e. 13% change in the temperature range). This is due to the fact that for large resistivity values, resistance control prevails over diffusion control, and the limiting current density loses its significance.

Increase of corrosion rate with temperature for different values of resistivity is illustrated in Figure 5.8. As concrete resistivity increases, the corrosion rate decreases significantly. In addition, as concrete resistivity increases, the effect of temperature on the corrosion rate for all limiting current densities becomes less significant (i.e. the slope of the lines approach to zero as resistivity increases). It is also obvious from Figure 5.8 that corrosion rate is inversely related to the concrete resistivity.

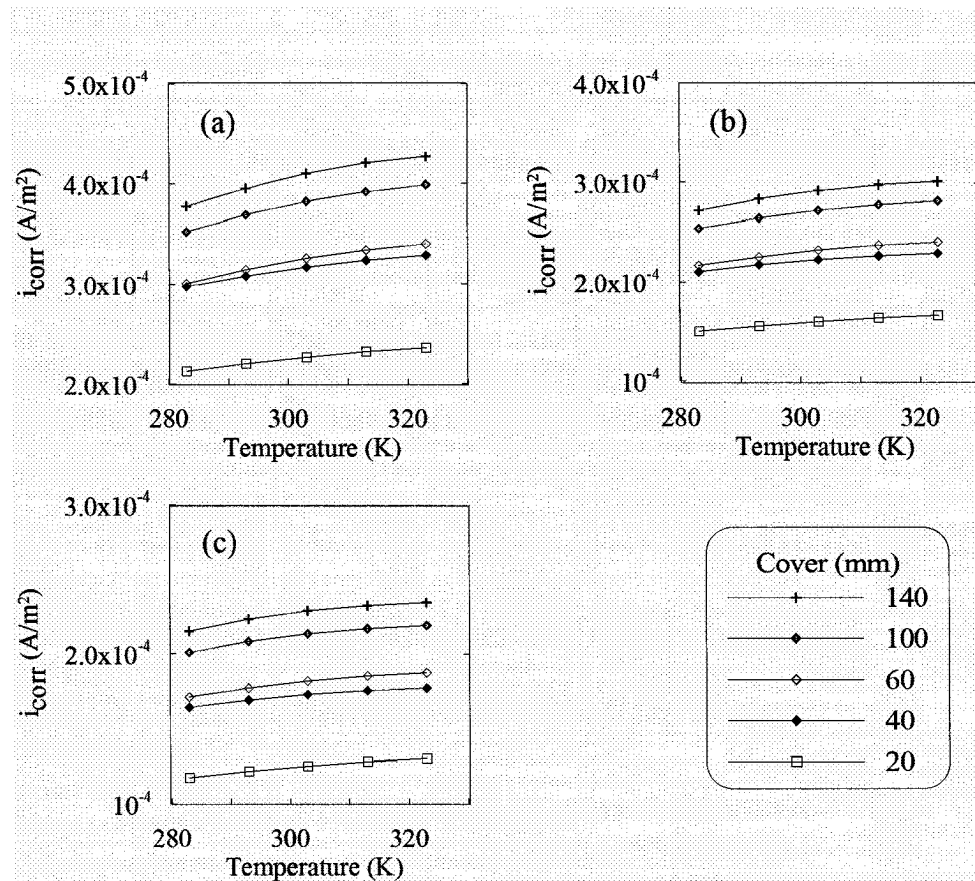


Figure 5.6: Variation of corrosion rate with temperature for different values of cover thickness: (a)  $i_L = 0.2 \text{ A/m}^2$  and  $\rho = 5000 \Omega\cdot\text{m}$ , (b)  $i_L = 0.008 \text{ A/m}^2$  and  $\rho = 7500 \Omega\cdot\text{m}$ , (c)  $i_L = 0.005 \text{ A/m}^2$  and  $\rho = 10000 \Omega\cdot\text{m}$

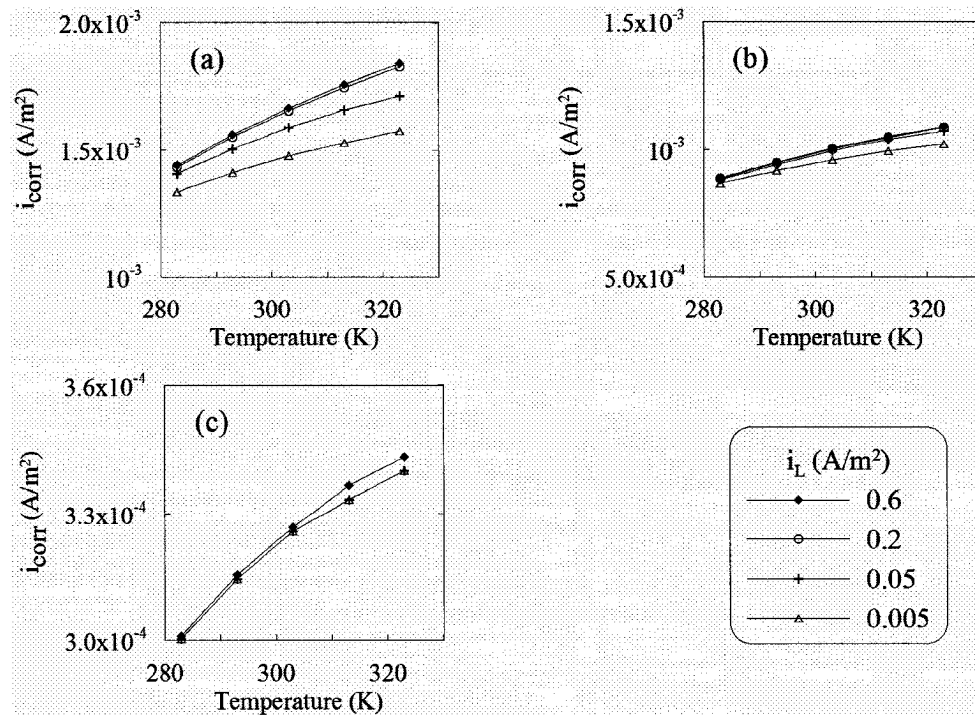


Figure 5.7: Variation of corrosion rate with temperature for different values of  $i_L$  (60 mm cover thickness): (a)  $\rho = 650 \Omega \cdot \text{m}$ , (b)  $\rho = 1250 \Omega \cdot \text{m}$ , (c)  $\rho = 5000 \Omega \cdot \text{m}$

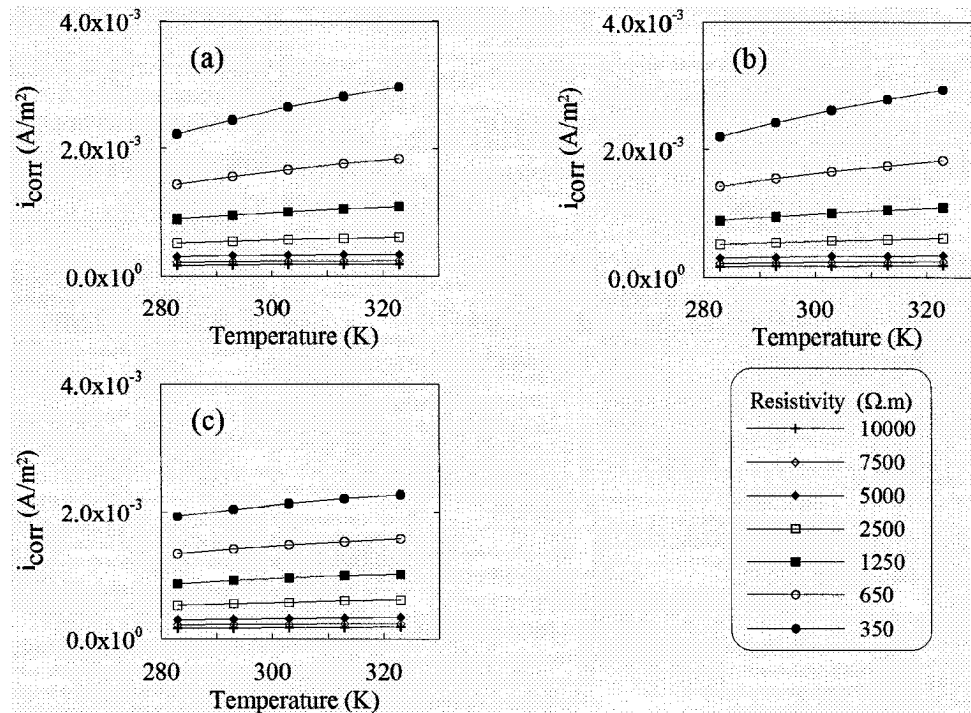


Figure 5.8: Variation of corrosion rate with temperature for different values of concrete resistivity (60 mm cover thickness): (a)  $i_L=0.2$  A/m<sup>2</sup>, (b)  $i_L=0.05$  A/m<sup>2</sup>, (c)  $i_L=0.005$  A/m<sup>2</sup>

Figure 5.9 illustrates the effect of cover thickness on the corrosion rate. It is interesting to note that an increase in cover thickness increases the corrosion rate; however, Figure 5.9 is constructed with the assumption that the limiting current density is independent from cover thickness. If the limiting current density is a function of cover thickness (according to Eq. (4.25)), by increasing the cover thickness, the limiting current density should decrease, resulting in a decrease in the corrosion rate. The investigation of this phenomenon will be carried out in Chapter 6. The increase of corrosion rate with cover thickness in Figure 5.9 is due to better distribution of potential in the bulk of the concrete. As cover thickness increases there

is more space available for ions to travel between anodic and cathodic sites, hence, larger length of the anodic and cathodic sections polarize which results in higher corrosion current. The polarized length of anode and cathode is also dependent on the relative distance of the anode and cathode and as this distance increases the effect of cover thickness decreases; this results in decreases of effect of cover thickness. The decrease in the effect of cover thickness for higher cover thicknesses can be seen in Figure 5.9 where the slope of the line (corrosion rate vs. cover thickness) decreases as cover thickness increases.

Figure 5.10 illustrates the variation of corrosion rate with cover thickness for different values of concrete resistivity. The same trend of increase in corrosion rate with cover thickness as Figure 5.9 can be seen in Figure 5.10. In addition, with the increase of resistivity in this figure the slopes of the lines decrease, suggesting that the effect of cover thickness on the corrosion rate is less significant for large resistivities. In other words, when corrosion is under resistance control, the cover thickness (i.e. potential distribution in the bulk of the concrete) is not a significant factor affecting the corrosion process.

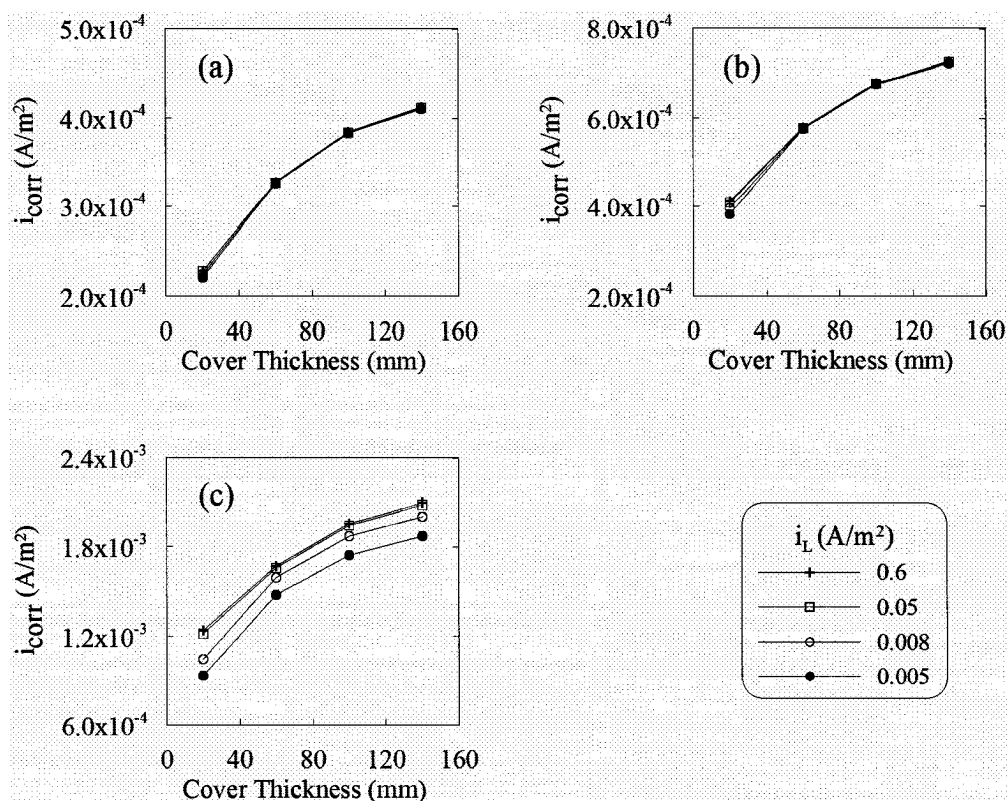


Figure 5.9: Variation of corrosion rate with cover thickness for different values of limiting current density at constant temperature ( $303^\circ\text{K}$ ): (a)  $\rho = 5000 \Omega \cdot \text{m}$ , (b)  $\rho = 2500 \Omega \cdot \text{m}$ , (c)  $\rho = 650 \Omega \cdot \text{m}$

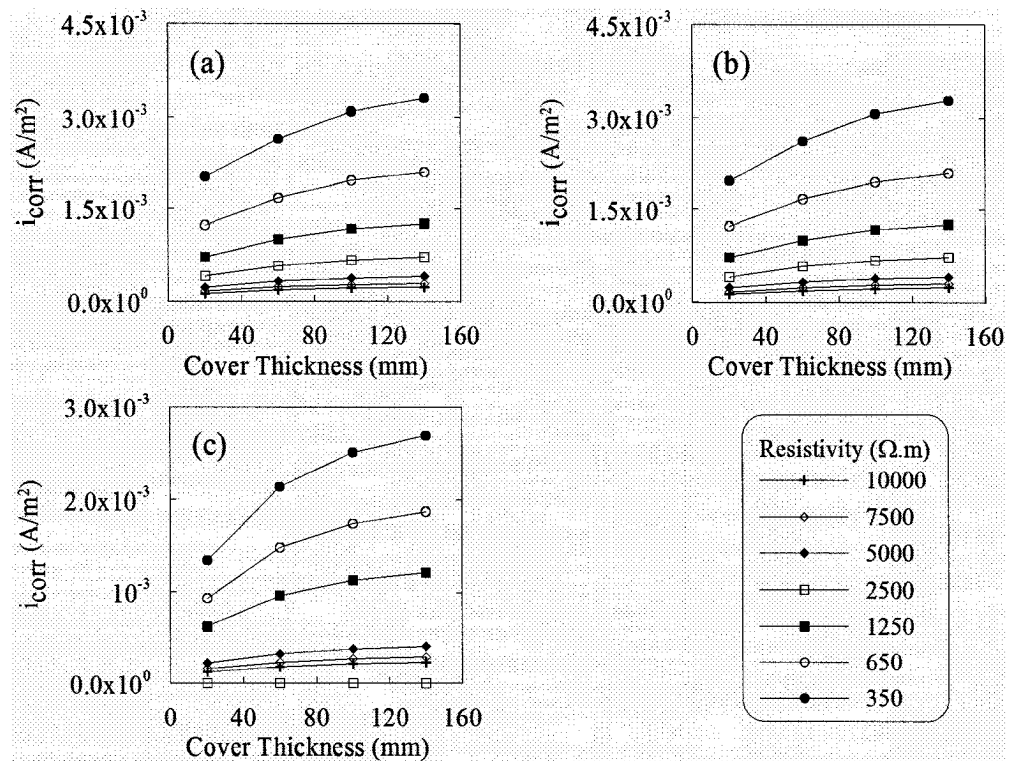


Figure 5.10: Variation of corrosion current with cover thickness for different values of resistivity at constant temperature (303°K): (a)  $i_L=0.2 \text{ A/m}^2$ , (b)  $i_L=0.05 \text{ A/m}^2$ , (c)  $i_L=0.005 \text{ A/m}^2$

Figure 5.11 illustrates the effect of  $i_L$  on the corrosion rate for different cover thicknesses and temperatures. All the plots are constructed for resistivity of  $50 \text{ } \Omega \cdot \text{m}$  since for higher values of resistivity the effect of  $i_L$  decreases significantly as was discussed previously. The corrosion rates in Figure 5.11, initially increase exponentially and approach to a plateau for larger values of  $i_L$ . This observation is in line with polarization behaviour of steel: as  $i_L$  increases corrosion rate also increases, however, as  $i_L$  reaches to large values, the anodic and cathodic polarization curves converge before reaching to  $i_L$  and after this point increase of  $i_L$  does not impose any

effect on the corrosion rate. Also, increase of corrosion rate with cover thickness can be observed here, which is a result of better distribution of electric potential.

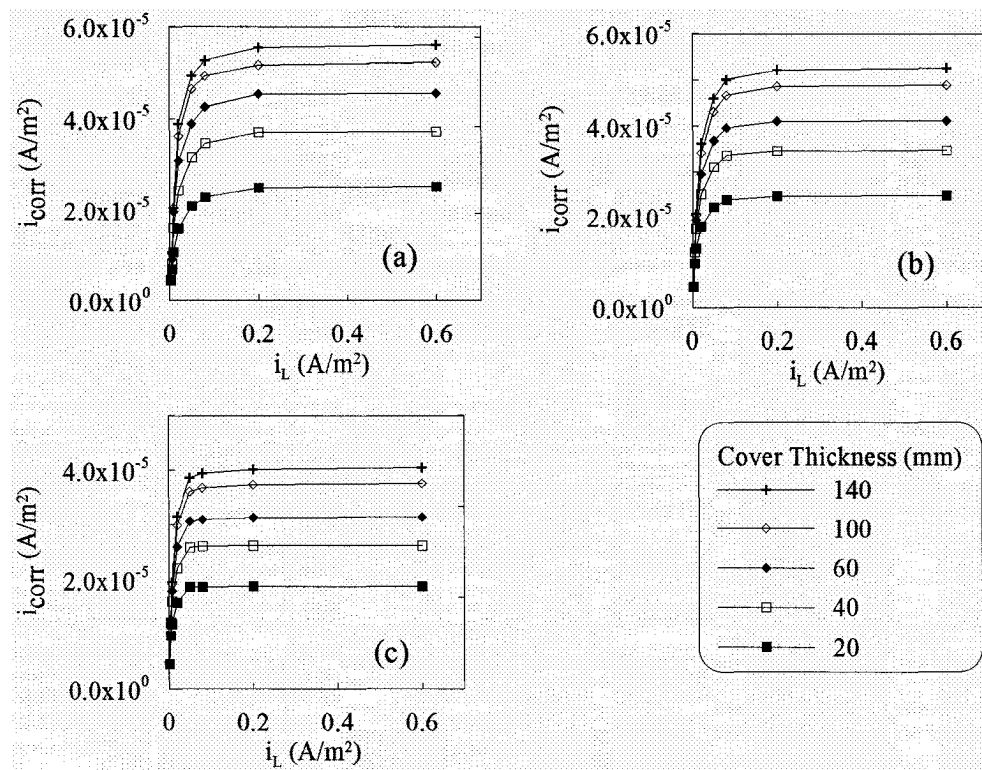


Figure 5.11: Variation of corrosion rate with  $i_L$  for different cover thicknesses ( $\rho = 50$

$\Omega.m$ ): (a)  $T = 323^\circ\text{K}$ , (b)  $T = 303^\circ\text{K}$ , (c)  $T = 283^\circ\text{K}$

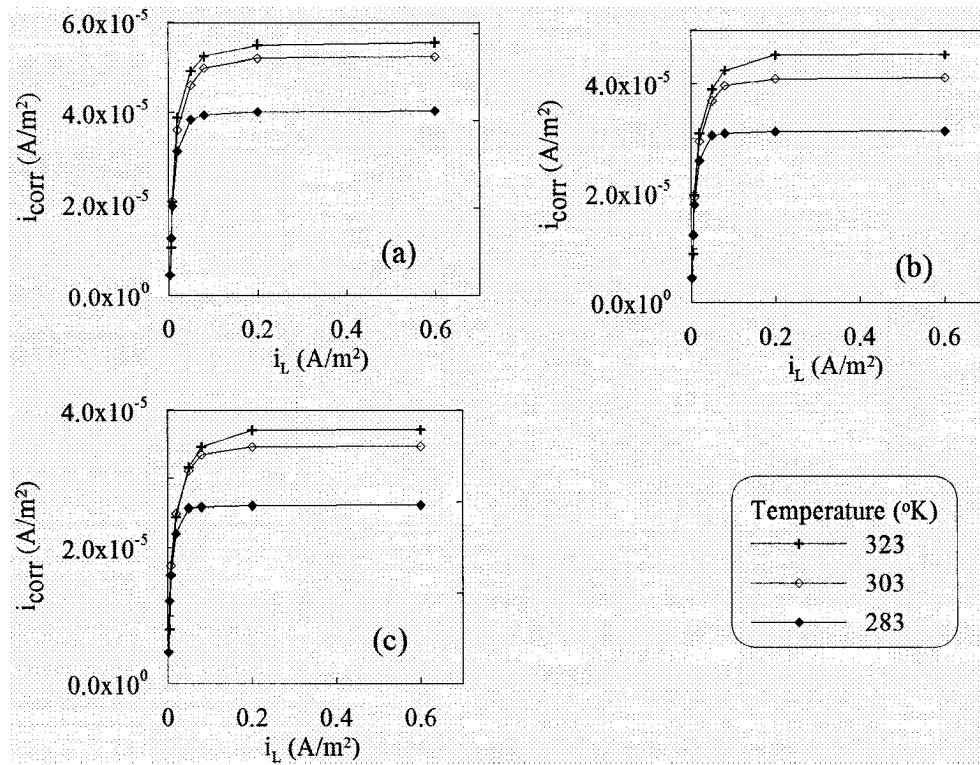


Figure 5.12: Variation of corrosion rate with  $i_L$  for different temperatures ( $\rho = 50$

$\Omega \cdot \text{m}$ ): (a)  $d = 140$  mm, (b)  $d = 60$  mm, (c)  $d = 40$  mm

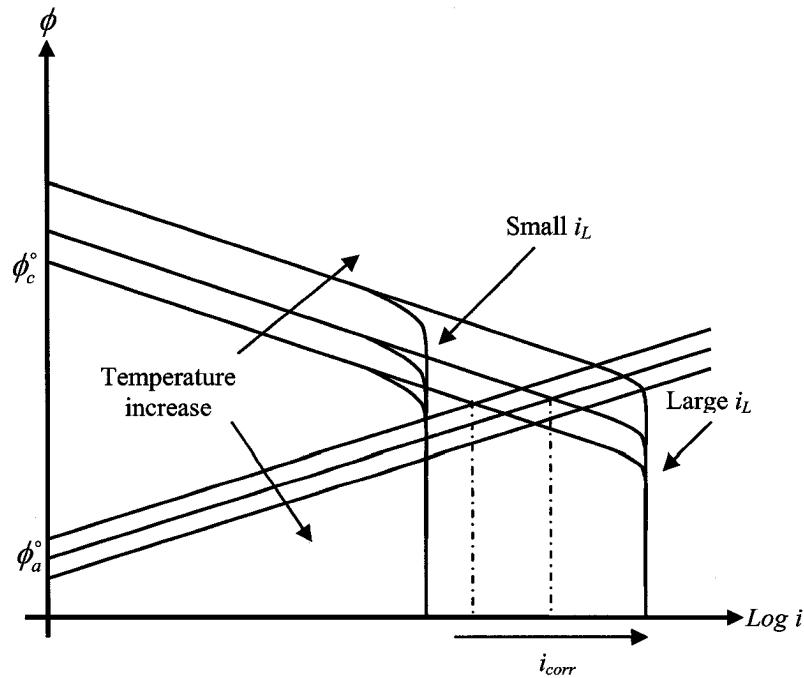


Figure 5.13: Schematic illustration of effect of temperature on the corrosion rate for large and small values of  $i_L$

Figure 5.12 presents the effect of temperature on the variation of corrosion rate with  $i_L$ . The same trend as Figure 5.11 is observed, furthermore, the increase of corrosion rate with temperature for different values of cover thickness can be seen. For very low value of limiting current density, all the curves in Figure 5.12 converge to the same value suggesting that the effect of temperature decreases as limiting current density decreases. This is illustrated schematically in Figure 5.13. As shown in this figure, for large  $i_L$  values, as temperature increases the corrosion rate also increases until it reaches to  $i_L$ ; however, for low values of  $i_L$ , the increase of

temperature does not affect the corrosion rate, and corrosion will proceed with values very close to the limiting current density.

## 5.5. Summary

Based on the results of the virtual experiments, which investigated the independent effects of temperature, cover thickness, limiting current density and concrete resistivity on the rate of steel corrosion, the following observations can be made:

- Corrosion rate of steel in concrete increases almost linearly with temperature, and the rate of increase decreases with increasing concrete resistivity.
- Corrosion rate of steel in concrete increases with cover thickness due to better distribution of potential in the bulk of concrete, and the rate of this increase decreases with increasing concrete resistivity.
- For large concrete resistivities the effect of limiting current density on the corrosion rate vanishes.
- Corrosion rate of steel in concrete shows an initial exponential increase with limiting current density, and the rate of the increase decreases rapidly (reaching to a plateau) for larger values of limiting current density.
- The effect of temperature on the corrosion rate of steel decreases as the limiting current density decreases

These observations are in agreement with experimental studies (Uhlig and Revie 1985, Jones 1996). The data obtained from the virtual experiments will be used to carry out a statistical analysis to develop a closed-form model. This process is described in the following chapter.

## 6. Model Development

---

### 6.1. General

Although the introduced finite element approach implemented in this thesis (see Chapter 3) for solving the Laplace's equation can be considered to be very efficient in terms of computation time when compared with similar problems, it requires good understanding of the fundamental principles of the corrosion theory and the underlying numerical approach; therefore it is not practical for use by the general engineering community. A closed-form equation which uses easily measurable/predictable parameters as input variables can help eliminate this problem. Obtaining an analytical closed-form solution that is based on the solution of the Laplace's equation subjected to Stern-Geary (polarization) boundary conditions in the considered domain is not possible. However, a closed-form solution that is based on

the non-linear multivariable regression analysis of the data obtained from the virtual experiments that are conducted as part of this study can be obtained, and such an approach is carried out in this thesis. Due to the large number of cases that have been analyzed (see Chapter 5) through virtual experiments, the considered parameters, which can be considered to be the main factors affecting corrosion of steel in concrete, are in a wide range that covers most of the real-world scenarios, the outcome of the regression analysis is expected to have a large scope of applicability.

This chapter presents the results of the statistical analysis performed on the data obtained from the virtual experiments for developing the practical closed-form model to predict the maximum (i.e. maximum value of corrosion current density on the reinforcement, representing pitting behaviour) and average (i.e. the corrosion current density averaged over the anodic length of the reinforcement, representing uniform corrosion) corrosion of steel in concrete structures. The results of three experimental investigations are compared with the developed model to verify the applicability and the accuracy.

## **6.2. Non-linear regression analysis**

As it was mentioned in Chapter 5, the maximum corrosion current density shows the same trend of variation with the considered parameters (i.e. temperature, concrete resistivity, limiting current density and cover thickness) as the average current density; therefore, the final model representing both average and maximum corrosion current densities will be almost of the same format. However, since the rates of the variation of the average and maximum corrosion current density with each parameter (e.g. variation of corrosion rate with cover thickness) are different, the

coefficients of the parameters in the model representing the two cases will be different. Therefore, before developing the model for the maximum current density, the variation of the average corrosion current density with considered parameter is examined, the mutual effects of these parameters are investigated, and the model for predicting the average corrosion current density is obtained. Then, a regression analysis on the data associated with the maximum corrosion current density is conducted considering the final format of the equation obtained for the average corrosion current density. The coefficients for the model representing the maximum corrosion current density are obtained. The following describes the development of the seed equation for the non-linear regression analysis.

The dependence of the average corrosion current density on temperature can be observed in Figure 5.6 to Figure 5.8. These figures suggest that the average corrosion current density increases almost linearly with temperature; hence it can be considered to be a linear function of temperature. However, since the effect of temperature decreases with an increase in concrete resistivity (see Figure 5.8) all the terms including temperature should also include reciprocal of concrete resistivity. See Eq. (6.1).

Figure 5.9 suggests that the average corrosion current density increases with cover thickness; however, this increase is not linear and the slope of the curve (corrosion current density vs. cover thickness) decreases for higher values of cover thickness. Hence, the average corrosion current density is a polynomial function of cover thickness, and the power of cover thickness is a positive value smaller than 1. Figure 5.10 also suggests that the effect of cover thickness decreases with an increase

in resistivity; thus, the reciprocal of resistivity should be multiplied with cover thickness. See Eq. (6.2).

The effect of the concrete resistivity on the average corrosion current density also shows a polynomial behaviour since with an increase in resistivity corrosion rate decreases significantly, and the rate of this decrease diminishes for high values of concrete resistivity. Therefore, the average corrosion current density is polynomial function of concrete resistivity, and the power of resistivity is a negative value greater than -1 (i.e. between 0 and -1). See Eq. (6.3).

A mutual effect exists between concrete resistivity and limiting current density such that as resistivity increases the effect of limiting current density decreases (resistance control), and when resistivity decreases the effect of limiting current density increases (diffusion control). To consider this effect, a term that includes limiting current density divided by the concrete resistivity should be implemented in the model. See Eq. (6.4).

The relationship between limiting current density and the average corrosion current density is in the form of a modified root fit function since by increase of the limiting current density corrosion current density increases rapidly to a certain point and ceases to increase afterwards (See Eq. (6.5)); therefore, the limiting current density should be introduced to the model in the form of modified root fit function.

Having these observations, the following relationships can be established:

$$i_{corr} \propto \frac{T}{\rho} \quad (6.1)$$

$$i_{corr} \propto \frac{d^{\text{constant}_1}}{\rho} \quad (6.2)$$

$$i_{corr} \propto \frac{1}{\rho^{\text{constant}_2}} \quad (6.3)$$

$$i_{corr} \propto \frac{i_L}{\rho} \quad (6.4)$$

$$i_{corr} \propto (\text{constant}_3)(\text{constant}_4)^{i_L^{\text{constant}_5}} \quad (6.5)$$

The last equation, using the modified fit function, provides a very accurate approximation for the variation of corrosion rate with limiting current density. Figure (6.1) illustrates two cases with different properties and the fitted curve using Eq. (6.5).

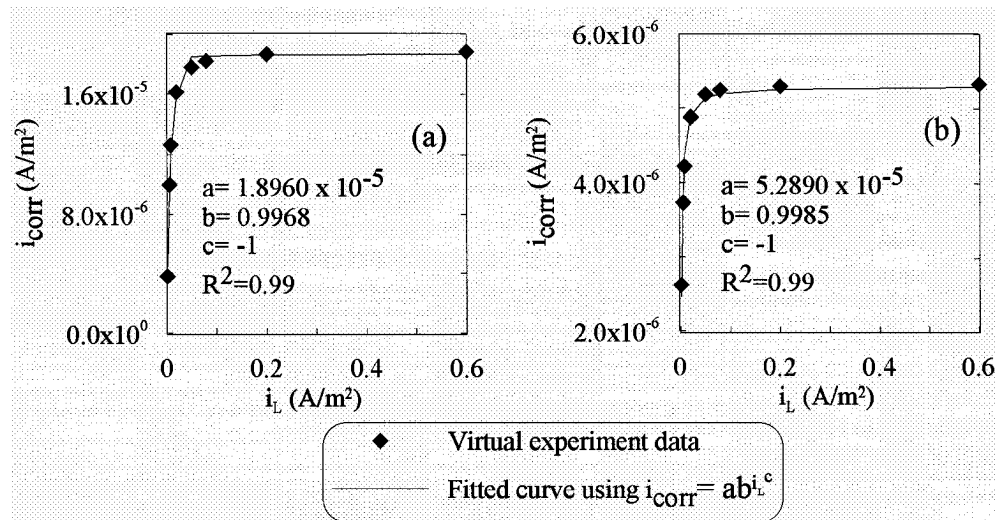


Figure 6.1: Correlation between corrosion rate and limiting current density using modified root fit function. (a)  $T=283^\circ\text{K}$ ,  $d=20\text{ mm}$  and  $\rho=50\ \Omega\cdot\text{m}$ , (b)  $T=283^\circ\text{K}$ ,  $d=20\text{ mm}$  and  $\rho=350\ \Omega\cdot\text{m}$

Each of the aforementioned variations (Eqs. (6.1) to (6.5)) of the corrosion current density with different parameters is considered as a separate term in the seed equation with unknown coefficients. In addition, the interactions of these terms (in

the form of the product of each pair) with unknown coefficients are considered. Consequently, the following seed equation considering all the terms and their interactions is developed:

$$\begin{aligned}
i_{corr} = & a_1 \frac{T^{b_1}}{\rho^{c_1}} + a_2 \frac{d^{b_2}}{\rho^{c_2}} + a_3 \frac{1}{\rho^{c_3}} + a_4 \frac{i_L^{b_4}}{\rho^{c_4}} + a_5 b_5^{i_L^{c_5}} & (6.6) \\
& + a_{12} \frac{T^{b_1} d^{b_2}}{\rho^{c_1} \rho^{c_2}} + a_{13} \frac{T^{b_1}}{\rho^{c_1} \rho^{c_3}} + a_{14} \frac{T^{b_1} i_L^{b_4}}{\rho^{c_1} \rho^{c_4}} + a_{15} \frac{T^{b_1} b_5^{i_L^{c_5}}}{\rho^{c_1}} \\
& + a_{23} \frac{d^{b_2}}{\rho^{c_2} \rho^{c_3}} + a_{24} \frac{d^{b_2} i_L^{b_4}}{\rho^{c_2} \rho^{c_4}} + a_{25} \frac{d^{b_2} b_5^{i_L^{c_5}}}{\rho^{c_2}} \\
& + a_{34} \frac{i_L^{b_4}}{\rho^{c_3} \rho^{c_4}} + a_{35} \frac{b_5^{i_L^{c_5}}}{\rho^{c_3}} + a_{45} \frac{i_L^{b_4} b_5^{i_L^{c_5}}}{\rho^{c_4}} \\
& + a_{123} \frac{T^{b_1} d^{b_2} 1}{\rho^{c_1} \rho^{c_2} \rho^{c_3}} + a_{124} \frac{T^{b_1} d^{b_2} i_L^{b_4}}{\rho^{c_1} \rho^{c_2} \rho^{c_4}} + a_{125} \frac{T^{b_1} d^{b_2}}{\rho^{c_1} \rho^{c_2}} b_5^{i_L^{c_5}} \\
& + a_{134} \frac{T^{b_1} 1 i_L^{b_4}}{\rho^{c_1} \rho^{c_3} \rho^{c_4}} + a_{135} \frac{T^{b_1} 1}{\rho^{c_1} \rho^{c_3}} b_5^{i_L^{c_5}} + a_{145} \frac{T^{b_1} i_L^{b_4}}{\rho^{c_1} \rho^{c_4}} b_5^{i_L^{c_5}} \\
& + a_{234} \frac{d^{b_2} 1 i_L^{b_4}}{\rho^{c_2} \rho^{c_3} \rho^{c_4}} + a_{235} \frac{d^{b_2} 1}{\rho^{c_2} \rho^{c_3}} b_5^{i_L^{c_5}} + a_{345} \frac{1 i_L^{b_4}}{\rho^{c_3} \rho^{c_4}} b_5^{i_L^{c_5}} \\
& + a
\end{aligned}$$

It should be noted that in Eq. (6.6), for better approximation, a power is considered for all independent variables, and also the powers of interaction terms are changed to new unknowns; this provides higher flexibility of the seed equation:

$$\begin{aligned}
i_{corr} = & a_1 \frac{T^{b_1}}{\rho^{c_1}} + a_2 \frac{d^{b_2}}{\rho^{c_2}} + a_3 \frac{1}{\rho^{c_3}} + a_4 \frac{i_L^{b_4}}{\rho^{c_4}} + a_5 b_5 i_L^{c_5} \\
& + a_{12} \frac{T^{b_{12}} d^{b'_{12}}}{\rho^{c_{12}}} + a_{13} \frac{T^{b_{13}}}{\rho^{c_{13}}} + a_{14} \frac{T^{b_{14}} i_L^{b'_{14}}}{\rho^{c_{14}}} + a_{15} \frac{T^{b_{15}} b_{15}^{i_L^{c_{15}}}}{\rho^{c_{15}}} \\
& + a_{23} \frac{d^{b_{23}}}{\rho^{c_{23}}} + a_{24} \frac{d^{b_{24}} i_L^{b'_{24}}}{\rho^{c_{24}}} + a_{25} \frac{d^{b_{25}} b_{25}^{i_L^{c_{25}}}}{\rho^{c_{25}}} \\
& + a_{34} \frac{i_L^{b_{34}}}{\rho^{c_{34}}} + a_{35} \frac{b_{35}^{i_L^{c_{35}}}}{\rho^{c_{35}}} + a_{45} \frac{i_L^{b_{45}} b_{45}^{i_L^{c_{45}}}}{\rho^{c_{45}}} \\
& + a_{123} \frac{T^{b_{123}} d^{b'_{123}}}{\rho^{c_{123}}} + a_{124} \frac{T^{b_{124}} d^{b'_{124}} i_L^{b''_{124}}}{\rho^{c_{124}}} + a_{125} \frac{T^{b_{125}} d^{b'_{125}} b_{125}^{i_L^{c_{125}}}}{\rho^{c_{125}}} \\
& + a_{134} \frac{T^{b_{134}} i_L^{b'_{134}}}{\rho^{c_{134}}} + a_{135} \frac{T^{b_{135}} b_{135}^{i_L^{c_{135}}}}{\rho^{c_{135}}} + a_{145} \frac{T^{b_{145}} i_L^{b'_{145}} b_{145}^{i_L^{c_{145}}}}{\rho^{c_{145}}} \\
& + a_{234} \frac{d^{b_{234}} i_L^{b'_{234}}}{\rho^{c_{234}}} + a_{235} \frac{d^{b_{235}} b_{235}^{i_L^{c_{235}}}}{\rho^{c_{235}}} + a_{345} \frac{i_L^{b_{345}} b_{345}^{i_L^{c_{345}}}}{\rho^{c_{345}}} \\
& + a
\end{aligned} \tag{6.7}$$

A non-linear multivariable regression analysis is conducted using a specialized computer program (NLREG 2005) on the data obtained from the virtual experiments to obtain all the unknown coefficients, and insignificant terms are eliminated from the original seed equation. An insignificant term is a term whose coefficient is very close to zero such that eliminating this term does not change the values of  $R^2$  significantly. Since the value of the coefficient of each term is dependent on the values of the parameters included in that term, after eliminating each insignificant term a new regression analysis was conducted to control the significance of the eliminated term. The following equation resulted after eliminating all insignificant terms:

$$\begin{aligned}
 i_{corr} = & a_3 \frac{1}{\rho^{c_3}} + a_{14} \frac{T^{b_{14}} i_L^{b'_{14}}}{\rho^{c_{14}}} + a_{15} \frac{T^{b_{15}} b_{15}^{i_L^{q_{15}}}}{\rho^{c_{15}}} \\
 & + a_{124} \frac{T^{b_{124}} d^{b'_{124}} i_L^{b''_{124}}}{\rho^{c_{124}}} + a
 \end{aligned} \tag{6.8}$$

To minimize the number of constants in the above equation additional changes were implemented: (1) Since it was observed that the power of resistivity,  $\rho$ , in all terms was almost equal, it was forced to be equal in all terms; (2) The power of temperature,  $T$ , and limiting current density,  $i_L$ , in the second term on the right hand side of Eq. (6.8) was observed to be almost equal, hence, the power of these two parameters was considered to be equal; (3) The power of temperature,  $T$ , in the fourth term on the right hand side of Eq. (6.8) was forced to be equal to unity since the obtained value from regression was very close to unity. The following equation is the final format of the equation:

$$i_{corr} = a_3 \frac{1}{\rho^{c_1}} + a_{14} \frac{(Ti_L)^{b_{14}}}{\rho^{c_1}} + a_{15} \frac{T^{b_{15}} b_{15}^{i_L^{q_{15}}}}{\rho^{c_1}} + a_{124} \frac{Td^{b_{124}} i_L^{b''_{124}}}{\rho^{c_1}} + a \tag{6.9}$$

By conducting another regression analysis on the data associated with the maximum corrosion current density, and considering the same format as the model for the average corrosion current density, a new set of coefficients is obtained. Equation (6.10) is the outcome of the regression analysis for both average and maximum current density:

$$\left\langle \frac{i_{corr,ave}}{i_{corr,max}} \right\rangle = \frac{1}{\tau \rho^\gamma} \left( \eta T d^\kappa i_L^\lambda + \mu T \nu^{i_L^\xi} + \theta (Ti_L)^g + \chi \rho^\gamma + \zeta \right) \tag{6.10}$$

where  $\rho$  ( $\Omega.m$ ) is the concrete resistivity,  $T$  ( $^\circ K$ ) is temperature,  $d$  (m) is cover thickness,  $i_L$  ( $A/m^2$ ) is the limiting current density. The coefficients of the equation

(i.e.  $\tau, \gamma, \eta, \kappa, \lambda, \mu, \nu, \varpi, \theta, \varrho, \chi, \zeta$ ) are provided in Table 6.1. The average deviation from any observation for Eq. (6.10) for average current density,  $i_{corr,ave}$ , is  $5 \times 10^{-4}$  A/m<sup>2</sup> (in the range of passivating current density);  $R^2$  for this model is close to 0.99 (both the adjusted coefficient of multiple determination and the proportion of variance explained). The corresponding  $R^2$  for the maximum current density,  $i_{corr,max}$ , model is close to 0.91 (both the adjusted coefficient of multiple determination and the proportion of variance explained). Although a better expression with a higher  $R^2$  value can be obtained for maximum corrosion current density by changing the format of the equation, it was decided that it is more practical to have the same format for both equations. Figure 6.2 compares the results of the finite element analysis with that of the model for average corrosion current density.

Table 6.1: Constants of the model

$i_{corr,ave}$		$i_{corr,max}$	
Constant	Value	Constant	Value
$\tau$	$1.181102362 \times 10^{-3}$	$\tau$	1
$\eta$	$1.414736274 \times 10^{-5}$	$\eta$	0.32006292
$\zeta$	-0.00121155206	$\zeta$	-53.1228606
$\kappa$	0.0847693074	$\kappa$	0.00550263686
$\lambda$	0.130025167	$\lambda$	0.120663606
$\gamma$	0.800505851	$\gamma$	0.787449933
$\mu$	$1.23199829 \times 10^{-11}$	$\mu$	$-3.73825172 \times 10^{-7}$
$\theta$	-0.000102886027	$\theta$	47.2478753
$\varrho$	0.475258097	$\varrho$	0.00712334564
$\chi$	$5.03368481 \times 10^{-7}$	$\chi$	0.003482058
$\nu$	90487	$\nu$	784679.23
$\varpi$	0.0721605536	$\varpi$	0.0102616314

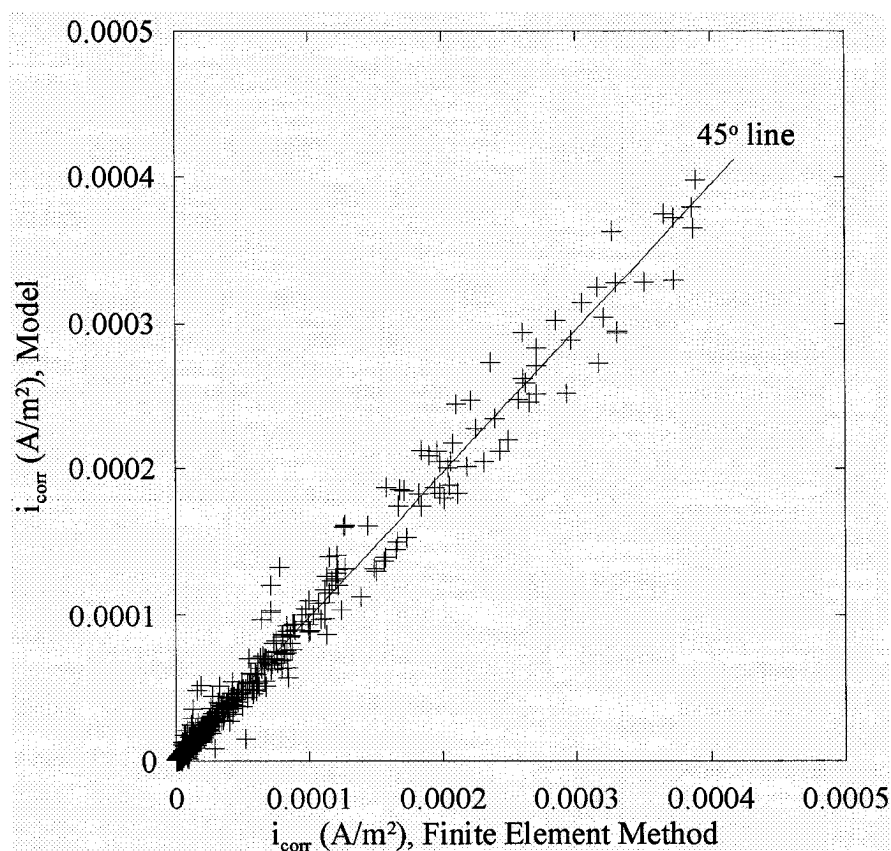


Figure 6.2: Comparison of the actual results (the finite element method) with the regression analysis

### 6.3. Experimental verification

In this section three experimental studies from the literature are compared with the model. A brief summary of the methods and materials used in each experiment are presented; further details of the experiments can be found in the corresponding original references.

#### 6.3.1. Lopez et al. 1993

The first experimental work to verify the developed model is obtained from Lopez et al. (1993). This verification is chosen to illustrate the capability of the model

in capturing the variation of corrosion rate with temperature. The general setup of the experiments conducted by Lopez et al. (1993) is as follows: Two rebars of 10 mm diameter were embedded in mortar specimens of dimensions 2x5.5x8 cm in symmetric positions along with a central stainless steel bar as working electrode. The mortars had 1:3:0.5 cement/sand/water ratio and contained 0%, 2%, 4% and 6% chloride content that was added in the form of NaCl by the weight of cement. After curing for 40 days in 100% relative humidity, specimens were exposed to three levels of temperature (0°C, 30°C, 50°C), three levels of relative humidity (50%, 90% and full immersion) resulting in 36 cases. The corrosion rate of rebars were measured with the polarization resistance method.

The temperature and concrete cover thickness are provided in the original work (Lopez et al. 1993), however, the concrete resistivity and the limiting current density should be estimated for each one of 36 cases. For estimating the concrete resistivity through the available data the following procedure is implemented: the corresponding degree of saturation to the each relative humidity is calculated using the adsorption isotherm proposed by Xi et al. (1994). This isotherm is included in the appendix A. The required data of the isotherm (i.e. w/c ratio, age of concrete and temperature) are provided in the original reference. Since the w/c ratio and the saturation of concrete are known the resistivity of concrete at 20°C is calculated using the experimental data obtained by (Gjørv et al. 1977). To ease the estimation of concrete resistivity through these experimental data, a regression analysis is conducted and a mathematical expression relating the concrete resistivity to degree of saturation is obtained which can be found in appendix A. The resistivity of the

desired temperature then is calculated using the activation energy proposed by Chrisp et al. (2001).

The limiting current density also is estimated for each of cases in this experimental study using the following procedure: the amount of dissolved oxygen in water for each temperature is calculated using the Henry's law (see appendix A). The diffusion coefficient of the concrete is calculated using the model proposed by Papadakis et al. (1991). Having calculated the latter parameters, using the formula presented in Chapter 4 the limiting current density is calculated. It should be noted that the effect of chloride content on concrete properties such as resistivity is not considered herein and hence only 9 sets of data will be obtained for calculating the corrosion rate. Table 6.2 represents the input data.

Table 6.2: Input data for the model used to compare the model with experiments conducted by Lopez et al. (1993)

<b>RH (%)</b>	<b>Temperature (°K)</b>	<b>Cover thickness (m)</b>	<b>Limiting current density (A/m<sup>2</sup>)</b>	<b>Resistivity (Ω.m)</b>
50	273	0.0065	0.926	33179
90	273	0.0065	0.02684	252
F.I.*	273	0.0065	0.008	149
50	303	0.0065	2.4	5356
90	303	0.0065	0.070	68
F.I.	303	0.0065	0.015	43
50	323	0.0065	4.15	1908
90	323	0.0065	0.12	32
F.I.	323	0.0065	0.026	21

\* Full immersion: for calculating the oxygen diffusion coefficient the relative humidity of F.I. is considered 99%.

Figure 6.3 compares the results of the experiments conducted by Lopez et al. (1993) with the average and maximum corrosion current densities obtained using the model. The results of the experimental work for all values of relative humidity and temperature are almost always between the average and maximum corrosion current densities predicted by the model, except for experimental data related to samples with 0% chloride contamination. This is due the fact that, in the latter samples the depassivation had not occurred (i.e. steel was not actively corroding), and the model presented in this work is applicable to cases in which depassivation has already taken place.

As it can be observed in Figure 6.3, the models for the average and maximum corrosion current density predicts the experimental observations well; however, there is up to one order of magnitude difference between the values of average and maximum corrosion current density obtained by the model, which may appear to be unrealistically wide. On the other hand, it should be noted that the experimental data is also widely scattered, even on a larger scale. For example, in Figure 6.3-(a) the corrosion rate of samples with 6% chloride contamination decreases with increase of temperature, and highest corrosion rate is seen at 0°C. This can only be explained as experimental noise since with decreasing temperature (1) the resistivity of concrete increases, (2) the diffusion coefficient of concrete decreases; therefore, it is expected that the corrosion rate would decrease. The overall trend of variation of experimental data with temperature also confirms the increase of corrosion rate with temperature. The model perfectly predicts this trend. The range between the maximum and average corrosion current density includes all experimental data points. It is worthwhile

mentioning that the maximum corrosion current density is an indicator of pitting corrosion, which can easily occur in real-world scenarios. Experimental investigations of Gonzalez et al. (1995) show that the pitting corrosion rate can be up to 8 times larger than the measured values with common polarization resistance instruments, which cannot capture the behaviour since they average the measuring current over the entire length of the reinforcement. The maximum corrosion current density suggested herein can be regarded as the upper limit of the corrosion rate, representing possible pitting behaviour; therefore it provides more information than common polarization resistance tests.

It has been reported in the literature that the polarization resistance method can be associated with errors as large as 100% (Andrade and Gonzalez 1978). Liu and Weyers (1998) have reported 15 times (more than one order of magnitude) difference between the results obtained with 3LP and Gecor instruments while both instruments use the same method of measurement, i.e. polarization resistance. These observations suggest that the range of the values between the average and maximum corrosion current densities is a reasonable range that can be encountered in experimental observations; therefore the results should be interpreted accordingly.

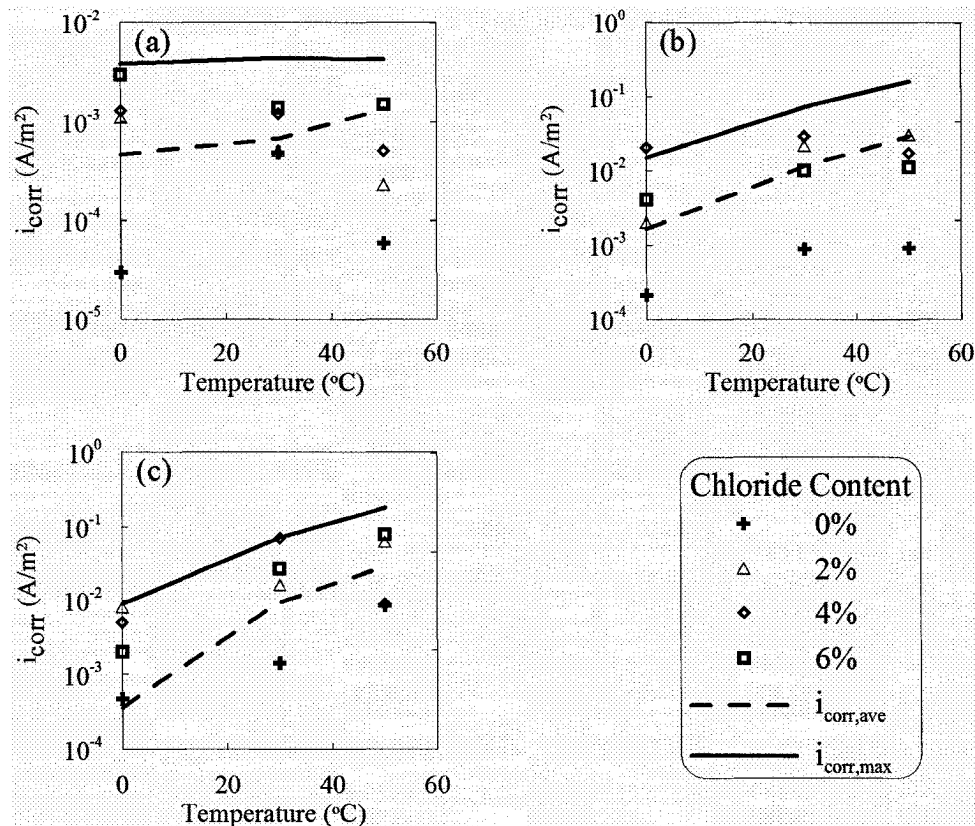


Figure 6.3: Comparison of the results of Lopez et al. (1993) with the average and maximum corrosion current densities obtained using the developed model: (a) Relative humidity = 50%, (b) Relative Humidity = 90%, (c) Saturated conditions

### 6.3.2. Lopez and Gonzalez 1993

The second experimental work for verification is taken from Lopez and Gonzalez (1993) to illustrate the capability of the developed model in accurately capturing the variation of corrosion rate with the degree of saturation,  $S_r$ . In the experiments conducted by Lopez and Gonzalez (1993) two sets of mortar specimens were prepared with cement/sand/water ratio of 1:3:0.5, one set of which was contaminated with 2% chloride ions by the weight of cement. Each set was cast in

two dimensions: 8x2x2 cm for resistivity measurements and 8x5.5x2 cm for electrochemical measurements. All mortar specimens were cured for 40 days in a standard fog chamber (at 23°C), then they were exposed to relative humidities higher than 90% for 60 days. Mortar specimens were finally stored at 50°C temperature and 50% relative humidity for 500 days.

For measuring the resistivity (i.e. 8x2x2 cm samples) the 2x2 face of the specimens were coated with graphite paint after mechanically polishing the specimens for better bond between the paint and surface of concrete. The samples used for electrochemical measurements (i.e. 8x5.5x2 cm samples) had two carbon steel bars embedded at symmetric positions as working electrode with a stainless steel bar as counter electrode in the middle.

All the input parameters of the model are provided in the reference except for limiting current density to calculate which the same method as used in the previous section (i.e. Papadakis et al. 1991) is used. The input data for the model are presented in Table 6.3.

Figure 6.4 compares the results of experiments conducted by Lopez and Gonzalez (1993) with the average and maximum corrosion current densities predicted by the developed model. All experimental results are mostly within the predicted range of average and maximum corrosion current densities, except for the specimens which were chloride free. As it was mentioned previously, since these samples were still in passive state, the model is not applicable to predict their behaviour. It is important to note that the developed model can predict the decrease in the corrosion rate as the relative humidity increases. It is well documented in the literature that

when concrete is submerged in water, due to oxygen deficiency, the corrosion slows down due to concentration polarization. This behaviour is captured by the developed model very accurately.

Table 6.3: Input data for the model used to compare the results with experiments conducted by Lopez and Gonzalez (1993)

$S_r$ (%)	Temperature (°K)	Cover thickness (m)	Limiting current density (A/m <sup>2</sup> )	Resistivity (Ω.m)
32	323	0.0065	4.65	80000
36	323	0.0065	3.84	8000
41	323	0.0065	2.47	5000
45	323	0.0065	1.90	1500
48	323	0.0065	1.42	900
50	323	0.0065	1.42	350
52	323	0.0065	1.01	300
56	323	0.0065	0.68	150
65	323	0.0065	0.41	90
78	323	0.0065	0.090	40
82	323	0.0065	0.055	30
90	323	0.0065	0.02	20
99	323	0.0065	0.005	20

It should also be mentioned that the maximum corrosion current density in Figure 6.4 is always larger than the average corrosion current density, and as discussed earlier the value of the maximum corrosion current density can be regarded as corresponding to the pitting corrosion rate. Since the experimental corrosion rates at all degrees of saturation are closer to the predicted average corrosion current density, it can be concluded that these specimens are mostly experiencing uniform corrosion.

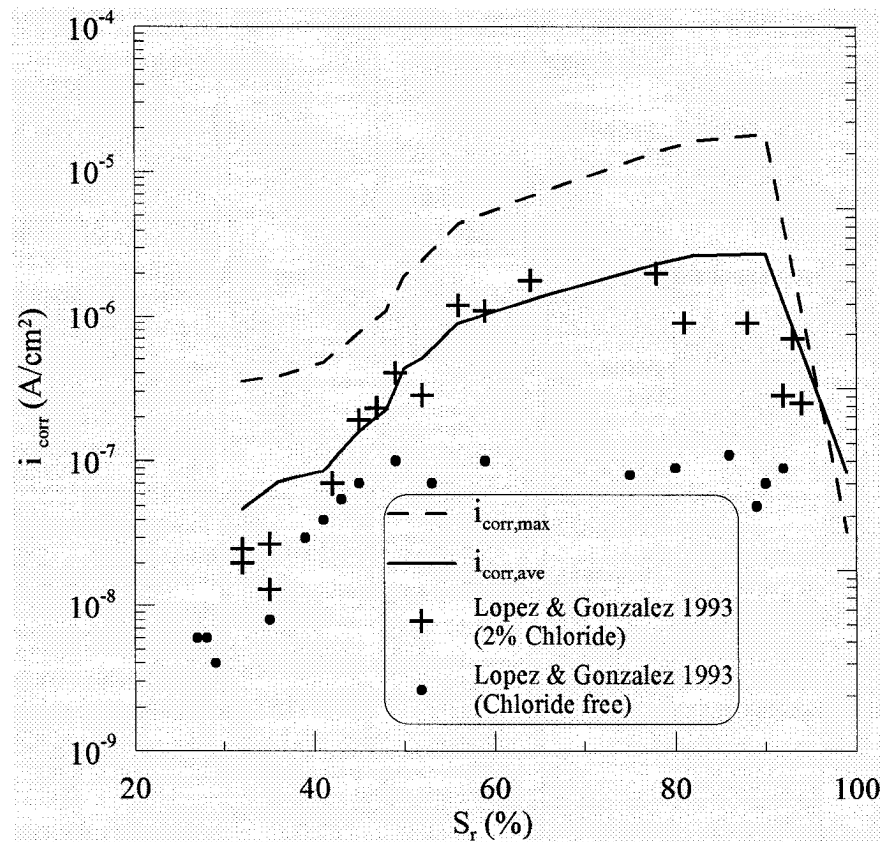


Figure 6.4: Comparison of the predicted average and maximum corrosion current density with the experimental data from Lopez and Gonzalez (1993)

### 6.3.3. Ramezaniapour et al. 2007

As the third verification, the model is compared with the results of an investigation conducted in the Persian Gulf region. The main purpose of this verification is to illustrate the ability of the model to capture the effect of cover thickness on corrosion rate. Table 6.4 shows the mixture properties of the concrete samples used by Ramezaniapour et al. (2007). Cover thickness of the samples were 35mm, 50mm and 70 mm. The air content of samples was kept between 3 to 5%, and all samples were moist cured for 7 days, followed with 14 days of curing in air.

Finally, samples were moved to the Gulf region and were exposed to two different conditions: air and tidal exposures. The corrosion rate and the concrete resistance of the samples were measured using galvanostatic pulse technique after 1 year and 4 years of exposure.

Table 6.4: Mixture proportions of specimens tested by Ramezaniapour et al. (2007)

Mixture	Cement type	w/cm	Water (kg/m <sup>3</sup> )	Cement (kg/m <sup>3</sup> )	Sand (kg/m <sup>3</sup> )	Gravel (kg/m <sup>3</sup> )
A1	II	0.40	160	400	760	1050
A2	II	0.35	140	400	760	1050
B1	V	0.40	160	400	760	1050
B2	V	0.35	140	400	760	1050

The resistance of the concrete cover is provided in the original work, however, this resistance should be converted to concrete resistivity. This is done by referring to the manual of the instrument used to measure the concrete resistance by Ramezaniapour et al. (2007); see appendix A.

The same method used to calculate the limiting current density for the concrete samples used by Lopez et al. (1993) is implemented here for calculating the limiting current density. The cement paste porosity, which is required for determining the limiting current density, is calculated using the model proposed by Papadakis et al. (1991) and the chemical composition provided by Ramezaniapour et al. (2007) for different types of cements used. The Relative humidity and temperature of the exposure conditions were not mentioned in the reference therefore the average relative humidity (65% for air exposure and 90% for tidal exposure) and average annual temperature (27°C) of the Gulf region has been used in calculating the oxygen

diffusion coefficient. Table 6.5 presents the input data of the model for each mixture and exposure.

Figure 6.5 compares the results of the experimental study for samples with 35 mm cover thickness with the predicted average and maximum corrosion rates obtained using the developed model. Although some fluctuations are observed, the average corrosion rate is in perfect agreement with experimental results. The observed fluctuations can be attributed to the approximations (i.e. considering the average relative humidity and temperature) in calculating the required parameters of the model and also to the uncertainties in the experimental measurements. It should be noted that the galvanostatic pulse technique used in the experimental study is significantly affected by the polarization rate and the duration of polarization (Luping 2002). Hence it can be stated that the model predicts the corrosion rate with acceptable accuracy.

It is obvious from the figure that the maximum corrosion rate obtained using the model is significantly larger than the average corrosion rate and the experimental data. As discussed earlier, this corrosion rate is highly probable since, in some cases, corrosion proceeds in the form of pitting corrosion but instruments normalize the obtained value of corrosion current over the polarized length of the reinforcement. Therefore these instruments may well underestimate the corrosion rate. The maximum corrosion rate provided herein is, in effect, the compensation for this underestimation.

Figure 6.6 and Figure 6.7 compare the results of the model with experimental data for 50 mm and 75mm cover thickness, respectively. The same trend of behaviour

as Figure 6.5 can be seen in these figures, suggesting the model perfectly captures the effect of cover thickness and predicts the corrosion rate with good accuracy.

Table 6.5: Input data of the model used for comparing the model with experimental study by Ramezani-pour et al. (2007)

Cover thickness			30		50		70	
duration of exposure	Mixture	Exposure	$i_L$ (A/m <sup>2</sup> )	$\rho$ ( $\Omega$ .m)	$i_L$ (A/m <sup>2</sup> )	$\rho$ ( $\Omega$ .m)	$i_L$ (A/m <sup>2</sup> )	$\rho$ ( $\Omega$ .m)
1 Year	A1	Dry	0.078	132	0.054	162	0.039	234
		Tidal	0.012	108	0.008	102	0.006	96
	A2	Dry	0.060	234	0.042	270	0.030	258
		Tidal	0.009	126	0.006	156	0.004	132
	B1	Dry	0.074	162	0.052	186	0.037	168
		Tidal	0.011	60	0.008	114	0.005	114
	B2	Dry	0.056	270	0.039	330	0.028	300
		Tidal	0.008	30	0.006	150	0.004	156
4 Years	A1	Dry	0.075	360	0.053	390	0.037	360
		Tidal	0.011	48	0.008	72	0.005	72
	A2	Dry	0.057	360	0.040	366	0.028	366
		Tidal	0.008	48	0.006	90	0.004	102
	B1	Dry	0.072	294	0.050	288	0.036	336
		Tidal	0.011	24	0.007	30	0.005	42
	B2	Dry	0.054	312	0.038	342	0.027	348
		Tidal	0.008	30	0.005	78	0.004	84

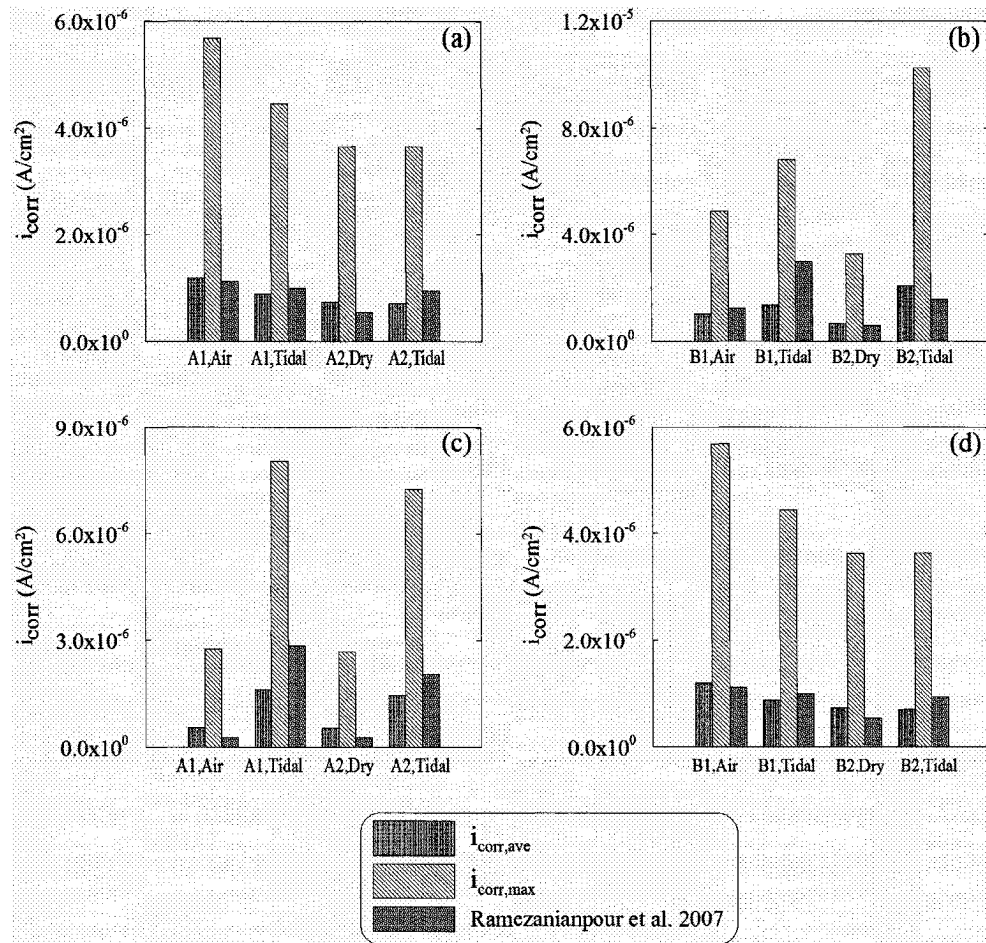


Figure 6.5 : Comparison of the results of experiments by Ramezani pour et al. (2007) with predicted average and maximum corrosion rates for concrete specimens with 35 mm cover depth: (a, b) After one year of exposure, (c, d) After four years of exposure

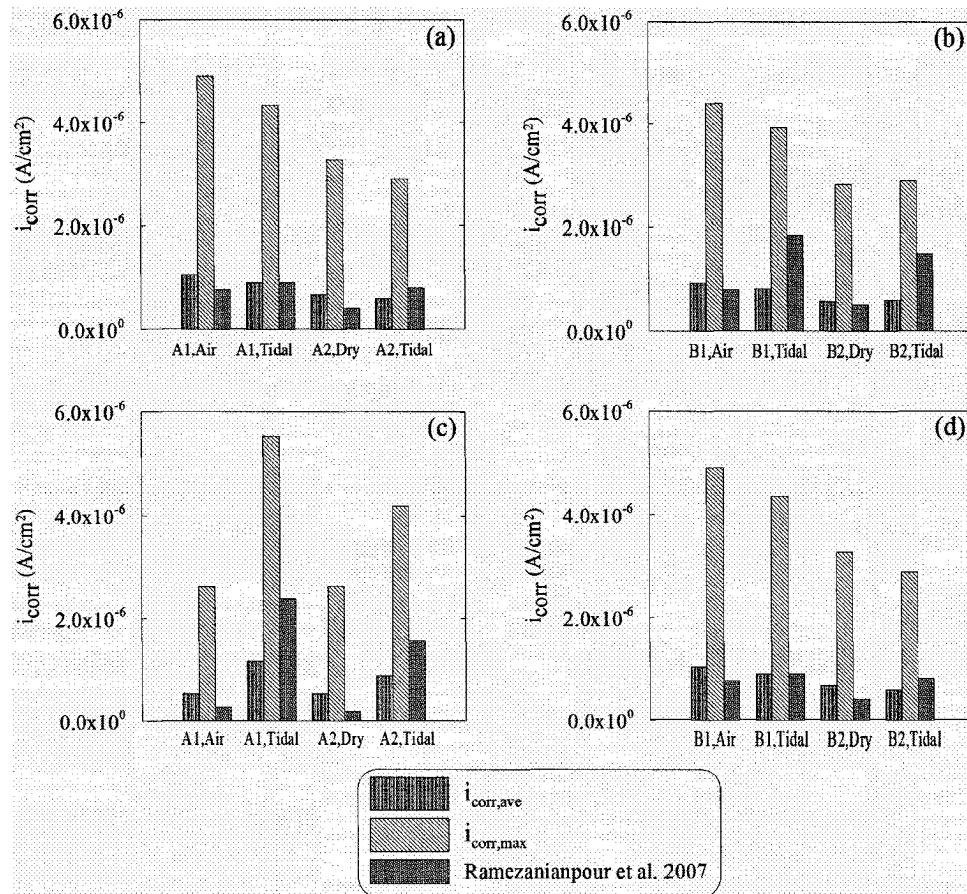


Figure 6.6: Comparison of the results of experiments by Ramezani pour et al. (2007) with predicted average and maximum corrosion rates for concrete specimens with 50 mm cover depth: (a, b) After one year of exposure, (c, d) After four years of exposure

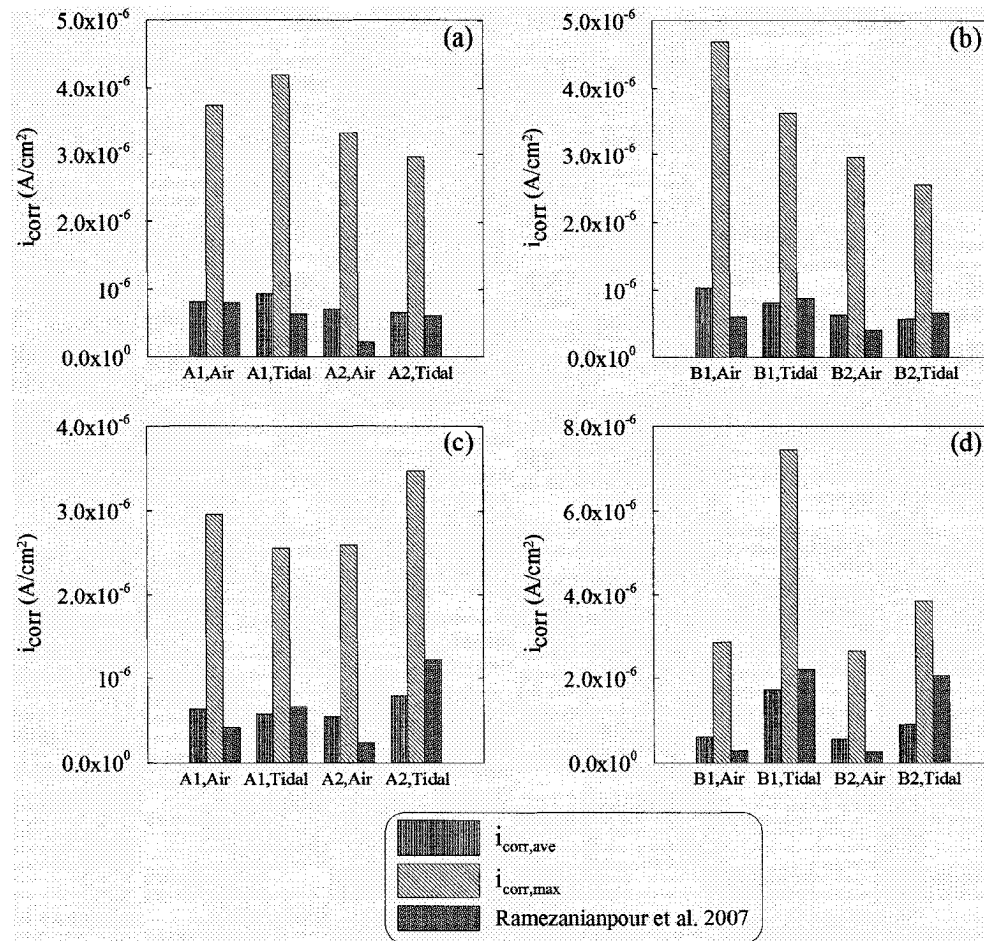


Figure 6.7: Comparison of the results of experiments by Ramezani pour et al. (2007) with predicted average and maximum corrosion rates for concrete specimens with 70 mm cover depth: (a, b) After one year of exposure, (c, d) After four years of exposure

#### 6.4. Case Study: Coupled effect of concrete properties and environmental factors on the corrosion rate

To investigate the coupled effect of concrete properties and environmental factors on the corrosion rate of steel in concrete using the developed model, a

hypothetical case study is presented here. The basic variables of the case study and the range in which they are investigated are as follows: (1) w/c ratio (0.4 to 0.6), (2) temperature (20 to 50°C); (3) cover thickness (20 and 140 mm).

To calculate the concrete resistivity,  $\rho$ , using these variables the following method is implemented: Considering a value for w/c ratio and hydration time (assumed to be 4 years in this case), the pore saturation corresponding to a given relative humidity is calculated using the adsorption isotherm (Xi et al. 1994, see appendix A). Using the calculated pore saturation, the concrete resistivity is estimated through experimental curves suggested by GjØrv et al. (1977, see appendix A). Then, the calculated concrete resistivity is converted to the concrete resistivity at the desired temperature; this is done using the activation energy approach, proposed by Chrips et al. (2001, see appendix A). It is noted that the activation energy of concrete resistivity is a function of the degree of pore saturation.

To calculate the limiting current density,  $i_L$ , the amount of dissolved oxygen in water at the surface of concrete,  $C_{O_2}^s$ , and the oxygen diffusion coefficient of concrete,  $D_{O_2}$ , are needed. The amount of dissolved oxygen can be readily calculated using Henry's law (Eaton and Mary 2005, see appendix A). To calculate the oxygen diffusion coefficient, the porosity of concrete for a given w/c ratio and hydration time is calculated using the method proposed by Papadakis et al. (1991, see appendix A). Then oxygen diffusion coefficient is calculated using the porosity of cement paste and the relative humidity using Eq. (4.35). The effect of temperature on oxygen diffusion coefficient is considered using the activation energies proposed by Page and Lambert (1987, see appendix A). It should be noted that the activation energy of oxygen

diffusion coefficient is a function of w/c ratio (Page and Lambert 1987). Having calculated the value of resistivity and limiting current density, the corrosion current densities at a given temperature and cover thickness can be calculated using the developed model.

Figure 6.8 illustrates the variation of corrosion rate with relative humidity for different w/c ratios. According to this figure corrosion rate increases with w/c ratio; this is due to the increase of oxygen permeability and the decrease of concrete resistivity with increasing w/c ratio (i.e. decreasing concrete quality). However, the effect of w/c ratio is not the same at different values of relative humidity: Between 80 to 95% relative humidity, the corrosion rate increases more significantly with increasing w/c ratio, and for all other values of relative humidity, the effect of w/c ratio is nominal.

It should be noted that the corrosion rate in Figure 6.8 does not increase linearly with increasing w/c ratio. There is up to 100% difference in corrosion rate between w/c = 0.4 and w/c = 0.6; however, the difference between the w/c = 0.5 and w/c = 0.6 is significantly smaller. Hence it can be concluded that the effect of w/c ratio on corrosion rate is a function of the controlling mechanism of corrosion: When corrosion is under pure resistance control (i.e. relative humidity between 40 to 80 %) or under diffusion control (i.e. relative humidity larger than 95%), the effect of w/c ratio is insignificant; whereas when the corrosion is under mixed control (relative humidity between 80% to 95%) the effect of w/c ratio is significant.

The effect of temperature under the coupled influence of the considered variables can also be observed in Figure 6.8. As it can be seen in this figure from (a)

to (d), changing temperature has a considerable effect on corrosion rate for all w/c ratios. The maximum corrosion occurs at about 90-95% relative humidity (Lopez and Gonzalez 1993). For relative humidity larger than 95%, the corrosion rate decreases with increasing relative humidity since the process is controlled by the diffusion of oxygen. For relative humidity less than 70%, the system is under resistance control: with decreasing relative humidity, the corrosion rate decreases rapidly. Between 80% and 95% relative humidity, the system is under mixed control.

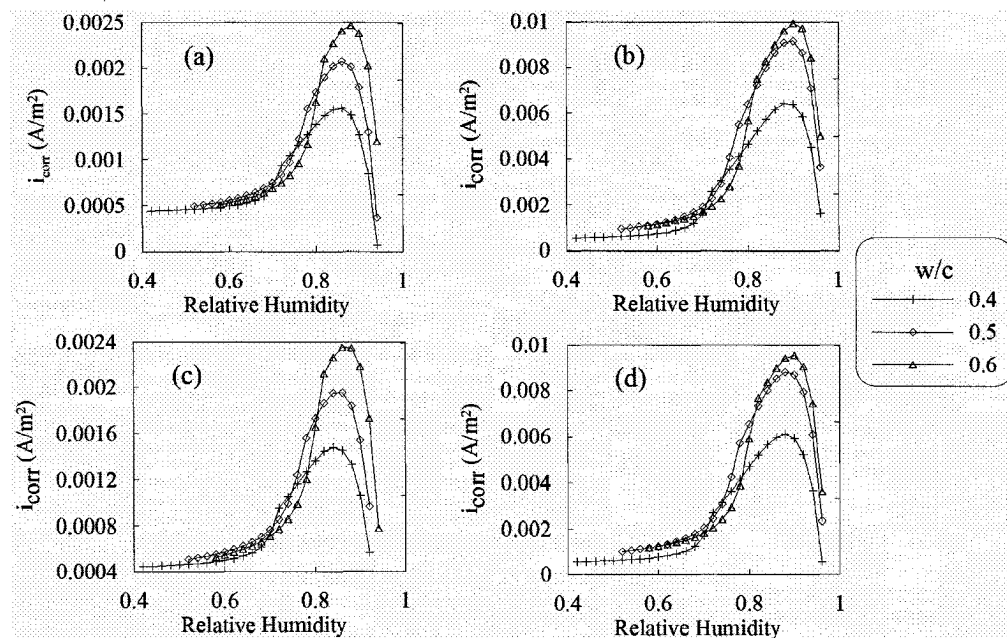


Figure 6.8: Variation of corrosion rate with relative humidity for different w/c ratios:

(a)  $T = 273^{\circ}\text{K}$ , (b)  $T = 298^{\circ}\text{K}$ , (c)  $T = 303^{\circ}\text{K}$ , (d)  $T = 323^{\circ}\text{K}$

In Chapter 5, the independent effect of cover thickness on corrosion rate was discussed, and it was demonstrated that corrosion rate showed an increase with increasing cover thickness. However, when the coupled effect of all parameters are considered, corrosion rate seems to be independent of the cover thickness for all

temperatures and w/c ratios, as illustrated in Figure 6.9. It was shown before that with increase of cover thickness the electric potential resulting from the electrochemical reaction is distributed better in the bulk of the concrete. On the other hand, this effect is compensated by the decreasing limiting current density due to increasing cover thickness. At the end, the two effects cancel each other.

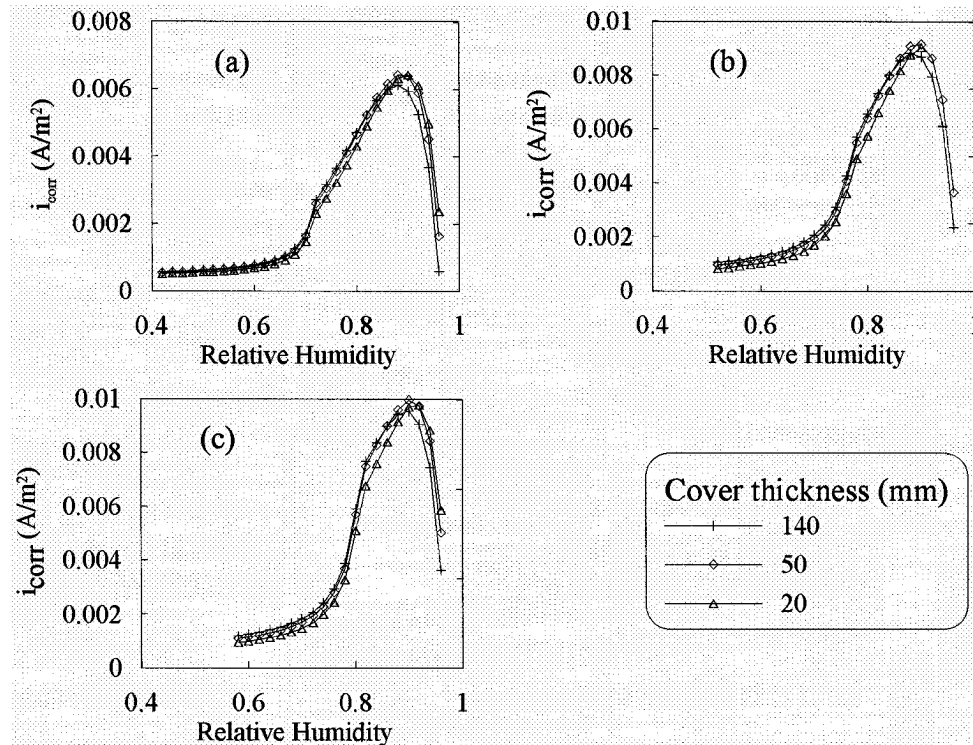


Figure 6.9: Variation of corrosion rate with cover thickness for different cover thickness: (a) w/c ratio = 0.4, (b) w/c ratio = 0.5, (c) w/c ratio = 0.6

## 6.5. Case Study: Comparison with existing models

The main purpose of this case study is to compare the corrosion rate of steel in concrete estimated using the model developed in this thesis with some of the existing models introduced in the literature. Six models from Chapter 2 are selected for this

purpose. Although a wide range for each parameter can be considered in constructing this hypothetical case, the parameters in this section are chosen to present a reinforced concrete structure encountered in usual civil engineering practices. The design parameters are summarized in Table 6.6, and Figure 6.10 represents the exposure conditions of the structure. Furthermore, it is assumed that uniform depassivation has occurred due to chloride contamination (2% by cement weight) after 2-year of exposure. The values of concrete resistivity, dissolved oxygen content and the oxygen diffusion coefficient are calculated based on the design parameters and exposure conditions using the same procedures described in the previous case study and are provided in Figure 6.11, Figure 6.12 and Figure 6.13, respectively.

Table 6.6: Concrete and structural design parameters

<b>Concrete Mix Proportions and Structural Parameters</b>	<b>Value</b>
w/c	0.5
a/c	3.0
Cement Type	OPC I
Cement Content	400 kg/m <sup>3</sup>
Air Content	3%
Cover Thickness (average)	45 mm
Rebar Diameter (average)	20 mm

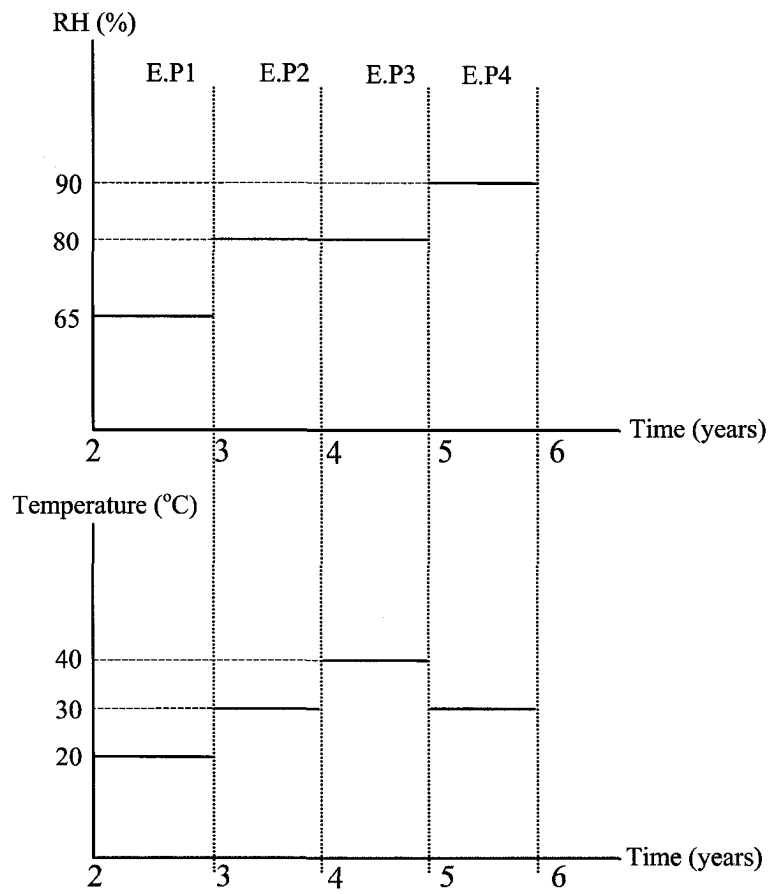


Figure 6.10: Exposure condition for the hypothetical case (“E.P” stands for “Exposure Period”)

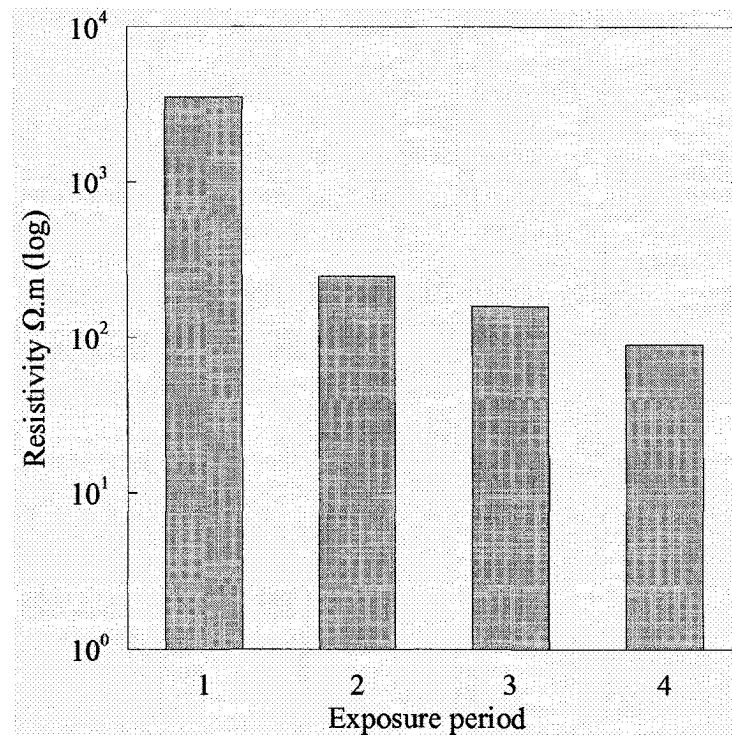


Figure 6.11: Concrete resistivity corresponding to each exposure period

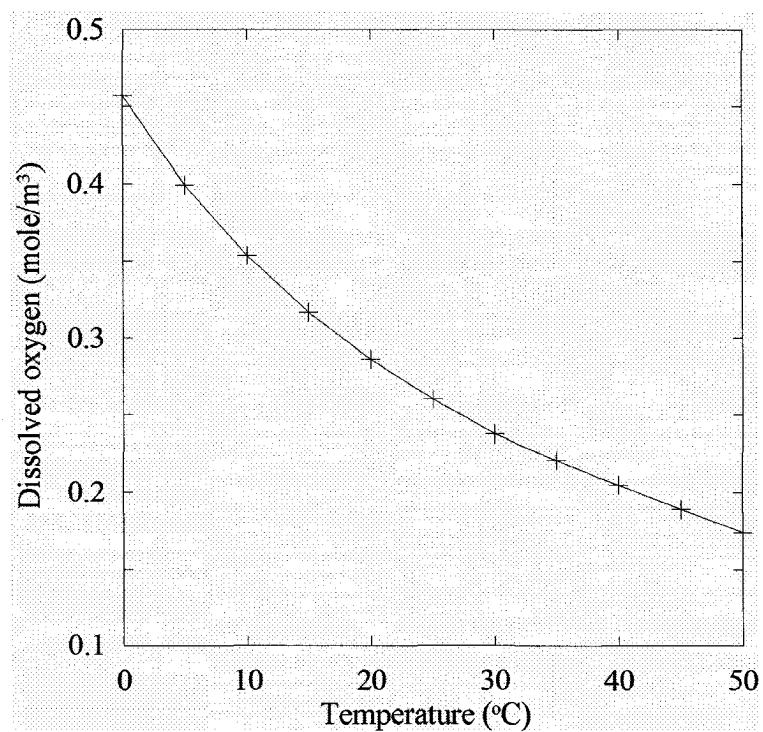


Figure 6.12: Amount of dissolved oxygen in water as a function of temperature

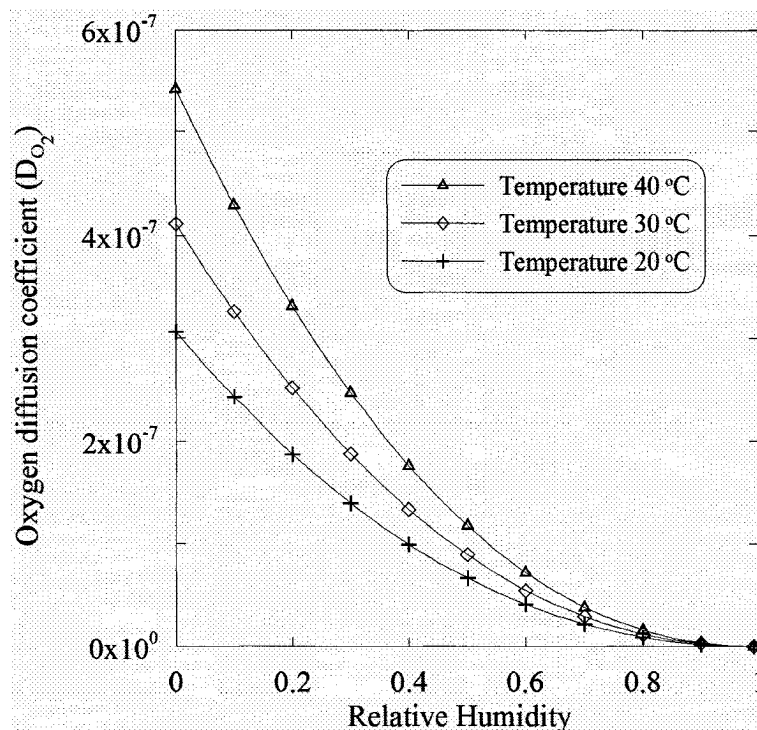


Figure 6.13: Variation of oxygen diffusion coefficient with relative humidity

Table 6.7 summarises the models used for estimating the corrosion rate, their required input values and the equations numbers presenting these models. Figure 6.14 represents the corrosion rate for the hypothetical case using all the models.

It can be observed from this figure that the model proposed by Alonso et al. (1988) overestimates the corrosion rate in all exposure periods compared to other models. Two major reasons contribute to this overestimation: (1) this model only considers the concrete resistance; (2) this model is developed for carbonation-induced corrosion but is applied to chloride-induced corrosion here. Carbonation of concrete tends to increase the concrete resistivity, whereas, chloride contamination of concrete reduces it.

The model proposed by Alonso et al. (1988) implicitly considers the effects of temperature and relative humidity through concrete resistivity. The implicit consideration of relative humidity and temperature causes the model to show increasing trend for corrosion rate with increase of relative humidity and temperature. Also, this model ignores the diffusion control mechanism which is the dominant controlling mechanism in high values of relative humidity. Since this mechanism is ignored corrosion rate does not decrease at high values of relative humidity, as illustrated in Figure 6.14.

Table 6.7: Models used for estimating the corrosion rate and their input parameters

<b>Model</b>	<b>Equation</b>	<b>Input parameters</b>
Alonso et al. (1988)	(2.1)	concrete resistance chloride content,
Liu and Weyers (1998)	(2.4)	temperature, concrete resistance, age of exposure
Ahmad and Bhattachajee (2000)	(2.6)	w/c, chloride content, cement content
Morinaga (1990) Design Parameters Model	(2.10)	chloride content, w/c, rebar diameter, cover thickness
Morinaga (1990) Environmental Parameters Model	(2.11)	temperature, RH, oxygen concentration, chloride content
Gulikers (2005)	(2.21)	concrete resistivity concrete resistivity, cover
Proposed Model	(6.10)	thickness, temperature, limiting current density

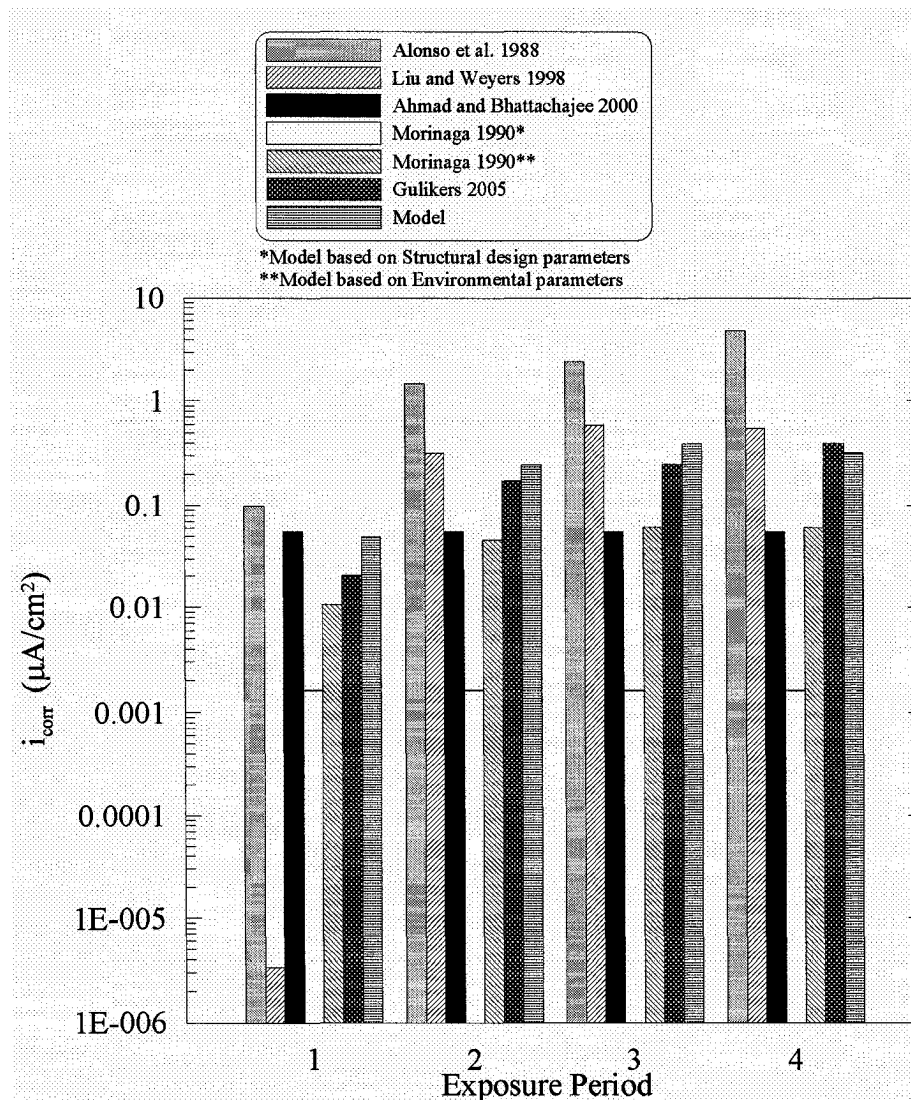


Figure 6.14: Comparison of the corrosion rate obtained by different models

The model proposed by Liu and Weyers (1998) considers the effect of temperature explicitly and captures the variation of corrosion rate with temperature through the exposure periods. This model, similar to the model proposed by Alonso et al. (1988), considers the effect of relative humidity implicitly through the concrete resistance. Both models are empirical, however, the model proposed by Liu and

Weyers (1988) is developed for chloride-induced corrosion. As a result, the Liu and Weyers' model shows smaller values for all exposure periods than Alonso's model. Since the model proposed by Liu and Weyers (1998) is developed specifically for chloride-induced corrosion, it is reasonable to expect more accurate results from this model compared to the model proposed by Alonso et al. (1988).

The model developed by Ahmad and Bhattachajee (2000) estimates a constant corrosion rate for all exposure periods. This is due to the fact that the model requires constant values of all input parameters (i.e. w/c, chloride content and cement content). Moreover, this model underestimates the corrosion rate compared to the two previously mentioned models.

Morinaga (1990) has introduced two separate models for estimating the corrosion rate of rebar due to chloride contamination: the first model considering the effect of design parameters and the second model considering the effect of environmental parameters. The corrosion rates of rebar using both models are presented in Figure 6.14. The model that is based on design parameters predicts very small corrosion rates for all exposure periods; in fact, the corrosion rate obtained using this model gives corrosion rates that are smaller than passive current density. This small corrosion current density is constant for all exposure periods since the design parameters are constant. The model that is based on the environmental parameters predicts higher corrosion rates compared to the model that is based on design parameters and shows rates very close to the model proposed by Ahmad and Bhattachajee (2000). In contrast to Ahmad and Bhattachajee's model, the model proposed by Morinaga (1990) that is based on environmental parameters shows a

little variation during the exposure periods due to temperature and relative humidity changes. The results of both models proposed by Morinaga (1990) are smaller than the results of the model proposed by Alonso et al. (1988) and the model proposed by Liu and Weyers (1998).

The model proposed by Gulikers (2005), although very similar to the model proposed by Alonso et al. (1988), gives substantially smaller results compared to the latter model. The results of this model are also smaller than the results of the model proposed by Liu and Weyers (1998). In the model proposed by Gulikers (2005) the effect of relative humidity and temperature are implicitly considered through the resistivity of concrete, and similar to the model proposed by Alonso et al. (1988) with increase of relative humidity and temperature the corrosion rate increases due to decrease of concrete resistivity.

As shown in Figure 6.14, the corrosion rate estimated using the model developed in this thesis is between the models proposed by Liu and Weyers (1998) and Gulikers (2005). According to the observed variation of the corrosion rate for all the six models, the developed model captures variation of corrosion rate with relative humidity and temperature accurately, and follows the same trend as the model proposed by Liu and Weyers (1998). All other models, except Liu and Weyers (1998), fail to predict the expected trend for the variation of corrosion with the exposure conditions. It should be emphasized that the model proposed in this thesis is based on the theory of corrosion, but all other models compared in this case study are empirical or semi-empirical (e.g. Gulikers' model).

## 6.6. Corrosion rate monitoring

As discussed previously, corrosion rate monitoring is one of the major applications of the developed model. Since this application has practical importance, a computer program is developed to assist engineers with corrosion rate monitoring in different scenarios. Figure 6.15 illustrates the interface of the program. The input parameters of the developed model (i.e. temperature, resistivity, limiting current density and cover thickness) can be provided to the program in different ways. For example, temperature can be assumed constant, or a temperature profile can be provided using an Excel file (see Figure 6.16). The temperature and relative humidity profile windows are illustrated in Figure 6.17 and Figure 6.18, respectively. It should be noted that the program can also estimate the resistivity using the method described previously based on the average relative humidity data provided to the program. The relative humidity for each month can be entered separately for day and night or can be considered equal for both. The limiting current density can also be input or estimated by the program. This calculation is done through the oxygen diffusion coefficient, which can be predicted using provided temperature and relative humidity profiles.

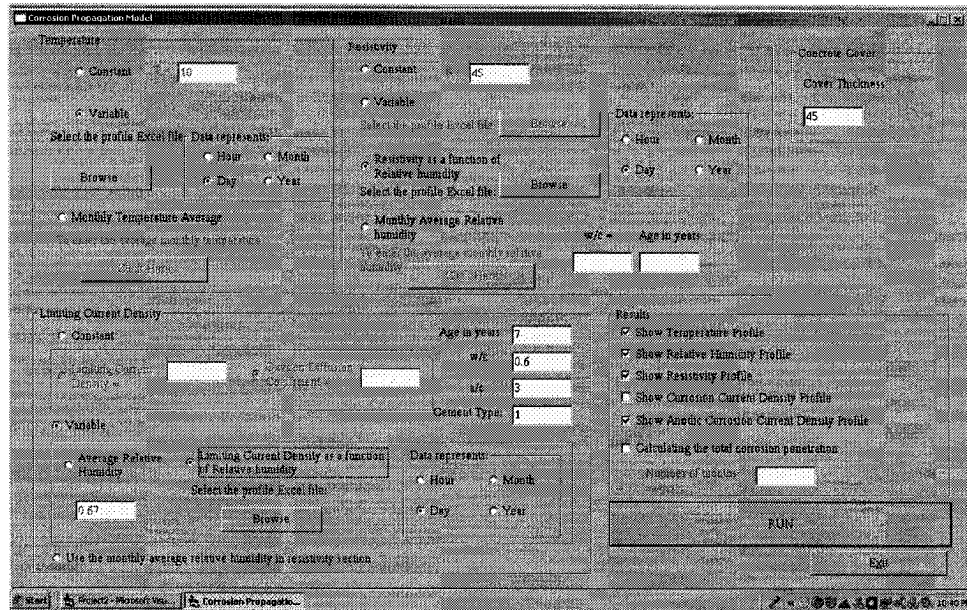


Figure 6.15: User interface of the developed computer program

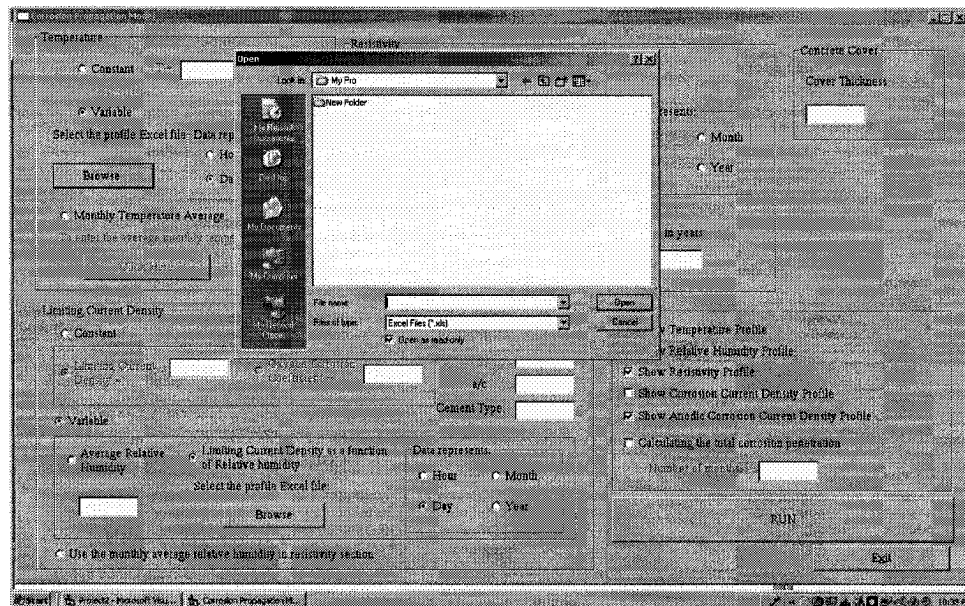


Figure 6.16: Excel data input window

**Average Temperature Values**

Please enter the average values of temperature for day and night

	Day	Night		Day	Night
January	2	0	July		
February	1	0	August		
March	3	2	September		
April			October		
May			November		
June			December		

Consider the same value as day for night

OK Cancel

Figure 6.17: Temperature profile window

**Average Relative Humidity Values**

Please enter the average values of Relative Humidity for day and night

	Day	Night		Day	Night
January			July		
February			August		
March			September		
April			October		
May			November		
June			December		

Consider the same value as day for night

OK Cancel

Select the profile Excel file:

Day  Year

Use the monthly average relative humidity in resistivity section

Figure 6.18: Relative humidity profile window

## **7. Quantitative Interpretation of Half-Cell Potential Tests**

---

### **7.1. General**

In this chapter, using the data obtained from the virtual experiments carried out in this study, the half-cell potential testing method is numerically investigated, and the effect of concrete cover thickness, concrete resistivity, limiting current density, and A/C ratio on the half-cell potential measurements are studied. A model relating the half-cell potential method to kinetics of the corrosion is developed, and the interpretation of the results of the model is discussed. It is demonstrated that with the new approach the half-cell potential mapping results can be used to obtain more useful information (with respect to the rate and the type of corrosion) than the probability of corrosion in a reinforced concrete member.

## 7.2. Half-cell potential mapping

One of the most widely used, practical, and standardized non-destructive method for monitoring steel corrosion in concrete structures is half-cell potential mapping (ASTM C876-91, RILEM TC 154-EMC). In this method, the potential difference between an external electrode located at the surface of concrete and the embedded reinforcement is measured with a high impedance voltmeter. A solid electrical connection between the reinforcement and the voltmeter, and a wet connection between the external electrode and the reinforcement through the concrete cover are essential for obtaining reliable readings. Figure 7.1 schematically illustrates the test setup for a typical half-cell potential test in reinforced concrete structures.

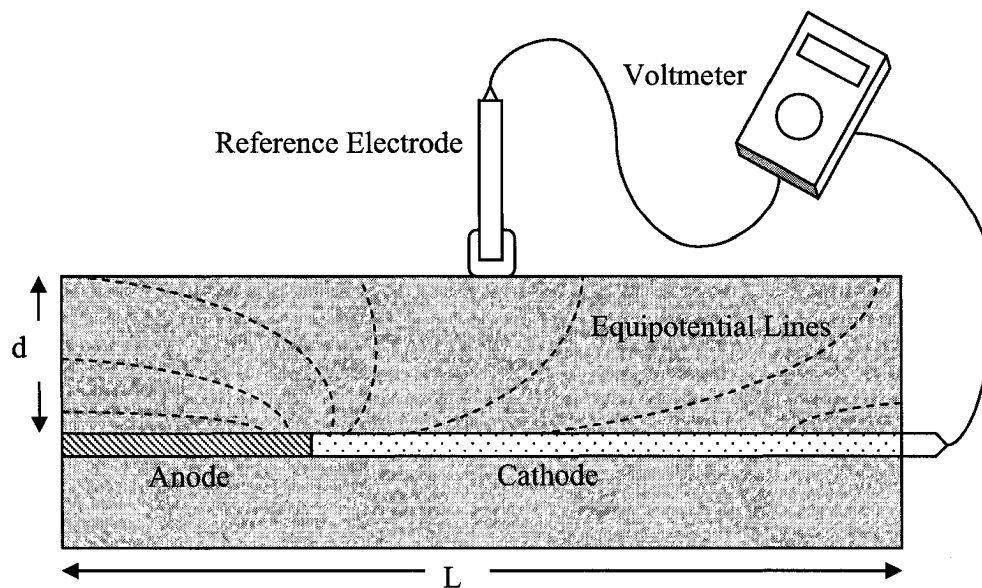


Figure 7.1: Schematic illustration of the half cell potential measurement set up that is simulated in the present study

Despite its widespread application, half-cell potential mapping is usually associated with a number of practical difficulties which can be summarized as follows (Berkeley and Pathmanaban 1990): (1) Establishing a solid connection to the reinforcement, particularly in the case of densely reinforced members, such as bridge decks, can be a difficult task; (2) Establishing a proper wet connection between the external electrode and the reinforcement through the concrete cover can be problematic since a moisture (hence, resistivity) gradient always exists in the bulk of concrete, affecting the half-cell measurements; (3) The time required to establish an equilibrium condition between the external electrode and concrete is a function of a number of parameters including the thickness and the composition of the concrete cover (RILEM TC 154-EMC). It should also be noted that half-cell potential measurement is also a function of the type of corrosion process. In the case of uniform corrosion, the potential readings at the surface of concrete are generally close to the potential at the interface of steel and concrete (Sagues and Kranc 1992); however, in the case of non-uniform corrosion the measured potentials at the surface of concrete can be substantially different from those of the steel/concrete interface. This potential difference is generally known as IR drop, and it is a function of cover thickness and concrete resistivity, and increases with both (Uhlig and Revie 1985). Several methods for IR drop compensation are available in the literature (Uhlig and Revie 1985, Jones 1996); however, majority of these methods are not applicable for eliminating the IR drop associated with half-cell potential measurements of non-uniform corrosion of steel reinforcement.

Although some of these practical difficulties can be minimized with the aid of experienced staff and accurate instrumentation, the interpretation of the half-cell potential mapping results remains to be a major challenge for engineers. Concrete resistivity, oxygen availability, A/C ratio and cover thickness are some of the factors that can influence the test (Bohni 2005, Elsener 2002, Bertolini et al. 2004); therefore, the results of the tests should be interpreted considering these factors. Furthermore, half-cell potential mapping only provides information to predict the probability of corrosion occurrence, and it does not give any insight to the rate (or kinetics) of corrosion (ASTM C876-91, RILEM TC 154-EMC). Potential ranges indicating the corrosion state of steel in concrete, established by the existing standards (e.g. ASTM and RILEM), have been subject to debate since they have been set based on limited number of experimental studies (Bertolini et al. 2004). The following is the probability of corrosion that is based on the measured half-cell potential readings (with respect to Cu/Cu(SO)<sub>4</sub> electrode, i.e. CSE) as per ASTM C876-91:

Half-cell potential > - 200 mV: less than 10% probability of corrosion

Half-cell potential = -200 mV > E > -350 mV: uncertain

Half-cell potential < -350 mV: greater than 90% of probability of corrosion

In addition to these shortcomings of the half-cell method, it should also be added that this technique does not provide any information about the type of corrosion (i.e. uniform or pitting). Having information about the type of corrosion in some cases is more important than knowing the probability of corrosion: A less probable pitting corrosion can propagate 8 times faster than highly probably uniform corrosion (Gonzalez et al. 1995).

To the knowledge of the author, no quantitative relationship has been introduced in the literature among the results of half-cell potential mapping, the factors affecting the corrosion kinetics, and the corrosion rate of steel in concrete. The main objective of this chapter is to develop such an approach (using the same data obtained from the virtual experiments conducted in this study) which quantitatively relates the potential readings on the surface of the concrete to the rate of reinforcement corrosion through concrete resistivity, cover thickness and oxygen availability, allowing the engineers to gain more information from the half-cell tests. The developed approach will be verified with available experimental data from the literature so that the level of accuracy of the method is assessed with respect to more commonly used corrosion rate measurement techniques, such as galvanostatic pulse technique, that are based on polarization resistance. The following section describes in detail the approach that was used to develop the quantitative relationship between the results of half-cell potential mapping and corrosion rate of steel in concrete.

### **7.3. Potential mapping through numerical modelling**

Using the numerical approach described in Chapter 3, the distribution of the potentials in the bulk of the concrete can be obtained. For example, Figure 5.1 illustrates the potential distribution in the bulk of the concrete for four different A/C ratios. The effect of influential parameters such as resistivity, cover thickness, oxygen availability, and A/C on the potential distribution and corrosion rates can be studied by examining the potential distribution along the interface of steel/concrete and on the surface of concrete. It should also be noted that half-cell tests measure the potential on the surface of the concrete; therefore, it is important to correlate the surface

potentials to the corrosion rates. In the following sections the numerical investigation on the effects of concrete resistivity, cover thickness, oxygen availability and A/C ratio on the potential mapping and corrosion rates in a simulated half-cell test are presented.

#### **7.4. The effect of concrete resistivity**

It is well known that concrete resistivity affects the corrosion rate of steel reinforcement (Alonso et al. 1988, Gulikers 2005, Ghods et al. 2007). With respect to half-cell potential tests, as the resistivity of concrete increases, the detection of corrosion becomes harder. This is due to the fact that in high resistivity concrete only a small portion of cathodic area is polarized, whereas, in low resistivity concrete larger portion of cathodic area is polarized (driving the potentials to more negative values), making the detection of corrosion easier (Elsener 2002). In this chapter, the effect of concrete resistivity on the potential mapping and corrosion rates in a simulated half-cell test was investigated by varying concrete resistivity, cover thickness and limiting current density in the range discussed in Chapter 4.

Figure 7.2 illustrates the effect of concrete resistivity on the potential distribution at the interface of steel/concrete and on the surface of concrete when A/C = 1. As it can be seen in the plots shown in Figure 7.2, the increase of resistivity shifts the potential of the anodic sites to more negative values and the potential of cathodic sites to more positive values. In low resistivity concrete, as illustrated in Figure 7.2-(a), the potential distribution along the surface of the concrete closely represents the potential distribution at the interface of steel/concrete. As the resistivity of concrete increases, as shown in Figure 7.2-(b) and Figure 7.2-(c), the potential distribution at

concrete surface tends to part noticeably from that of the steel/concrete interface. This difference is more significant at sections close to the transition zone between the anode and the cathode. This potential difference is due to the IR drop effect that was mentioned previously. IR drop increases logarithmically with increasing resistivity, as illustrated in Figure 7.3. The extrapolation of the fitted line for very low resistivity values in Figure 7.3 suggests that IR drop can not be eliminated completely. This observation is in line with electrochemical experiments (Uhlig and Revie 1985).

Figure 7.4 illustrates the potential distribution on the surface of the concrete to demonstrate that the shift in potential distribution curves with increasing concrete resistivity is not the same for anodic and cathodic surfaces: increase in resistivity affects the cathodic sites more than the anodic sites. At significantly high resistivities, the change in resistivity does not affect the potential distribution of the anodic sites, however, the cathodic potentials continue increasing to more positive values, signifying smaller cathodic polarization. This observation is in line with deductions and observations from polarization behaviour of corroding steel (Uhlig and Revie 1985, Elsener 2002). When resistivity is not significantly large, the cathodic section of the passive steel is polarized by anodic sites to more negative values; therefore, more negative potentials measured by half-cell potential mapping can be indicative of higher probability of corrosion (RILEM TC 154-EMC). It should be noted that Figure 7.4 also suggests that with increasing resistivity, the potential difference between the anodic and cathodic sites increases. Thermodynamically, the tendency to corrode increases with larger potential difference; however, the corrosion rate is inversely related to concrete resistivity by Ohm's law. This implies that while carrying out half-

cell measurements, potential readings should be interpreted in accordance with the resistivity of the system; otherwise, the results can be misleading.

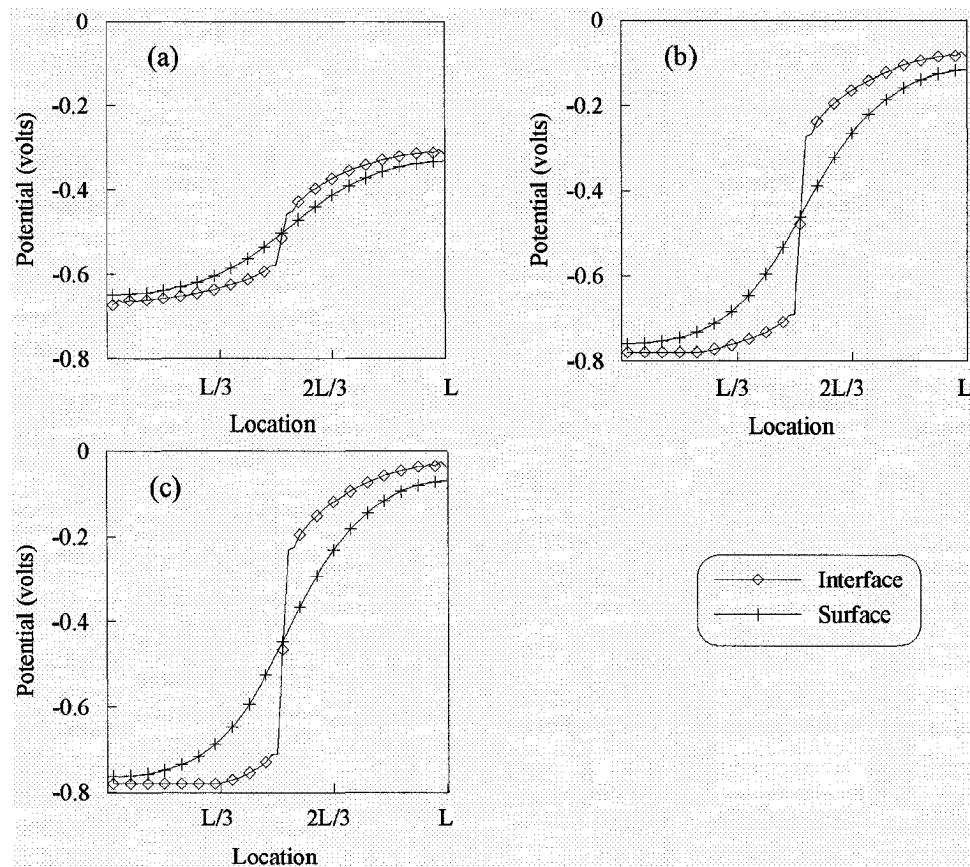


Figure 7.2: Potential distribution at the surface of steel and concrete: (a)  $\rho = 50 \Omega \cdot \text{m}$ ,  
(b)  $\rho = 5000 \Omega \cdot \text{m}$ , (c)  $\rho = 10000 \Omega \cdot \text{m}$

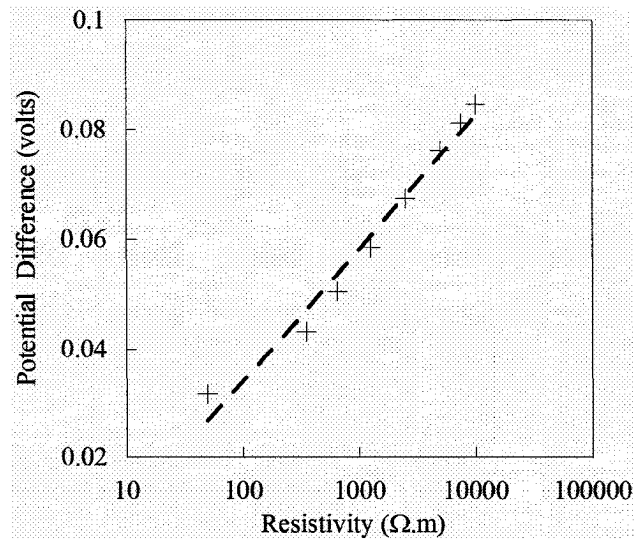


Figure 7.3: Dependence of internal IR drop to resistivity

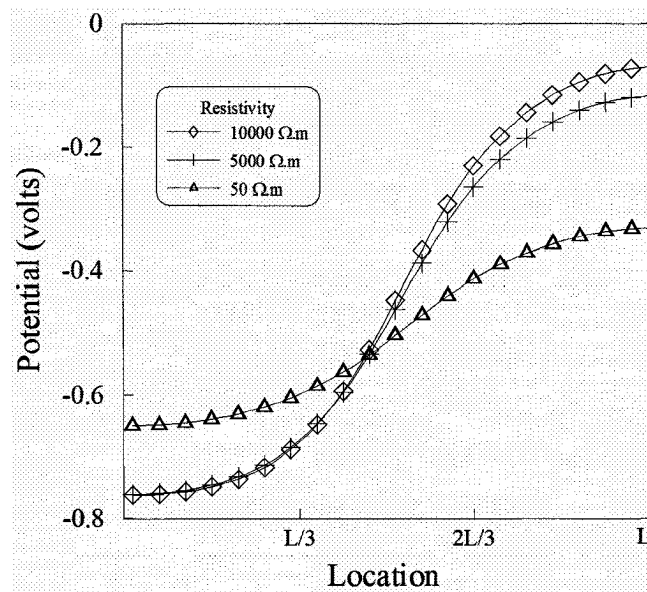


Figure 7.4: Potential distribution at the surface of concrete for different values of concrete resistivity

These observations indicate high dependency of potential mapping to the resistivity of concrete, which is influenced by relative humidity. For the same corrosion rate, one can measure different potentials at the surface of concrete, corresponding to different resistivities, and thus have more than one probability for the same state of corrosion. Based on these observations, author suggest that a potential mapping should be interpreted in the presence of resistivity and humidity mapping.

### **7.5. The effect of cover thickness**

Figure 7.5 illustrates the potential at the interface of steel/concrete for different cover thicknesses. Cover thickness mainly manifests its effect on the distribution of potentials at the surface of concrete, as illustrated in Figure 7.6. If the cover thickness is small (e.g. 20 mm) as shown in Figure 7.6-(a), the potential distribution on the surface of concrete is almost the same as potential distribution at the interface of steel/concrete. However, such a small cover thickness is not practical, and usually thicker covers are used in practice. As cover thickness increases, the potential of the surface differs from that of interface significantly, as illustrated in Figure 7.6-(b) to Figure 7.6-(d). When cover thickness reaches to values larger than 100 mm, the potential of the surface does not reveal accurate information about the potential distribution at the steel/concrete interface. It is interesting to note that (RILEM TC 154-EMC) has also made this observation by stating that “the potential difference between the position above the anode and a distant cathode becomes smaller with increasing cover depth.” Figure 7.6 also suggests that the increase of cover thickness increases the IR drop considerably, and the potential values measured

over active and passive areas become more similar, as also observed by Elsener (2002). The effect of cover thickness on the IR-drop is illustrated in Figure 7.7, and IR-drop increases linearly with increase of cover thickness. Thus, in half-cell potential measurements, one should consider the effect of cover thickness on the potential distribution.

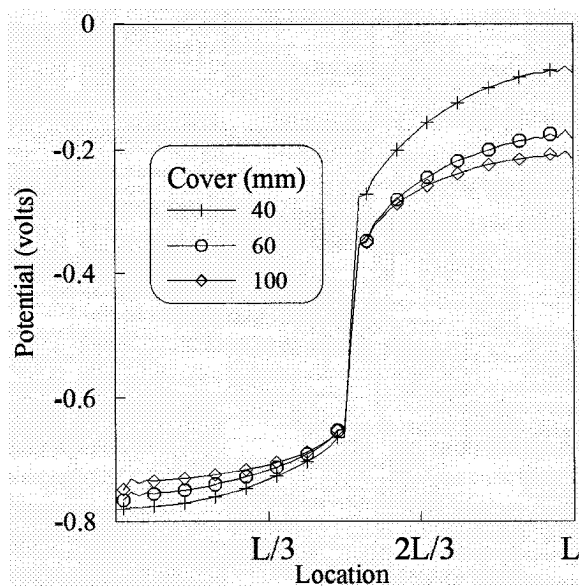


Figure 7.5: Distribution of potential and corrosion current density at the steel/concrete interface ( $A/C=1$ ).

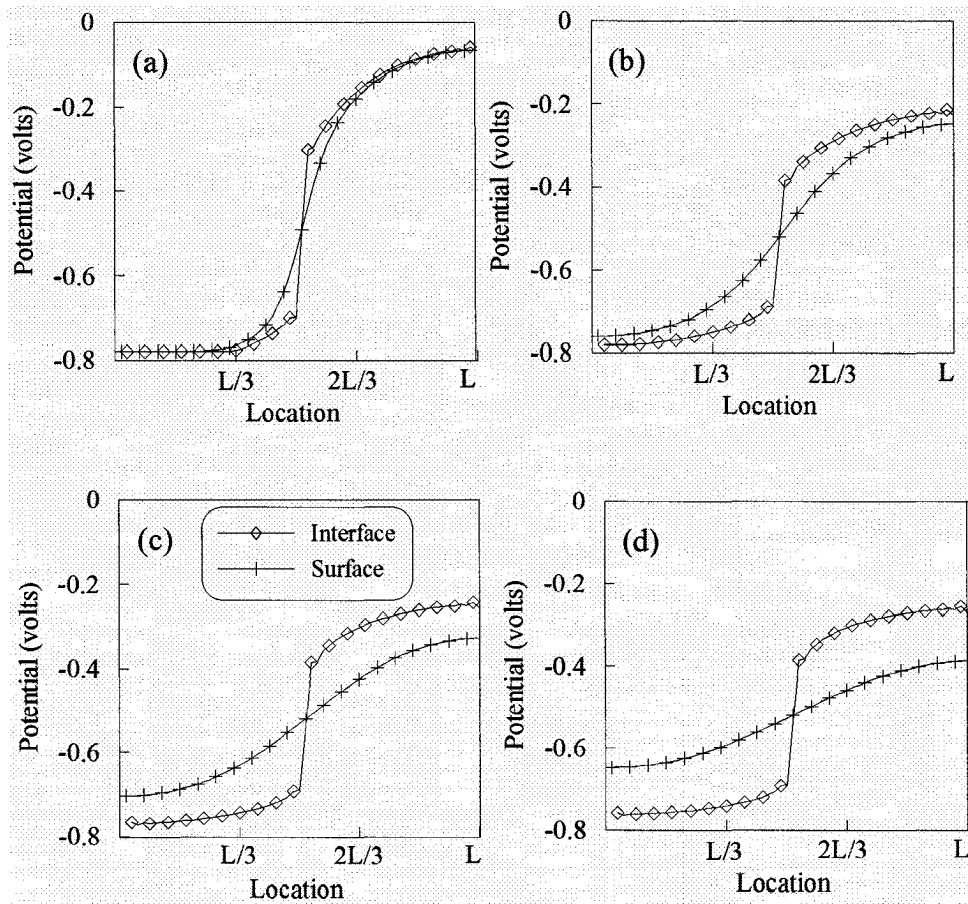


Figure 7.6: Potential distribution at the surface and steel/concrete interface: (a)

$d = 20$  mm, (b)  $d = 60$  mm, (c)  $d = 100$  mm, (d)  $d = 140$  mm

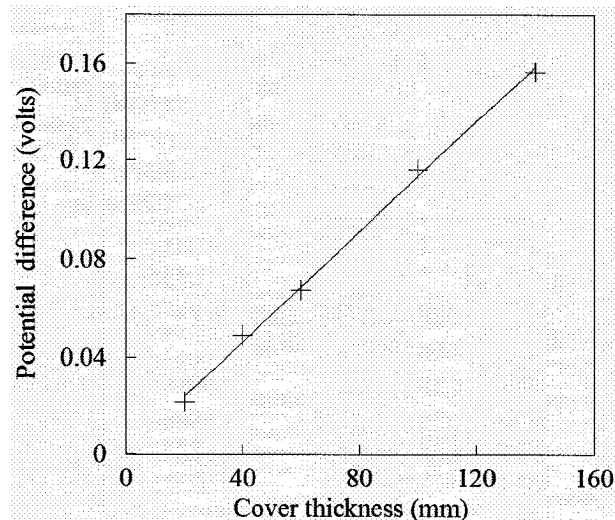


Figure 7.7: Dependence of IR-drop to cover thickness

## 7.6. The effect of oxygen availability

As discussed in Chapter 3, Stern-Geary polarization is used as boundary conditions at anodic and cathodic surfaces of steel. Cathodic polarization, given by Eq. (1.6), considers the effect of oxygen availability through limiting current density. Limiting current density is proportional to the dissolved oxygen at the surface of concrete and the oxygen diffusivity of concrete via Eq. (4.25).

Figure 7.8 illustrates three cases of oxygen availability to the rebar by considering corresponding limiting current densities of 0.002, 0.02 and 0.2 A/m<sup>2</sup>. As it can be observed in Figure 7.8, as oxygen availability increases, the potential of cathodic sites approaches to more positive values; however, with further increase of oxygen potential of these sites seem to remain unaffected. This is due to the fact that concentration polarization does not impose any effect on the polarization of the cathodic sites for large values of limiting current density. Potential distribution of the

anodic sites is not affected with oxygen availability, as expected. A number of experimental studies, on the other hand, suggest that during the periods of low oxygen availability, the overall potential approaches to more negative values; however, this occurs when oxygen is very low and corrosion tends to stop for a period of time or convert to active low potential corrosion (Page and Treadaway 1982). This type of corrosion generally does not obey the Stern-Geary equation and is not considered in the present work. The present model accurately predicts the effect of low oxygen availability on the half-cell potential mapping to the point that steel polarizes in accordance with Stern-Geary polarization equations.

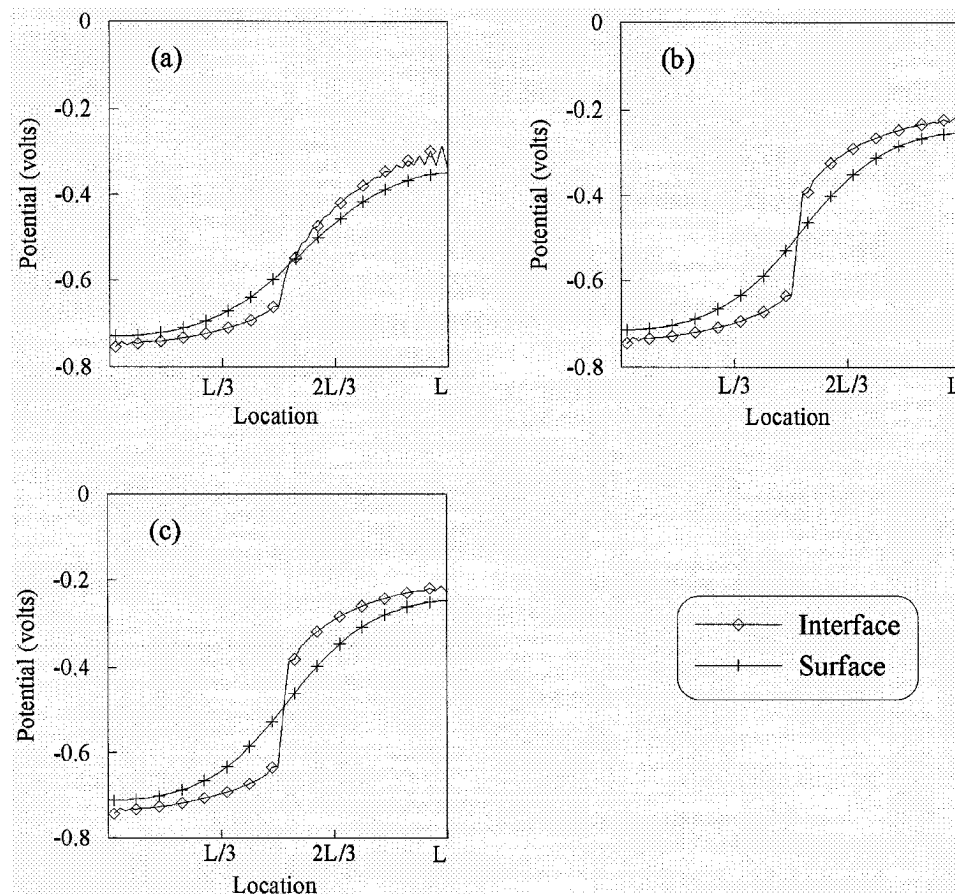


Figure 7.8: Potential distribution at the surface and steel/concrete interface: (a) Low oxygen, (b) Medium oxygen, (c) High oxygen

## 7.7. The effect of A/C

Figure 7.9 illustrates the potential distribution at the interface of steel/concrete for different values of A/C. As it can be observed from this figure, the potential for all A/C converge to the standard half-cell potential at distances away from the anode/cathode interface. This suggests that the corrosion rate slows down as the relative distance and resistance between the anodic and cathodic sites increases. Figure 7.10 illustrates the effect of A/C on the potential distribution on the surface of concrete and along the steel/concrete interface. For small values of A/C, the potential distribution of anodic sites at the surface of concrete is substantially different from that of the steel/concrete interface; however, for cathodic sites the difference between the potential at the surface and steel/concrete interface is much smaller. As the A/C gets larger, the potential difference between the surface and interface of anodic sites diminishes. This implies that accurate detection of pitting corrosion, in which A/C ratio can be small, may not be feasible with half-cell potential measurement method, as also confirmed by existing standards (ASTM C876-91) and (RILEM TC 154-EMC). The detection of pitting corrosion becomes even harder for thick concrete covers. These observations are in line with conclusions of Elsener (2002), who experimentally studied the potential distribution at different distances above anodic and cathodic sites of rebar in simulated concrete solutions with different resistivities. It can be concluded from these observations that the accuracy of potential mapping in detecting the corrosion is dependent on A/C.

Among all the mentioned parameters, A/C, although significant, can not be measured directly; however, since the potential of the surface of concrete is a function

of A/C, results of half-cell potential can be used to estimate the A/C which in turn can be used to relate the potential mapping to corrosion current. A relationship based on the effect of A/C on potential distribution is developed between the potential at the surface of concrete and the corrosion rate of steel in concrete, which will be presented in the following section.

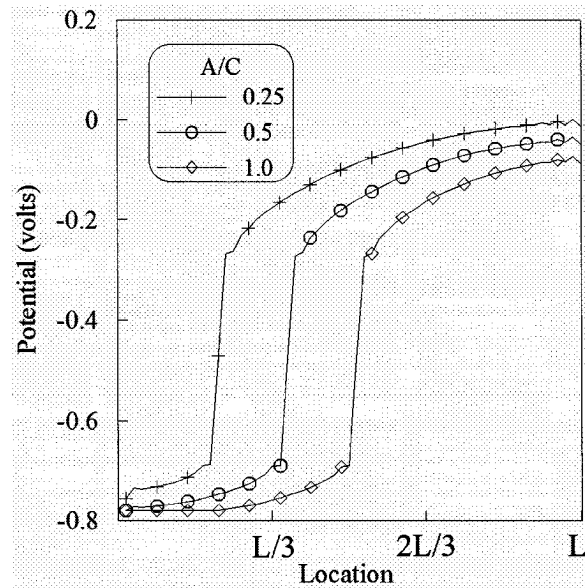


Figure 7.9: Distribution of potential at the steel/concrete interface

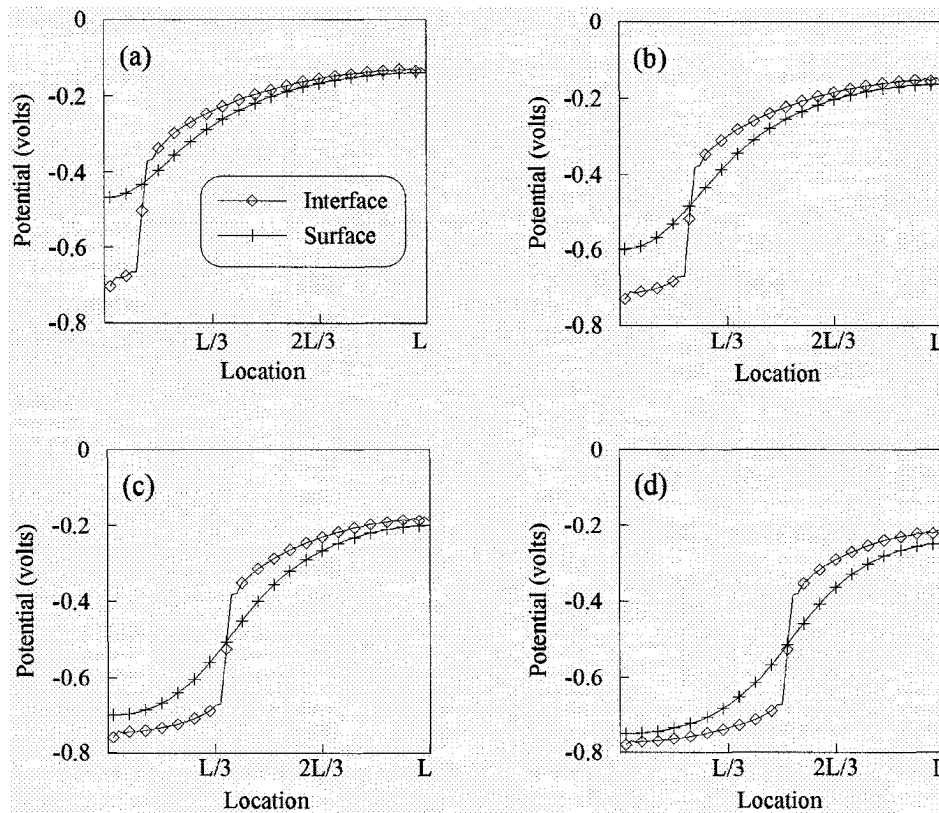


Figure 7.10: Potential distribution at the surface and interface of steel and concrete:

(a)  $A/C = 0.1$ , (b)  $A/C = 0.25$ , (c)  $A/C = 0.5$ , (d)  $A/C = 1.0$

## 7.8. Half-cell testing and corrosion rate

The model developed here relates the half-cell test results to steel corrosion rate in concrete is based on two hypotheses:

(1) From the plots in Figure 7.10, it can be observed that as  $A/C$  ratio gets smaller the average potential on the surface of concrete approaches to more positive values and when the  $A/C$  ratio increases the average potential on the surface of concrete tends to be more negative. Hence, it can be hypothesised that the average of the potentials on the concrete surface may be an indicator of the  $A/C$  ratio in a

corroding system. It should be emphasised that, the hypothesis refers to a corroding system.

(2) The potential difference between the anodic and cathodic sections of the steel reinforcement is in fact the driving force of the corrosion. This potential difference can not be measured directly in the field; however, an approximate value of this potential difference can be obtained by half-cell method since the potential distribution at the surface of concrete can be correlated with the potential distribution along the steel surface. As it can be observed in Figure 7.10, the correlation gets better as A/C ratio becomes larger.

If the potential difference between the anodic and cathodic sections of the reinforcement is known, Ohm's law can be applied to the corroding system:

$$\frac{\Delta\phi}{I_{corr}} = \tilde{R} \quad (7.1)$$

where  $\Delta\phi$  (volts) is the maximum potential difference at the surface of concrete,  $I_{corr}$  (A) is the corrosion current, and  $\tilde{R}$  ( $\Omega$ ) is the equivalent resistance of the system, which is a function of concrete resistivity and cover thickness since the travel path of ions in the bulk of concrete is affected by these two parameters. In addition,  $I_{corr}$  is a function of A/C ratio, which can be estimated using the average potential at the surface of concrete. Hence, we can write:

$$I_{corr}(\phi_{ave}) = \frac{\Delta\phi}{\tilde{R}(\rho, T, d)} \quad (7.2)$$

or

$$i_{corr,ave} = f(\Delta\phi, \phi_{ave}, \rho, T, d) \quad (7.3)$$

where  $\phi_{ave}$  (with respect to standard calomel electrode, i.e. SCE, volts) is the average potential on the surface of concrete. All parameters in Eq. (7.3) can be easily obtained in the field by simple half-cell potential measurements and resistivity measurements. If such a model can be developed, the results of the half-cell potential measurements can be related to the kinetics of the corrosion. By conducting a non-linear regression analysis on the data obtained by virtual experiments the following equation is obtained:

$$i_{corr} = \left( \frac{17.043 \times 10^3}{\phi_{ave}^2} \right) \left( -9.124 \times 10^{-8} d \right. \quad (7.4)$$

$$\left. + 1.718 \times 10^{-7} \frac{T}{\rho} + 1.576 \times 10^{-7} \Delta\phi \right)$$

$$- 2.043 \times 10^{-3}$$

where  $R^2$  of the equation is 0.90. It is noted that in developing Eq. (7.4) the limiting current density is not considered as a parameter since limiting current density does not influence the results of the half-cell potential measurement significantly as mentioned previously.

Figure 7.11 illustrates the variation of corrosion rate obtained from the model with average potential at the surface of concrete. According to this figure, increasing values of average potential (toward more positive values) the corrosion rate increases, and vice versa. However, ASTM C-876 suggests that the probability of corrosion decreases as the potential increases to more positive values. Although this observation may seem controversial, it should be noted that the results of the model presented here should be interpreted in terms of probability: when the average potential at the

surface of concrete is a large value (i.e. more positive) the probability of the corrosion is low as per ASTM C-876; however the rate of such a corrosion, if occurs, can be very high, and it will most likely proceed in the form of pitting corrosion. On the other hand, if the average potential at the surface of concrete is a small value (i.e. more negative), the probability of the corrosion is higher, but such corrosion will most likely proceed more uniformly. It should also be noted that there will be cases in which pitting corrosion can occur when average potential on the surface of concrete is negative and uniform corrosion can occur when average potential on the surface of concrete is positive.

To clarify this, Figure 7.12 illustrates all the possible A/C ratios in different ranges of potential. This figure shows that as the average potential decreases the probability of pitting corrosion decreases, and the corrosion tends to proceed in a more uniform manner. For example, according to Figure 7.12, in the potential range of -400 mV to -200 mV (S.C.E), the A/C ratio is always smaller than 0.3. However, if the average potential is close to -600 mV (S.C.E), the corrosion can proceed at all A/C ratios. It is noted that the model, Eq. (7.4), is constructed through the same data in Figure 7.12; hence, this model includes the effect of changes in A/C ratio with the average potential. The figure also illustrates why higher corrosion rates are more likely to be observed for more positive average potential readings.

The increase of corrosion rates with increasing average half-cell potential measurements may also seem to be in contrast with field observations: Higher corrosion rate measurements with the linear polarization technique are generally associated with more negative values of potential on the surface of concrete (Luping

2002). This observation can be attributed to the inherent error associated with corrosion rate measurements by linear polarization technique when the main corrosion mechanism is pitting. The linear polarization technique normalizes the measured corrosion rate over the polarized length of reinforcing steel, and in the case of pitting corrosion, since the corroding area (i.e. anode) is significantly smaller than the polarized length of the steel, these instruments underestimate the corrosion rate (Elsener 2002). In this scenario, most of the polarized area is cathodic (i.e. more positive); therefore, the potential on the surface of concrete can be observed to be more positive.

Having said this, it should also be mentioned that the instruments that are based on linear polarization technique may overestimate the corrosion rate in the case of uniform corrosion, in which the average potential on the surface of concrete is more negative. In this case, the anodic current produced by the counter electrode on the concrete surface flows mostly to the anodic area. This is due to the fact that the anodic current follows the path of lowest resistance (i.e. ohmic and polarization resistance), and since the polarization resistance of the anodic area is much smaller than that of cathodic area, the current flows to anodic surface even if the counter electrode is aligned with passive steel (Elsener 2002). This may generally result in the overestimation of corrosion current in the case of uniform corrosion. In most instruments a guard ring is used to minimize the overestimation due to this effect; however the functionality of the guard ring depends on the location of the counter electrode relative to the anodic area (Elsener 2002).

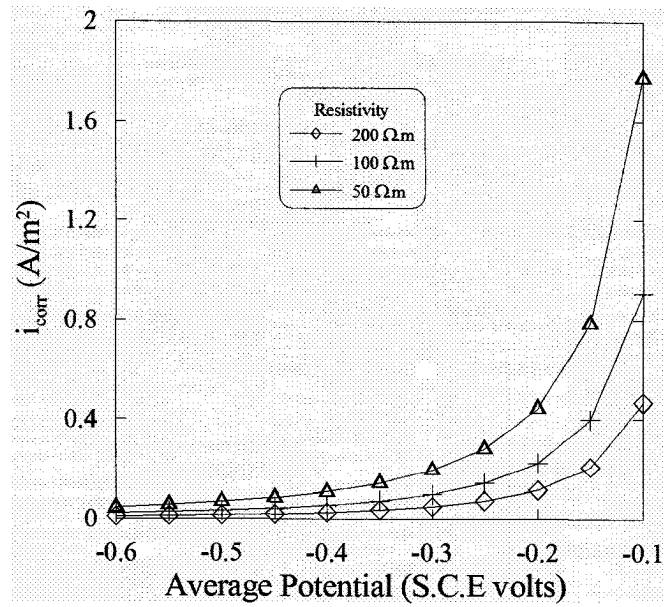


Figure 7.11: Variation of corrosion rate with average potential at the surface of concrete

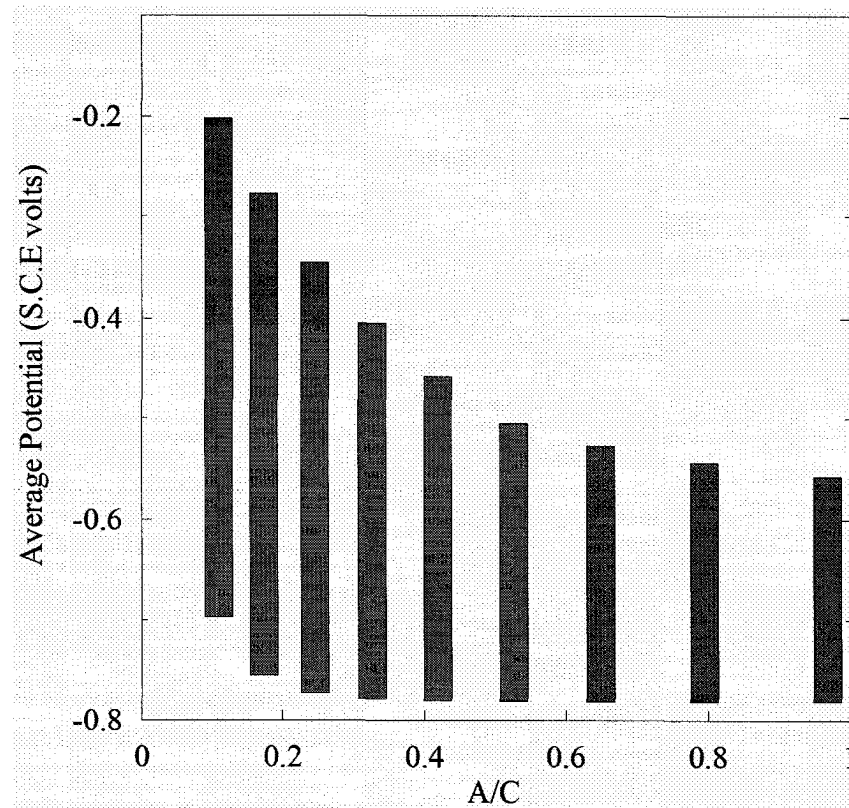


Figure 7.12: Possible A/C ratios for different ranges of average potential

## 7.9. Case study

To compare the predictions of the model (i.e. Eq. (7.4)) with experimental results, a study by Luping (2002) is chosen. In this study, galvanostatic pulse (GP1 and GP2) and linear polarization (LP1 and LP2) techniques are used to measure the corrosion rate of steel rebar embedded in concrete. For each of these techniques, two instruments produced by different companies were used (i.e. GP1, GP2, LP1 and LP2). In addition to the corrosion rate measurements, all instruments measure the concrete resistance and half-cell potentials. A short summary of the test setup and procedure used by Luping (2002) is presented in the following: Concrete slabs of size 250x250x70 mm with w/c ratio of 0.5 and four different chloride contents (0, 1.5, 3 and 6% in the form of NaCl by the weight of cement) were cast using Swedish SRPC (corresponding to CEM I 42.5R). Two steel rebars of 10 mm diameter were embedded in symmetric positions in the slabs (see Figure 7.13). The ends of each rebar were coated with cement grout to prevent crevice corrosion. Slabs were cured for 21 days in partially immersed condition, and then were subjected to 85% relative humidity (RH) up to 1 year. During this period, the electrochemical data were recorded using the four different instruments described above. At the ages of 4 and 13 weeks, the data collected from different instruments were compared. At four weeks (Comparison 1), LP2, GP1 and GP2 results were compared. At week 13 (Comparison 2), LP1, LP2 and GP2 results were taken.

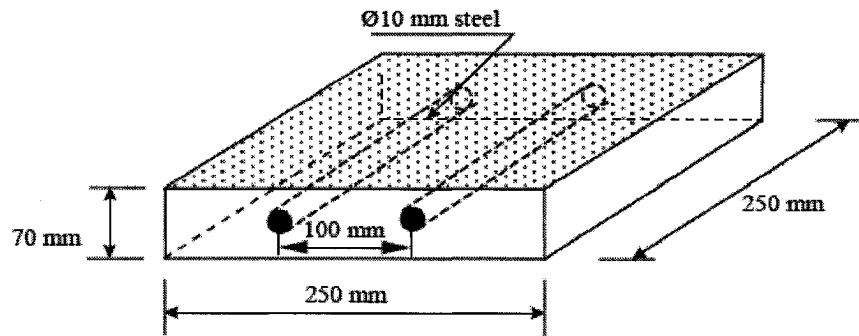


Figure 7.13: Illustration of the sample used by Luping (2002) (Taken from the original paper)

All the required data except for the maximum potential difference on the surface of concrete for comparing the model with the instruments are provided in the reference (Luping 2002). Due to lack of data, the value of the maximum potential difference,  $\Delta\phi$ , for the comparison presented here is neglected (i.e. the term in Eq.(7.4) containing  $\Delta\phi$  has been considered to be equal to zero). Furthermore, since three values of resistivity were reported for each instrument in the aforementioned reference, the average of the three values is used in the model.

Figure 7.14 illustrates the results of the first comparative test along with the predictions of the model. Since the scan rate of the instrument can affect the results of the corrosion measurement (Gonzalez et al. 1985, Gowers et al. 1994), this test parameter is noted in the figure for each instrument (e.g. 100  $\mu\text{A}/5\text{s}$  for GP1). A large scatter in the results of different instruments can be observed in Figure 7.14.

The prediction of the model is higher than all instruments at -485 mV (C.S.E) average potential. The reason for the underestimation of the polarization resistance

technique at larger potentials (i.e. more positive) as mentioned before is that these instruments normalize the measured corrosion rate over entire polarized length of the steel. However, the proposed model here considers the effect of A/C. By referring to Figure 7.12, the A/C corresponding to -485 mV (C.S.E.) which is -408 mV (S.C.E) is always smaller than 0.3. Hence, the instruments used in this study are underestimating the corrosion rate of steel in concrete significantly.

As the average potential at the surface of concrete approaches to more negative values, the prediction of the model is in more agreement with the instruments used in the experiments. As mentioned before, although linear polarization technique tends to overestimate the corrosion rate at more negative potentials, its behaviour is dependent on the relative location of external electrode with respect to anodic area (due to presence of guard ring). In the present experimental study, the instruments used in the first comparative test predict lower values compared to the model.

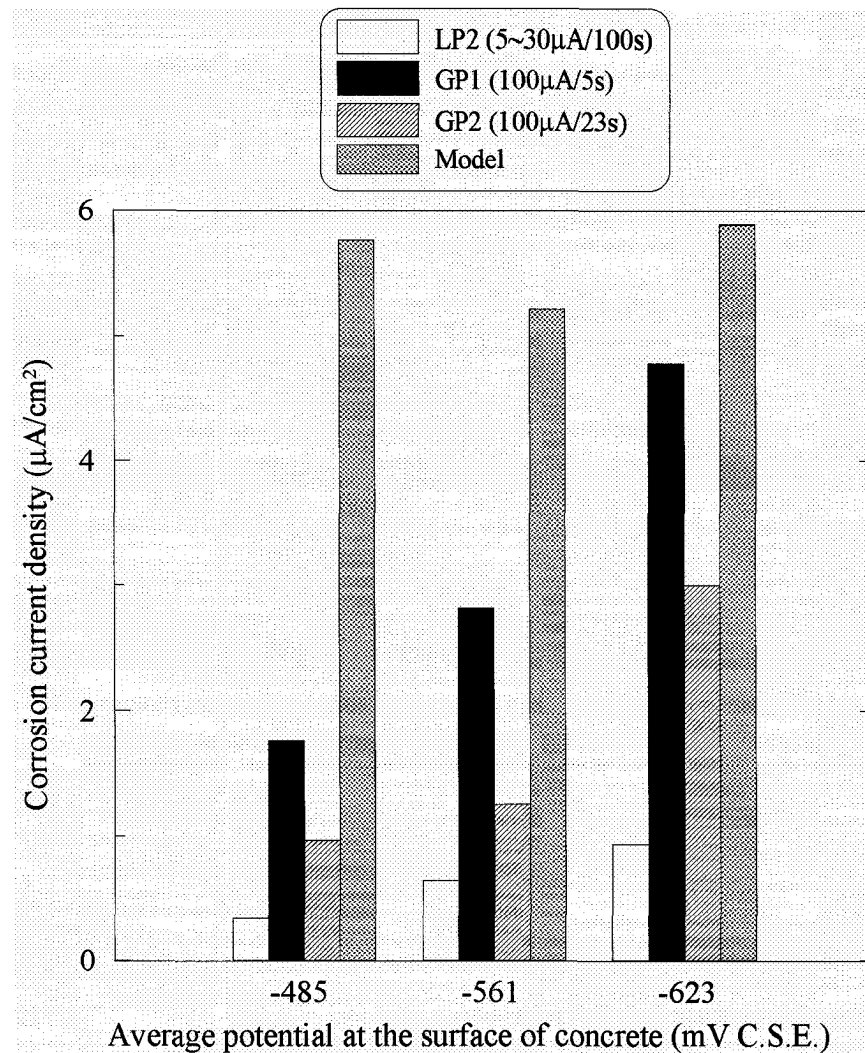


Figure 7.14: Results of the first comparative test (after 4 weeks)

In the second comparative test, two linear polarization instruments and one galvanostatic pulse instrument are used, and the results of the latter instrument is also extrapolated to a smaller scan rate (smaller scan rate i.e. 100µA/100s); this is done to decrease the difference in corrosion rate estimation between LP and GP instruments observed in first comparative test.

The results of the second comparative test are very similar to the first comparative test. All three instruments predict significantly lower values of corrosion rate when compared to the results of the model. In the case of -408 mV (C.S.E), the A/C corresponding to this potential (-331 mV S.C.E) according to Figure 7.12 is always smaller than 0.2. The instruments used in experimental study, however, do not consider the effect of A/C and hence underestimate the corrosion rate.

As the average potential approaches to more negative value the corrosion rate measured with different instruments get closer to the prediction of the model. This is in fact due to increase of area of anode as the potential moves toward more negative values which compensates for underestimation of the instruments since these instruments normalize the corrosion rate over the entire polarized length of steel.

It is noted that, as the average potential at the surface moves toward more negative values the corrosion rate estimated with model decreases. This is due to the fact the model takes the A/C effect into account, and the corrosion rate is in fact the corrosion rate of anodic area. The corrosion rate measured with the polarization resistance technique, however, is the corrosion rate over the entire anodic and cathodic area.

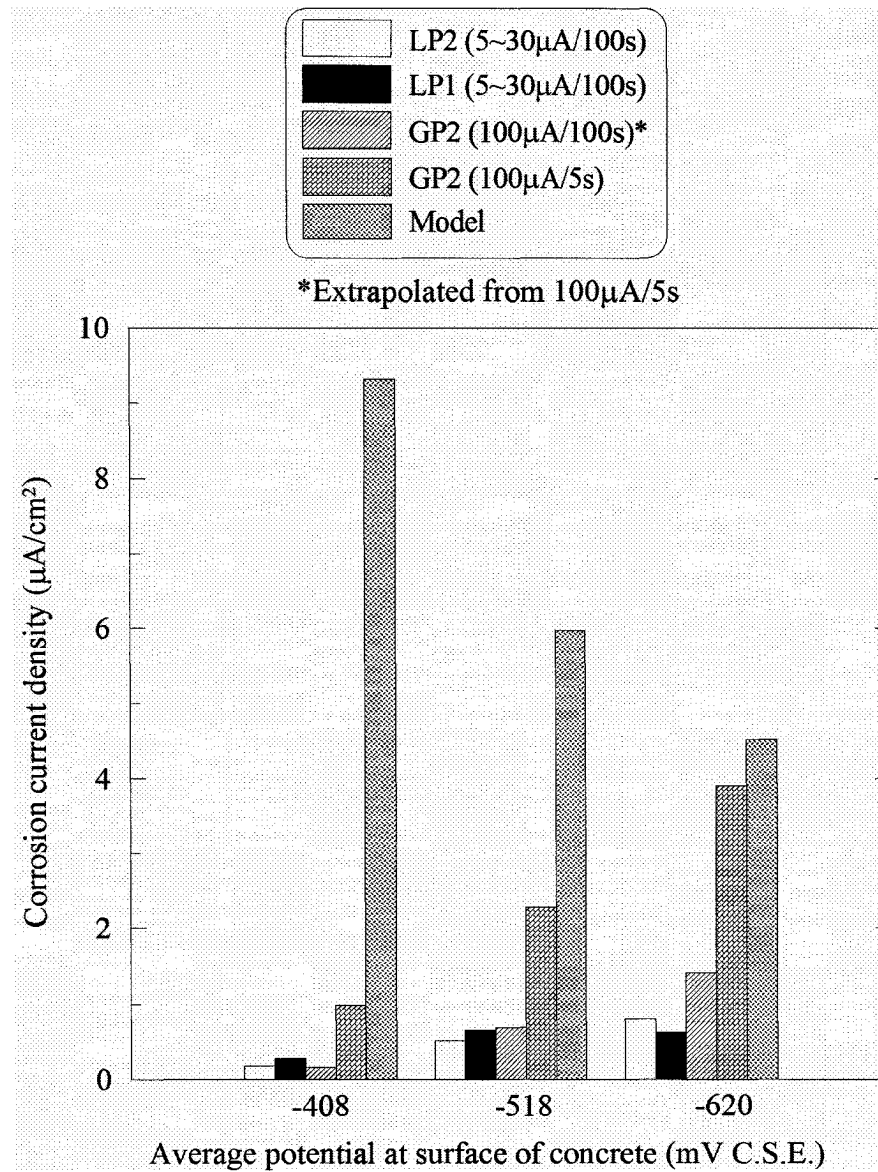


Figure 7.15: Results of the second comparative test (after 13 weeks)

## **8. Conclusions**

---

### **8.1. General**

Corrosion of reinforcing steel in concrete is a major cause of deterioration of reinforced concrete structures in the areas where exposure to de-icing salts and seawater is prominent. Therefore, predicting the corrosion rate of steel in concrete is significantly important in estimating the service life of structures. During the last decade, there has been a growing interest in developing mathematical models for predicting corrosion rate of steel in RC structures. One of the reasons of this interest is to overcome the experimental difficulties associated with the corrosion measurement techniques. However, the models that are based on the solution of the Laplace's equation are restricted to simple geometries due to the numerical difficulties associated with the nonlinear boundary conditions of the problem. The

models that are based on empirical studies do not cover all the factors that may affect the corrosion process.

In this thesis, a novel and practical model for predicting the corrosion rate of the steel reinforcement in concrete is introduced. This model is based on Stern-Geary equations and includes the effects of concrete properties and the environmental conditions on corrosion. The influence of temperature, cover depth, concrete resistivity and the limiting current density is incorporated in the model. In addition, the half-cell potential measurement technique is modelled numerically, and guidelines for quantitative and qualitative interpretation of the half-cell results are provided. The half-cell potential measurements are related to the kinetics of the corrosion process, and a separate model for predicting the corrosion of steel in concrete through half-cell data is developed. A comprehensive verification study demonstrated the strength and the applicability of the developed models in different scenarios.

The developed model can be used in three applications: (1) research, (2) monitoring, and (3) service-life prediction. As a research application, the model can be used to investigate the effects of different parameters such as relative humidity, w/c ratio, porosity, etc. on the corrosion of steel in concrete. As a monitoring application, the model can be used with input data provided by relatively simple and inexpensive in-situ measurements. For example, measuring concrete resistivity, cover thickness and temperature allows the model to be used efficiently with minimum amount of effort. The only parameter which cannot be measured directly is the limiting current density. However, this parameter can be calculated if the oxygen diffusion coefficient is known. The oxygen diffusion coefficient either can be

estimated or calculated using the existing models in the literature such as the one proposed by Papadakis et al. (1991). These predictive models require basic information about the structure such as w/c and a/c ratios and are easily programmable. A computer program for monitoring corrosion in reinforced concrete structures that is specifically developed around the model presented in this thesis has been developed; a screenshot of the program is provided in Figure 6.15.

The developed model can also be used for service life prediction of concrete structures. However, it should be noted that this model does not provide any information about the initiation stage of corrosion (i.e. chloride diffusion and depassivation) and only provides information about the propagation stage during which active corrosion takes place. The duration of initiation stage can be determined using specific models available (e.g. Isgor 2001). Having said this, the remaining service life of structures (after initiation of corrosion) can be estimated using the model introduced here. For using the model for service life predictions, the following information is required: (1) temperature variation of the environment, (2) relative humidity variation of the environment, (3) concrete properties (i.e. w/c ratio, a/c ratio, cement content, cement type). In the following section a list of conclusions of the research presented in this thesis is provided.

## **8.2. Conclusions of the study**

- The numerical procedure developed in this thesis for solving the Laplace's equation subjected to polarized boundary conditions is highly efficient and reduces the number of iterations significantly.

- The developed model for predicting the corrosion rate captures the effect of temperature, the degree of saturation, and concrete cover thickness on the corrosion rate of steel in concrete accurately. The model captures the increasing effect of temperature on the corrosion rate accurately and yields excellent agreement with experimental results. It is well documented in the literature that when concrete is submerged in water, due to oxygen deficiency, the corrosion slows down due to concentration polarization. This behaviour is captured by the developed model closely. The developed model considers the both effects of cover thickness (i.e. distribution of potential in the bulk of the concrete and its effect on oxygen availability) and experimental verification confirms the capability of the model in accurately predicting the corrosion rate of steel with different cover thicknesses.
- The coupled effect of individual factors can also be predicted with the developed model. For example temperature tends to increase the corrosion rate by decreasing the concrete resistivity and increasing the oxygen diffusion coefficient and also tends to decrease the corrosion rate by decreasing the amount of dissolved oxygen in water; the coupled effect of temperature on the corrosion rate can be perfectly predicted using the model.
- The developed model for relating the half-cell potential to the kinetics of corrosion is in agreement with results of corrosion rate measurement with linear polarization technique.

- The developed model for relating the half-cell potential to the kinetics of corrosion provides significant information about the type and rate of steel corrosion in concrete. This model, provides an estimate of the corrosion rate while considering the effect of A/C, and also considers the effect of concrete resistivity, cover thickness and temperature.
- Instruments that are based on linear polarization technique may overestimate the corrosion rate in the case of uniform corrosion and underestimate the corrosion rate in the case of pitting corrosion. Furthermore, these instruments do not provide any information regarding to the type of corrosion. Whereas, the developed model for relating the kinetics of corrosion to half-cell potential provides all the necessary information regarding to the type and rate of corrosion.

### **8.3. Recommendations for future work**

- The developed model only considers geometries that can be simulated with two-dimensional domains. There are a number of specific cases which require three-dimensional solution of Laplace's equation. To accommodate these cases, virtual experiments need to be expanded to cover these three-dimensional cases.
- A comprehensive experimental study is recommended to further verify the applicability of the study to a wide range of scenarios. The coupled effects need to be investigated further using this experimental study.

- The theoretical considerations provided in this thesis outline the importance of the A/C ratio on the corrosion rate of steel in concrete; however, well-designed experiments are necessary for better understanding of this concept.
- There is a lack of data related to the kinetic parameters of the steel corrosion in concrete. Determination of the kinetic parameters of steel corrosion in concrete experimentally will be a significant contribution.

## References

- Ahmad, S., and Bhattacharjee, B. (2000). "Empirical Modelling of Indicators of Chloride-Induced Rebar Corrosion." *J. Struct. Eng.*, 27(3), 195-207.
- Alonso, C., Andrade, C., and Gonzalez, J. A. (1988). "Relation between Resistivity and Corrosion Rate of Reinforcements in Carbonated Mortar Made with Several Cement Types." *Cem. Concr. Res.*, 18(5), 687-698.
- Andrade, C., and Gonzalez, J. A. (1978). "Quantitative Measurements of Corrosion Rate of Reinforcing Steels Embedded in Concrete Using Polarization Measurements." *Werkst. Korros.*, 29(8), 515-519.
- ASTM. (1999). "Standard Test Method for Half-Cell Potentials of Uncoated Reinforcing Steel in Concrete." ASTM C876-91(1999). Philadelphia.
- Balabanic, G., Bicanic, N., and Durekovic, A. (1995). "Numerical Analysis of Corrosion Cell in Concrete." *Int. J. Eng. Modell.*, 8(1-2), 1-5.
- Bazant, Z. P. (1979). "Physical Model for Steel Corrosion in Concrete Sea Structures – Application." *ASCE J. Struct. Div.*, 105(6), 1155-1166.
- Bazant, Z. P. (1979). "Physical Model for Steel Corrosion in Concrete Sea Structures – Theory." *ASCE J. Struct. Div.*, 105(6), 1137-1153.
- Berkeley, K. G. C., and Pathmanaban, S. (1990). *Cathodic Protection of Reinforcement Steel in Concrete*, Butterworth-Heinemann, London, U.K.
- Bertolini, L., Elsener, B., Pedferri, P., and Polder, R. (2004). *Corrosion of Steel in Concrete*, WILEY-VCH Verlag GmbH & Co. KGaA, Weinheim, Germany.
- Bhat, R. B., and Chakraverty, S. (2004). *Numerical Analysis in Engineering*, Alpha Science International, Pangbourne, U.K.

- Bockris, J. O'M., Mannan, R. J., and Damjanovic, A. (1968). "Dependence of the Rate of Electrode Redox Reactions on the Substrate." *J. Chem. Phys.*, 48(5), 1898-1904.
- Bohni, H. (2005). *Corrosion in Reinforced Concrete Structures*, CRC Press, New York.
- Brad, A. J., and Faulkner, L. R. (2001). *Electrochemical Methods Fundamentals and Applications*, 2<sup>nd</sup> Ed., John Wiley & Sons, New York.
- Brad, A. J., Parsons, R., and Jordan, J. (1985). *Standard Potentials in Aqueous Solution*, M. Dekker, New York.
- Chrip, T. M., Starrs, G., McCarter, W. J., Rouchotas, E., and Blewett, J. (2001). "Temperature-Conductivity Relationship for Concrete: An Activation Energy Approach." *J. Mater. Sci. Lett.*, 20(12), 1085-1087.
- Clear, K. C. (1989). *Measuring the Rate of Corrosion of Steel in Field Concrete Structures*, Transportation Research Record 1211, Transportation Research Board, National Research Council, Washington, DC.
- Conway, B. E., Tessier, D. F., and Wilkinson, D. P. (1989). "Temperature Dependence of the Tafel Slope and Electrochemical Barrier Symmetry Factor,  $\beta$ , in Electrode Kinetics." *J. Electrochem. Soc.*, 136(9), 2486-2493.
- DuraCrete (2000). *Modelling of Degradation*, Document BE95-1347/R4-5, Gouda, CUR.
- Eaton, A. D. F., and Mary, A. H. (2005). *Standard Methods for the Examination of Water and Wastewater*, 21<sup>st</sup> Ed., American Public Health Association, Washington, DC.

- Elsener, B. (2002). "Macrocell Corrosion of Steel in Concrete - Implications for Corrosion Monitoring." *Cem. Concr. Compos.*, 24(1), 65-72.
- Elsener, B. (2005). "Corrosion Rate of Steel in Concrete – Measurements beyond the Tafel Law." *Corros. Sci.*, 47(12), 3019-3033.
- Feliu, S., Gonzalez, J. A., Feliu, S. Jr., and Andrade, M. C. (1990). "Confinement of the Electrical Signal for in situ Measurement of Polarization Resistance in Reinforced Concrete." *ACI Mater. J.*, 87(5), 457-460.
- Garces, P., Andrade, M. C., Saez, A., and Alonso, M. C. (2005). "Corrosion of Reinforcing Steel in Natural and Acid Solutions Simulating the Electrolytic Environments in the Micropores of Concrete in the Propagation Period." *Corros. Sci.*, 47(2), 289-306.
- Ge, J. (2006). "On the Numerical Solution of Laplace's Equation with Nonlinear Boundary Condition for Corrosion of Steel in Concrete." M.A.Sc. Thesis, Carleton University, Ottawa, Canada.
- Ge, J., and Isgor, O. B. (2006). "On the Numerical Solution of Laplace's Equation with Nonlinear Boundary Conditions for Corrosion of Steel in Concrete." ISCCBE Conference (CD-Rom), Montreal, QC, Canada.
- Ghods, P., Isgor, O. B., and Pour-Ghaz, M. (2007). "A Practical Method for Calculating the Corrosion Rate of Uniformly Depassivated Reinforcing Bars in Concrete." *Mater. Corros.*, 58(4), 265-272.
- Gileadi, E. (1987). "Anomalous Temperature Dependence of the Tafel Slope." *J. Electrochem. Soc.*, 134(1), 117-120.

- GjØrv, O. E., Vennesland, Ø., and El-Busiady, A. H. S. (1977). "Electrical Resistivity of Concrete in the Oceans." *Proc., 9th Annual Offshore Technology Conference*, Houston, Texas, 581-588.
- Gonzalez, J. A., Andrade, C., Alonso, C., and Feliu, S. (1995). "Comparison of Rates of General Corrosion and Maximum Pitting Penetration on Concrete Embedded Steel Reinforcement." *Cem. Concr. Res.*, 25(2), 257-264.
- Gonzalez, J. A., Molina, A., Escudero, M. L., and Andrade, C. (1985). "Errors in the Electrochemical Evaluation of Very Small Corrosion Rates - I. Polarization Resistance Method Applied to Corrosion of Steel in Concrete." *Corros. Sci.*, 25(10), 917-930.
- Gowers, K. R., Millard, S. G., Gill, J. S., and Gill, R. P. (1994). "Programmable Linear Polarization Meter for Determination of Corrosion Rate of Reinforcement in Concrete Structures." *Br. Corros. J.*, 29(1), 25-32.
- Gulikers, J. (2005). "Theoretical Considerations on the Supposed Linear Relationship between Concrete Resistivity and Corrosion Rate of Steel Reinforcement." *Mater. Corros.*, 56(6), 393-403.
- Hope, B. B., and Ip, K. A. C. (1987). *Report ME-87-02*, Ontario Ministry of Transportation and Communication, Ontario, Canada.
- Huet, B., L'hostis, V., Santarini, G., Feron, D., and Idrissi, H. (2007). "Steel Corrosion in Concrete: Determinist Modelling of Cathodic Reaction as a Function of Water Saturation Degree." *Corros. Sci.*, 49(4), 1918-1932.

- Hunkeler, F. H. K. (1994). "Mortol und Beton-Wassergehalt, Porositat und Elektrischer Widerstand." *Schweizer Ingenieur und Architekt*, Heft Nr. 27/28, 534-541.
- Hurlen, T. (1960). "Corrosion of Iron: Effect of pH and Ferrous Ion Activity." *Acta. Chem. Scand.*, 14(7), 1555-1563.
- Hurlen, T. (1960). "Heat of Activation in Electrode Kinetics: The Fe/Fe<sup>++</sup>aq. Electrode." *Acta. Chem. Scand.*, 14(7), 1564-1570.
- Isgor, O. B. (2001). "A Durability Model for Chloride and Carbonation Induced Steel Corrosion in Reinforced Concrete Members." Ph.D. Thesis, Carleton University, Ottawa, Canada.
- Isgor, O. B., and Razaqpur, A. G. (2004). "Finite Element Modelling of Coupled Heat Transfer, Moisture Transport and Carbonation Processes in Concrete Structures." *Cem. Concr. Compos.*, 26(1), 57-73.
- Isgor, O. B., and Razaqpur, A. G. (2006). "Modelling Steel Corrosion in Concrete Structures." *Mater. Struct.*, 39(287), 291-302.
- John, D. G., Hladky, K., Gaydecki, P. A., and Dawson, J. L. (1992). "Utilization of Electrochemical Impedance Techniques to Estimate Corrosion Damage of Steel Infrastructures." in *Corrosion Forms and Control for Infrastructure*, Ed. Chaker, ASTM STP 1137, 155-169, American Society for Testing and Materials, Philadelphia.
- Jones, D. A. (1996). *Principles and Prevention of Corrosion*, 2<sup>nd</sup> Ed., Prentice-Hall Inc., Upper Saddle River, NJ.

- Kranc, S. C., and Sagues, A. A. (1994). "Computation of Reinforcing Steel Corrosion Distribution in Concrete Marine Bridge Substructures." *Corrosion*, 50(1), 50-61.
- Kranc, S. C., and Sagues, A. A. (1997). "Modelling the Time-Dependent Response to External Polarization of Corrosion Macrocell on Steel in Concrete." *J. Electrochem. Soc.*, 144(8), 2643-2652.
- Kriksunov, L. (1995). "The Temperature Dependence of the Tafel Slope for Parallel Electrochemical Reactions." *Electrochim. Acta.*, 40(15), 2553-2555.
- Liu, T., and Weyers, R. W. (1998). "Modelling the Corrosion Process in Chloride Contaminated Concrete Structures." *Cem. Concr. Res.*, 28(3), 365-379.
- Lopez, W., and Gonzalez, J. A. (1993). "Influence of the Degree of Pore Saturation on the Resistivity of Concrete and the Corrosion Rate of Steel Reinforcement." *Cem. Concr. Res.*, 23(2), 368-376.
- Lopez, W., Gonzalez, J. A., and Andrade, C. (1993). "Influence of Temperature on the Service Life of Rebars." *Cem. Concr. Res.*, 23(5), 1130-1140.
- Luping, T. (2002). *Calibration of the Electrochemical Methods for the Corrosion Rate Measurement of Steel in Concrete*, NORDTEST Project No. 1531-01, SP REPORT 2002:25, SP Swedish National Testing and Research Institute. <<http://www.nordicinnovation.net/nordtestfiler/tec521.pdf>> (May, 2007).
- Maruya, T., Hsu, K., Takeda, H., and Tangtermsirikul, S. (2003). "Numerical Modelling of Steel Corrosion in Concrete Structures due to Chloride Ion, Oxygen and Water Movement." *J. Adv. Concr. Technol.*, 1(2), 147-160.
- Morinaga, S. (1990). "Prediction of Service Life of Reinforced Concrete Buildings Based on the Corrosion Rate of Reinforcing Steel." *Proc. of the 5<sup>th</sup>*

*International Conference on Durability of Building Materials and Components*, Brighton, U.K.

- Morinaga, S. (1996). "Remaining Life of Reinforced Concrete Structures After Corrosion Cracking." *Proc. of the 7<sup>th</sup> International Conference on Durability of Building Materials and Components*, Stockholm, Sweden.
- Munn, R. S., and Devereux, O. F. (1991). "Numerical Modelling and Solution of Galvanic Corrosion Systems. Part I. Governing Differential Equation and Electrode Boundary Conditions." *Corrosion*, 47(8), 612-618.
- Neville, A. M. (1995). *Properties of Concrete*, 4<sup>th</sup> Ed., Pearson Education Limited, New York.
- NLREG. (2005). Nonlinear Regression Analysis Program Version 6.3, Copyright © 1992-2005, Phillip H. Sherrod, <<http://www.nlreg.com>> (June, 2007).
- Page, C. L., and Lambert, P. (1987). "Kinetics of Oxygen Diffusion in Hardened Cement Pastes." *J. Mater. Sci.*, 22(3), 942-946.
- Page, C. L., and Treadaway, K. W. J. (1982). "Aspects of the Electrochemistry of Steel in Concrete." *Nature*, 297(5862), 109-115.
- Page, C. L., Short, N. R., and El Tarras, A. (1981). "Diffusion of Chloride Ions in Hardened Cement Pastes." *Cem. Concr. Res.*, 11(3), 395-406.
- Papadakis, V. G., Vayenas, C. G., and Fardis, M. N. (1991) "Physical and Chemical Characteristics Affecting the Durability of Concrete." *ACI Mater. J.*, 8(2), 186-196.
- Ramezani-pour, A. A., Pourkhorshidi, A.R., and Ramezani-pour, A. M. (2007). "Long Term Durability of Pozzolanic Cement Concretes in Severe

- Environments.” *Proc. of 12<sup>th</sup> International Congress on the Chemistry of Cement*, Montreal, Canada.
- Raupach, M. (2006). “Models for the Propagation Phase of Reinforcement Corrosion – an Overview.” *Mater. Corros.*, 57(8), 605-613.
- Raupach, M., and Gulikers, J. (1999). “A Simplified Method to Estimate Corrosion Rates – A New Approach Based on Investigations of Macrocells.” *Proc. of 8<sup>th</sup> International Conference on Durability of Building Materials and Components*, Vancouver, Canada.
- Redaelli, E., Bertolini, L., Peelen, W., and Polder, R. (2006). “FEM-Models for the Propagation Period of Chloride Induced Reinforcement Corrosion.” *Mater. Corros.*, 57(8), 628-635.
- RILEM TC 154-EMC. (2003). “Half-Cell Potential Measurements – Potential Mapping on Reinforced Concrete Structures.” *Mater. Struct.*, 36(7), 461-471.
- Rodriguez, J., Ortega, L. M., Garcia, A. M., Johansson, L., and Petterson, K. (1995). “On-Site Corrosion Measurements in Concrete Structures.” *Constr. Repair*, 9(6), 27-30.
- Sagues, A. A., and Kranc, S. C. (1992). “On the Determination of Polarization Diagrams of Reinforcing Steel in Concrete.” *Corrosion*, 48(8), 624-633.
- Song, H. W., Kim, H. J., Kwon, S. J., Lee, C. H., Byun, K. J., and Park, C. K. (2005). “Prediction of Service Life in Cracked Reinforced Concrete Structures Subjected to Chloride Attack and Carbonation.” *Proc. of the International Conference on Cement Combinations for Durable Concrete*, Dundee, Scotland, U.K.

- Stanish, K., Hooton, R. D., and Thomas, M. D. A. (2004). "A Novel Method for Describing Chloride Ion Transport due to an Electrical Gradient in Concrete: Part 1. Theoretical Description." *Cem. Concr. Res.*, 34(1), 43-49.
- Stern, M., and Geary, A. L. (1957). "Electrochemical Polarization, I. Atheoretical Analysis of the Shape of Polarization Curves." *J. Electrochem. Soc.*, 104(12), 56-63.
- Takewaka, K., Yamaguchi, T., and Maeda, S. (2003). "Simulation Model for Deterioration of Concrete Structures due to Chloride Attack." *J. Adv. Concr. Technol.*, 1(2), 139-146.
- Tanaka, N., and Tamamushi, R. (1964). "Kinetic Parameters of Electrode Reactions." *Electrochim. Acta.*, 9(7), 963-989.
- Uhlig, H. H., and Revie, R. W. (1985). *Corrosion and Corrosion Control*, 3<sup>rd</sup> Ed., John Wiley & Sons, New York.
- Warkus, J., Brem, M., and Raupach, M. (2006). "BEM-Models for the Propagation Period of Chloride Induced Reinforcement Corrosion." *Mater. Corros.*, 57(8), 636-641.
- Xi, Y., Bazant, Z. P., and Jennings, H. M. (1994). "Moisture Diffusion in Cementitious Materials." *Adv. Cem. Based. Mat.*, 1(6), 248-257.

## **Appendix A: Auxiliary models used in the thesis**

### **A.1. Concrete resistivity as a function of w/c ratio and degree of saturation (GjØrv et al. 1977)**

The following tables are prepared for calculation of concrete resistivity using w/c ratio and degree of saturation ( $S_r$ ) using the experimental data obtained by GjØrv et al. (1977). It is noted that since this data is a function of w/c and the degree of saturation, two sets of curves are prepared for convenience. Table A.1 presents the concrete resistivity as a function of w/c ratio at different degrees of saturation, and Table A.2 presents the concrete resistivity as a function of degree of saturation at different w/c ratios. For better fit, these curves are divided into two intervals. Should the concrete resistivity of other values of w/c ratio and degree of saturation be of interest, they can be found by interpolation of the data presented by curves in Table A.1 and Table A.2.

Table A.1: Concrete resistivity as a function of w/c ratio at different degrees of saturation

Saturation ( $S_r$ )	w/c	
	0.4 ~ 0.48	0.48 ~ 0.7
40%	$\rho = -1.366 \times 10^7 (w/c)^3$ $+ 2.419 \times 10^7 (w/c)^2$ $- 1.415 \times 10^7 (w/c)$ $+ 2.737 \times 10^6$	$\rho = -16500$ $+ 112500(w/c)$ $- 125000(w/c)^2$
60%	$\rho = -2.197 \times 10^5 (w/c)^3$ $+ 3.936 \times 10^5 (w/c)^2$ $- 2.335 \times 10^5 (w/c)$ $+ 4.612 \times 10^4$	$\rho = 1837.72$ $- 4197.72(w/c)$ $+ 2613.63(w/c)^2$
80%	$\rho = -1.728 \times 10^4 (w/c)^3$ $+ 3.078 \times 10^4 (w/c)^2$ $- 1.819 \times 10^4 (w/c)$ $+ 3.640 \times 10^3$	$\rho = 156.55$ $- 149.55(w/c)$ $+ 22.73(w/c)^2$
100%	$\rho = -3.145 \times 10^3 (w/c)^3$ $+ 5.643 \times 10^3 (w/c)^2$ $- 3.382 \times 10^3 (w/c)$ $+ 7.110 \times 10^2$	$\rho = 77.10$ $- 99.10(w/c)$ $+ 45.45(w/c)^2$

Table A.2: Concrete resistivity as a function of degree of saturation for different values of w/c ratio

w/c	Saturation ( $S_r$ )	
	0.4 ~ 0.6	0.6 ~ 1.0
0.41	$\rho = -1.135 \times 10^6 S_r^3$ $+ 2.701 \times 10^6 S_r^2$ $- 2.111 \times 10^6 S_r$ $+ 5.418 \times 10^5$	$\rho = \frac{1}{0.02151859 - 0.081174284S_r + 0.07761231S_r^2}$
0.42	$\rho = -9.749 \times 10^5 S_r^3$ $+ 2.352 \times 10^6 S_r^2$ $- 1.855 \times 10^6 S_r$ $+ 4.780 \times 10^5$	$\rho = \frac{1}{0.0215410 - 0.082270S_r + 0.07960S_r^2}$
0.43	$\rho = -8.402 \times 10^5 S_r^3$ $+ 1.999 \times 10^3 S_r^2$ $- 1.563 \times 10^6 S_r$ $+ 4.014 \times 10^5$	$\rho = \frac{1}{0.021209416 - 0.082571614S_r + 0.081340819S_r^2}$
0.44	$\rho = -6.839 \times 10^5 S_r^3$ $+ 1.628 \times 10^6 S_r^2$ $- 1.273 \times 10^6 S_r$ $+ 3.271 \times 10^5$	$\rho = \frac{1}{0.020217491 - 0.081047418S_r + 0.081973823S_r^2}$
0.45	$\rho = -5.797 \times 10^5 S_r^3$ $+ 1.380 \times 10^6 S_r^2$ $- 1.080 \times 10^6 S_r$ $+ 2.776 \times 10^5$	$\rho = \frac{33.596613 + 13.481421S_r}{1 - 3.963255S_r + 3.9702737S_r^2}$
0.6	$\rho = -1.127 \times 10^5 S_r^3$ $+ 2.723 \times 10^5 S_r^2$ $- 2.154 \times 10^5 S_r$ $+ 5.579 \times 10^4$	$\rho = 0.71666 \times (47.44)^{S_r} \times S_r^{-7.005}$
0.7	$\rho = -1.290 \times 10^4 S_r^3$ $+ 3.20 \times 10^4 S_r^2$ $- 2.630 \times 10^4 S_r$ $+ 7.225 \times 10^3$	$\rho = (-0.06871 + 0.333S_r)^{-2.554931}$

## A.2. Amount of dissolved oxygen in water (Eaton and Mary 2005)

The amount of the dissolved oxygen in water can be calculated using the following equation. This equation is derived using Henry's law:

$$\begin{aligned} \text{Ln}C_{O_2}^s = & -139.34411 + \frac{1.575701 \times 10^5}{T} - \frac{6.642308 \times 10^7}{T^2} \\ & + \frac{1.243800 \times 10^{10}}{T^3} - \frac{8.621949 \times 10^{11}}{T^4} \\ & - \text{Chl} \left[ 3.1929 \times 10^{-2} - \frac{1.9428 \times 10}{T} + \frac{3.8673 \times 10^3}{T^2} \right] \end{aligned} \quad (\text{A.1})$$

where  $C_{O_2}^s$  (mg/litre) is the amount of dissolved oxygen in water,  $T$  ( $^{\circ}\text{K}$ ) is the temperature, and Chl is the Chlorinity. Chlorinity is a dimensionless parameter, and it is not equivalent to chloride concentration. However, for practical purposes it can be considered equal to chloride concentration of water (g/kg).

Equation (A.1) gives  $C_{O_2}^s$  at standard pressure (i.e. 101.325 kPa); for non-standard conditions of pressure the following correction can be implemented:

$$C_{O_2}^{s*} = C_{O_2}^s P \left( \frac{(1 - \frac{P_{wv}}{P})(1 - \omega P)}{(1 - P_{wv})(1 - \omega)} \right) \quad (\text{A.2})$$

$$\text{Ln}P_{wv} = 11.8571 - (3840.70/T) - (216961/T^2) \quad (\text{A.3})$$

$$\omega = 0.000975 - (1.426 \times 10^{-5} T_c) + (6.436 \times 10^{-8} T_c^2) \quad (\text{A.4})$$

where  $C_{O_2}^{s*}$  (mg/litre) is the amount of dissolved oxygen at non-standard pressure,  $P$  (atm) is the non-standard pressure,  $P_{wv}$  (atm) is the partial pressure of water vapour, and  $T_c$  ( $^{\circ}\text{C}$ ) is the temperature. Since the above calculations are rather lengthy, the following formula is proposed in this thesis for practical purposes:

$$C_{O_2}^s = \frac{0.45755224 - 0.0047766866T_c}{1 + 0.018798679T_c - 0.00027691116T_c^2} \quad (\text{A.5})$$

where  $C_{O_2}^s$  is in (mole/m<sup>3</sup>) and  $T_c$  is between 0 to 50°C.

### **A.3. Activation energy of resistivity (Chrisp et al. 2001)**

The following formulation representing the activation energy of resistivity is obtained by conducting a regression analysis on the experimental data obtained by Chrisp et al. (2001). In this equation the activation energy of resistivity is a function of degree of saturation,  $S_r$ .

$$\Delta U_\rho = \frac{26.753349}{1 - 4.3362256 \times \exp(-5.2488563S_r)} \quad (\text{A.6})$$

where  $\Delta U_\rho$  (kJ/mole) is activation energy of resistivity and the degree of saturation,  $S_r$  is between 0.5 and 1.0.

### **A.4. Activation energy of oxygen diffusion (Page and Lambert 1987)**

The following equation is obtained by conducting a regression analysis through the experimental data obtained by (Page and Lambert 1987), which relates the activation energy of oxygen diffusion to w/c ratio.

$$\Delta U_D = -505(w/c)^2 + 484.5(w/c) - 94 \quad (\text{A.7})$$

where  $\Delta U_D$  (kJ/mole) is the activation energy of oxygen diffusion through cement paste. It should be noted that the above equation is only valid for w/c ratios between 0.4 and 0.6.

### **A.5. Conversion of concrete resistivity to concrete resistance (Luping 2002)**

To convert the concrete resistance measured with Gecor to concrete resistivity the following formula can be used:

$$\rho = 2D_{counter}R_{con} \quad (\text{A.8})$$

where  $\rho$  ( $\Omega\cdot\text{m}$ ) is the concrete resistivity,  $D_{counter}$  (mm) is the counter electrode diameter and  $R_{con}$  (kOhm) is the concrete resistance measured with Gecor instrument.

### **A.6. Conversion of concrete resistivity to concrete resistance used by Lopez and Gonzalez (1993)**

The following equation is used for converting the concrete resistance to concrete resistivity for samples used Lopez and Gonzalez (1993):

$$R_{con} = 0.2930\rho - 531.50 \quad (\text{A.9})$$

where  $R_{con}$  ( $\Omega$ ) is the concrete resistance,  $\rho$  ( $\Omega\cdot\text{cm}$ ) is concrete resistivity.

### **A.7. Hydration of cement paste and oxygen diffusion coefficient calculation (Papadakis et al. 1991)**

The effective oxygen diffusion of cement paste can be calculated using:

$$D_{O_2} = 1.92 \times 10^{-6} \varepsilon_p (1 - h/100)^{2.2} \quad (\text{A.10})$$

where  $D_{O_2}$  ( $\text{m}^2/\text{s}$ ) is the effective oxygen diffusion coefficient,  $\varepsilon_p$  is the porosity of cement paste, and  $h$  is the relative humidity. In the latter equation the porosity of cement paste is calculated using:

$$\varepsilon_p(t) = \varepsilon(t) \left( 1 + \frac{\frac{a \rho_c}{c \rho_a}}{1 + \frac{w \rho_c}{c \rho_w}} \right) \quad (\text{A.11})$$

where in the above equation  $\varepsilon_p(t)$  is the porosity of the hardened cement paste at time  $t$  (sec),  $\varepsilon(t)$  is the porosity of concrete at time  $t$ ,  $a/c$  is the aggregate cement ratio,  $w/c$  is water-cement ratio,  $\rho_c$ ,  $\rho_a$  and  $\rho_w$  are densities of cement, aggregate and water respectively. The porosity of concrete in Eq. (A.11) is calculated using:

$$\varepsilon(t) = \varepsilon_o - \Delta\varepsilon_H(t) - \Delta\varepsilon_c \quad (\text{A.12})$$

where  $\varepsilon_o$  is the porosity of fresh concrete,  $\Delta\varepsilon_H(t)$  is reduction in porosity due to hydration, and  $\Delta\varepsilon_c$  is reduction in porosity due to carbonation. The value of the porosity of fresh concrete can be calculated using:

$$\varepsilon_o = \frac{\frac{w \rho_c}{c \rho_a} (1 - \varepsilon_{air})}{\left( 1 + \frac{w \rho_c}{c \rho_w} + \frac{a \rho_c}{c \rho_a} \right)} + \varepsilon_{air} \quad (\text{A.13})$$

where  $\varepsilon_{air}$  is the volume fraction of entrapped (or entrained) air. Reduction in porosity due to hydration is calculated by:

$$\begin{aligned}
\Delta\varepsilon_H(t) = & [C_3S]_0 F_{C_3S} \Delta\bar{V}_{C_3S} \\
& + [C_2S]_0 F_{C_2S} \Delta\bar{V}_{C_2S} \\
& + [C_3A]_0 F_{C_3A}(t^*) \Delta\bar{V}_{C_3A,\bar{S}} \\
& + [C_3A]_0 (F_{C_3A} - F_{C_3A}(t^*)) \Delta\bar{V}_{C_3A} \\
& + [C_4AF]_0 F_{C_4AF}(t^*) \Delta\bar{V}_{C_4AF,\bar{S}} \\
& + [C_4AF]_0 (F_{C_4AF} - F_{C_4AF}(t^*)) \Delta\bar{V}_{C_4AF}
\end{aligned} \tag{A.14}$$

$$t^* = \frac{1}{k_{H,C_3A}(1-n_{C_3A})} \left[ 1 - \left( 1 - \frac{[C\bar{S}H_2]_0}{[C_3A]_0} \right)^{1-n_{C_3A}} \right] \tag{A.15}$$

$$F_j(t) = 1 - (1 - k_{H,j} t (1 - n_j))^{1/(1-n_j)} \tag{A.16}$$

and the reduction in porosity due to carbonation is calculated using:

$$\Delta\varepsilon_c = [Ca(OH)_2] \Delta\bar{V}_{CH} + [CSH] \Delta\bar{V}_{CSH} \tag{A.17}$$

$$\begin{aligned}
[Ca(OH)_2] = & \frac{3}{2} [C_3S]_0 F_{C_3S} + \frac{1}{2} [C_2S]_0 F_{C_2S} \\
& - 4 [C_4AF]_0 - [C_3A]_0 F_{C_3A} + [C\bar{S}H_2]_0
\end{aligned} \tag{A.18}$$

$$[CSH] = \frac{1}{2} [C_3S]_0 F_{C_3S} + \frac{1}{2} [C_2S]_0 F_{C_2S} \tag{A.19}$$

where  $[j]_0$  (mole/m<sup>3</sup>) ( $j = C_3S, C_2S, C_3A, C_4AF$ ) is the initial molar concentration of component  $j$ , (see Table A.3)  $[C\bar{S}H_2]_0$  (mole/m<sup>3</sup>) is initial molar concentration of gypsum.  $[Ca(OH)_2]$  (mole/m<sup>3</sup>) and  $[CSH]$  (mole/m<sup>3</sup>) are molar concentrations of  $Ca(OH)_2$  and  $CSH$ .  $\Delta\bar{V}_j$  in Eqs. (A.14) and (A.17) is the molar volume differences of each components are presented in Table A.4. It is noted that all equations above are only valid for  $t > t^*$ , where  $t^*$  represents the time after which all the gypsum in the cement has been consumed. The value of  $t^*$  can be calculated using Eq. (A.15). Also,  $F_j$  represents the fraction of component  $j$  which has been hydrated and the values of

coefficient  $k_{H,j}$  and exponent  $n_j$  are given in Table A.5. The initial molar concentration of each component used in Eqs. (A.14) to (A.19) is calculated using:

$$[j]_0 = \frac{m_j m_{cl} \rho_c (1 - \varepsilon_{air})}{MW_j \left( 1 + \frac{w \rho_c}{c \rho_w} + \frac{a \rho_c}{c \rho_a} \right)} \quad (\text{A.20})$$

$$[\text{C}\bar{\text{S}}\text{H}_2]_0 = \frac{m_{gy} \rho_c (1 - \varepsilon_{air})}{MW_{gy} \left( 1 + \frac{w \rho_c}{c \rho_w} + \frac{a \rho_c}{c \rho_a} \right)} \quad (\text{A.21})$$

where  $MW_j$  and  $MW_{gy}$  (kg/mole) are the molar weight of  $j$  component and gypsum respectively (see Table A.3),  $m_j$  the weight fraction of component  $j$ ,  $m_{cl}$  is the weight fraction of clinker and  $m_{gy} = 1 - m_{cl}$  is the weight fraction of gypsum. The weight fraction of clinker for different cement component can be calculated using the followings and oxide analysis (Neville 1995):

$$\text{C}_3\text{S} = 4.071(\text{CaO}) - 7.60(\text{SiO}_2) - 6.718(\text{Al}_2\text{O}_3) - 1.43(\text{Fe}_2\text{O}_3) - 2.852(\text{SO}_3) \quad (\text{A.22})$$

$$\text{C}_2\text{S} = 2.867(\text{SiO}_2) - 0.7544(\text{C}_3\text{S}) \quad (\text{A.23})$$

$$\text{C}_3\text{A} = 2.65(\text{Al}_2\text{O}_3) - 1.692(\text{Fe}_2\text{O}_3) \quad (\text{A.24})$$

$$\text{C}_4\text{AF} = 3.043(\text{Fe}_2\text{O}_3) \quad (\text{A.25})$$

Table A.3 : Main components of Portland cement

Name of Component	Oxide composition	Abbreviation
Tricalcium silicate	3CaO.SiO <sub>2</sub>	C <sub>3</sub> S
Dicalcium silicate	2CaO.SiO <sub>2</sub>	C <sub>2</sub> S
Tricalcium aluminate	3CaO.Al <sub>2</sub> O <sub>3</sub>	C <sub>3</sub> A
Tetracalcium aluminoferrite	4Cao.Al <sub>2</sub> O <sub>3</sub> .Fe <sub>2</sub> O <sub>3</sub>	C <sub>4</sub> AF

Table A.4: Values of molar volume difference for different cement components

<b>Molar Volume Difference</b>	<b><math>\times 10^6 \text{ m}^3/\text{mole}</math></b>
$\Delta \bar{V}_{C_3S}$	53.28
$\Delta \bar{V}_{C_2S}$	39.35
$\Delta \bar{V}_{C_4AF,S}$	220
$\Delta \bar{V}_{C_3A,S}$	155.86
$\Delta \bar{V}_{C_4AF}$	230
$\Delta \bar{V}_{C_3A}$	149.82
$\Delta \bar{V}_{CH}$	3.85
$\Delta \bar{V}_{CSH}$	15.39

Table A.5: Molar weight and coefficient of reaction rates of major components of Portland cement

<b>Component</b>	<b>C<sub>3</sub>A</b>	<b>C<sub>3</sub>S</b>	<b>C<sub>4</sub>AF</b>	<b>C<sub>3</sub>A</b>	<b>C<math>\bar{S}</math>H<sub>2</sub></b>
$n_j$	2.65	3.10	3.81	2.41	----
$k_{H,j} \times 10^5 \text{ (s}^{-1}\text{)}$	1.17	0.16	1.00	2.46	----
$MW_j \times 10^3 \text{ kg/mole}$	228.30	172.22	485.96	270.18	172.17

Using the above formulation the concrete and cement paste porosity for three different cement types with chemical analysis illustrated in Table A.6 is calculated. The corresponding values of concrete and cement paste porosity are presented in Table A.7 to Table A.9.

Table A.6: Chemical composition of clinker

	<b>Cement Type I (Papadakis et al. 1991)</b>	<b>Cement Type II (Ramezani pour et al. 2007)</b>	<b>Cement Type V (Ramezani pour et al. 2007)</b>
SiO <sub>2</sub>	23.55	20.96	21.47
Al <sub>2</sub> O <sub>3</sub>	6.12	4.2	3.95
Fe <sub>2</sub> O <sub>3</sub>	2.51	4.6	4.4
MgO	1.30	3.4	2.3
CaO	65.28	61.88	63.84
SO <sub>3</sub>	0.47	1.79	2.17
Other	0.77	1.47	1.01

Table A.7: The total porosity and the porosity of hardened cement paste with chemical composition provided by Papadakis et al. (1991) for Cement Type I

Age		w/c						
		0.4	0.45	0.5	0.55	0.6	0.65	0.7
100	$\varepsilon(t)$	0.112	0.136	0.158	0.178	0.198	0.217	0.235
days	$\varepsilon_p(t)$	0.293	0.339	0.379	0.415	0.447	0.476	0.502
200	$\varepsilon(t)$	0.109	0.132	0.154	0.175	0.195	0.214	0.232
days	$\varepsilon_p(t)$	0.283	0.330	0.371	0.407	0.439	0.468	0.495
1	$\varepsilon(t)$	0.106	0.130	0.152	0.173	0.193	0.212	0.230
year	$\varepsilon_p(t)$	0.277	0.324	0.365	0.402	0.434	0.464	0.490
2	$\varepsilon(t)$	0.104	0.128	0.150	0.171	0.191	0.210	0.228
years	$\varepsilon_p(t)$	0.271	0.319	0.361	0.397	0.430	0.460	0.486
4	$\varepsilon(t)$	0.103	0.126	0.148	0.169	0.190	0.209	0.227
years	$\varepsilon_p(t)$	0.267	0.315	0.357	0.394	0.427	0.457	0.484

Table A.8: The total porosity and the porosity of hardened cement paste with chemical composition provided by Ramezaniapour et al. (2007) for Cement Type II

Age		w/c						
		0.4	0.45	0.5	0.55	0.6	0.65	0.7
100	$\varepsilon(t)$	0.106	0.124	0.141	0.157	0.173	0.188	0.202
days	$\varepsilon_p(t)$	0.370	0.411	0.447	0.479	0.507	0.533	0.556
200	$\varepsilon(t)$	0.104	0.122	0.139	0.155	0.171	0.186	0.200
days	$\varepsilon_p(t)$	0.362	0.404	0.441	0.473	0.502	0.527	0.551
1 year	$\varepsilon(t)$	0.103	0.120	0.137	0.154	0.169	0.185	0.199
	$\varepsilon_p(t)$	0.358	0.400	0.436	0.469	0.498	0.524	0.547
2 years	$\varepsilon(t)$	0.102	0.119	0.136	0.153	0.168	0.184	0.198
	$\varepsilon_p(t)$	0.354	0.396	0.433	0.466	0.495	0.521	0.545
4 years	$\varepsilon(t)$	0.101	0.119	0.152	0.152	0.168	0.183	0.197
	$\varepsilon_p(t)$	0.351	0.393	0.463	0.463	0.493	0.519	0.543

Table A.9: The total porosity and the porosity of hardened cement paste with chemical composition provided by Ramezaniapour et al. (2007) for Cement Type V

Age		w/c						
		0.4	0.45	0.5	0.55	0.6	0.65	0.7
100 days	$\varepsilon(t)$	0.103	0.121	0.138	0.154	0.170	0.185	0.200
	$\varepsilon_p(t)$	0.359	0.401	0.438	0.470	0.499	0.525	0.548
200 days	$\varepsilon(t)$	0.101	0.119	0.136	0.152	0.168	0.183	0.198
	$\varepsilon_p(t)$	0.352	0.395	0.432	0.465	0.494	0.520	0.544
1 year	$\varepsilon(t)$	0.100	0.118	0.135	0.151	0.167	0.182	0.197
	$\varepsilon_p(t)$	0.348	0.391	0.428	0.461	0.491	0.517	0.541
2 years	$\varepsilon(t)$	0.099	0.117	0.134	0.150	0.166	0.181	0.196
	$\varepsilon_p(t)$	0.345	0.388	0.425	0.458	0.488	0.514	0.538
4 years	$\varepsilon(t)$	0.098	0.116	0.133	0.150	0.165	0.181	0.195
	$\varepsilon_p(t)$	0.343	0.385	0.423	0.456	0.486	0.513	0.537

#### A.8. Moisture diffusion and degree of saturation (Xi et al. 1994):

The total water content for unit value of material,  $W_t$ , can be calculated using:

$$W_t = \frac{C_{ad}k_{ad}V_m h}{(1 - hk_{ad})[1 + (C - 1)hk_{ad}]} \quad (\text{A.26})$$

and,

$$V_m = \left( 0.068 - \frac{0.22}{t} \right) \left( 0.85 + 0.45 \frac{w}{c} \right) V_{ct} \quad (\text{A.27})$$

where  $V_m$  is the monolayer capacity,  $t$  (days) is time and it is larger than 5; for smaller values of  $t$ , it should be set equal to 5. In the above equation w/c ratio is between 0.3 and 0.7, and for smaller and larger values of w/c ratio it should be considered w/c = 0.3 and w/c = 0.7 respectively.  $V_{ct}$  in Eq. (A.27) is a factor dependent of the cement type and its value can be found in Table A.10. Parameter  $k_{ad}$  which is resulting from assumption that the number of adsorbed layers in finite and can be calculated by:

$$k_{ad} = \frac{\left[ C_{ad} \left( 1 - \frac{1}{n_{ad}} \right) - 1 \right]}{C_{ad} - 1} \quad (\text{A.28})$$

where  $n_{ad}$  is the number of adsorbed layers in saturated state:

$$n_{ad} = \left( 2.5 + \frac{15}{t} \right) \left( 0.33 + 2.2 \frac{w}{c} \right) N_{ct} \quad (\text{A.29})$$

Also in this equation  $t$  is larger than 5; for smaller values  $t$  should be set equal to 5, and  $w/c$  ratio is between 0.3 and 0.7, and for smaller and larger values of  $w/c$  ratio it should be considered  $w/c = 0.3$  and  $w/c = 0.7$  respectively.  $N_{ct}$  in this equation is a factor dependent of the cement type and its value can be found in Table A.10. The value of parameter  $C_{ad}$  which is representative of the heat of adsorption can be found using the following:

$$C_{ad} = \exp\left(\frac{855}{T}\right) \quad (\text{A.30})$$

where  $T$  ( $^{\circ}\text{K}$ ) is temperature.

Table A.10: Cement type dependent parameters

<b>Cement Type</b>	<b>Type I</b>	<b>Type II</b>	<b>Type III</b>	<b>Type IV</b>
$V_{ct}$	0.9	1	0.85	0.6
$N_{ct}$	1.1	1	1.15	1.5

## Appendix B: Results

### B.1. Maximum corrosion current density

This section provides the figures related to the variation of maximum corrosion current density with different parameters.

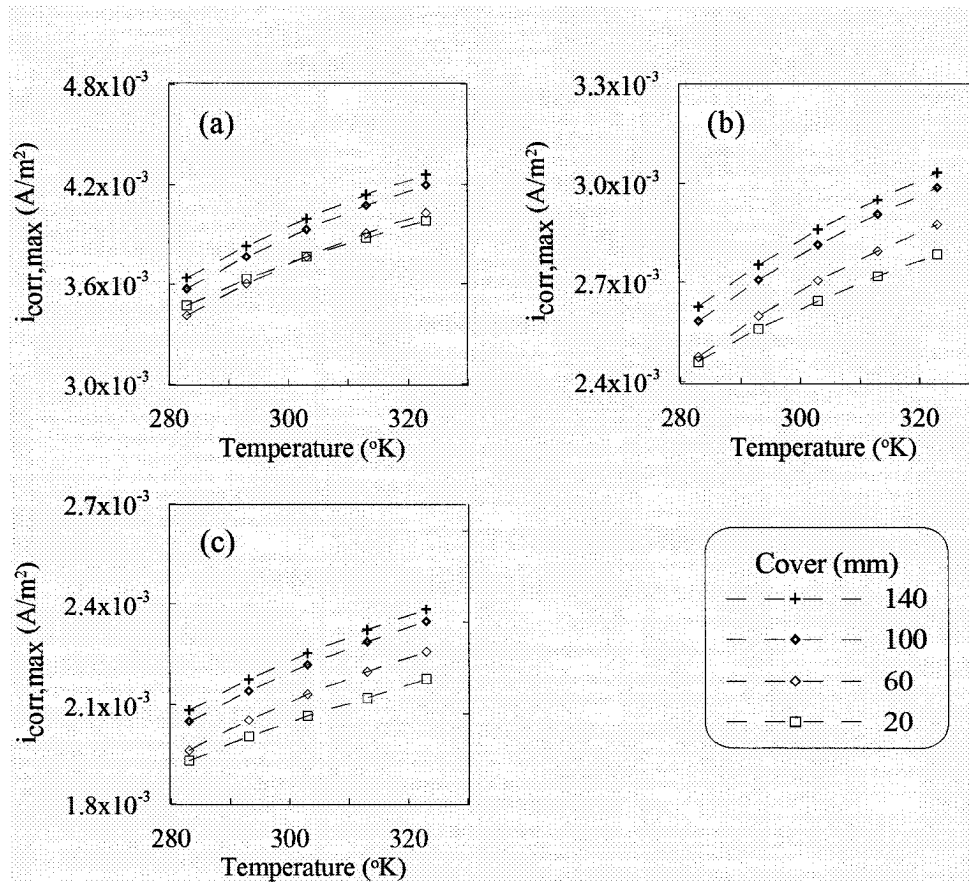


Figure B.1: Variation of maximum corrosion rate with temperature for different values of cover thickness: (a)  $i_L = 0.2 A/m^2$  and  $\rho = 5000 \Omega.m$ , (b)  $i_L = 0.008 A/m^2$  and  $\rho = 7500 \Omega.m$ , (c)  $i_L = 0.005 A/m^2$  and  $\rho = 10000 \Omega.m$

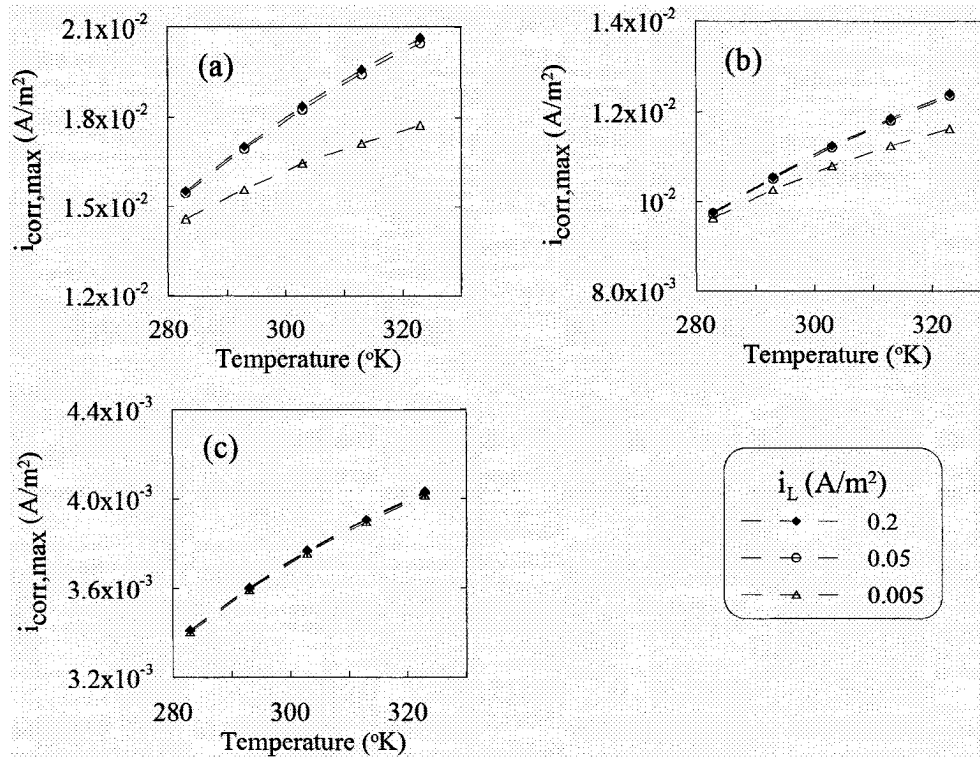


Figure B.2: Variation of maximum corrosion rate with temperature for different values of  $i_L$  (60 mm cover thickness): (a)  $\rho = 650 \Omega\cdot\text{m}$ , (b)  $\rho = 1250 \Omega\cdot\text{m}$ ,  
(c)  $\rho = 5000 \Omega\cdot\text{m}$

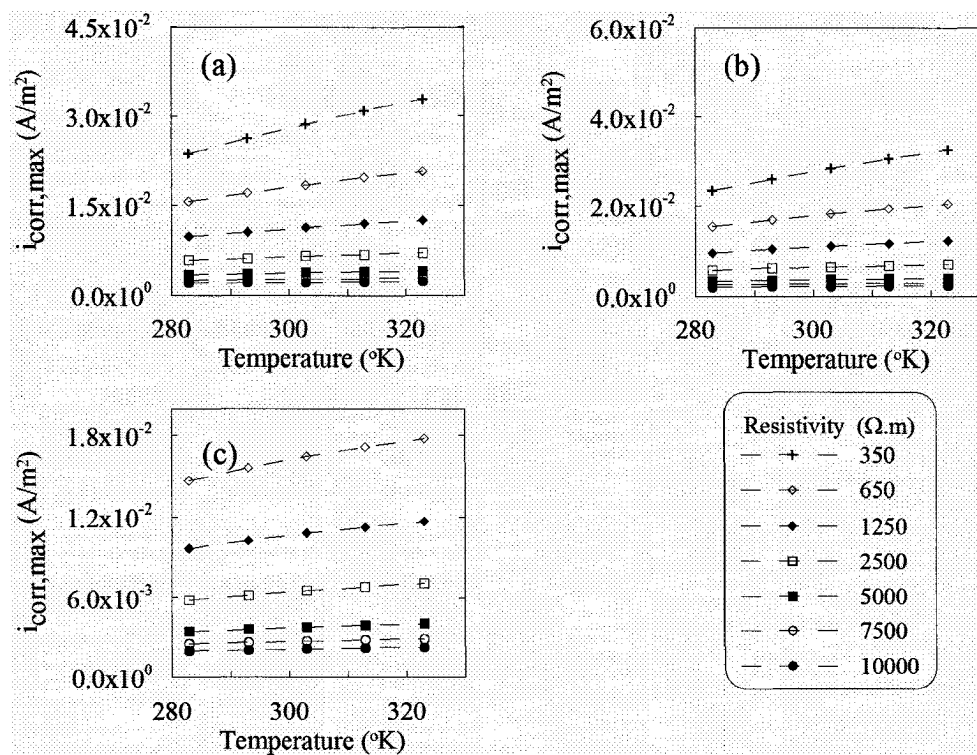


Figure B.3: Variation of maximum corrosion rate with temperature for different values of concrete resistivity (60 mm cover thickness): (a)  $i_L=0.2 A/m^2$ , (b)  $i_L=0.05 A/m^2$ , (c)  $i_L=0.005 A/m^2$

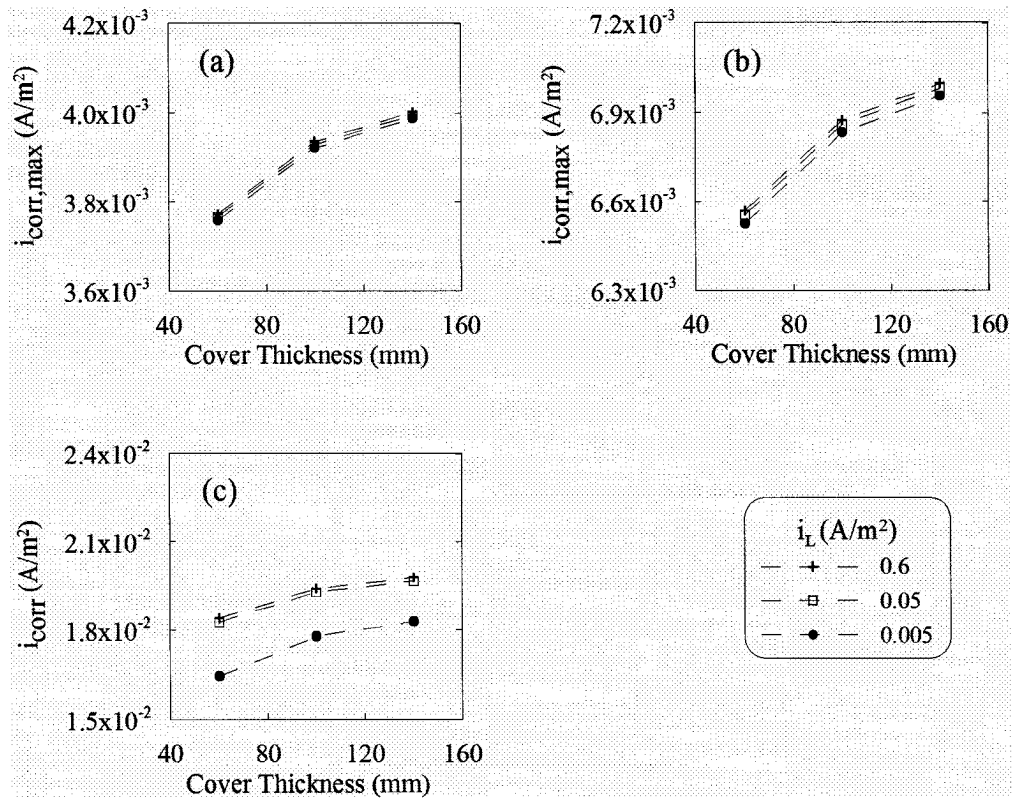


Figure B.4: Variation of maximum corrosion rate with cover thickness for different values of limiting current density at constant temperature ( $303^\circ\text{K}$ ): (a)  $\rho = 5000 \Omega\cdot\text{m}$ , (b)  $\rho = 2500 \Omega\cdot\text{m}$ , (c)  $\rho = 650 \Omega\cdot\text{m}$

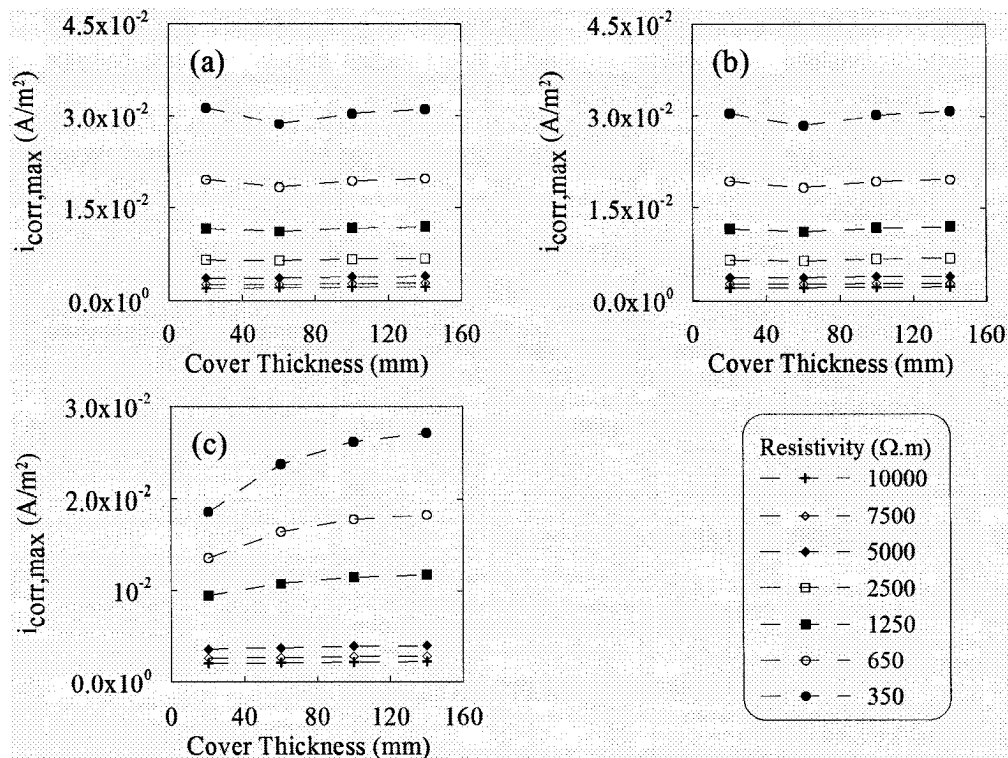


Figure B.5: Variation of maximum corrosion current with cover thickness for different values of resistivity at constant temperature (303°K): (a)  $i_L=0.2 \text{ A/m}^2$ , (b)  $i_L=0.05 \text{ A/m}^2$ , (c)  $i_L=0.005 \text{ A/m}^2$

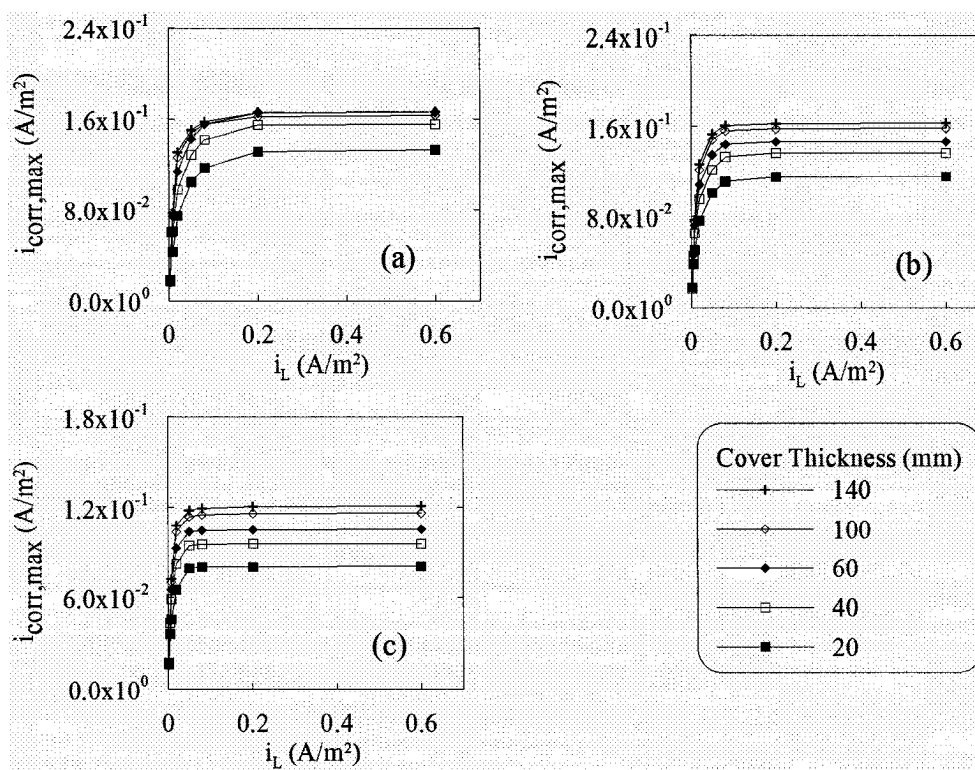


Figure B.6: Variation of maximum corrosion rate with  $i_L$  for different cover thicknesses ( $\rho = 50 \Omega \cdot \text{m}$ ): (a)  $T = 323^\circ\text{K}$ , (b)  $T = 303^\circ\text{K}$ , (c)  $T = 283^\circ\text{K}$

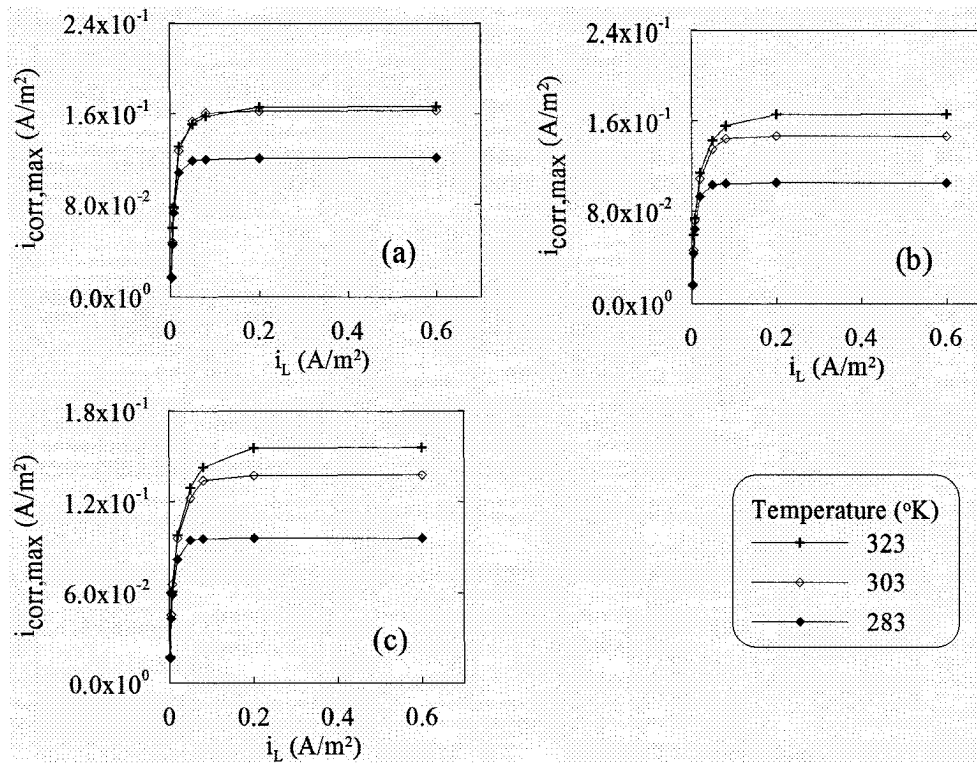


Figure B.7: Variation of maximum corrosion rate with  $i_L$  for different temperatures ( $\rho = 50 \Omega.m$ ): (a)  $d = 140$  mm, (b)  $d = 60$  mm, (c)  $d = 40$  mm

## B.2 DVD contents

The enclosed DVD contains all obtained results of the virtual experiments in four folders. The contents of the folders are explained below:

“Results” folder includes five folders each corresponding to one temperature. Furthermore, each temperature folder includes five other folders containing the results related to five cover thicknesses. Also, each of the cover thickness folders contains eight folders which include data related to each concrete resistivity values, and each of these folders includes eight more folders including the results of each limiting current density. Each limiting current density folder contains one text file and 12 Ms Excel files. The text file contains the kinetic parameters of corrosion used in

obtaining all the results in that specific folder. 10 of the 12 Excel files include the potential and gradient at each node of the domain for 10 A/C ratios. The name of these files is as follows: “ODATA” which stands for Out-put data plus the number of anodic nodes (e.g. ODATA18 which is representative of  $A/C = 18/54 = 0.33$ ). In each Excel file the potential of all the nodes are presented first and the gradient of all nodes follow after which are given in both  $\frac{\partial\phi}{\partial x}$  and  $\frac{\partial\phi}{\partial y}$ . The other two excel files (data.xls and comdata.xls) include the following information: data.xls includes the calculated corrosion current and the number of iterations to convergence for each case in the respective folder. comdata.xls (stands for complete data) includes the potential and current distribution at the surface of steel for each case in the respective folder.

“Equilibrium State” folder on the DVD, includes only one Excel file, Optimumdata.xls which includes the information about the equilibrium state in the following format: temperature, cover thickness, resistivity, limiting current density, optimum A/C and corrosion current.

“Maximum Corrosion Rate” folder includes an Excel file (MaximumRate.xls) which contains the following information: temperature, cover thickness, resistivity, limiting current density and the maximum corrosion current.

The last folder, “Potential Distribution”, includes an Excel file (Potentials.xls) which contains the potential distribution at the surface of concrete and steel/concrete interface and representative data of each case (i.e. temperature, cover thickness, limiting current density, resistivity and A/C).